

ABSTRACT

Title of Document: **DESIGN AND ANALYSIS OF
EXAGGERATED RECTILINEAR GAIT-BASED
SNAKE-INSPIRED ROBOTS**

**James Kendrick Hopkins
Doctor of Philosophy, 2014**

Dissertation directed by: **Professor S. K. Gupta
Department of Mechanical Engineering**

Snake-inspired locomotion is much more maneuverable compared to conventional locomotion concepts and it enables a robot to navigate through rough terrain. A rectilinear gait is quite flexible and has the following benefits: functionality on a wide variety of terrains, enables a highly stable robot platform, and provides pure undulatory motion without passive wheels. These benefits make rectilinear gaits especially suitable for search and rescue applications. However, previous robot designs utilizing rectilinear gaits were slow in speed and required considerable vertical motion. This dissertation will explore the development and implementation of a new exaggerated rectilinear gait that which will enable high speed locomotion and more efficient operation in a snake-inspired robot platform. The exaggerated rectilinear gait will emulate the natural snake's rectilinear gait to gain the benefit a snake's terrain adaptability, but the sequence and range of joint motion will be greatly exaggerated to achieve higher velocities to support robot speeds within the range of human walking speed.

The following issues will be investigated in this dissertation. First, this dissertation will address the challenge of developing a snake-inspired robot capable of executing exaggerated rectilinear gaits. To successfully execute the exaggerated rectilinear gait, a

snake-inspired robot platform must be able to perform high speed linear expansion/contraction and pivoting motions between segments. In addition to high speed joint motion, the new mechanical architecture must also incorporate a method for providing positive traction during gait execution. Second, a new exaggerated gait dynamics model will be developed using well established kinematics and dynamics analysis techniques. In addition to the exaggerated rectilinear gaits which emphasize high speed, a set of exaggerated rectilinear gaits which emphasize high traction will also be developed for application on difficult terrain types. Finally, an exaggerated rectilinear that emphasizes energy efficiency is defined and analyzed. This dissertation provides the foundations for realizing a high speed limbless locomotion capable of meeting the needs of the search, rescue, and recovery applications.

Design and Analysis of Exaggerated Rectilinear Gait-Based
Snake-Inspired Robots

By

James Kendrick Hopkins

Dissertation submitted to the Faculty of the Graduate School of the
University of Maryland, College Park, in partial fulfillment
of the requirements for the degree of
Doctor of Philosophy
2014

Advisory Committee:

Professor Satyandra K. Gupta, Chair/Advisor
Professor Shapour Azarm
Professor Hugh A. Bruck
Professor Jaydev P. Desai
Professor P.S. Krishnaprasad

©Copyright by
James Kendrick Hopkins
2014

Dedication

To my lost loved ones. Special dedication to my grandfather, Varnell Hopkins, Sr., my grandmother, Zetha Smith, and my father-in-law, Lee Hargrove, Sr.

Acknowledgments

First of all, I would like to thank my academic advisor, Dr. Satyandra K. Gupta, for accepting me as a student and guiding me throughout my research. Dr. Gupta's knowledge and analytical skills are only matched by his dedication to his students. His inspiration and patience have helped me immensely during my most difficult times, while pursuing my doctoral degree.

I would like to thank Dr. Shapour Azarm, Dr. Hugh A. Bruck, Dr. Jaydev P. Desai, and Dr. P.S. Krishnaprasad for serving on my dissertation committee in spite of their busy schedules. I am also thankful to my colleagues (past and current) in the Simulation Based System Design Laboratory (SBSD) and Advanced Manufacturing Laboratory (AML) for their guidance and advice. Special thanks given to Brent Spranklin, Krishnanand Kaipa, Luke Roberts, Atul Thakur, Arvind Ananthanarayanan, and Wojciech Bejgerowski.

Finally, I would like to thank my wonderful family. I am especially thankful for the love and support given to me by my beautiful wife, Patrice Hopkins. Without her understanding, I would not have progressed this far. I am also very thankful to my parents, James and Zelma Hopkins, and my brother, Dexter Hopkins, for always being there whenever I needed a listening ear and for keeping me grounded. Finally, I give thanks to my second family, my mother-in-law and her husband, Patricia and William Hobbs, Jr., my sister-in-law, LaShonda Hargrove, and my brother-in-law, Lee Hargrove, Jr., for their understanding and encouragement throughout this journey.

Supporting Published Work

This dissertation is partially comprised of work, published in several revered conferences and journals, in support of this research. These supporting publications and their associated chapters are presented as follows:

Chapter 2:

- Hopkins, J. K., Spranklin, B. W., and Gupta, S. K., 2009, “A Survey of Snake-Inspired Robot Designs,” *Bioinspiration and Biomimetics*, **4**(2), 021001.

Chapter 3:

- Hopkins, J. K., and Gupta, S. K., 2011, “Design of a Drive Mechanism for a Rectilinear Gait-Based Snake-Inspired Robot,” *ASME Mechanisms and Robotics Conference*, Washington DC, **6**, pp. 817-825.
- Hopkins, J. K., and Gupta, S. K., 2012, “Characterization of Forward Rectilinear-Gait Performance for a Snake-Inspired Robot,” *Performance Metrics for Intelligent Systems (PerMIS’12) Workshop*, College Park, MD, pp. 136-144.

Chapter 4:

- Hopkins, J. K., and Gupta, S. K., 2012, “Dynamics-Based Model for a New Class of Rectilinear-Gait for a Snake-Inspired Robot,” *ASME Mechanisms and Robotics Conference*, Chicago, IL, **4**, pp. 151-160.
- Hopkins, J. K., and Gupta, S. K., 2014, “Design and Modeling of a New Drive System and Exaggerated Rectilinear-Gait for a Snake-Inspired Robot” *ASME Journal of Mechanisms and Robotics*, **6**(2), 021001.

Chapter 5:

- Hopkins, J. K., Spranklin, B. W., and Gupta, S. K., 2008, “System-Level Optimization Model for a Snake-Inspired Robot Based on a Rectilinear Gait,” *ASME Mechanisms and Robotics Conference*, Brooklyn, NY, **2**, pp. 913-924.
- Hopkins, J. K., Spranklin, B. W., and Gupta, S. K., 2011, “A Case Study in Optimization of Gait and Physical Parameters for a Snake-Inspired Robot Based on a Rectilinear Gait,” *ASME Journal of Mechanisms and Robotics*, **3**(1), 014503.
- Hopkins, J. K., and Gupta, S. K., 2013, “Analysis of a Low Effort Gait for a Snake-Inspired Robot,” *ASME Mechanisms and Robotics Conference*, Portland, OR.

Table of Contents

ABSTRACT	i
1 Introduction	1
2 Related Work	13
2.1 Overview	13
2.2 Serpentine Motion through Passive Wheels.....	13
2.2.1 Active Cord Mechanism 3 (ACM III)	14
2.2.2 ACM-R3	16
2.2.3 ACM-R5	18
2.2.4 AmphiBot I	19
2.2.5 AmphiBot II	21
2.3 Serpentine Motion with Active Wheels	22
2.3.1 Koryu-II (KR-II)	23
2.3.2 GMD-SNAKE2.....	25
2.3.3 ACM-R4	26
2.3.4 NTUA Robotic Snake.....	27
2.4 Snake-Like Robots with Active Treads	29
2.4.1 Koryu-I (KR-I).....	30
2.4.2 OmniTread OT-8	31
2.4.3 OmniTread OT-4	33
2.4.4 Reconfigurable Robot JL-I	35
2.5 Rectilinear Motion through Vertical Traveling Waves.....	37
2.5.1 Inchworm Robot Introduced by Kotay and Rus 1996	39

2.5.2	Snake Robot Introduced by Dowling 1997.....	40
2.5.3	PolyBot Reconfigurable Robots	42
2.5.4	CMU's Modular Snake Robots.....	44
2.6	Rectilinear Motion through Rigid Body Linear Expansion	46
2.6.1	Slim Slime Robot.....	47
2.6.2	Planar Walker: Planar Inchworm Robot.....	48
2.6.3	Telecubes: Self-Reconfigurable Robots	50
2.7	Rectilinear Motion through Soft Body Peristaltic Motion.....	51
2.7.1	SMA Meshworm Robot by Seok et al. 2010	52
2.7.2	A Braided Mesh Robot by Boxerbaum et al. 2010.....	53
2.7.3	An Inchworm Robot using Electro-conjugate Fluid (ECF).....	54
2.8	Mechanics Models for Snake-Inspired Robots and Gaits	55
2.8.1	Mechanics Analysis Techniques for Manipulators.....	55
2.8.2	Kinematics and Dynamics Models of Snake-Inspired Robots	57
2.8.3	Rectilinear Gait Models for Snake-Inspired Robots.....	62
2.9	Summary	64
3	Design of a Snake-Inspired Robot Capable of Executing a High Speed Gait	66
3.1	Overview	66
3.2	Exaggerated Rectilinear Gait Concept.....	66
3.2.1	High Speed Exaggerated Forward Gait	67
3.2.2	High Speed Exaggerated Turning Gait.....	69
3.3	Design of a New Parallel Mechanism	71
3.3.1	Actuation System Options	72

3.3.2	2RRP Parallel Mechanism	75
3.3.3	Joint Module Final Design.....	82
3.4	Analysis of the Parallel Mechanism.....	84
3.4.1	Mechanism Geometry.....	86
3.4.2	Inverse Kinematics.....	89
3.4.3	Direct Kinematics	90
3.4.4	Jacobian Analysis.....	92
3.4.5	Inverse Dynamics.....	95
3.4.6	Validation of Mechanism Analysis.....	101
3.5	Design of a Multi-Material Variable Friction Force Anchor	105
3.5.1	Variable Friction Force Concept.....	105
3.5.2	Multi-Material Anchor Concept	106
3.5.3	Multi-Material, Variable Friction Anchor Final Design.....	114
3.6	Analysis of Variable Friction Force Anchoring.....	118
3.7	Snake-Inspired Robot Prototype	130
3.7.1	Prototype Fabrication Options	130
3.7.2	R2G2 Prototype	132
3.7.3	R2G2 Robot Performance.....	135
3.8	Summary	142
4	Development of a Dynamics Model for an Exaggerated Rectilinear Gait	144
4.1	Overview	144
4.2	Friction Anchor Module Dynamics Model	146
4.2.1	Friction Anchor Link Characteristics.....	147

4.2.2	Friction Anchor Link Inertia and Jacobian Matrices	154
4.2.3	Friction Anchor Lagrangian Equations of Motion.....	156
4.3	Joint Mechanism Module Dynamics Model	158
4.3.1	Joint Mechanism Module Link Characteristics	159
4.3.2	Joint Mechanism Module Link Inertia and Jacobian Matrices.....	167
4.3.3	Joint Mechanism Module Lagrangian Equations of Motion	168
4.4	1-Module Gait Dynamics Model.....	170
4.4.1	1-Module Dynamics Model Link Characteristics.....	171
4.4.2	1-Module Model Link Inertia and Jacobian Matrices.....	177
4.4.3	1-Module Model Lagrangian Equations of Motion	179
4.5	General n-Module Exaggerated Rectilinear Gait Dynamics Model	181
4.6	Developing an Exaggerated Rectilinear Gait for High Traction.....	192
4.6.1	High Traction Exaggerated Rectilinear Gait Concept	192
4.6.2	Modeling High Traction Gait using n -Module Gait Model.....	196
4.6.3	High Traction Exaggerated Rectilinear Gait Performance	201
4.7	Summary	204
5	Analysis of an Low Effort Exaggerated Rectilinear Gait	206
5.1	Overview	206
5.2	Gait Performance Metric.....	207
5.3	Analysis of a Typical Vertical Wave Rectilinear Gait.....	209
5.4	Low Effort Exaggerated Rectilinear Gait.....	212
5.5	Robot Parametric Model	215
5.6	Analysis of Extension Type Rectilinear Gaits	221

5.7	Case Study.....	226
5.8	Summary	231
6	Conclusion	233
6.1	Intellectual Contributions.....	233
6.1.1	Robot Capable of Executing Exaggerated Rectilinear Gaits	233
6.1.2	Dynamics-Based Gait Model for Exaggerated Rectilinear Gaits	234
6.1.3	Low Effort Exaggerated Rectilinear Gait for Various Missions	234
6.2	Anticipated Industrial Benefits.....	235
6.2.1	Enabling New Applications for Snake-Inspired Robots.....	235
6.2.2	Enabling More Efficient Operation	235
6.3	Future Research.....	236
6.3.1	Expanding the Gait Dynamics Model for Spatial Applications.....	236
6.3.2	System Level Optimization of the Gait and Robot.....	236

List of Figures

Figure 2.1: ACM III [5]	16
Figure 2.2: ACM-R3 [15]	17
Figure 2.3: ACM-R5 [17]	19
Figure 2.4: AmphiBot I [19]	20
Figure 2.5: AmphiBot II [20]	22
Figure 2.6: Koryu-II [14]	24
Figure 2.7: GMD-Snake2 [22]	26
Figure 2.8: ACM-R4 [14]	27
Figure 2.9: Koryu-I [14]	31
Figure 2.10: OmniTread OT-8 [26]	32
Figure 2.11: OmniTread OT-4 [27]	35
Figure 2.12: (a) Reconfigurable Robot JL-I and (b) Separate Modules [29]	36
Figure 2.13: Inchworm Robot by Kotay and Rus 1996 [40]	40
Figure 2.14: Dowling's Complete Snake Robot [1]	41
Figure 2.15: Reconfigurable Robot, PolyBot [42]	43
Figure 2.16: CMU Snake Robot [44]	45
Figure 2.17: Slim Slime Robot [48]	48
Figure 2.18: Planar Inchworm Robot: Planar Walker [50]	49
Figure 2.19: Telecube: (a) CAD model extended and (b) prototype contracted [51]	51
Figure 2.20: SMA Meshworm Robot [55]	53
Figure 2.21: Braided Mesh Robot [56]	54
Figure 2.22: Inchworm Robot using Electro-conjugate Fluid [57]	55

Figure 2.23: Nomenclature for Hirose’s Serpentine Curve [5]	58
Figure 2.24: Parameters in Chirikjian and Burdick’s approach [59]	59
Figure 2.25: Three link model of ACM III [62]	61
Figure 2.26: Two-extensor robot Gait and Mapping [46].....	62
Figure 2.27: Transverse Gait (Forward, Initially retracted) [50]	62
Figure 2.28: Turning Gait (Clockwise, Initially retracted) [50]	63
Figure 3.1: Theoretical High Speed Forward Gait Sequence	69
Figure 3.2: Theoretical High Speed Turning Gait Sequence	70
Figure 3.3: Hitec HS-985MG	74
Figure 3.4: Parallel Mechanism Concepts (Kinematic Representation).....	77
Figure 3.5: Mechanism (a) Contracting, (b) Extending, (c) Pivoting Up and (d) Down..	81
Figure 3.6: Parallel Mechanism Concept CAD Model.....	83
Figure 3.7: Joint Module Final CAD Model.....	83
Figure 3.8: Prototype Module (a) Contracted and (b) Extended	84
Figure 3.9: Parallel Mechanism Kinematic Representation	86
Figure 3.10: Limb 1 (RPR) Kinematic Representation	87
Figure 3.11: Limb 2 (RPR) Kinematic Representation	88
Figure 3.12: Kinematics Model Inputs (a) Output Link and (b) Input Links	101
Figure 3.13: Inverse Kinematics: Pro-E vs. Model: (a) Theta1 and (b) Theta2	102
Figure 3.14: Direct Kinematics: Pro-E vs. Model: (a) x_A and (b) Beta	102
Figure 3.15: Jacobian Analysis: Pro-E vs. Model: (a) Theta1 and (b) Theta2 Velocity. 102	
Figure 3.16: Dynamics Inputs: (a) Output Link Kinematics and (b) Forces	103
Figure 3.17: Dynamics: Pro-E vs. Model: (a) Torque1 and (b) Torque2	104

Figure 3.18: Dynamics Input w/Gravity: (a) Output Link Kinematics and (b) Forces...	104
Figure 3.19: Dynamics w/Gravity: Pro-E vs. Model: (a) Torque1 and (b) Torque2	104
Figure 3.20: Friction Anchor Concept	105
Figure 3.21: Multi-Surface Anchor Concepts (Kinematic Representation)	108
Figure 3.22: Multi-Surface Anchor Down Selected Concept.....	113
Figure 3.23: Single Surface, Selectable Anchor Concept.....	114
Figure 3.24: Friction Anchor Module Final CAD Model.....	115
Figure 3.25: Multi-Material, Variable Friction Anchor Prototype	116
Figure 3.26: Variable Friction Anchoring	118
Figure 3.27: Variable Friction Anchoring CAD Model.....	119
Figure 3.28: Friction Anchoring Geometric Model	120
Figure 3.29: Force Normal, F_l , at the Friction Anchor-Terrain Contact.....	129
Figure 3.30: R2G2: Final Design CAD Model.....	132
Figure 3.31: R2G2: Prototype of the Snake-Inspired Robot Design	133
Figure 3.32: Control Architecture Schematic	135
Figure 3.33: High Speed Forward Gait.....	136
Figure 3.34: High Speed Turning Gait	136
Figure 3.35: Robot Cross-Section vs. Velocity Performance.....	141
Figure 3.36: Robot Length vs. Velocity Performance	141
Figure 3.37: Snake-Inspired Robot Froude Number	142
Figure 4.1: Snake-Inspired Robot Design and Simplified Kinematic Representation ...	145
Figure 4.2: CAD Model of Actual Friction Anchor	146
Figure 4.3: Dynamics Model Representation of a Friction Anchor.....	146

Figure 4.4: CAD Model of FA Link 0	147
Figure 4.5: CAD Model of FA Link 1	150
Figure 4.6: CAD Model of FA Link 2	152
Figure 4.7: Validation Results of FA Dynamics Equations.....	157
Figure 4.8: CAD Model of Actual Joint Mechanism Module	158
Figure 4.9: Dynamics Model Representation of a Joint Mechanism Module	159
Figure 4.10: CAD Model of JM Link 2 (Base Link)	159
Figure 4.11: CAD Model of JM Link 3 (2 nd Link)	162
Figure 4.12: CAD Model of JM Link 4 (3 rd Link).....	164
Figure 4.13: Validation Results of JM Dynamics Equations.....	169
Figure 4.14: CAD Model of a 1-Module Robot	170
Figure 4.15: Dynamics Model Representation of a 1-Module Robot.....	170
Figure 4.16: CAD Model of 1-Module Model Link 2	171
Figure 4.17: CAD Model of 1-Module Model Link 4 (End Link)	174
Figure 4.18: FA Validation Results of 1-Module Model Dynamics Equations	181
Figure 4.19: JM Validation Results of 1-Module Model Dynamics Equations	181
Figure 4.20: CAD Model of n-Module Model Link 4'	182
Figure 4.21: 5-Module Robot Initial Position before High Speed Turning Gait Step 2. 189	
Figure 4.22: 5-Module Robot Final Position after High Speed Turning Gait Step 2	189
Figure 4.23: <i>n</i> -Module Model Validation, FA Reaction Forces	190
Figure 4.24: <i>n</i> -Module Model Validation, JM 1 Reaction Forces	190
Figure 4.25: <i>n</i> -Module Model Validation, JM 2 Reaction Forces	190
Figure 4.26: <i>n</i> -Module Model Validation, JM 3 Reaction Forces	191

Figure 4.27: <i>n</i> -Module Model Validation, JM 4 Reaction Forces	191
Figure 4.28: <i>n</i> -Module Model Validation, JM 5 Reaction Forces	191
Figure 4.29: Shifting Center of Mass.....	193
Figure 4.30: Theoretical High Traction Forward Gait Sequence	194
Figure 4.31: Theoretical High Traction Turning Gait Sequence	196
Figure 4.32: <i>n</i> -Module Model of High Speed Forward Gait Step 1	197
Figure 4.33: <i>n</i> -Module Model of High Speed Forward Gait Step 2	197
Figure 4.34: Friction Anchor Reaction Forces for High Speed Forward Gait Steps 1-2	198
Figure 4.35: <i>n</i> -Module Model of High Traction Forward Gait Step 1	199
Figure 4.36: <i>n</i> -Module Model of High Traction Forward Gait Step 2	199
Figure 4.37: FA Reaction Forces for High Traction Forward Gait Steps 1-2	199
Figure 4.38: <i>n</i> -Module Model of High Traction Forward Gait Step 4	200
Figure 4.39: FA Reaction Forces for High Traction Forward Gait Steps 2-4	200
Figure 4.40: High Traction Forward Gait.....	201
Figure 4.41: High Traction Turning Gait.....	203
Figure 5.1: Vertical Wave Rectilinear Gait [84].....	210
Figure 5.2: Cumulative Effort over Time for Typical Vertical Wave Rectilinear Gait..	211
Figure 5.3: Low Effort Rectilinear Gait.....	213
Figure 5.4: Computing Effort for an Expansion Rectilinear Gait.....	215
Figure 5.5: Joint Mechanism Module	217
Figure 5.6: Friction Anchor Module.....	220
Figure 5.7: Complete R2G2 Robot CAD Model	221
Figure 5.8: High Speed Forward Gait.....	222

Figure 5.9: High Traction Forward Gait	222
Figure 5.10: Cumulative Effort over Time for Expansion Type Rectilinear Gaits	223
Figure 5.11: Experimental Low Effort Gait Trial	225
Figure 5.12: Predicted Solenoid Mechanism Engagement	227
Figure 5.13: Cumulative Effort over Time for Case Study Expansion Gaits	228
Figure 5.14: Performance of Expansion Type Gaits with no Potential IEDs	230
Figure 5.15: Performance of Expansion Type Gaits with Potential IEDs	230

List of Table

Table 1.1: Characteristics of Typical Vertical Wave Gaits	8
Table 1.2: Characteristics of Exaggerated Rectilinear Gaits	10
Table 3.1: Parallel Mechanism Design Comparison.....	81
Table 3.2: Kinematics Constants	101
Table 3.3: Dynamics Constants	103
Table 3.4: Traction Study Results ($\theta_{FA} = 15^\circ$).....	117
Table 3.5: Traction Study Results ($\theta_{FA} = 25^\circ$).....	117
Table 3.6: Traction Study Results ($\theta_{FA} = 35^\circ$).....	118
Table 3.7: Robot Performance Data.....	140
Table 4.1: D-H Link Parameters for FA Module.....	154
Table 4.2: D-H Link Parameters for JM Module.....	167
Table 4.3: D-H Link Parameters for FA-JM Model	177
Table 4.4: High Traction Forward Gait Mapping to Gait Model for Odd n -Modules....	202
Table 4.5: High Traction Forward Gait Mapping to Gait Model for Even n -Modules ..	202
Table 4.6: High Speed Forward Gait Mapping to Gait Model for all n -Modules	202
Table 4.7: High Traction Turning Gait Mapping to Gait Model for Odd n -Modules	204
Table 4.8: High Traction Turning Gait Mapping to Gait Model for Even n -Modules...	204
Table 4.9: High Speed Turning Gait Mapping to Gait Model for all n -Modules.....	204
Table 5.1: Vertical Wave Gait Parameters	210
Table 5.2: Expansion Type Gait Parameters.....	221
Table 5.3: Cyclic Performance of Gaits.....	222
Table 5.4: Experimental Gait Performance Data	225

Table 5.5: Case Study Expansion Type Gait Parameters	227
Table 5.6: Case Study Gait Performance	228

1 Introduction

1.1 Background

1.1.1 Advantages of Snake Locomotion

Because of their long, slender, limbless bodies, snakes possess the ability to traverse small enclosed environments, such as small holes, tunnels, and gaps, which would prohibit most legged animals. Another advantage is terrainability, which is the ability of an animal to traverse rough or difficult terrain. A snake can crawl over rugged terrain as effortlessly as it can traverse smooth terrains and environments, allow much more maneuverability compared to conventional man-made locomotion concepts. Although legged locomotion has a high degree of terrainability, there are environments which are difficult even for legged locomotion, such as soft sand or soil, whereas snakes are able to effectively traverse these environments due to high traction. Traction is the force that can be applied to propel an animal forward. Traction is usually a product of the animal's weight, its distribution, and the coefficient of friction between the animal and the terrain. Traction forces of a snake can be quite high, for example, a snake can exert a force up to a third of its own weight [1]. In contrast with legged animals, the mass of a snake is distributed over a large area and the resulting forces per unit area are small enough to prevent the snake from significantly sinking into the soil and sand. However, most legged animals will have higher force concentrations between their feet and the terrain, resulting in the animal sinking into the terrain. A final advantage of snakes over most limbed animals and man-made locomotion mechanisms comes from their unique skeletal and muscular structure. Snakes are composed of a long chain of vertebra and muscles and use changes in their body shape to move and grasp objects. Because this long chain of

similar segments has more Degrees of Freedom (DOF) than is usually necessary for a given task, the snake's body has a certain degree of redundancy. This means that if segments of the snake are restrained from movement by some means, the snake is still capable of limited but effective locomotion through use of its other segments.

Upon examination of the various abilities of snakes, the advantages of artificial locomotors capable of snake-like motion become readily apparent. Advantages such as terrainability in a snake-inspired robot would be very useful in applications like exploration and reconnaissance. This allows the snake-inspired robot to navigate a variety of surface types without the need for physical modifications to adapt to the changing terrain types, such as, larger wheels or incorporating tracks compared to wheeled robots. Such ability is also very useful in exploration missions where the terrain type and surface roughness may be largely unknown and the possibility of modification of the exploration vehicle is impracticable. Another advantage of snake-inspired robots is the redundancy of their locomotion mechanism. The locomotion for a snake-inspired robot would be accomplished through numerous actuators and segments and typically would not require all the actuators for effective locomotion. Therefore, if a number of actuators were damaged, the ability of the robot to advance may not be impaired -- a very useful feature in search and rescue missions where unstable environments may damage portions of the robot.

1.1.2 Types of Snake Locomotion

There are four basic snake locomotion gaits, which have served as inspiration for all snake-inspired robotic locomotion to date. These four gaits are known as: (1) lateral undulatory, (2) concertina, (3) crotaline and (4) rectilinear progression [2, 3]. All snakes

are capable of performing some combination of these locomotion gaits. By switching between these gaits, a snake is capable of traversing a wide variety of terrestrial obstacles and environments.

Lateral undulatory motion, also known as serpentine motion, is considered one of the fastest, most common modes of the travel for snakes and is employed by both land bound snakes and swimming snakes [2]. Serpentine motion is also one of the most recognizable snake locomotion gaits by the general public. It is described by a series of S-shaped, sinusoidal-like curves formed by the body while moving forward. The body moves forward along the S-shaped path while the head lays out additional curves. Typically, serpentine locomotion is exhibited by a snake when moving through grass or over a rocky surface of sufficient irregularities. Each segment of the snake pushes laterally against small discontinuities in the terrain, such as rocks and sticks. Through this action, the snake is able to continuously move forward in the S-shaped pattern. Serpentine motion is illustrated in Figure 1.1 where the snake glides over the surface of a smooth metal plate from which a number of smooth glass pegs protrude, depicted as circles in contact with the snake.

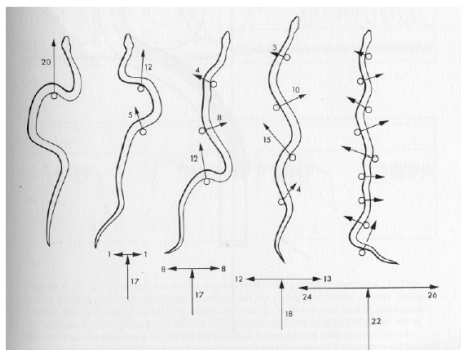


Figure 1.1: Serpentine Motion [2]

Concertina motion is a specialized locomotion gait that is exhibited by a snake either when confined within a channel, shown in Figure 1.2, or used by tree climbing snakes when reaching for a branch [2]. In this motion, the snake first compresses its length, as an accordion-like shape. Next, it stretches the foremost portion of its body outward or upward, depending on the environment, using its tail as an anchor. Finally, the snake anchors the forward portion of its body and pulls the tail along. Although concertina movement is highly characteristic of snakes moving in channels, it may also occur in a modified form when a snake is moving over open ground of fairly uniform surface. An example of this is given in Figure 1.3.

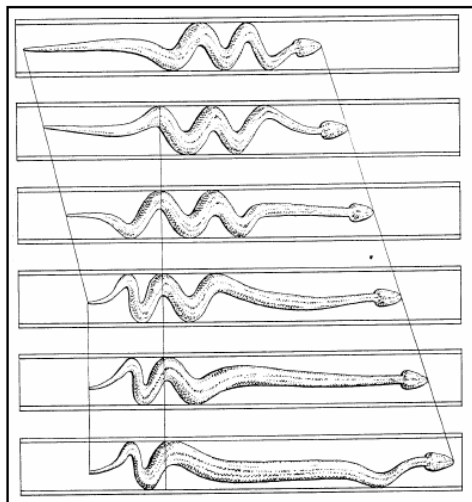


Figure 1.2: Concertina Motion in a Channel [2]

When a snake moves over a relatively smooth and uniform surface, its mode of progression tends to be irregular, and serpentine motion is replaced either by concertina or crotaline motion. Crotaline motion, also known as sidewinding motion, allows some snakes to move across smooth surfaces such as sand [2]. While executing sidewinding only two short portions of the snake's body are in contact with the terrain at any given time. The remaining segments of the body are lifted from the terrain. A snake executing

side-winding leaves a series of parallel tracks inclined at an angle to the path of motion of the animal's head, illustrated in Figure 1.4 [2]. These tracks represent lines along which each segment of the body is placed and, in turn, lifted in order to be moved to the next track in the series.

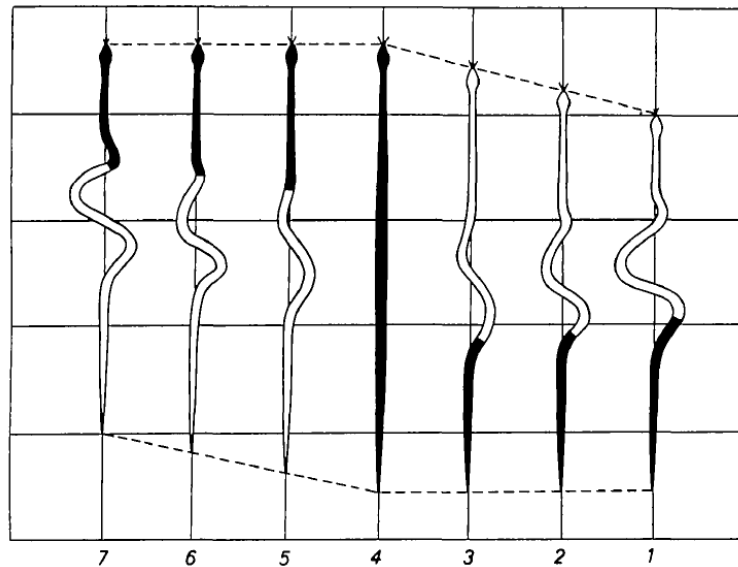


Figure 1.3: Concertina Motion through Open Ground [2]

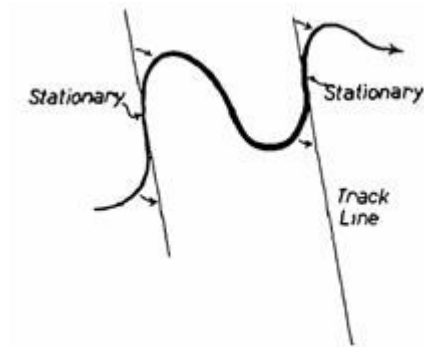


Figure 1.4: Tracks left by sidewinding motion [2]

The final natural snake gait is rectilinear locomotion, which is described as the whole snake moving forward along a straight line, sliding against the terrain [3]. Lateral bending of the body and lateral resistances do not contribute to the motion in contrast to the other locomotion modes. An explanation of the mechanics of this gait can be summed

rectilinear gait is highly stable due to the fact that the majority of the robot's mass is in contact with the terrain and only a small portion of the robot is lifted from the terrain at any given time. This feature also allows rectilinear motion to function on a wide variety of terrains; the shape of the robot can easily contour to changes in the terrain. In general, robot platforms which demonstrate serpentine motion have only been successful through the inclusion of passive wheels on each segment (or other methods to impart anisotropic friction) to simulate the snake pushing laterally against small discontinuities in the terrain. These passive wheels result in a system which can only be effective over smooth hard terrains. Rectilinear motion provides pure undulatory motion without passive wheels.

Although rectilinear gaits are very useful, the current platforms that demonstrate them are relatively slow. Average human walking speed is approximately 2-3 mph [4]. For a robot utilizing rectilinear gait-based locomotion to be useful in real world applications, such as exploration, rescue operations, and general military reconnaissance, the robot must at least achieve human walking speed in order to keep pace with the human field team that it supports. Typical rectilinear gaits, which we designate as vertical wave type gaits, also have other limitations beyond low forward velocity as presented in Table 1.1. In addition to high speed, robots supporting search, recovery, and rescue operations must also possess appropriate traction, cross-sectional area and energy efficiency characteristics to traverse the various terrains and environments. In order to achieve the desired forward velocity while maintaining a small cross section, a novel approach to emulating rectilinear motion is needed for snake-inspired robots.

Terrain Versatility	Basic characteristics of rectilinear gait
Traction	Limited traction
Small Cross Section	Lead to low forward velocity
High Speed	Requires large cross-sectional area
Energy Efficiency	Vertical wave gaits inefficient

Table 1.1: Characteristics of Typical Vertical Wave Gaits

The challenges involved in employing rectilinear motion in high speed applications can be classified into two categories: gait design challenges and robot design challenges.

- i. *High speed rectilinear gait challenges.* Most robots utilizing rectilinear gaits advance by propagating a vertical pulse along the body length by successive lifting and displacing adjacent segments. In these vertical wave type gaits, forward displacement per cycle is considerably limited since a significant amount of the robot displacement per cycle is normal to the surface being traversed. Therefore, to achieve human walking speeds, the segments of the robot would have to be drastically lengthened and larger joint motors would be needed to actuate the longer segments, making the robot unsuitable for use in small, tight spaces. An alternative is to develop an exaggerated rectilinear gait which emulates motion observed in snakes in a high speed fashion, where the segments expand and contract linearly very quickly with little to no vertical displacement. This exaggerated gait will allow most of the joint motion to be directly used in forward displacement. However, successful implementation of such a gait requires developing a method of anchoring the robot to the terrain at desired points to provide positive forward displacement during extension. In addition, a gait will need to be developed for changing the orientation of the robot. Finally, the development of a kinematics and dynamics-based model of the new exaggerated

rectilinear gait type will be necessary to make accurate predictions of gait behavior and robot performance.

- ii. *Snake-inspired robot platform design challenges.* In addition to the challenges involved with developing a high speed exaggerated rectilinear gait, there also issues with executing the gait on available snake-inspired platforms. Prior to this work, a snake-inspired robot capable of high speed linear joint motion while remaining compact in cross-section did not exist. The challenges preventing development of a high speed platform include: developing a high speed linear actuator with a compact cross-section, compact length, and light weight; developing a high speed platform which carries its own power source on-board; and developing an anchoring mechanism which is effective on various terrains. Throughout this work, both the gait and platform design challenges are further discussed and the approaches for overcoming these challenges are presented.

1.3 Dissertation Goals and Scope

The goal of this work is to develop and demonstrate a class of exaggerated rectilinear gaits, which enable high speed limbless locomotion. The exaggerated rectilinear gait emulates the natural snake rectilinear gait to gain the benefit a snake's terrain adaptability, but the sequence and range of joint motion greatly exaggerated to achieve velocities within the range of human walking speed. Within the scope of this work, the new exaggerated gait class is defined and a dynamics model is developed to predict the gait behavior. Also, a new mechanical architecture is developed for a snake-inspired robot capable of executing the exaggerated rectilinear gait class, while maintaining a small cross-sectional area for utilization in various locations and conditions. Finally, new

gaits for high traction and energy efficiency are introduced based on the high speed gait.

Table 1.2 shows the impacts of the new exaggerated gait on the operational needs for search, rescue and recovery missions.

Terrain Versatility	Basic characteristics of rectilinear gait
Traction	Enabled using variable force anchoring
Small Cross Section	Enabled with new mechanism design
High Speed	Fast body extension and contraction
Energy Efficiency	Enabled with gaits for different missions

Table 1.2: Characteristics of Exaggerated Rectilinear Gaits

Specific objectives of this dissertation include the following:

- i. *Development of a snake-inspired robot capable of executing exaggerated rectilinear gaits.* Demonstration of a new high speed exaggerated rectilinear gait class is executed using a novel mechanical design for a snake-inspired robot platform, which is developed and presented in this work. To achieve the functional requirements of the gait, a snake-inspired robot platform must be able to perform high speed linear expansion/contraction and pivoting motions between segments. The mechanical design is limited to locomotion which mimics snake-like motion. This restriction eliminates design solutions that include wheels, tracks, legs, or any other joint motion which cannot be observed in natural snakes. This limitation serves to prevent design solutions which may be susceptible to the same terrain and environmental limitations as wheel or leg based modes of locomotion. In addition to high speed, the new mechanical architecture must also incorporate a method for providing positive traction for the robot to counter to the reaction forces of the joints during gait execution. Chapter 3 of this dissertation presents the design and fabrication of such a platform.

- ii. *Development of an exaggerated rectilinear gait dynamics model.* The concept for the high speed exaggerated rectilinear gait centers about the ability of the robot platform to rapidly expand and contract its segments linearly with little to no vertical displacement. This ability allows most of the joint motion and energy to be used in forward displacement, as opposed to typical rectilinear gaits observed in most snake-inspired robots. The concept also employs a method of anchoring the robot to the terrain to provide traction on multiple surfaces. Due to the possibility of high impact forces generated during sudden stops in high speed actuation, we must also understand the forces generated between robot segments through gait execution. We address this need through the development of a new exaggerated gait dynamics model. In addition to modeling internal forces, the gait model can be used to support the selection of gait and robot parameters. The new gait dynamics model is presented in detail in Chapter 4.
- iii. *Design of exaggerated gaits to support different types of missions.* An expansion type rectilinear gait which emphasizes energy efficiency is identified and analyzed. Many published snake-inspired robots mimic rectilinear motion by utilizing a travelling vertical wave, propagated from one end of the robot to the other. This motion results in forward progression of the robot through the lifting and displacement of adjacent segments relative to one another as the wave passes through the body. However, much of the motion observed in the robot throughout the gait cycle is normal to the surface being traversed and does not directly change the forward position. Therefore, these gaits tend to be highly energy inefficient and limited in terms critical performance factors, such as, range. The

proposed energy efficient exaggerated rectilinear gait will propagate a wave throughout the body of the robot via expansions and contractions of the segments, nearly eliminating all vertical motion in the robot during gait execution, resulting in more energy efficient forward motion. In addition to energy efficiency, an exaggerated rectilinear gait is developed with higher traction potential. The gait will be utilized for difficult terrain types, such as hard smooth and rugged loose surfaces. The high traction gait and an analysis demonstrating the improved traction potential are presented in Chapter 4. A complete analysis of the energy efficient gait and comparison to other rectilinear gaits are presented in detail in Chapter 5. In addition, a case study demonstrating advantages of the gait is conducted.

2 Related Work

2.1 Overview

In this chapter, we will review prior work in field of snake-inspired and snake-like robotics. Some of the work surveyed has yielded snake-inspired robots capable of executing rectilinear gaits; however, none of the designs or gaits to date has demonstrated high speed on a small platform. The robot designs surveyed in this chapter are divided into major subcategories: (1) Robots with Passive Wheels, (2) Robots with Active Wheels, (3) Robots with Active Treads, (4) Rectilinear Motion through Vertical Traveling Waves, (5) Rectilinear Motion through Rigid Body Linear Expansion and (6) Rectilinear Motion through Soft Body Peristaltic Motion. Finally, we will review some of the previous work to develop rectilinear gait models.

2.2 Serpentine Motion through Passive Wheels

The first category of snake-inspired robot designs is arguably the most well-known: snake-inspired robots with passive wheels. Since their introduction by Shigeo Hirose, a large number of current robot designs executed lateral undulation using passive wheels to mimic snake motion [5]. Lateral undulatory motion, also known as serpentine motion, is considered one of the fastest, most common modes of the travel for natural snakes and is employed by both land-bound and swimming snakes [2]. Serpentine motion is also one of the most recognized snake locomotion gaits by the general public. Serpentine motion is described by a series of S-shaped, sinusoidal-like curves formed by the body as the snake moves forward. In most robots, this motion is usually mimicked by the utilization

of the serpenoid curve, introduced by Hirose, and using passive wheels to resist lateral movement of the robot's segments [5].

In this section, we will discuss Active Cord Mechanism designs and AmphiBot robot designs. Additionally, noteworthy robot designs with passive wheels also include the Michigan Snake 1 (MS-1), the Variable Geometry Truss (VGT), G.S. Miller's snake robots, and a robot design introduced by Dalilsafaei 2008. The MS-1 design introduced an interesting variation of the passive wheel-based, snake-inspired robot design. MS-1 utilized links with linear solenoids with sharp tip pins and ball casters to achieve forward motion [6]. The VGT consisted of a longitudinal repetition of 10 identical truss modules, each one equipped with idler wheels and linear actuators in a 3-DOF planar parallel manipulator configuration [7-9]. G.S. Miller developed a series of snake-inspired robot, S1-S5, which utilized passive wheels to assist in movement using a lateral serpentine gait [10-12]. In addition to mimicking the movements of snakes, Miller's design goals also included realism and aesthetics as part of the robot design, which led to his most sophisticated design, called the S5. The robot design, introduced by Dalilsafaei, used an artificial muscle actuator which consisted of a motor and a set of ropes to control the relative motion between robot modules [13]. The modules were connected to one another through rubber joints.

2.2.1 Active Cord Mechanism 3 (ACM III)

The ACM III, introduced by S. Hirose, consisted of 20 links and was capable of only planar motion [5, 14]. At the core of Hirose's theories about snake locomotion was the idea that the scale pattern produces anisotropy in the friction coefficients between the lateral and tangential frictions on their ventral surface. This concept is the basis for

forward propulsion using the serpentine gait. In order to mimic the function the snake's scale pattern in a robot, Hirose placed small wheels on casters on the bottom of each link, facing in the tangential direction of the length of the robot. This resulted in a very low friction coefficient in the tangential or forward direction and a high friction coefficient in the lateral direction. The links were connected using powered joints that allowed rotation relative to one another. Locomotion was accomplished by propagating a wave in the form of the serpenoid curve throughout the robot. This meant that locomotion was only accomplished through shape changing, like a real snake.

The primary applications of the robot platform were to further Hirose's study of snake-like motion and demonstrate the serpenoid curve developed by Hirose. The robot was mostly demonstrated over smooth surfaces and labyrinths with walls equal in height to the robot. The robot, shown in Figure 2.1, had a length of 2000 mm and weighed 28 kg. Each link was 162 mm in height, 102 mm in length, and 144 mm in width. Each joint was actuated using a servo system that consisted of a 10W DC motor and a potentiometer. The servomotor in each segment could bend each trailing segment to the left and right. In laboratory experiments, the ACM III utilized limit switches as tactile sensors to signal the robot when it was in contact with walls or obstacles. The tactile sensors allowed the robot to react to its environment and conform to irregular channels in labyrinth experiments. The ACM III achieved a forward velocity of 400 mm/s.



Figure 2.1: ACM III [5]

2.2.2 ACM-R3

Hirose later applied his findings from the initial ACM robots to an improved robot design called the ACM-R3, illustrated in Figure 2.2 [14-16]. The most obvious differences in the ACM-R3 compared to previous designs were that it was capable of 3D motion and it had large wheels on all sides of the body. These large passive wheels had a diameter of 110 mm, and added additional functionality to the system because they can roll against obstacles. The links were designed to contain all the components within a shell that had orthogonal axes of rotation on each end. In addition to serpentine locomotion, the robot could also lift its body up to move over obstacles. Hirose also experimented with other gaits using this mechanism, including lateral rolling and sidewinding gaits. The design of the ACM-R3 provided significant improvements over the earlier ACMs, because it was self-contained, meaning that it had on-board power and could be radio-controlled.



Figure 2.2: ACM-R3 [15]

The ACM-R3 was designed to be more functional in an actual search and rescue application. The ACM-R3 had a width and height of 110 mm due to its 110 mm diameter passive wheels. It had a total length of 1755 mm and weighted 12.1 kg. The maximum twist angle of any of the joints was 62.5 degrees in each direction (without wheels it is 91 degrees). A key requirement in the development of this design was that the robot be able to lift body segments. Hirose accomplished this by using servomotors that could provide a maximum of 19.1 Nm of torque and a joint speed of 36 deg/s, and the design could lift 8 units. It was not documented if the robot was equipped with sensors or not, however, the robot was commanded by an operator with an R/C controller. Unlike the initial ACM robots, that used an electrical power supplying tether, the ACM-R3 contained batteries for power. Each unit contained its own battery and controller, making the design fully modular. The design provided an extra DOF such that the robot could lift up to maneuver over obstacles. The design, however, still required a flat enough surface to allow the wheels to roll in order to achieve locomotion.

2.2.3 ACM-R5

The ACM-R5, shown in Figure 2.3, was an amphibious design also introduced by Hirose and his design team [14, 17, and 18]. The joint mechanism between each segment or module of the robot consisted of a universal joint and bellows. The universal joint acted as the bones and bellows acted as an integument, an enveloping layer (as a skin, membrane, or cuticle) of a snake. The universal joint had one passive twist joint at the intersection point of two bending axes to prevent mechanical interference with bellows. The robot consisted of nine segments with 2-DOF joints between the segments. To generate propulsive force through undulation, the robot required a resistance property to allow it to glide freely in a tangential direction but not in a normal direction. Due to the inclusion of paddles and passive wheels around the body of each segment, the robot obtained the required resistance property on both ground and in water.

The ACM-R5 measured 1750 mm in length and 80 mm in diameter. The robot's total weight was 7.5 kg. Actuation was achieved by a pair of servomotors in each water tight module, which were capable of 9 Nm of torque each. Maximum joint speed was 70 deg/s. The ACM-R5 incorporated an advanced control system. Each modular unit had a CPU, battery and motors so that they could operate independently. Each unit automatically recognized its number from the head and how many units were in the robot through communication between the modules. Using this system, an operator could easily remove, add, and exchange units without major modification to the robot. Although the robot was quite advanced and performed well on flat surfaces and in the water, the robot was still mostly a demonstration platform. Hirose and his design team stated that "a large

number of problems still remain for realization of practical snake-like robots, both in software and hardware.”



Figure 2.3: ACM-R5 [17]

2.2.4 AmphiBot I

AmphiBot I, shown in Figure 2.4, was a modular amphibious snake-inspired robot, constructed out of several identical segments, known as elements [19]. Quoting the authors, “The project does not aim at mimicking a snake or a lamprey per se, but to take inspiration of their body shape and their neuronal control mechanisms to develop novel types of robots that exhibit dexterous locomotion.” The robot design included seven actuated elements. Each of the robot’s elements had a one DOF and the elements were fixed such that all axes of rotation were aligned. The robot was designed to have distributed actuation, power and control; therefore, each element carried its own DC motor, battery, and microcontroller. For motion on a terrain, the robot could be equipped with removable sets of passive wheels. To support its amphibious role, each individual element was made waterproof, as opposed to having a covering over the entire chain of elements. This approach was deemed preferable since it ensures that a possible would

only damage a single element. Also, each element was made to be slightly buoyant, so that the robot would passively float at the surface of the water when inactive. In addition, the center of gravity of each element was purposely placed below the geometrical center, in order to obtain a vertical orientation that self-stabilized in water.



Figure 2.4: AmphiBot I [19]

The purpose of the robot was to serve as a test bed to support two research goals: (1) to take inspiration from snakes and elongated fish such as lampreys to produce a novel type of robot with dexterous locomotion abilities, and (2) to use the robot to investigate hypotheses of how central nervous systems implement these abilities in animals. Each element of AmphiBot I had a length of 70 mm and a cross-section of 55 mm by 33 mm. The robot had a total length of approximately 490 mm. Each element was actuated using a 0.75W DC motor which drives a set of reduction gears with a reduction factor of 400 and an efficiency of approximately 60%. The DC motors had a maximum torque of 1.2 Nm. The output axis of the gears was connected to a potentiometer and the next element. Each joint could achieve a maximum oscillation frequency of approximately 0.3 Hz if the full amplitude (± 45 deg) was used. The speed of the robot had been measured by running the robot on a Styrodur® plain surface, a type of rigid

polystyrene foam. This material was chosen by the authors due to its frictional properties between the material and the wheels of the robot. During trials, the robot achieved a maximum surface locomotion speed of 35 mm/s.

2.2.5 AmphiBot II

AmphiBot II, shown in Figure 2.5 was the newer version of AmphiBot I equipped with improvements based on trials of the first robot prototype [20]. The construction of AmphiBot II had been simplified, allowing all of the components to be assembled without soldering. The second robot was also equipped with more powerful motors, with maximum torque increased by a factor of 3.5 compared to the first robot design. Like AmphiBot I, the robot design included seven actuated elements, however with the new electronics suite; a robot with up to 127 segments can theoretically be built by adding other elements to the chain. Also, the robot had been designed to be tether-less, using wireless communication through an internal transceiver. Finally, AmphiBot II was equipped with central pattern generators (CPGs). The motor commands were generated directly in the robot, by the central pattern generator running on a microcontroller, therefore removing the need of running the controller on an external computer. The robot was still amphibious and made use of removal wheel sets to achieve locomotion on surface terrains.

Like AmphiBot I, the application of the robot was to serve as a test bed to support two new research goals: (1) to build an amphibious snake-like robot that can both crawl and swim for outdoor robotics tasks, taking inspiration from snakes and elongate fish, such as lampreys, and (2) to demonstrate the use of CPGs as a powerful method for online trajectory generation for crawling and swimming in a real robot. Each element of

AmphiBot II had a length of 94 mm and a cross-section of 55 mm by 37 mm. The total length of the robot was 772 mm. Each element was actuated using a 2.83W DC motor which had a maximum torque of 4.2 Nm and drove a gearbox with a reduction factor of 125. The output of the gear set was fixed to a connection piece that inserted into the next element. Internal to each element, a water detector circuit was incorporated at the bottom of the element and used internally to detect and localize any leakage. When water was detected, the circuit activated a blinking LED mounted on the top of the element, alerting the user of the leakage. Unlike AmphiBot I, the robot was primarily tested on wooden surfaces, as opposed to the Styrodur® plain surface, during speed trials. During trials, the robot was reported to have achieved a maximum surface locomotion speed of 400 mm/s. The robot was also reported to have achieved a maximum swimming speed of 230 mm/s.



Figure 2.5: AmphiBot II [20]

2.3 Serpentine Motion with Active Wheels

The second snake-inspired robot category encompasses robots that utilize active driven wheels to provide propulsion for the robot. However, the robot designs still exhibit snake-like motion due to the multi-segment configuration. One of the main advantages of using powered wheels is ability to simulate snake-like motion without a large number of segments [14]. Powered wheels also generally are more able to deal with non-smooth terrain types. Although the introduction of powered wheels adds additional flexibility in terms of active DOF, it also adds additional complexity to the robot, which now has to

actively control these additional DOF and coordinate them with the rest of the actuated joints during global movement.

In this section, we will discuss the following four robot designs in detail: Koryu-II, GMD-SNAKE2, ACM-R4 and the NUTA Robotic Snake. In addition to these robots, two additional examples of robots with active wheels were the OBLIX and the Genbu robots. OBLIX was an oblique swivel mechanism-based 16 segment robot arm prototype which was equipped with drive wheels and used mimic snake-inspired locomotion [5]. The oblique swivel joint rotated around an axis that formed an angle from the central axis of the arm and a coaxial swivel joint. Genbu1 was characterized by multiple bodies connected by passive joints and multiple active wheels of large diameter [14, 21]. The bodies of Genbu2 were connected by elastic joints so that the robot can adapt to changes in the terrain. Genbu3 was loaded with a motor driver and battery in each wheel, and micro controller in each body, providing it with adaptive control for the terrain.

2.3.1 Koryu-II (KR-II)

The KR-II, seen in Figure 2.6, had a similar configuration to the KR-I [5, 14]. The robot was composed of a lead unit (link 0) and six cylindrically shaped units (link 1-6) which had three DOF: the first in the rotational axis which swings to the left and right of each segment (*q-axis*), the second in the perpendicular axis (*z-axis*) which slides the segments up and down, and the third in the wheel axis (*s-axis*) for the purpose of forward advancement. Unlike its processor, KR-I, KR-II used wheels instead of crawlers on the *s-axis* for the purpose of lightening the unit. The robot configuration also made use of a unique construction, where each unit was supported by an independently powered single wheel. This configuration allowed the robot to adapt to a variety of ground shapes

through use of the powered z -axis. The robot was also equipped with a large manipulator arm mounted on the lead unit.



Figure 2.6: Koryu-II [14]

The robot was designed to further the development of robots which made use of an articulated body to distribute loads and carry them, much like a train. This type of robot was meant to function in environments where large body robots were typically not maneuverable enough to negotiate turns in a cramped space. KR-II was also useful for applications where smaller robots would prove unable to transport needed operational equipment. KR-II had a total length of 3300 mm and a total height of 1080 mm. The link 0 had weight of 25 kg and links 1-6 had a weight of 50 kg. The robot had a width of 460 mm and had a total weight of approximately 370 kg. The driving system for each wheel was a DC motor. The robot was able to propel itself over rough surfaces and elevated surfaces by impedance control through the use of optical force sensors attached to the z -axis and the s -axis. The robot had been demonstrated on steps, outdoors, and city street environments, while running autonomously. The robot was able to travel on a sloping surface of up to maximum incline of 48 deg. The maximum speed of the robot observed on a flat terrain was 500 mm/s.

2.3.2 GMD-SNAKE2

In 1999, Klaassen and Paap introduced an improvement over their previous GMD-Snake robot; the newer GMD-Snake2 imitated the rectilinear motion of a snake [22]. The robot is illustrated in Figure 2.7. Klaassen and Paap noticed that the main propulsion of a snake during rectilinear motion came from hundreds of tiny scales that are moving forward and back on the bottom side of the snake. To imitate this motion, they determined that the sections of their mechanism needed to follow two main principles: (1) each section should be actively moveable in direction of its longitudinal axis and (2) each joint should bend according to the movement of its predecessor with a certain delay. The GMD-Snake2 design consisted of six active segments and a head segment.

The robot was designed to be rugged for practical applications, such as, inspection of sewage pipes. The diameter of this robot was 180 mm and the length was 1500 mm. The robot had a mass of 15 kg. The GMD-Snake2 consisted of cylindrical segments that were connected by universal joints and had an array of 12 electrically driven wheels evenly spaced around each segment, driven by small motors. Additionally, the position of each joint was controlled by three motors that used small ropes to move the joint. Links were built around an aluminum cylinder with holes on the surface. The device could be operated on a tether, or the last section could carry batteries. Each section contained its own processor, and the communication was achieved via a bus. Therefore, every section could calculate the delay after which its own joint position must be identical to the predecessor's former position and determine when it had to send this data to its successor. The robot was also equipped with an array of sensors, including six infrared

distance sensors, three torque sensors, one tilt sensor, two angle sensors in each segment, and a video camera.



Figure 2.7: GMD-Snake2 [22]

2.3.3 ACM-R4

Building upon the success of the ACM-R3 design, Hirose's lab developed a version of the ACM which utilized powered wheels known as the ACM-R4, illustrated in Figure 2.8 [14]. The robot followed the same basic structure of the ACM-R3 by utilizing a series of joint units, each with one DOF. The robot consisted of 18 units. The robot design was reported to have the following advantages: (1) the design of a 3D motion capable ACM became relatively easy, (2) the joints range of motion became relatively large, and (3) the robot could be equipped with large wheels at the same axis as the joints. The ACM-R4 used motors to drive the wheels. In general, snake-inspired robots could generate propulsive force by undulation and omit the use of motors to drive the wheels. However, this movement required a large number of joints, so the developers adopted active wheels

from the viewpoint of practical use and reduced complexity of the robot through other elements of the design.



Figure 2.8: ACM-R4 [14]

The robot was designed to explore practical use of snake-inspired robots in a narrow environment such as inside a pipe, or in a disordered environment such as a disaster site. The ACM-R4 robot had a total length of 1100 mm and a cross-section of 135 mm by 135 mm. The robot's total weight was 9.5 kg. The joints were actuated by electric motors capable of a maximum torque of 20 Nm and a maximum joint speed of 30 deg/s. To function within its mission environment, the robot was designed to resist water and dust. Experiments using the robot have confirmed the ability to make right-angle turns in a 240 mm wide passage and climbing of 400 mm high step. In addition, experiments confirmed a continuous 3 hours of operation in muddy water.

2.3.4 NTUA Robotic Snake

The National Technical University of Athens (NTUA) robotic snake was introduced as a multi-articulated mobile robot design to access complicated and unstructured areas inaccessible to human operators [23]. The robot consisted of seven links which were connected by six revolute joints. The first link had free space to carry a payload or instrumentation. With the exception of the first link, the robot was composed of three

modules which were made up of two links and the six revolute joints. Two of the revolute joints provided relative motion between two successive links about a horizontal and vertical axis. Another two revolute joints provided relative motion about the central axis of the robot's cylinder-shaped body. The last two joints provided relative motion on vertical axis for each wheel through small servomotors, which allowed precision turning control for each wheel. Additionally, the forward half of each module was equipped with two independently driven wheels to provide forward propulsion. The total robot had 24 DOF.

The primary purpose of this robot design was to experiment with a robot that was able to perform inspections and minor repairs in industrial environments such as nuclear power plants. One of the main design points was to ensure that the robot would be able to traverse inside medium and large size pipes. Each module of the robot was 541 mm in length and 12 mm in height. The modules each weighed 5.5 kg. The total length of the robot was 1650 mm in length and 16.5 kg in weight. The robot's configuration allowed it to traverse a minimum piping internal diameter of 150 mm. The maximum load capacity of the robot was 0.5 kg. Each revolute joint about the vertical and horizontal axes was powered by a brushed 22W DC motor and gear chain. The system provided a maximum torque of 14.4 Nm at the joint at an average speed of 45 deg/s. The revolute joints about the central axis were powered by small brushed 6V DC motor with a gear reduction ratio of 102. The wheels were driven by small DC motors. The robot had the ability to lift the front link to a maximum height of 700 mm enabling it to overpass obstacles with a maximum height of 250 mm.

2.4 Snake-Like Robots with Active Treads

The need for natural disaster relief efforts, such as search and rescue operations following a major earthquake, had inspired the design of several snake-inspired robots which utilized powered treads or crawlers to traverse extremely rough terrain [14]. Considering that it was very difficult and dangerous to crawl into the debris to find victims, robots which could maneuver in this environment in order to find these victims with TV cameras and microphones were highly desired. Such robots, which combined the capability of treads with the advantages of snake-inspired robots, would be able to navigate small, tight openings within the debris and locate and assess the condition of possible survivors. These robots would also allow rescuers to focus their effort more efficiently in extremely time critical scenarios.

In this section, we will discuss in detail four robot designs: Koryu-I, the two OmniTread robots and the JL-I. Other noteworthy examples of such robot designs were Souryu I and II and MOIRA snake-inspired robots. In 1997, Hirose-Fukushima Robotics Lab introduced the Souryu I and II robot designs for search and rescue operations following disasters such as earthquakes [14]. The robots were composed of three parts: (1) front body, (2) center body, and (3) rear body, and each body segment was equipped with a crawler on both sides. The front body included a CCD camera and a microphone to find victims, the center body included the driving actuators and batteries, and the rear body included the radio receiver. The crawlers were driven simultaneously by the motor at the center of the body through the use of universal joints. The MOIRA robot was a serpentine robot that used tracks for propulsion and pneumatics for joint actuation [24, 25]. MOIRA was comprised of four segments, each with two longitudinal tracks on each

of its four sides, for a total of eight tracks per segment. The 2-DOF joints between segments were actuated by pneumatic cylinders.

2.4.1 Koryu-I (KR-I)

The first Koryu robot design illustrated in Figure 2.9, the prototype KR-I, was developed by Hirose to explore the possibility of a functional ACM being used in restricted spaces [5, 14]. The full scale robot design was meant to carry manipulators, visual equipment, communication equipment, and computer hardware. The full scale design would also have to traverse slopes of 40 deg, overcome level differences of 300 mm in height and breadth and operate in passage way with a maximum width of 600 mm and height of 1500 mm. The robot prototype consisted of six cylindrical sections with 16 DOF. The robot was characterized as being able to allow two DOF of movement to operate: the z -axis and the θ -axis. The translation of the sections mutually at their coupling points on a vertical axis was known as the z -axis. The rotational movement around a vertical axis of each section was known as the θ -axis. In addition, there was an s -axis that described the crawlers, mounted at the bottom of each section, used to generate propulsive movement for the robot. There were five z -axis actuated joints, each between two robot sections, and similarly five θ -axis actuated joints. There were six powered s -axis drives, each underneath a section of the robot, which gave the robot the total 16 DOF.



Figure 2.9: Koryu-I [14]

The purpose of the robot design was meant to negotiate passages meant for service workers inside a nuclear reactor and carry out inspections and other tasking. Each section of the robot had a diameter of 206 mm. The robot had a length of 1391 mm and a total height of 393 mm. The mass of robot was 27.8 kg. The z -axis was actuated with a 30W drive motor with a rated torque output of 180 Nm and a maximum speed of 80 mm/s. The θ -axis was actuated with a 30W drive motor with a rated torque output of 4.7 Nm and a maximum speed of 50 deg/s. The s -axis was powered by a 12W drive motor with a rated torque output of 44 Nm and a rated speed of 532 mm/s. The crawler unit was driven with a reduction ratio of 0.5. Each section was equipped with a force sensor between the crawler segment and the body of the section. The force sensor was based on an optical detection system and provided information to the impedance based control system of the robot. The robot was demonstrated on flat surfaces, climbing over obstacles and crossing gaps. The robot was capable of a maximum forward velocity of 266 mm/s.

2.4.2 OmniTread OT-8

The first OmniTread robot was called the OT-8 and is shown in Figure 2.10 [26]. This robot consisted of five segments that were connected by four, 2-DOF joints. The

propulsion of the robot was achieved by an innovative means: using tank treads on the four sides of every link. The tank tread design maximized the “propulsion ratio,” the ratio of surface area that was active in propulsion to the surface area that was not. In order to maximize this ratio, tank treads covered as much of the sides as possible and the gap size between the links were minimized. The idea behind the maximization of this ratio was that any environmental feature that contacts the robot at a location covered by treads would not impede the motion. Treads on each side also made the design indifferent to rolling over. The second innovative feature of the OmniTread design was that it is designed with pneumatic bellows that acted as the actuators between the segments. The bellows allowed compliance between the segments, allowing the robot to passively conform to the terrain to maximize traction. The pneumatic bellows meant that stiffness could be adjusted “on the fly.” An example of when this would be needed was when the robot was climbing over a gap. Thus, the bellows were used to both actuate the joints and adjust the compliance. A total of 16 bellows were used, which gave the robot 16 position parameters and 16 stiffness parameters. Two valves were used to control each bellow.



Figure 2.10: OmniTread OT-8 [26]

Like many other snake-inspired robot designs, the robot was designed to support research into a platform which can perform operations in difficult-to-reach areas or in environments which are very dangerous to human operators. The dimensions of the OmniTread OT-8 segments were 200 mm by 185 mm by 185 mm and the entire robot was 1270 mm long, including the 68 mm of joint space between each segment. The complete robot weighed 13.6 kg. One motor provided the power to all of the tracks in the robot using a central drive shaft running the entire length of the robot, using universal joints. Each universal joint was located in the center of the space between segments (between the bellows) in order to maintain structural rigidity. The drive motor was a 70W DC motor using a 448:1 total gear reduction from the motor to each of the tread driving sprockets. Using the unique pneumatic bellows configuration, the robot was able to achieve a minimum turning radius of 530 mm. The robot has demonstrated the ability to climb up a curb more than 36% of its length, and 240% of its height. Additionally, the robot could lift up two of its forward or rear segments. The OT-8 operated off of a power and pneumatic tether. The OT-8 demonstrated a maximum forward velocity of 100 mm/s.

2.4.3 OmniTread OT-4

The OT-4, shown in Figure 2.11, was the improved version of the OT-8 and was named as such because the OT-4 could pass through an opening as small as a diameter of 4 in (101.6 mm), while the OT-8 could only traverse openings no smaller than a diameter of 8 in (203.2 mm) [27, 28]. The robot consisted of seven segments as opposed to the five of the original OT-8. Besides the smaller size, the OT-4 possessed other improvements in design over the OT-8, such as, a tether-less design. The OT-8 required a tether to provide

compressed air and electric power to the pneumatic bellows and electric drive motor. The OT-4 carried onboard compressed gas tanks and electric batteries. The robot also had the ability to selectively disengage individual tracks from the shaft spine through the use of electrically actuated micro-clutches to reduce power consumption when the tracks were not needed. Finally, the OT-4 contained payload compartments in the first and last segments to carry sensor equipment, tooling or any other required payload for an operation.

The OT-4 shared the same intended application as the OT-8: the robot was designed to perform operations in difficult to reach areas or environments which may prove very dangerous to human operators. The motor or drive segment of the robot was 109 mm in length and the actuator segments are 103 mm in length. The pneumatic joint assemblies had a length of 36 mm. This gave the OT-4 a total length of 940 mm and a cross-section of 82 mm by 82 mm. The robot was a much lighter design at 3.6 kg, compared to the 13.6 kg OT-8. The pneumatic bellows were powered using a miniature air compressor and liquid CO₂ tanks. The pneumatic system allowed the robot to lift a maximum of three of its segments from the terrain. Also, utilizing the pneumatic bellows for steering, the robot was able to achieve a minimum turning radius of 229 mm. The DC drive motor was powered by onboard Lithium-Polymer batteries that could provide power for up to 60 minutes of operation. The micro clutch mechanism consisted of a 6 mm diameter micro-motor, which drove a lead screw to engage and disengage a worm gear using a 4-bar mechanism. Electric limit switches prevented improper engagement of the gear and worm. Like the OT-8, the OT-4 demonstrated operation over many terrain types such as

gravel, dirt, ramp conditions and smooth surfaces. Similar to the OT-8, the OT-4 demonstrated a maximum forward velocity of 150 mm/s through various testing.



Figure 2.11: OmniTread OT-4 [27]

2.4.4 Reconfigurable Robot JL-I

A novel reconfigurable modular robotic system named JL-I was introduced in 2006 by Zhang et al., with the ability to traverse terrain with snake-like motion [29, 30]. JL-I, illustrated in Figure 2.12, was really a three-part robot system that utilizes a unique docking mechanism, which endowed the robot with the ability to change shapes in 3D space. The three modules were identical and were capable of individual locomotion through a pair parallel powered treads. The docking mechanism consisted of 3-DOF active spherical joints between modules and enabled the adjacent modules to adopt configurations to negotiate difficult terrain or to split into three small units to perform tasks simultaneously. The robot was capable of climbing stairs, crossing gaps, and recovering from roll-over conditions. The robot was also capable of performing rolling about the x -axis, pitching about the y -axis, and yawing about the z -axis to change its posture. A parallel mechanism was responsible for the yawing and pitching movements of the robot. The rotation about the x -axis was achieved by the use of a serial mechanism.

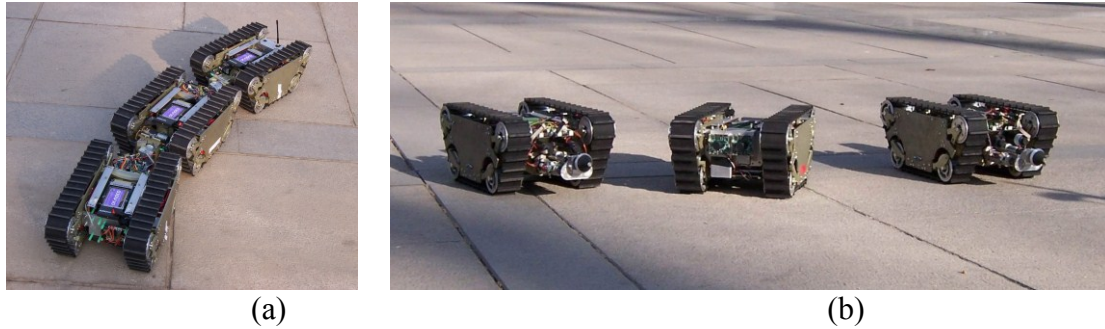


Figure 2.12: (a) Reconfigurable Robot JL-I and (b) Separate Modules [29]

The design purpose for this robot was to develop an automatic “field” robot for unstructured environments to meet the requirements of high flexibility, robustness, and low cost. A single module dimensions were about 350 mm in length, 250 mm in width and 150 mm in height. A module weighed approximately 7 kg, including the on-board batteries. A single module had two powered tracks, a serial mechanism, a parallel mechanism, and a docking mechanism. The tracks were driven by two DC motors which provided each unit with skid-steering ability in order to realize omni-directional movement. The docking mechanism consisted of two parts: a cone-shaped connector at the front of the module and a matching coupler at the rear of the module. The coupler was composed of two sliders propelled by a motor-driven lead screw. The sliders formed a matching funnel which guided the connector to mate with the cavity and enabled the modules to self-align with certain lateral offsets and directional offsets. Two mating planes between the sliders and the cone-shaped connector constrained the movement, thereby locking the two modules. The robot contained two types of external sensors: a CCD camera and tactile sensors. Its internal sensors included a GPS, a digital compass, a gyro sensor and limit switches which provided joint position information. In trials, the robot demonstrated that it was capable of climbing a maximum step height of 280 mm

and a maximum ditch length of 500 mm. The robot demonstrated a maximum forward velocity of 180 mm/s and a maximum slope angle of 40 deg.

2.5 Rectilinear Motion through Vertical Traveling Waves

Although the robots presented thus far mimicked snake-inspired locomotion, none of these robots advance using pure undulation or the changing of the robot's position resulting entirely from changes in body shape (e.g., wheels, treads or legs are not used). However, there exist a number of snake-inspired robot designs which do utilize pure undulation, in particular rectilinear motion, to mimic snake-inspired motion. The next two sections will introduce snake-inspired robots which demonstrate rectilinear motion in one of two forms: (1) rectilinear motion using vertical waves and (2) rectilinear motion using expanding/contracting segments. In this section, the former type of rectilinear motion will be covered, which can be described as a creeping motion where a segment of the robot advances an adjacent segment forward while anchoring itself to the terrain. In turn, the "advanced" segment repeats the process for a segment adjacent to it until the entire robot has advanced forward a distance equal to the displacement of the first segment in the sequence.

In this section, we will discuss the following four robot designs in detail: Kotay's Inchworm robot, Dowling's Snake robot, the PolyBot and CMU's Modular Snake robots. Other noteworthy examples of such robot designs were the NEC Quake Snake, GMD-Snake, Ver-Vite, CONRO and M-TRAN. One of the earliest recorded snake-like robot designs was the NEC Quake Snake, a 12-DOF teleoperated robot developed and introduced by Ikeda and Takanishi in 1987 [31]. The NEC Quake Snake consisted of six segments, each connected with a passive universal joint to prevent adjacent segments

from twisting, while allowing bending and rotation about a lengthwise axis through the segment. The robot was capable of lifting one or more of its segments and was equipped with a small video camera in the front segment. In 1996, Paap et al. introduced the GMD-Snake, the predecessor to the serpentine robot GMD-Snake2 [32-34]. The GMD-Snake robot was designed to “show useful behavior by reacting flexibly within various environments” as inspired by observing real snakes creep across rough surfaces. Each internal section consists of two joints, composed of octagon-shaped aluminum plates, which used rubber joints to allow flexible bending. The segments were connected by means of cables to produce curvature horizontally or vertically along several segments simultaneously. The inchworm robot Ver-Vite, introduced by Rincon et al. in 2003, simulated inchworm locomotion with friction only and the use of variable masses [35]. The locomotion mechanism in Ver-Vite was inspired by the actual locomotion process observed in inchworms, known as peristaltic contraction. In this process, the widening of several segments serves to anchor that part of the body against tunnel walls, while other sections of the body are narrowed and elongated to extend the leading segment forward. In the Ver-Vite robot, the variable mass, water, was moved back and forth between the aft and forward sections of the robot in order to vary the weight of the segments in contact with the surface and thus increase the frictional force to anchor the segment to the surface. The CONRO and M-TRAN robot systems were examples of self-reconfigurable modular robots [36, 37]. These systems consisted of individual robot “blocks” which were capable of docking with one another to form more complex robot systems, such as snake-inspired robots. In addition, Gonzalez-Gomez et al. presented set of modular snake robots, which incorporated touch strips [38]. The touch strips formed touch rings

which support tasks, such as grasping or climbing objects. The modular robots are an extension of a low-cost design introduced by the authors in 2009. Finally, Ohashi et al. introduced the ACM-R7 in 2010. ACM-R7 is an Active Cord Mechanism which can connect its head and tail and move in a rolling loop to improve forward velocity [39].

2.5.1 Inchworm Robot Introduced by Kotay and Rus 1996

An inchworm robot, inspired by inchworm and caterpillar motion, was introduced by Kotay and Rus in 1996 for use in vertical climbing of steel structures [40]. The robot is illustrated in Figure 2.13. The robot had four sections, linked with three joints providing three degrees of freedom. These joints allowed the inchworm to extend and flex. The first and fourth sections were the “feet” of the robot. These sections contained attachment mechanisms which allowed the robot to adhere to the surface being traversed and provided the anchoring force needed to support the robot when walking. The attachment mechanism of the robot was comprised of electromagnets. These electromagnets provided enough force to securely anchor a foot and support the weight of the robot when the other foot is completely extended. Although the choice of electromagnets provided a large amount of holding force in a small package, it limited the use of the robot to steel surfaces. In 2000, Kotay and Rus introduced a second variation of the inchworm robot, which included an additional degree of freedom [41]. The fourth degree of freedom was provided by a pivot joint mechanism attached to the rear foot, allowing the robot to rotate relative to the rear foot. This pivot joint provided the robot with the ability to turn.

When fully extended, the length of the first inchworm robot was 252 mm and its height was 52 mm. When fully contracted, the length of the robot was 180 mm and its height was 120 mm. The weight of the inchworm robot was 0.455 kg. Joint actuation was

achieved through the use of servomotors. The servomotors had a maximum torque of 0.52 Nm and a maximum joint speed of approximately 140 deg/s. The robot also possessed a suite of sensors in the form of four tactile and five infrared proximity sensors. The robot's power supply and control were provided through a tether. There were two 12-volt electromagnets per robot foot, arranged in-line with the body of the robot. The robot was designed to explore the possibility of using inchworm-like robots in general inspection of construction in 3D environments. The forward velocity of the robot was 4.2 mm/s, equivalent to one fully-extended robot length per minute. The second robot had a fully extended length of 330 mm and height of 80 mm. When contracted, it had a length of 175 mm and a height of 160 mm. The robot weight 0.566 kg and a forward velocity of 12.5 mm/s.

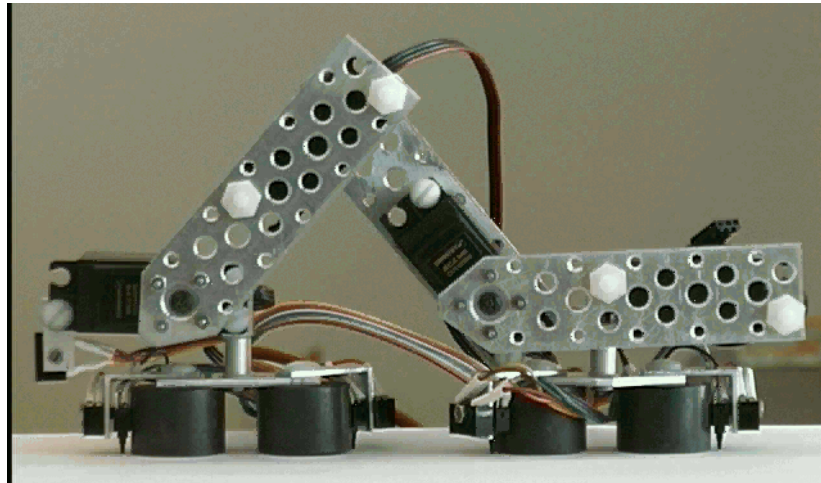


Figure 2.13: Inchworm Robot by Kotay and Rus 1996 [40]

2.5.2 Snake Robot Introduced by Dowling 1997

Another early design in snake-inspired robotics, which could utilize vertical waves, was developed by Dowling at Carnegie Mellon University [1]. The entire robot is shown in Figure 2.14. The robot was composed of 10 links, each with 2 DOF. Dowling

developed the snake-inspired robot while studying gait generation using machine learning. Dowling took a comprehensive look at a wide range of possible actuation technologies that could be utilized in snake-inspired robots. The author is quoted as stating that “some of these [actuation] technologies were initially examined with the intent of using scaled snake vertebrae in a robotic mechanism.” The final result of this study was a snake-inspired robot that could move in a 3D environment using only servomotor actuation. Dowling looked at the geometric design of a snake-inspired robot as it related to mission parameters. He determined the dimensions of curved and right-angle pathways that a snake could fit into as a function of link geometry and twist angle. Dowling found that the angle of motion was not as important as the link length. He determined that the link length should be as short as possible. The mechanical design of this robot consisted of an aluminum sheet with servos mounted to it. The servos were mounted orthogonally, so that each end of the link contained an actuated revolute joint. The rotating sections were mounted directly to the servo horn, and adjacent links were attached to each other such that orthogonal servos connect to each other.

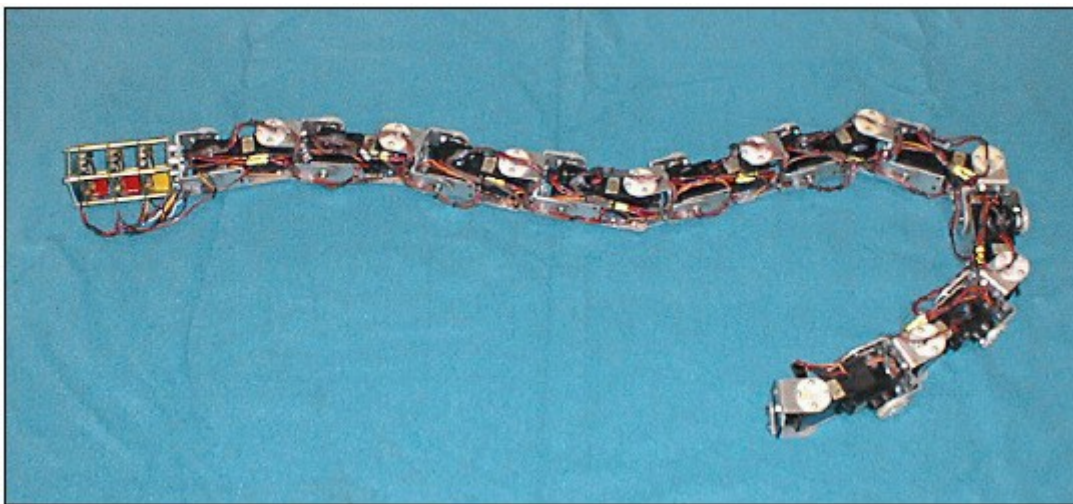


Figure 2.14: Dowling’s Complete Snake Robot [1]

The primary purpose for the robot's development was to support gait optimization studies. A gait optimization program would execute a given gait using the robot and observe its performance data to be used in an evaluation of the gait itself. Each link of the robot was 102 mm in length, thus the entire robot had an overall length of 1020 mm. The mass of the robot was 1.48 kg, and each link had a diameter of 65 mm. The joints of the robot were actuated using commercial servos which possessed a maximum torque of 0.84 Nm and a maximum joint speed of approximately 270 deg/s. The robot was controlled using centralized control and powered using a tether. The control circuitry was located in the "head" of the snake. NiCad batteries were proposed as a power source, but external power was used in the actual implementation. Additionally, a CCD camera was mounted on the head unit. An interesting feature of this robot was that the use of "skin" was investigated to provide desirable friction characteristics. Dowling proposed covering the entire robot in a fabric or material that would provide good friction characteristics in order to propel the snake forward. Several candidate materials were discussed and evaluated.

2.5.3 PolyBot Reconfigurable Robots

Another example of reconfigurable robots was developed by Yim et al. 2000, called PolyBot, illustrated in Figure 2.15 in a snake configuration [42]. The PolyBot mechanisms could be arranged in a form to mimic snake-inspired robot motion. The design philosophy behind PolyBot was that a number of small modules can be assembled into complex systems which could achieve complex tasks, even though the modules themselves are very simple. The segment module could be divided into three subsystems: 1) structure and actuation, 2) sensing, computation and communication, and

3) connection plate. The structure was made of a laser-cut stainless steel sheet and was basically cube shaped. The module's one DOF allowed these two faces to be rotated so they are no longer parallel. Each segment had two connection plates. The connection plate served two purposes: 1) to attach two modules physically together and 2) to attach two modules electrically together as both power and communications are passed from module to module. PolyBot allowed two connection plates to mate in 90 deg. increments which allowed two modules to act together in-plane or out-of-plane. The modules were used to simulate various locomotion types such as sinusoid snake-like locomotion, a rolling track, and a three-legged caterpillar-like locomotion. It is worth noting that this is an inactive project at Palo Alto Research Center (PARC) and does not represent its most current work in reconfigurable robotics, such as, the Proteo and Digital Clay projects.

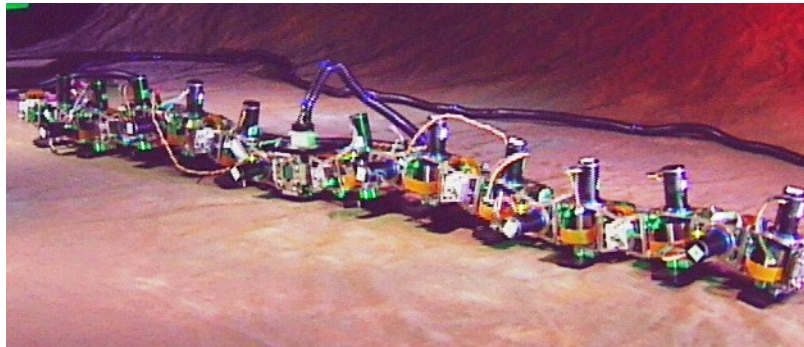


Figure 2.15: Reconfigurable Robot, PolyBot [42]

The primary purpose for the robot's development was to investigate the concept of developing modules which promised to be versatile, robust, and low cost, yet still could be used to assemble complex constructs. Each module was a 50 mm by 50 mm by 50 mm cube. A brushless DC motor with a four-stage 134:1 gear reduction was mounted in the middle of the segment on the axis of rotation. Future plans included the use of a form of harmonic drive to reduce gear box space allowing the motor to be mounted within the

module. In a snake-like configuration, the modules executed a sinusoid serpentine-like locomotion, which was demonstrated over a variety of obstacles including: crawling in 102 mm diameter aluminum ducting, up ramps (up to 30 deg.), climbing 45 mm steps, and traversing over loose debris and wooden pallets.

2.5.4 CMU's Modular Snake Robots

Several modular snake robots were designed and built by students from Carnegie Mellon University (CMU) [43]. These modular robots were used to demonstrate several snake-inspired gaits for accomplishing difficult tasks such as climbing, swimming, and crossing gaps. The each module consisted of a single servomotor, which created half of the structure of the module and provided the torque to move and maintain angles while resisting forces from the environment. To complete the other half of the joint a component was created, called the U case, which attaches to the output arm. The U case had one arm attached to the output of the servo and the other attached to the back of the servo to add strength. In addition to their mechanical design, the robots also utilized modifications to their outer surface to enhance performance in a number of environments. These modifications took the form of a full, possibly sealed, covering called skin or the adherence of additional material to the modules themselves, called compliance.

The latest work from CMU includes the introduction of a “Unified Snake” design by Wright et al. in 2012 [44], illustrated in Figure 2.16. The Unified Snake includes advanced electronics and software, a full suite of diagnostic and external sensors and SMA wire actuated bi-stable joint brake. In terms of sensors, the robot design includes a three-axis accelerometer and gyroscope, temperature, humidity, motor current, module position sensors and a head mounted camera with LED illumination. The novelty of the

joint brake is that while the brake requires energy to engage/disengage, it requires no energy to hold the joint position or allow free movement. This feature allows the robot to lock into a position, such as wrapped around a tree limb for long periods without power consumption from the joint actuator. The brake is actuated using by a pair of shape memory alloy (SMA) wires. With 16 modules, the robot has a diameter of 51 mm and a total length of 940 mm. The robot's total weight was 2.9 kg. The robot utilized 36 V brushed DC motors, which had a maximum torque of 3.76 Nm and a maximum rotational speed of 28.7 rpm. The forward velocity of the robot was approximately 102 mm/s (based on observations from demonstration videos) [43].



Figure 2.16: CMU Snake Robot [44]

In addition to advances in robot design, CMU has also introduced a simplified motion model for snake robots gaits [45]. The model outputs a close approximation to robot motion and does not consider the true forces acting on the robot or the true shape of terrain that the robot traverses. In this manner, the model provides a computationally inexpensive method for predicting gait behavior, while remaining reasonable accurate.

The model was designed for snake robots with architectures that consist of revolute joints alternately oriented in the lateral and dorsal planes of the robot such as [1] and [44]. The model uses a framework called the compound serpenoid curve, which models gait using separate parameterized sine waves that propagate through the lateral (even-numbered) and dorsal (odd-numbered) joints. This framework allows for modeling several gaits, including rolling, sidewinding, slithering and rectilinear motion.

2.6 Rectilinear Motion through Rigid Body Linear Expansion

The robots reported in Section 2.5 utilized rectilinear motion based on vertical waves formed by the robot's body to progress forward. However, rectilinear motion can also be achieved by linear expansion and contraction of the robot's body to form a gait similar to the gaits utilized by real snakes. In rectilinear motion demonstrated by natural snakes, lateral bending of the body and lateral resistances do not contribute to the motion in contrast to the other locomotion modes [3]. Instead, waves of muscular contraction travel through the snake in forward direction. These muscular contractions are capable of producing tensions between the vertebral column and the ventral skin and thus propel the ventral surface forward against frictional resistance.

In this section, we will discuss the following three robot designs in detail: the Slim Slime robot, Yeo's Planar Inchworm robot and the Telecubes. Another example of a robot which utilize linear actuation-based rectilinear motion is the inchworm robot introduced by Chen et al. 1999 [46]. The robot consisted of interconnected actuating modules that can either deform in the direction of travel (extensors) or grip against walls in the robot's environment (grippers). The robot was designed for use in traveling and conducting tasks in narrow and highly constrained environments, such as pipes and

conduits in industrial plants. Each module had a cart-like geometry moving along a horizontal track. The robot also served as the first iteration for the design of a planar inchworm robot, discussed in Section 2.6.2, which was able to change directions and climb smooth surfaces using pneumatics. Scalybot was a 2-link limbless robot with individually controlled sets of “belly” scales, can ascend inclines up to 45 deg. [47]. Scales for each of the robot’s sections mimicked those of a corn snake. The housing for each segment is composed of a steel casing and they are connected to one another by a pneumatic actuator.

2.6.1 Slim Slime Robot

The Slim Slime robot, pictured in Figure 2.17, was an ACM composed of serially-connected modules driven by pneumatic actuators, which allowed it to perform in a 3D workspace [14, 48]. Slim Slime robot was composed of six expandable modules. The robot maintained a high degree of freedom, while being pneumatically-driven without the use many air supply lines. Three flexible pneumatic actuators, known as bellows and a main distribution tube made up the actuation system of each module of the robot. Compressed air was provided into each bellows from the main tube through an inlet valve built in bellows. Inlet and outlet valves built in each bellows made the bellows stretch, shrink and lock its length; therefore the module could stretch and bend in any direction actively.

The robot was developed to perform operations too dangerous for a human worker such as in-pipe inspection at chemical or nuclear energy plants, or the rescue of victims under collapsed houses by making use of its shape and using the ability to distribute its weight evenly to perform mine detection. Each Slim Slime robot module had a

compressed length of 114 mm and a full extended length of 178 mm. The total extended length of the robot was 1120 mm, with a total compressed length of 730 mm. The robot had a diameter of 128 mm. The Slim Slime had a total mass of 12 kg. Through testing, the Slim Slime robot had demonstrated various locomotion types including: the creep motion of a snake, the pedal wave motion of a snail and limpet, lateral rolling and pivot turning. Slim Slime Robot was capable of a maximum forward velocity of approximately 60 mm/s.



Figure 2.17: Slim Slime Robot [48]

2.6.2 Planar Walker: Planar Inchworm Robot

The design of the inchworm robot by Chen et al. 1996 led to the development a planar inchworm robot, shown in Figure 2.18, based on the basic inchworm motion [49, 50]. The planar inchworm could mimic snake or inchworm-like creeping motions. In addition, the unique mechanical arrangement of the actuators allowed for quick change in travel direction and permitted rotational movement. The robot design was inspired by interest for walking/climbing systems for large surface inspection and maintenance tasks on ship hulls and oil tanks. The prototype system was based on pneumatic actuation and

called a Planar Walker. The unit featured a simple closed-loop planar 8-bar mechanism formed by four linear cylinders and four revolute joints. When the four cylinders were actuated independently, the shape of the mechanism changed to a square, a rectangle, or an irregular quadrilateral. Four pneumatic suction/gripper modules were mounted below each of the revolute joint to adhere the robot to the working surface. The robot was designed to be able to traverse forward, backward, and sideways a fixed distance or turn at a fixed angle. Based on the symmetry of the robot, the translation and rotation of the robot were decoupled; therefore, the robot could change its direction of travel very rapidly.



Figure 2.18: Planar Inchworm Robot: Planar Walker [50]

The robot was designed to explore locomotion principles and navigation of this design configuration. The robot was 500 mm by 500 mm in size and had a total weight of 6 kg. The robot system consisted of two major modules: the locomotion mechanism module and the system control module. Four pneumatic cylinders were connected through pivot joints. The cylinders had a bore size of 16 mm with a stroke length of 45 mm. The overall length of the pistons between the two pivot joints was 176 mm. The crossbar frame had a central revolve joint so that the two crossbars could rotate with

respect to each other with no restriction. The crossbar frame consisted of four sliding units that are integrated with the pivot joints. A gripper unit was attached to each slider unit to provide the vacuum suction force to the surface. The robot had a maximum transverse stride length of 32 mm/cycle and a maximum turning angle of 25 deg/cycle. The robot achieved a maximum transverse speed of 1.07 mm/s (30 s per cycle) and a maximum turning gait speed of 0.42 deg/s (60 s per cycle).

2.6.3 Telecubes: Self-Reconfigurable Robots

The Telecubes, shown in Figure 2.19, were another example of self-reconfigurable robots which were able to assemble in configurations that could mimic snake-inspired locomotion [51]. Each Telecube robot module had two basic mechanical functions: contracting/expanding and connecting/disconnecting from the faces of neighboring modules. Each robot possessed six DOF through six prismatic joints which could individually expand or contract each face of the cube. Each face, known as a connection plate, had a mechanism and means to reversibly clamp onto the neighboring robot's connection plate and transmit power and data to the neighboring robot. The two principle design goals of the robot were to achieve a 2:1 expanded-to-contracted ratio and maintain a design with relatively small overall dimensions. The designer believed these goals would allow the units to have a relatively low cost. This low cost could support manufacturing in large quantities, providing numbers of cheap, simple robots which can perform complex tasking. It is worth noting that this is an inactive project at Palo Alto Research Center (PARC) and does not represent their most current work in reconfigurable robotics, such as, the Proteo and Digital Clay projects.

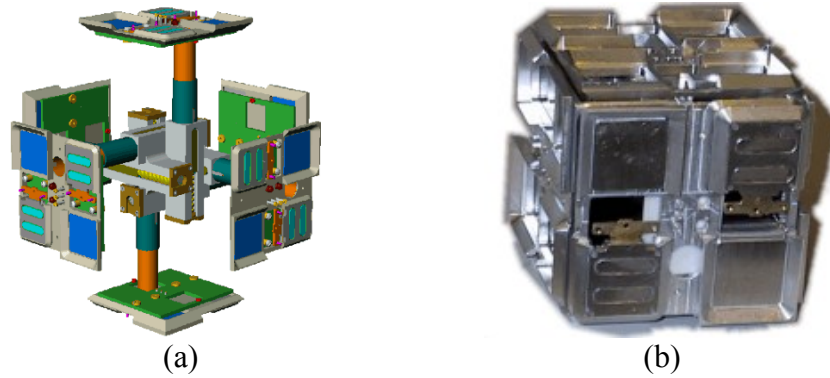


Figure 2.19: Telecube: (a) CAD model extended and (b) prototype contracted [51]

The robot system was designed to support experiments which explore local control methods, distributed sensing and actuation. Each Telecube robot was designed to be a 60 mm by 60 mm by 60 mm cube in dimensions. Each robot's mass was to be under 0.3 kg. Each prismatic joint, known as a telescoping-tube linear actuator was a lead screw assembly powered by a brushless 1.2W DC motor. The prismatic actuator was designed to achieve a 36-40 mm extension at a rate of 8-10 mm/s with maximum force output of 12 N. The docking mechanism of each cube consisted of a set of two “switching” permanent magnet devices and two mating metal plates on each face of the cube. The system allowed for passive and active docking between cubes. The docking system had about 5 kg force of holding force per face. Each robot was designed be equipped with a set of IR sensors and emitters on each face to provide communication between robot modules.

2.7 Rectilinear Motion through Soft Body Peristaltic Motion

In addition to rigid body robot designs, which emulate snake or inchworm motion, there also exist several examples of soft body robots that mimic earthworm motion. The gait motion exhibited by rectilinear motion closely relates the peristaltic crawling motion observed in these soft body robots. In this section, we will discuss the following three

robot designs in detail: a pneumatic inch-worm by Jinwan Lim et al. 2007, a Shape Memory Alloy (SMA) earthworm robotic platform developed by Seok et al. 2010, and a braided mesh robot introduced by Boxerbaum et al. 2010. Other noteworthy examples of such robot designs include a micro-robot fabricated from a natural rubber, which contains a magnetic fluid [52]. The robot is placed inside a tube and as a magnetic field moves along the length of the tube; segments of the robot bugle out and contract in sequence causing the robot to inch forward. A pneumatic inch-worm robot, introduced by Jinwan Lim et al. in 2007, uses only one pneumatic drive to actuate all the components of the robot [53]. As air flows into each chamber of the robot, it sequentially engages the rear clamp, the elongation module, and the front clamp, causing the platform to progress forward. Finally, a peristaltic crawling robot attached to an endoscope using bellows-type artificial rubber muscles was developed by Yanagida et al. in 2012 [54].

2.7.1 SMA Meshworm Robot by Seok et al. 2010

Seok et al. introduced a Shape Memory Alloy (SMA) earthworm robotic platform which utilized a flexible braided mesh-tube structure with NiTi coil actuators [55]. Due the entire robot being constructed from the flexible mesh, it was able to continue to function following multiple hammer strikes by a rubber mallet, as pictured in Figure 2.20. The robot is composed of a polyester braided mesh tube. The mesh tube is approximately 22mm in diameter and 200 mm in length in it's the unloaded state. Five NiTi actuators are wrapped around the tube, creating five defined segments for the robot. Each segment elongates, when the corresponding NiTi actuator contracts. As the adjacent segment contracts, the resulting elongation restores the previously elongated segment to it nominal

condition. Although the robot's theoretical velocity was predicted to be 4.00 mm/s, the robot achieved an actual forward was of 3.47 mm/s.

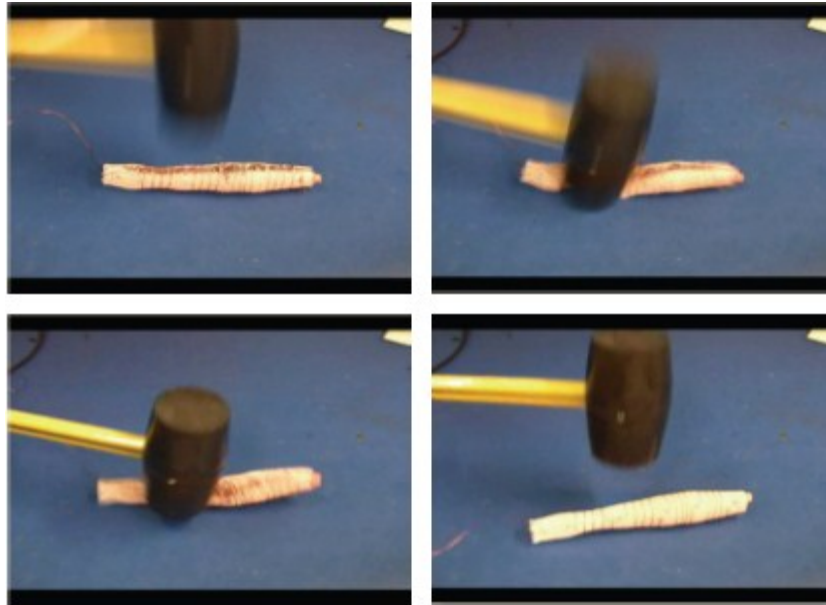


Figure 2.20: SMA Meshworm Robot [55]

2.7.2 A Braided Mesh Robot by Boxerbaum et al. 2010

Boxerbaum et al. developed a robot, pictured in Figure 2.21, composed of a braided mesh of brake cable sheathing with steel cables running through the sheathing to individual hoop actuators [56]. The novelty of this design was that a single cam mechanism drove all actuators within the robot and created two traveling waves along the length of the robot. The robot measures 1067 mm in length and 254 mm in diameter at the robot's rest state. The robot was composed of ten steel loops; all connected to a single drive motor. When the motor pulls on the loop, the loop contracts the local diameter of robot, causing that section of the robot to expand. When the loop is loosened, the section of robot returns to its nominal position. The prototype demonstrated up to six body lengths per minute, resulting in a forward velocity of 16 mm/s.



Figure 2.21: Braided Mesh Robot [56]

2.7.3 An Inchworm Robot using Electro-conjugate Fluid (ECF)

An inchworm robot with a flexible body and using two suckers, both of which are driven by the ECF flow, is introduced by Ueno et al. in 2012 and illustrated in Figure 2.22 [57]. The robot is composed of two suction devices and expansion/contraction actuator. Each component is actuated by flow of the ECF, a dielectric fluid, which works as a smart/functional fluid under the influence of an electric current. The prototype demonstrator is 59 mm in length and 12 mm in width. The prototype also weighs only 9.5 gm. The robot has demonstrated a forward velocity of 0.34 mm/s, 0.35 mm/s and 0.41 mm/s, for inclination angles of 0 degrees, 5 degrees and 10 degrees, respectively.



Figure 2.22: Inchworm Robot using Electro-conjugate Fluid [57]

2.8 Mechanics Models for Snake-Inspired Robots and Gaits

To predict the performance of snake-inspired robots and their associated gaits, a mechanics-based analysis must be conducted for the robot and gait. Because a snake-inspired robot can be considered as a serial chain of powered links, manipulator robotics analysis techniques can be used to develop the kinematics and dynamics-based models of the robot and associated gait. In this section, commonly used manipulator analysis techniques will be presented; various snake-inspired robot mechanics-based models will be reviewed; and rectilinear gait-based models will be surveyed. It is goal of this section to both develop a knowledge base of robot manipulator analysis techniques and determine if a rectilinear gait, rectilinear gait-based model, or mechanics-based analysis currently exists which can be applied to the robot design being developed in this dissertation.

2.8.1 Mechanics Analysis Techniques for Manipulators

In general, kinematics analysis is the process of deriving the relative motion between the mechanical links of a robot with respect to time [58]. This analysis consists of two problems: direct kinematics and inverse kinematics. Direct or forward kinematics is the

process of determining all the possible positions and orientations of the end effector (free end of a robot) with respect to the base of the robot (permanently or temporary fixed end of a robot) given a set of known trajectories for the robot joints. Inverse kinematics is the process of determining possible joint trajectories given a known set of positions and orientations of the end effector. In general, for serial robots the direct kinematics problem is fairly straightforward; however, the inverse kinematics problem becomes difficult. Two methods for solving the kinematics problem for serial manipulator are Denavit-Hartenberg method and the method of successive screw displacements. Two methods for solving the kinematics problem for parallel manipulators are Denavit-Hartenberg method and the geometric method. Although the Denavit-Hartenberg method is very general, the method is complicated by the existence of multiple closed loops, therefore it is often more convenient to employ geometric methods in the presence of closed loops [58]. Thus, it may be more appropriate to use the geometric method to solve the kinematics problem for parallel manipulators.

Dynamics is the study of the forces and torques required to cause the motion of a system of bodies [58]. Dynamics analysis deals with derivation of the equations of motion of a given manipulator. There are two types of dynamics analysis problems: direct dynamics and inverse dynamics. Direct dynamics can be defined as determining the resulting motion of the end effector of a manipulator as a function of time, given a set of actuated joint torques and force functions. Inverse dynamics can be defined as finding a set of actuated joint torques and force functions that will produce the motion of the manipulator, given a known trajectory of the end effector as a function of time. Two common methods for solving the dynamics problem for serial manipulators are the

recursive Newton Euler formulation and the Lagrangian-based method. Although the recursive method is more involved, it provides all the joint reaction forces which may be useful in sizing links and joint hardware. In contrast, the Lagrangian-based method formulates the problem with all the forces of constraint eliminated at the outset. Three methods for solving the dynamics problem for parallel manipulators are the Newton-Euler formulation, the principle of virtual work and the Lagrangian-based method.

2.8.2 Kinematics and Dynamics Models of Snake-Inspired Robots

In 1974, Hirose and Umetani presented the first mechanics-based analysis for a serpentine robot, which led to the development of the ACM family of robots [14]. This analysis was based on the assumption that the robot consisted of a series of links of infinitesimal length, moved by undulation in two dimensions. “Force density functions” were developed along a parameterized length, s , of the robot as functions of continuous torque, $T(s)$, and curvature, $\rho(s)$, through the summation of forces and torques acting on the body of the robot. The force density functions for the tangential direction, Equation 2.1, and the normal direction, Equation 2.2, were integrated over the length of the robot to determine the propulsive force and the lateral “pushing” force of the robot. A power density function was developed, using these equations, which expresses power in terms of torque, curvature, and tangential velocity.

$$f_t(s) = \frac{dT(s)}{ds} \rho(s) \quad (2.1)$$

$$f_n(s) = \frac{d^2T(s)}{ds^2} \quad (2.2)$$

To determine the kinematics of the robot, the body of the robot was assumed to take on a continuous curve where each segment followed the previous one. This curve, illustrated in Figure 2.23, varied sinusoidally with length and was dubbed the serpenoid curve by Hirose. The curve is given by Equations 2.3 and 2.4.

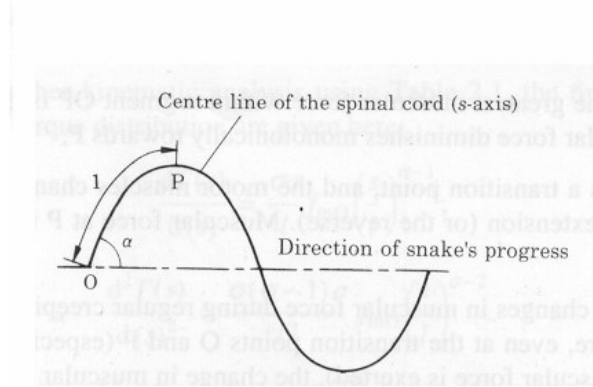


Figure 2.23: Nomenclature for Hirose's Serpenoid Curve [5]

$$x(s) = sJ_0(\alpha) + \frac{4l}{\pi} \sum_{m=1}^{\infty} \frac{(-1)^m}{2m} J_{2m}(\alpha) \sin\left(m\pi \frac{s}{l}\right) \quad (2.3)$$

$$y(s) = \frac{4l}{\pi} \sum_{m=1}^{\infty} (-1)^{m-1} \frac{J_{2m-1}(\alpha)}{2m-1} \sin\left(\frac{2m-1}{2} \pi \frac{s}{l}\right) \quad (2.4)$$

Where $x(s)$ and $y(s)$ represent the displacement of a point P in the x and y directions, respectively, measured along the curved body length s . J_m indicates the m^{th} order Bessel function and α is the winding angle, which defines the angle in which the robot's body intersects with the line that indicates the direction of progress at a point O , as shown in Figure 2.23. The body length between points O and P is l . Comparisons with natural snakes across constant friction surfaces showed close agreement between the serpenoid curve and the empirical data.

Chirikjian and Burdick performed an analysis of kinematics of a snake-inspired robot using a geometric approach [59]. A Variable Geometry Truss (VGT) was used as the

robot for the analysis. The VGT consisted of a longitudinal repetition of truss modules, each one of which was equipped with idler wheels and linear actuators in a planar parallel manipulator configuration. The VGT used periodic changes of shape to produce global robot motion. Two types of gaits were analyzed using this approach for the VGT -- gaits that used both stationary waves and gaits that used traveling waves. The gaits that used traveling waves would be those similar to rectilinear motion, where a wave is propagated through the length of the robot to propel it forward. The gaits that used stationary waves would be those similar to inchworm motion, where the entire robot's length conforms to the shape of the wave as it moves forward. The process to compute the kinematics of the robot was done in two steps. First, they assumed that the robot can be modeled by a continuous backbone curve. Second, they used the backbone curve to specify joint displacements. The model assumes that there is sufficient friction for execution of the gait. The robot is assumed to take the shape of a spline with the path of motion specified as a curve as illustrated in Figure 2.24. The spline is modeled by Equation 2.5, where s is the normalized arc length and t is time.

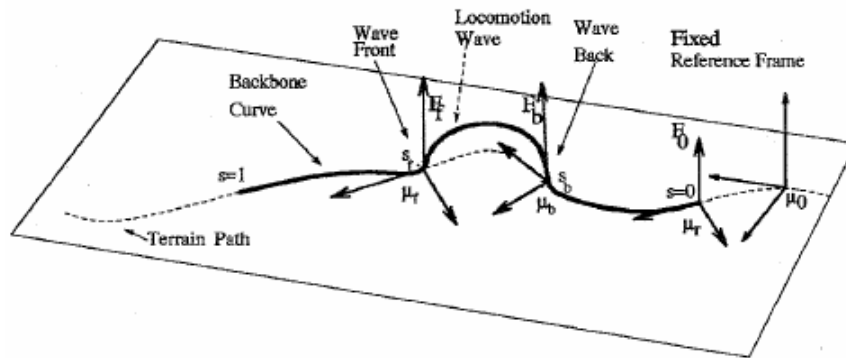


Figure 2.24: Parameters in Chirikjian and Burdick's approach [59]

$$\bar{x}(s, t) = \int_0^s l(\sigma, t) \bar{u}(\sigma, t) d\sigma \quad (2.5)$$

The variable l is the length of the curve tangent and u is the unit tangent vector of the curve, parameterized using Euler angles. In this formulation, the curve is a function of the shape function that specify the orientation and position of the backbone reference frame as a function of time and the parameterized arc length. The task is to develop a set of backbone curves that traverse the path curve. This approach was also used to analyze the kinematics of a serpentine robot performing serpentine locomotion [60].

In 1994, Krishnaprasad and Tsakiris used the VGT mechanism to develop models that employ no-slip wheel constraints and can be used to generate locomotion patterns [61]. These models were called “G-snakes,” in reference to the notion that each segment must move within a constrained subset of a Lie group, G . The trajectories of the G-snake’s global motion could be determined by explicitly integrating gaits by quadratures.

In 1996, Ostrowski and Burdick developed a kinematics-based connection or relationship between changes in joint variables (shape space) of Hirose’s Active Cord Mechanism Model 3 (ACM III) and its total change in position variables with respect to some arbitrary reference point [62]. Shape and position variables were determined to be coupled by the constraints acting on the robot. The total configuration of the space of the system, in which this connection resides, is known as a fiber bundle. The ACM III was a wheel-based, snake-inspired robot capable of propelling itself forward using only internal torques, without directly driving the wheels. However, before this work, the control of the robot’s position remained a heuristically derived procedure. Through the use of the derived fiber bundle, precise control could be developed for the ACM III. Hirose’s robot was modeled as a three link mechanism, as shown in Figure 2.25. The constraints, formed by the three sets of wheels, allowed the motion to be defined purely by the kinematics

and constrained the three dimensions of motion (x, y, θ) of the robot. These three links form the principle motion of the robot. However, the model was restricted to sinusoidal inputs. In addition to Ostrowksi's model, other works have also followed Hirose's foundational model of a serpentine robot and used many techniques to devise the kinematics model for the robot [63-68].

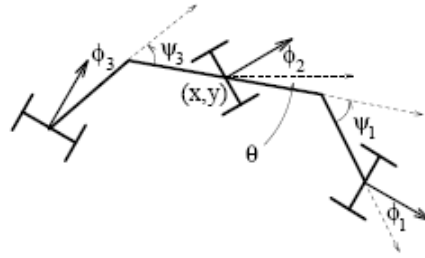


Figure 2.25: Three link model of ACM III [62]

In 2002, Saito et al. developed a dynamics model of the serpentine robot [69]. The robot snake model use anisotropic friction to move in a serpentine motion, however, the model did not contain wheels. The model computed the frictional forces and torques acting on each link as functions of shape and shaping changing parameters. These equations were used to develop Newton-based equations of motion for the robot which predicted velocity and acceleration of the center of mass for each link and the entire robot. Ma et al. also developed a similar model [70]. In 2003, Ma et al. used their framework to dynamically model a serpentine robot creeping up a slope [71]. In 2001, Cortes et al. developed a dynamics model of an eel-like robot which moved in the water using serpentine locomotion [72]. The dynamics model used a Lie group formulation and the friction was modeled using a fluid friction model. In addition to the dynamics model of Saito et al. and Ma et al., other works have also developed dynamics models for serpentine robots, which resemble Hirose's original ACM design [73-76].

2.8.3 Rectilinear Gait Models for Snake-Inspired Robots

In 2001, Chen et al. introduced a rectilinear gait-based model, based on a finite state model, for a multi-segment inchworm-like robot capable of 1-dimensional motion in a confined channel [46]. The robot advances or retreats through the use of linear joint actuators called extensors and grippers. In the finite state model, joints are modeled only with binary values states “0” and “1.” Rectilinear gaits are generated for the subject robot by developing exhaustive search path finding algorithms for use on directed graphical representations of the body segment states. Figure 2.26, illustrates a typical gait found for the inchworm robot using this method. This gait generation approach and locomotion mechanism was further expanded to apply to a planar inchworm robot in [49]. Figure 2.27 illustrates a forward gait for the planar inchworm robot. Figure 2.28 illustrates a turning gait.

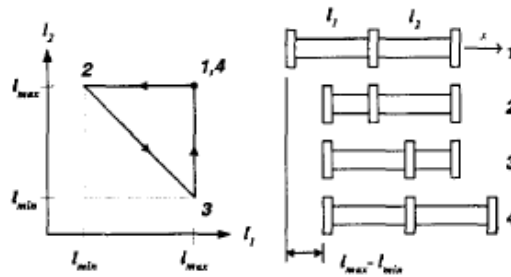


Figure 2.26: Two-extensor robot Gait and Mapping [46]

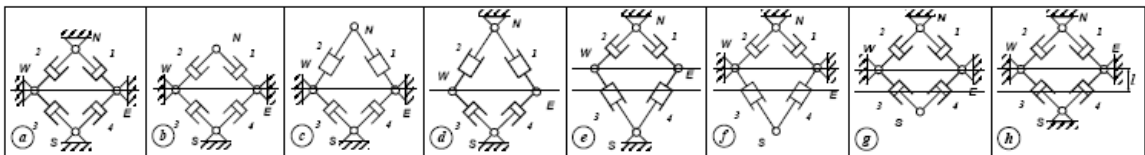


Figure 2.27: Transverse Gait (Forward, Initially retracted) [50]

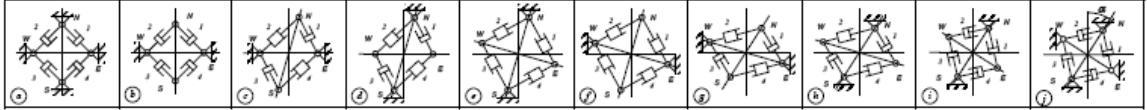


Figure 2.28: Turning Gait (Clockwise, Initially retracted) [50]

A rectilinear gait was introduced and analyzed by Merino et al. 2004 based on the propagation of a continuous vertical pulse (perpendicular to the terrain) for a discrete modular snake-inspired robot [77]. The gait was demonstrated on a redundant robot with 1-DOF modules capable of forward motion. Through the analysis of the gait, the theoretical velocity of a robot using the gait could be determined, as well as, the distance traveled by robot per cycle of the gait. The amount of progression per cycle is given by the following:

$$x = 2 \cdot L - 2 \cdot L \cdot \cos(\theta) \quad (2.6)$$

Where θ is the angle of the risen module and L is the module length. The velocity was then calculated as the distance traveled per cycle over the time needed to complete the cycle:

$$v = 2 \cdot L \cdot \frac{1 - \cos \theta}{14 \cdot \theta \cdot \frac{T}{2 \cdot \pi}} \quad (2.7)$$

The denominator is the time to complete a cycle, determined by adding the angular distances traveled by the joints of robot in a single cycle and multiplying this value by the rate of the joints. T is the period of the joint or servomotor. The concept of a traveling wave has also been addressed in gait models by others, such as Dowling in 1997, Poi et al. in 1998 and Chen et al. in 2003 [1, 78-83]. In 2006, Spranklin modified this gait and developed a kinematics and dynamics-based model of the gait [84]. This gait model will be discussed and utilized in the Chapter 4.

In 2006, Andersson introduced a method for generating a rectilinear gait using a pulse traveling through a finite continuous snake-inspired robot [85]. As with Merino's gait, a "bump" is generated along a given path at the tail end of the robot and then propagated forward along its body. The progression of the robot can be determined by the change of position of the tail with respect to the 1-dimensional path of the robot. After the completion of a cycle, every point of the snake would have advanced the length of a stride along the arbitrary path as given by the following:

$$L_{sl} = L_p - w \quad (2.8)$$

Where L_p denotes the length of the pulse as measured along the body of the snake and w is the parameter which denotes the width of the pulse along the path curve. The pulse shape determines the progression of the robot. Also, the curve representing the continuous snake was determined and can be given by the following equation:

$$x(\hat{s}) = x_p(\hat{s}) + N(\hat{s})h(\hat{s} - \hat{s}_1), \quad \hat{s} \in [\hat{s}_0, \hat{s}_1] \quad (2.9)$$

Where $N(s)$ is the unit vector field that describes the direction the snake is lifted from the surface. In practice, one would take N to be normal to the surface but in general it can be any transverse vector field. The position of the tail of the snake along the path curve is denoted by s_0 while the position of the tail end of the pulse is denoted s_1 . The symbol h is the function that describes the height of the pulse. Finally, s is the arc length along the path of the snake and the path itself is x_p .

2.9 Summary

Although snake-inspired robot designs have demonstrated functionality and a number of useful gaits, the current designs still have not been placed into widespread use. Even with better understanding of the current proven designs and their useful features, there are

still major design challenges which designers must resolve to increase the practicability of snake-inspired robots. There are at least three major design challenges which must be addressed to maximize the utility of snake-inspired robots: (1) small cross-sections, (2) high velocities, and (3) longer operational time. Currently, fully operational, tether-less snake-inspired designs have achieved cross-sectional areas as low as 0.002 m^2 . While robots with these cross-sectional areas may be very useful in activities such as searching for survivors through rubble, even smaller cross-sectional areas may enable more opportunities in activities such as military reconnaissance. Snake-inspired robot designs will also need to be able to achieve higher forward and turning velocities than what is currently possible. In many applications, robot designs will need to be capable of at least keeping pace with human personnel. Finally, snake-inspired robot designs will need to achieve longer operational time despite reduction in size. If a robot were capable of only an hour of operational time, it may only be capable of several minutes of actually performing its given task when the time to travel to the desired location is also considered.

3 Design of a Snake-Inspired Robot Capable of Executing a High Speed Gait

3.1 Overview

In this chapter, we introduce a concept for a high speed rectilinear gait-based on rapid expansion and contraction of body segments and a design for a snake-inspired robot capable of executing this gait. The new rectilinear gait is based on an exaggeration of the kinematics observed in natural snakes when executing rectilinear motion. This motion is described as the snake's body segments expanding and contracting linearly with little to no vertical displacement, which allows most of the joint motion to be directly utilized in forward displacement. To accomplish this goal, a new high speed, compact parallel mechanism is designed and fabricated. The parallel mechanism, capable of prismatic as well as revolute motion, is employed in the robot design, enabling turning as well as forward motion. Since the mechanism concept is new, thus are its kinematics and dynamics, therefore, a mechanical analysis of the mechanism is conducted and presented. In addition to the parallel mechanism, a method of anchoring the robot to the terrain through friction is developed. The anchoring concept provides positive forward displacement during extension. A design for a multi-surface friction anchor is presented and analyzed. Finally, a prototype of the snake-inspired robot design is fabricated and used to demonstrate the concepts introduced.

3.2 Exaggerated Rectilinear Gait Concept

Many published snake-inspired robots mimic rectilinear motion by propagating a vertical wave from the aft end of the robot to the front using its segments. This motion results in forward progression of the robot through the lifting and displacement of

adjacent segments relative to one another as the wave passes through the body. However, much of the motion observed in the robot throughout the gait cycle is normal to the surface being traversed and does not directly change the forward position. Therefore, these gaits tend to be highly energy inefficient and limited in terms critical performance factors, such as, speed and range. As a result, heavier power supplies will need to be incorporated to increase speed and range, which will require larger motors to carry the increased load. Ultimately, the entire robotic system will be required to be larger, resulting in a platform which is unsuitable for use in small, tight enclosed spaces. To address these issues, our approach utilizes exaggerated rectilinear gait motion, which executes at high extension and contraction rates in a straight line, while maintaining a small cross section.

3.2.1 High Speed Exaggerated Forward Gait

The concept for the proposed high speed forward gait, illustrated in Figure 3.1, is similar to the gait used by the robots introduced by Chen et al. [46]. The primary difference is that while Chen's design and gait seem to emphasize modularity, the gaits presented in this work focus on the motion of the snake-inspired robot as a whole. The proposed gait does not move one module at a time; rather it expands and contracts all the modules simultaneously during a global robot cycle. While we do recognize that Chen's gait has advantages, such as, minimum slippage, the goal of this gait was speed. The high speed forward gait concept used for this robot architecture is illustrated in Figure 3.1 and described in the following:

- Step 1 – The robot begins in its nominal configuration where the internal segments are contracted and the friction anchors' high friction surfaces are not in contact with the terrain.
- Step 2 – The rear friction anchor is “planted” into the terrain to resist the reaction forces of the prismatic joints of the internal segments and ensure that the position of the rear end of the robot remains unchanged during expansion of the segments during step three.
- Step 3 – Each internal segment of the robot expands to its maximum length – allowing the front of the robot to position itself a distance from the rear equal to the robot's original length plus the sum of the segments' total displacement.
- Step 4 – The rear friction anchor is lifted from the terrain while, simultaneously, the front friction anchor is “planted” into the terrain to resist the reaction forces of the prismatic joints of the internal segments during the contraction of step five.
- Step 5 – The robot segments contract to their nominal length, causing the entire robot to advance a distance equal to the sum of the displacements of each segment during expansion. The robot returns to nominal configuration and repeats the cycle.

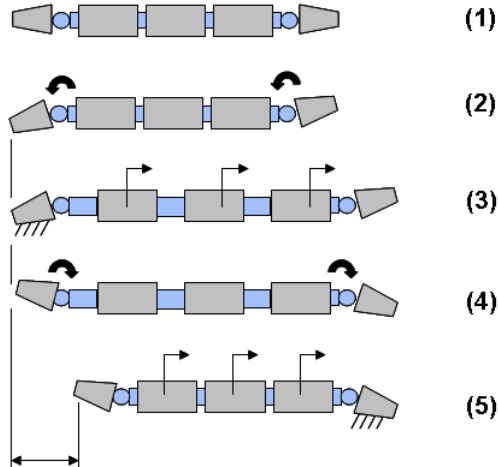


Figure 3.1: Theoretical High Speed Forward Gait Sequence

3.2.2 High Speed Exaggerated Turning Gait

The proposed concept for the high speed turning gait, illustrated in Figure 3.2, is unique, although it does somewhat resemble the global motions demonstrated in the turning gait for the planar inchworm robot introduced by Chen et al [50]. In this gait, only the friction anchors and the actuated revolute joints connecting the internal robot segments are used. The prismatic joints remain in their nominal position throughout the gait. The gait is described in the following:

- Step 1 – Observing from the side view of the robot, the robot begins in its nominal configuration where the internal segments are contracted and the friction anchors are not in contact with the terrain. The rear friction anchor is “planted” into the terrain to resist the reaction forces of the robot’s internal revolute joints. The rear friction anchor ensures that the position and orientation of the rear end of the robot remains unchanged during the change of position and orientation of the segments during step two.

- Step 2 – Observing from the top view of the robot, the actuated revolute joints change the orientation of the internal segments to produce a global change in the robot configuration. The robot’s configuration changes as the robot’s length curls toward the intended direction of turn.
- Step 3 – Observing from the side view of the robot, the rear friction anchor is disengaged from the terrain while, simultaneously, the front friction anchor is “planted” into the terrain to resist the reaction forces of the internal revolute joints during change of the position and orientation of the segments during step four.
- Step 4 – Observing from the top view of the robot, the actuated revolute joints return the orientation of the internal segments to their nominal position. As a result, the robot segments return to an inline state and the robot achieves the desired orientation. The friction anchors return to their nominal position, resulting in no contact between the terrain and either anchor. The gait cycle is complete.

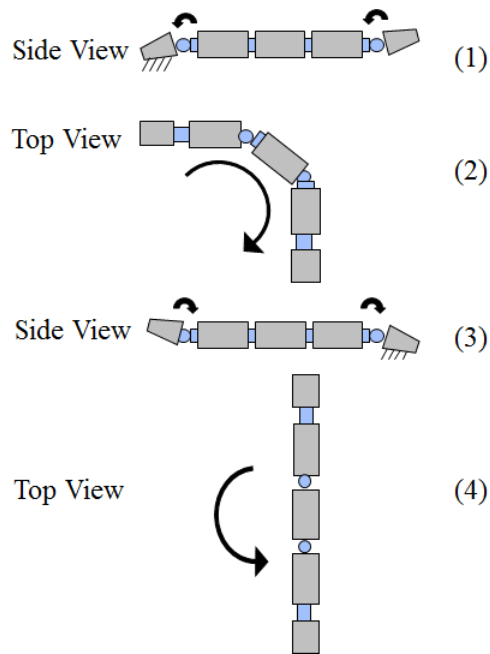


Figure 3.2: Theoretical High Speed Turning Gait Sequence

3.3 Design of a New Parallel Mechanism

The core challenge for the snake-inspired robot design problem is addressing the need for compact, high speed linear actuation. Converting stored energy into linear motion can be achieved by a wide variety of mechanisms and devices which are proven and well understood. These mechanisms include rack and pinion assemblies, DC powered solenoid devices, cam and follower mechanisms, pneumatic or hydraulic powered pistons, belt driven friction drives, and slider crank mechanisms. However, due to speed and power requirements, many of these solutions were quickly determined to be unsuitable for the design goals of this work. For example, DC powered solenoid devices are a simple and straight forward method to produce linear motion in a compact space, but they have large voltage requirements for relatively small loads and short translational distances. Therefore only four options were considered: hydraulics, pneumatics, DC motors with gearbox reduction and servomotors. These options are compared and a final option selected in Section 3.3.1.

Once the actuation system is defined, a mechanism must be devised to execute the desired joint motion based on the actuation system choice. Various mechanism concepts were considered and evaluated. The process of down selecting these options resulted in the introduction of a new planar parallel mechanism concept. The parallel mechanism concept is introduced in Section 3.3.2. The new parallel mechanism can also produce rotary motion as well as linear motion, eliminating the need for additional revolute joints for executing turning gaits.

3.3.1 Actuation System Options

In the initial phases of design, the choice of actuation is very important since it will drive many of the other design decisions. The joint actuation system often defines the overall size of the robot and defines other sub-systems to be included in the robot, such as power source and control methodology. There are various types of actuation systems, but for this design effort, the options were limited to four reliable systems: hydraulics, pneumatics, DC motors with gearbox reduction and servomotors.

- Hydraulics – Hydraulics consists of a system of actuators, piping, control valves, a pump, and an oil or hydraulic fluid. The hydraulic fluid is conveyed through the piping through use of a pump to the actuators. As the actuators fill with fluid, the rods of the actuators move linearly and do work. The control valves, which direct the fluid from one actuator to another, control the actuators and they direct whether the fluid is extending or contracting the actuator. Although the system is somewhat precise and powerful, it is usually not compact enough to support small tether-less, snake-inspired robots.
- Pneumatics – Pneumatics systems are very similar to hydraulic systems with the main difference being that air or gas is the power fluid instead of oil or some other hydraulic fluid. Pneumatic systems are very useful in the fact that the actuators can be sized to nearly any dimension given that the system possesses a powerful enough pump for the given task. However, this system may prove too complex for a small, self-contained snake robot with several degrees of freedom.
- DC Geared motors – Geared motors are simply electric motors with a gearbox attached, both to increase torque and decrease speed or increase speed and

decrease torque. These motors are appropriate for robot mechanisms which require continuous motion, high speed, and high torque within a compact package. However, for small, precise movements, such as, those required in snake-inspired robot applications, these motors they lack an inherent method of control or precision. If used for snake-inspired robots, they will require an addition system to control the position of the motors.

- Servomotor – A servomotor is a self-contained unit that consists of an electric DC motor with gear train to increase torque and a potentiometer. The potentiometer monitors the position of the servo output shaft and provides feedback to the servo controller. The unit can provide a great deal of power and control from a small package and power requirement. Given the versatility of the unit servomotors seem to be an ideal choice for use in small powerful robots. However, the one disadvantage of servomotors is their inherent speed is often quite slow. Standard servomotors move at speeds maximum speeds of around 60 degrees per 0.24 sec (41.67 rpm).

After reviewing the differences between the candidate actuation systems and surveying the commercial available linear actuator solutions, it was decided that commercial high torque servomotors will be utilized to power the robot joints. The major factors that influenced this decision were size and complexity of the various systems. Hydraulics and pneumatics could provide a direct linear solution, however, due to the number of actuators anticipated for the final robot prototype; we deemed that a single compressor and fluid storage unit would greatly exceed the size constraints for the prototype. In addition, multiple sets of smaller compressors and storage units were not

considered due to weight and complexity concerns. Similarly, due to concerns of complexity, DC motors with gear reduction were eliminated. In order to incorporate precision motion, each DC motor output shaft would need to be equipped with a shaft encoder to count revolutions. The shaft encoder alone would only provide change in position not actual position. Therefore, additional sensors would need to be added to the robot joints to define initial and/or final positions for the onboard controller for the DC motors.

The servomotor option was chosen because the system provides a compact, lightweight solution with no need for additional components to properly support the robot application. In order to address the inherent slow rotational speed of the motors and the lack of linear output, we chose to devise a new parallel mechanism which can provide high speed, linear output, based on servomotor rotational input. This new parallel mechanism design is described in Section 3.3.2. The selection of the actual servomotor unit for the parallel mechanism demonstration prototype was based on a determination of the most powerful commercially available standard sized servomotor at the time, the HS-985MG pictured in Figure 4.1.



Figure 3.3: Hitec HS-985MG

A survey of commercially available servomotors resulted in the selection of the Hitec HS-985MG unit, which is classified as both a high torque and high speed servomotor. The HS-985MG servomotor is capable of 12.4 kg-cm of maximum torque and a

maximum speed of 0.13 s/60 deg. from a 62 g package. The motor also consist of a metal gear train providing a range of 180 degrees. Finally, the commercial servo has an operational voltage range of 4.8-6.0 Volts.

3.3.2 2RRP Parallel Mechanism

To execute the range of motion described by the rectilinear gait concepts introduced in Section 3.2, the robot must be able to perform high speed linear expansion/contraction and pivoting motions between segments. A simplified solution would be compromised of separate prismatic actuators connected in series to revolute actuators between joints. However, this solution may impose concentrations of mass at the terminal ends of the segment and thereby increasing the torque required to rotate adjacent segments and reduced overall operational capability of the robot. Another approach is to apply a compact mechanism between segments which is capable of executing all the required joint motion while reducing the mass concentration on the terminal ends. In this work, we employed the second approach is the form of a new 2-DOF parallel mechanism which is capable of high speed linear motion and pivoting motion. In addition, the mechanism requires only the rotational input from two servomotors.

3.3.2.1 Parallel Mechanism Concepts

The conceptual design of the new parallel mechanism is based on an effort to couple of the output from two parallel, independently powered scotch yoke-like mechanisms. Typically, when designing a new mechanism, the goal is to generate all the possible mechanisms concepts which satisfy the customers' requirements and evaluate the resulting solutions to select the most promising design [86]. This process may be repeated several times until an optimum design is defined. In order to ensure all the feasible

mechanisms are identified and thereby identify an optimum design, the designer should employ a systematic design methodology such as the application of graph theory and combinatorial analysis [86]. When using this method, a feasible mechanism is first defined based on the customers' requirements, and then a graph representation is generated that uniquely defines the mechanism. From this graph all the possible kinematic structures that satisfied the structural characteristics are enumerated using combinatorial analysis [86].

In this work, however, the goal is not to generate an optimum design, but rather to identify an acceptable mechanism to support the demonstration of the exaggerated gait. At this stage in our research, we consider optimization of the platform to be unnecessary. Thus, we only generated enough possible solutions to find an acceptable mechanism to support gait demonstration. In our approach, we first generated a possible solution, Figure 3.4b, based inspiration while observing scotch yoke motion. Next, while maintaining the same kinematic relationships between both the ground and the input links and the ground and output links in Figure 3.4b, we varied the kinematic pairs between the input and output links. These variations results in several possible mechanisms which allow for translational motion of the output link. Also, all the resulting mechanisms were capable of being actuated using only direct input from standard servomotors. These mechanisms concepts served as the set of possibly designs from which an acceptable design solution would be determined. Most of the configurations were quickly eliminated due to the fact that the output link would be over constrained or under constrained. However, four configuration were defined which may meet the design intentions needed for the joints for the robot. The four configurations are illustrated in Figure 3.4.

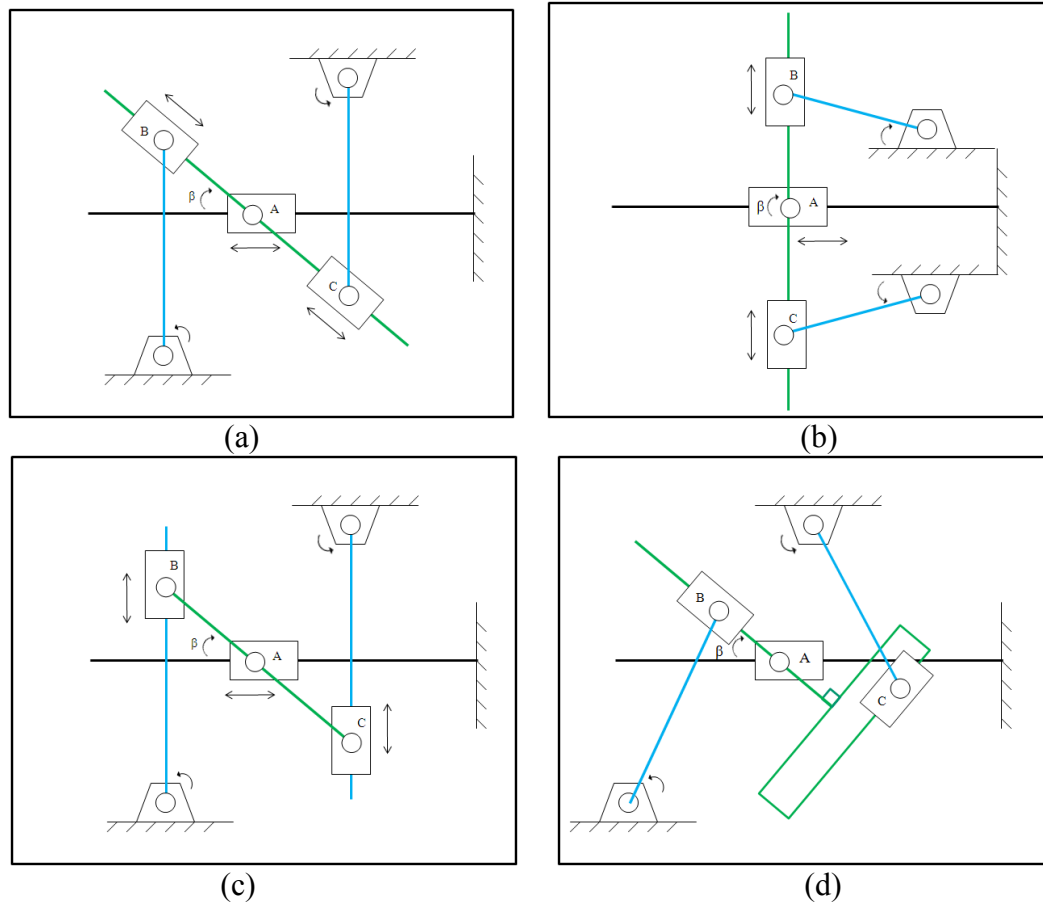


Figure 3.4: Parallel Mechanism Concepts (Kinematic Representation)

The four concepts share similar design elements and provide output in the form of linear translation and pivoting of the output link. However, the four concepts accomplish this motion in different fashions. Descriptions of each concept are given by the following:

- Concept A (Figure 3.4a) – The mechanism is composed of two input limbs, each consisting of a actuated revolute joint mounted to the base link, as well as a passive revolute and prismatic joint connecting to the mechanism’s output link. Also, there is a third passive limb which consists of a revolute and a prismatic joint (center link of the kinematic representation). The passive limb allows prismatic motion along the x -axis and pivoting motions (represented by the angle β) for the output link while resisting motion along the y -axis. Additional

constraints are provided by the fact that the points A , B and C remain collinear throughout the range of motion of the mechanism. These constraints prevent the output link from pivoting while the powered revolute joints are held stationary.

- Concept B (Figure 3.4b) – Similar to Concept A, the inputs to the mechanism are the rotational positions of the two input links driven by actuated revolute joints. However, the location of the input joints differs as they are mounted on near the midpoint of the linear travel of the mechanism in contrast to Concept A, where the input joints are mounted on the opposite edges of the mechanism boundary. The two input links rotate outward from the center of the mechanism with a range of 180 degrees and do not ever cross each other (Figure 3.4b). Similar to Concept A, the output link moves in a prismatic manner along the x -axis via the third passive limb. The revolute joint located on the third limb allows for the pivoting motion characterized by angle β . As in Concept A, additional constraints are provided by points A , B and C remaining collinear throughout the range of motion of the mechanism to prevent un-commanded pivoting of the output link.
- Concept C (Figure 3.4c) – In this mechanism, passive prismatic joints are attached and run along the length of the two input links (Figure 3.4c); as opposed to running along the length of the output link as in Concept A (Figure 3.4a). However, the constraints for pivoting of the output link, defined by points A , B and C remaining collinear (as seen in Concepts A and B) are not present. Instead, the constraints that prevent the output link from pivoting while the powered revolute joints are held stationary are imposed by the prismatic joints on the input

links. The remaining elements of the mechanism are very similar to Concept A, including the third passive limb and motion of the output link.

- Concept D (Figure 3.4d) – This mechanism, though planar and parallel, differs from the previous options in that the two input limbs do not mirror one another. Similar to Concept A and B, the two input links are actuated by a powered revolute joint mounted to the base link and are connected to the output link through a passive prismatic joint (on the output link side) and revolute joint (on the input link side). The third passive limb allows prismatic motion along the x -axis and pivoting motion for the output link while resisting motion along the y -axis. The primary difference between this mechanism and the mechanism in Concept A is that the sliding axis of each passive prismatic joint remains perpendicular to one another throughout the full range of motion, as seen in Figure 3.4d. Through this kinematic arrangement the input link attached at the origin primarily influences the pivoting motion of the output link. The other input link primarily influences the extension of the output link. Due to the simple but unique arrangement, the constraints imposed by the orientation of the prismatic joints prevent any movement of the output link while the powered revolute joints are held stationary.

3.3.2.2 Parallel Mechanism Concept Selection

All four concepts demonstrate the ability to perform prismatic as well as revolute motion along the output link of each parallel mechanism. Each mechanism also couples the output link to coordinated motion between the two input links. Thus, in order to select a concept for the parallel mechanism, we must first examine the limitations of each

concept. In Concept A, simply rotating the input links in opposite directions causes the output link to pivot, providing a wide range of revolute motion. In contrary, the linear expansion and contraction is significantly restricted due to the fact that the angle Beta defined in the nominal position, illustrated in Figure 3.4a, must be maintained to produce pure translation motion. Concept B is capable of a wide range of pure translational and rotational motion. However, the input links pivot outwardly from the centerline of the mechanism, requiring that the mechanism have a large cross-sectional area in order for the mechanism's output link to produce significant displacements. Concept C is capable of a wide range of pure translational motion and similar to Concept A and B, both input limbs contribute to load capacity of the mechanism. Contrary to Concept A and B, pivoting is only possible in inverse kinematics. Direct kinematics may only produce translational motion. Finally, Concept D possesses an output link which is capable of a wide range of translational and rotational motion. The primary limitation of this design is that forward limb contributes to rotational load capacity only, while the aft limb contributes to translational load capacity only. Due to this limitation, the mechanism's output link can carry significantly less load than the other three options assuming equally capable input motors.

	Length of Extension	Range of Rotation	DOF
Concept A	NA	NA	A
Concept B	NA	A	A
Concept C	A	NA	NA
Concept D	A	A	A

Table 3.1: Parallel Mechanism Design Comparison

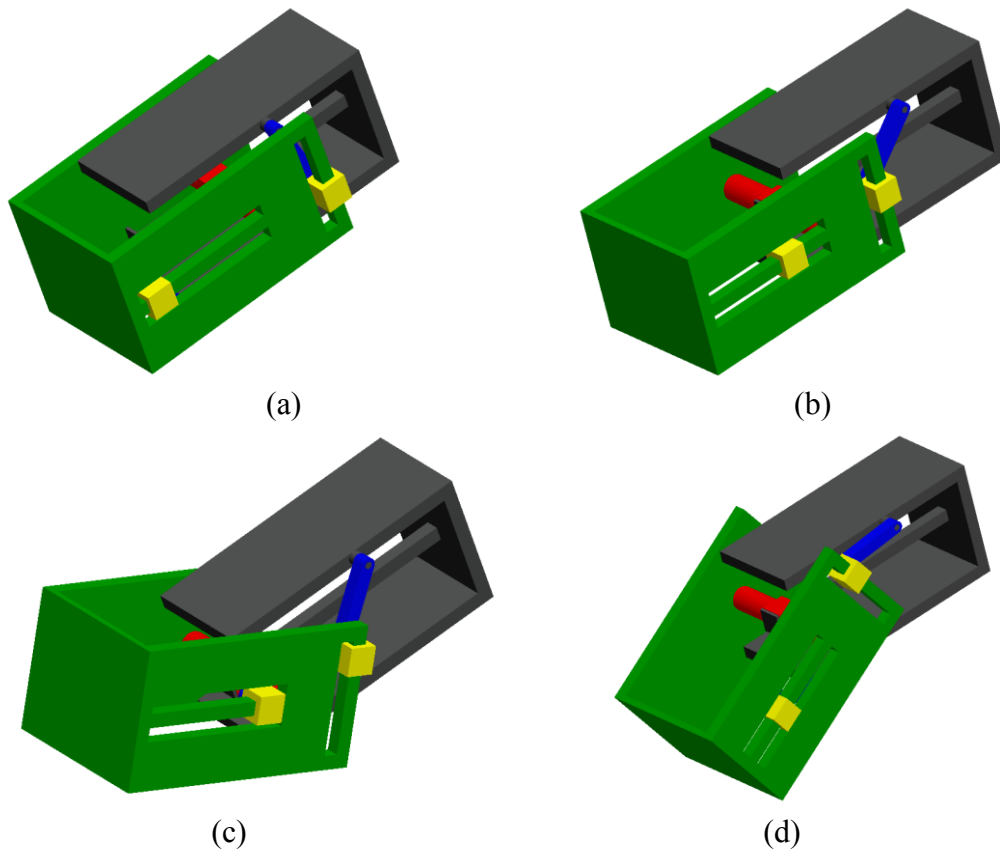


Figure 3.5: Mechanism (a) Contracting, (b) Extending, (c) Pivoting Up and (d) Down

The major criteria considered when down selecting the mechanism were as follows:

(1) Length of Extension, (2) Range of Rotation and (3) Output Link Degrees of Freedom

(DOF). Criterion 1 is a measure of the maximum linear travel of the output link about the passive prismatic joint as observed in Figure 3.4. In order to reduce the number of mechanisms needed to realize the desired speed of the robot, we must achieve the highest linear travel possible. Therefore, the goal for the criterion is a length of extension equal to the length of the contracted mechanism. If we use standard sized servomotors as the actuators for the mechanism, the goal for extension length is defined as 76 mm. A large number of snake-inspired robots utilize servomotors to achieve a wide range of motion. A standard servomotor achieves a 90 degree range of rotation; therefore for criterion 2, we choose to define the goal for range of rotation as 90 degrees. Finally, criterion 3 confirms whether the mechanism can support the required 2 DOF motion through a direct kinematics analysis. After thoroughly exploring the limitations of the four concepts and reviewing the acceptable (A) and non-acceptable (NA) ratings in Table 3.1, we eliminated Concepts A, B and C. Thus, Concept D was chosen for the basis of robot module. In order to verify that Concept D is physically feasible, a CAD model of the mechanism concept was developed and is presented in Figure 3.5a with the output link contracted, extended (Figure 3.5b) or pivoted up or down (Figure 3.5c-d).

3.3.3 Joint Module Final Design

The detailed design of the parallel mechanism concept utilizes slotted holes and sliding pin joints to replicate the functions of passive prismatic and revolute joints, observed in Figure 3.5. These features allow for fewer parts, fewer assemblies and a more compact design. Each parallel mechanism, pictured in Figure 3.6, is composed of two servomotors with servo arms attached to the output shafts acting as the input links to the mechanism, see right image of Figure 3.6. Each servo arm is attached to the output link

of the mechanism (a U bracket) through a slotted hole and pin joint, see left image in Figure 3.6. Because the mechanism is a 3-D object, the passive limb (the pin in which the U bracket pivots) is replicated on the opposite side of the mechanism to provide support and stability for the U bracket throughout the range of motion. This configuration allows the output link to move in a prismatic and revolute manner depending on the location of the pin within its associated slotted hole for each input link.

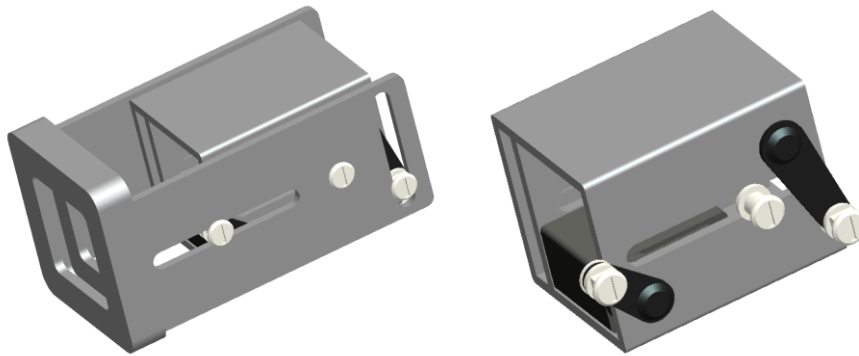


Figure 3.6: Parallel Mechanism Concept CAD Model

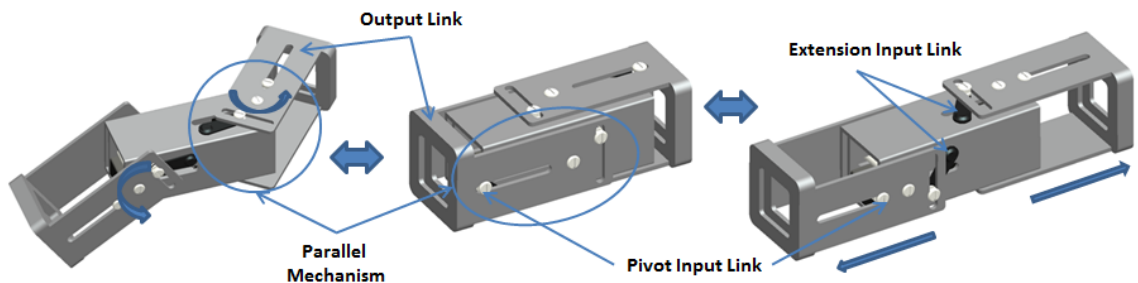


Figure 3.7: Joint Module Final CAD Model

Essentially, the complete robot is a serial collection of modules. Thus, a modular structure was devised in which two identical parallel mechanisms were assembled in a single module, Figure 3.7 [87, 88]. The two mechanisms are assembled serially in a single housing; with the mechanisms' orientation offset 90° apart about the x-axis (direction of the linear expansion) of the module. Both mechanisms contribute to the total

linear displacement of the adjacent module (see right image of Figure 3.7), while one mechanism is capable of providing yawing motion and the other provides pitching motion (see left image of Figure 3.7). This assembly provides the potential for full spatial motion for the robot through the fact that the modules are able to lift as well as pivot horizontally. In addition, this configuration allows all modules to contribute to the expansion-contraction capability of the robot, significantly increasing its speed. A prototype module was fabricated and is pictured in Figure 3.8. The prototype module is made primarily from 6061 aluminum and has a 64 x 64 mm cross-section and a length of 165 mm. Each of the prototype parallel mechanisms is capable of 90 degrees of motion and 38 mm of extension. Each parallel mechanism consists of two standard sized Hitec HS-985MG High Torque servomotors. They are capable of 12.4 kg-cm maximum torque and a maximum speed of 0.13 s/60 deg. from a 62 g package. The servomotors also consist of a metal gear train providing a range of 180 deg.

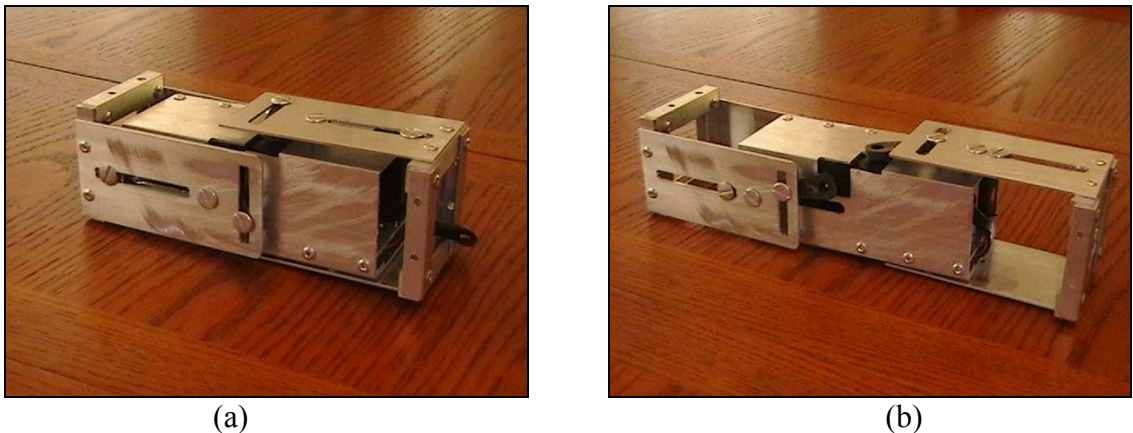


Figure 3.8: Prototype Module (a) Contracted and (b) Extended

3.4 Analysis of the Parallel Mechanism

Due to the fact that both input links actuate only on one side of the parallel mechanism, illustrated in Figure 3.6, the mechanism can be analyzed in 2-D space using

a kinematic representation shown in Figure 3.9. In the kinematics illustration, the slotted hole and pin joints are represented using a passive revolute joint attached to a passive prismatic joint. From observation, it can be determined that the mechanism possesses 2 DOF: one translational and one rotational. Note that the axis of rotation moves along the translational axis. The degrees of freedom are observed in Figure 3.5: demonstrating the mechanism's output link contracting and extending about the translational axis and pivoting about the center rotational joint. The DOF of the mechanism is confirmed using the *Grübler criterion* [58]:

$$F = \lambda(n - j - 1) + \sum_i f_i \quad (3.01)$$

$$F = 3(7 - 8 - 1) + 8 = 2$$

Where λ is the degrees of freedom of space in which a mechanism is intended to function. The number of links in a mechanism, including the fixed link, is represented by n and j represents the number of joints in a mechanism, assuming that all the joints are binary. Finally, f_i is the number of degrees of relative motion permitted by joint i . With the planar nature of the mechanism confirmed, the kinematics and dynamics equations of motion for the mechanism will be determined in the following section based on the kinematic representation of the planar parallel mechanism illustrated in Figure 3.9. Note, for the all analyses $c\theta_1 = \cos \theta_1$ and $s\theta_1 = \sin \theta_1$.

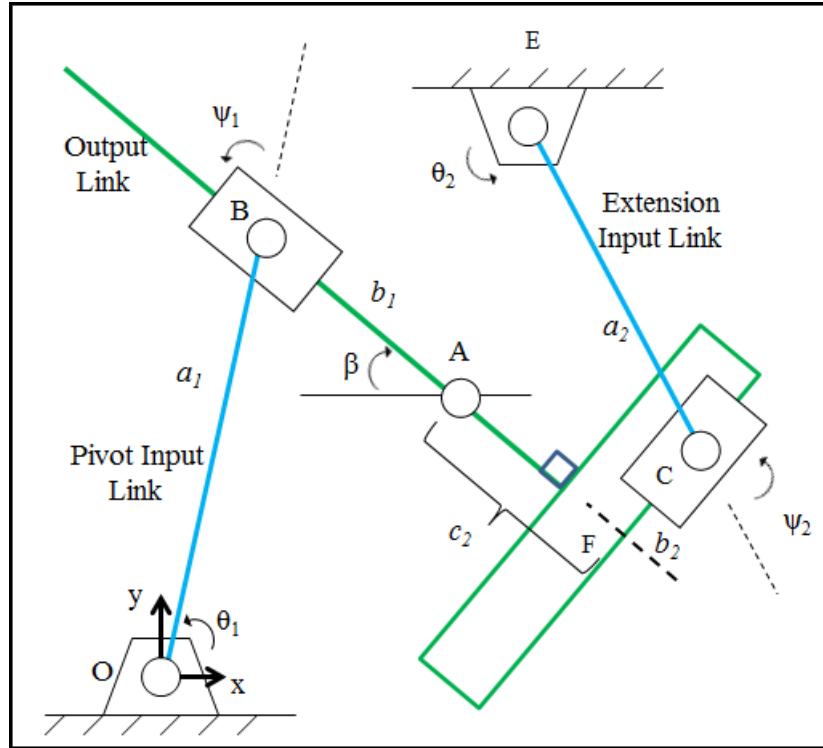


Figure 3.9: Parallel Mechanism Kinematic Representation

3.4.1 Mechanism Geometry

Referring to Figure 3.9, the origin of the fixed coordinate frame is located at point O . We assume that the center of mass of the output link is point A . The location of the moving platform can be specified in terms of the x -position of point A and an orientation angle β . The orientation angle β can be calculated using the known values of the position of point B (x_B, y_B) and A (x_A, y_A). Note that point A can only move in the x -direction due to the constraints imposed by the prismatic joint, therefore y_A is a constant. Thus there are only two unknowns to describe the 2-DOF motion of the planar parallel mechanism. Figure 3.10 shows the link lengths and joint angles of limb 1. From the geometry of Figure 3.10, a vector-loop equation can be written as shown in Equation 3.02 and expressed in the fixed coordinate frame in Equation 3.03.

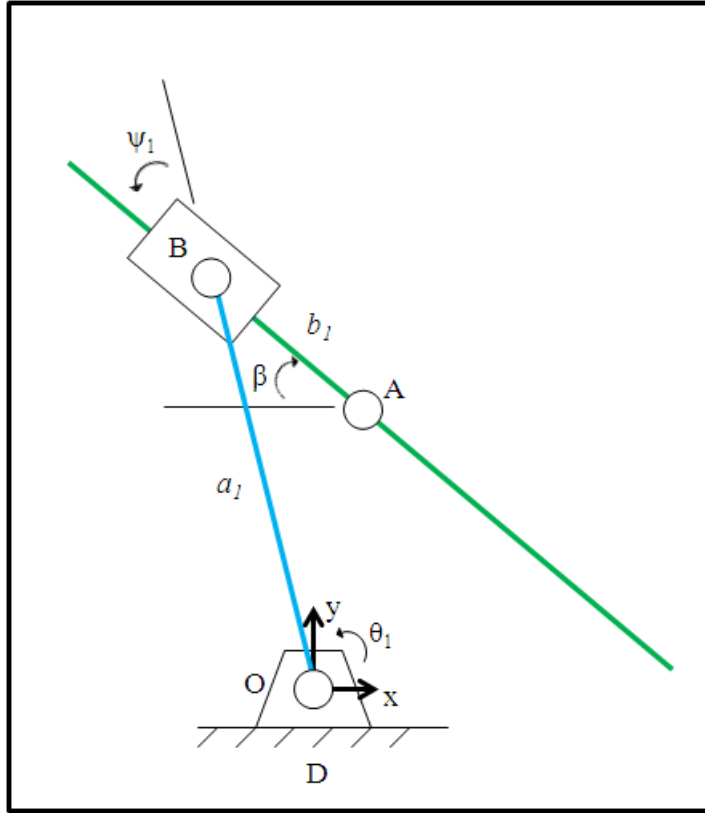


Figure 3.10: Limb 1 (RPR) Kinematic Representation

$$\overline{OA} = \overline{OD} + \overline{DB} + \overline{BA} \quad (3.02)$$

$$\begin{aligned} x_A &= x_D + a_1 c \theta_1 - b_1 c (\theta_1 + \psi_1) \\ y_A &= y_D + a_1 s \theta_1 - b_1 s (\theta_1 + \psi_1) \end{aligned} \quad (3.03)$$

Since D is located at the origin, $x_D = y_D = 0$. Since ψ_1 is a passive joint angle, it should be eliminated from Equation 3.03. Therefore, we substitute the following expression into Equation 3.03, which yields Equation 3.05:

$$\theta_1 + \psi_1 = 180 - \beta \quad (3.04)$$

$$\begin{aligned} x_A &= a_1 c \theta_1 + b_1 c \beta \\ y_A &= a_1 s \theta_1 - b_1 s \beta \end{aligned} \quad (3.05)$$

Note that b_1 represents a passive prismatic joint introduced by the slotted hole and pin joint. The passive prismatic joint b_1 can be written as:

$$b_1 = \left(\frac{x_A - x_B}{c\beta} \right) = \left(\frac{x_A - a_1 c \theta_1}{c\beta} \right) \quad (3.06)$$

Next we substitute Equation 3.06 into Equation 3.05 and add the x - and y -terms which yields the geometric relationship for limb 1 given as:

$$y_A - a_1 s \theta_1 + s\beta \left(\frac{x_A - a_1 c \theta_1}{c\beta} \right) = 0 \quad (3.07)$$

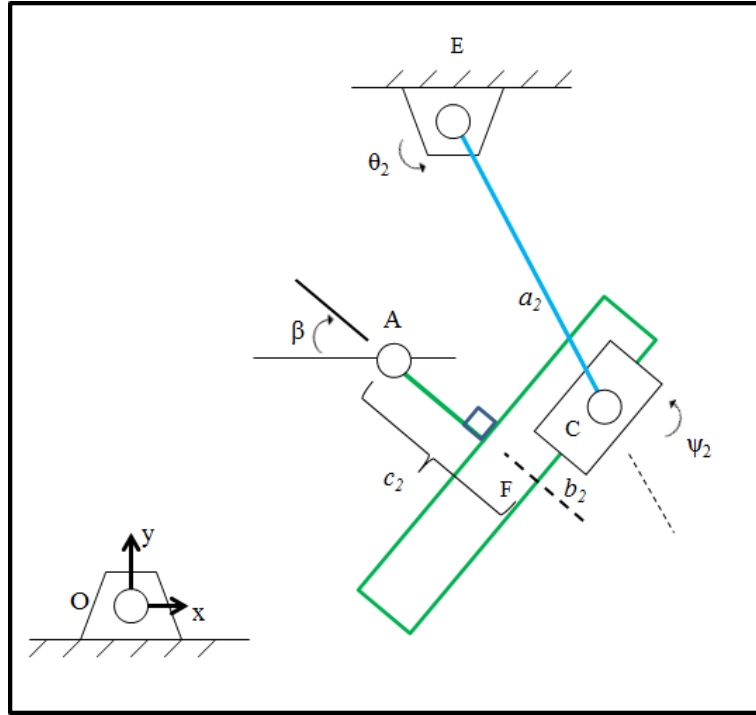


Figure 3.11: Limb 2 (RPR) Kinematic Representation

Similarly, the geometric relationship for limb 2 is obtained. The vector-loop equation is shown in Equation 3.08 and expressed in the fixed coordinate frame in Equation 3.09.

$$\overline{OA} = \overline{OE} + \overline{EC} + \overline{CF} + \overline{FA} \quad (3.08)$$

$$\begin{aligned} x_A &= x_E - a_2 c \theta_2 + b_2 c (\theta_2 + \psi_2) + c_2 c (\theta_2 + \psi_2 + 90) \\ y_A &= y_E - a_2 s \theta_2 + b_2 s (\theta_2 + \psi_2) + c_2 s (\theta_2 + \psi_2 + 90) \end{aligned} \quad (3.09)$$

Since ψ_2 is a passive joint angle, it should be eliminated from Equation 3.09. Therefore, we substitute Equation 3.10 into Equation 3.09 which yields Equation 3.11:

$$\theta_2 + \psi_2 = 90 - \beta \quad (3.10)$$

$$\begin{aligned} x_A &= x_E - a_2 c \theta_2 + b_2 s \beta - c_2 c \beta \\ y_A &= y_E - a_2 s \theta_2 + b_2 c \beta + c_2 s \beta \end{aligned} \quad (3.11)$$

The representation of the limb 2 passive prismatic joint is shown in Equation 3.12. After summing the squares of Equation 3.11, Equation 3.12 is substituted into Equation 3.11 to yield the geometric relationship given in Equation 3.13.

$$\begin{aligned} b_2^2 &= (x_F - x_C)^2 + (y_F - y_C)^2 \\ b_2^2 &= ((x_A + c_2 c \beta) - (x_E - a_2 c \theta_2))^2 + ((y_A - c_2 s \beta) - (y_E - a_2 s \theta_2))^2 \end{aligned} \quad (3.12)$$

$$c\beta(x_A - x_E) + s\beta(y_E - y_A) + a_2 c(\beta + \theta_2) + c_2 = 0 \quad (3.13)$$

3.4.2 Inverse Kinematics

For the inverse kinematics the position (x_A, β) of the moving platform is given and the joint angles θ_1 and θ_2 need to be found. Starting with limb 1, Equation 3.07 is arranged as the following:

$$d_{11} s \theta_1 + d_{12} c \theta_1 + d_{13} = 0 \quad (3.14)$$

$$\begin{aligned} d_{11} &= -a_1 \\ d_{12} &= -a_1 \frac{s\beta}{c\beta} \end{aligned} \quad (3.15)$$

$$d_{13} = y_A + x_A \frac{s\beta}{c\beta}$$

Similarly, the expression for limb 2, Equation 3.13, is arranged as the following:

$$d_{21} s \theta_2 + d_{22} c \theta_2 + d_{23} = 0 \quad (3.16)$$

$$\begin{aligned} d_{21} &= -a_2 s \beta \\ d_{22} &= a_2 c \beta \\ d_{23} &= c\beta(x_A - x_E) + s\beta(y_E - y_A) + c_2 \end{aligned} \quad (3.17)$$

Using the following half-angle trigonometric identities, Equation 3.14 and Equation 3.16 are rewritten as Equation 3.19:

$$s\theta_i = \frac{2t_i}{1+t_i^2} \quad c\theta_i = \frac{1-t_i^2}{1+t_i^2} \quad \text{where } t_i = \tan \frac{\theta_i}{2} \quad (3.18)$$

$$At_i^2 + Bt_i + C = 0 \quad (3.19)$$

$$\begin{aligned} A_i &= d_{i3} - d_{i2} \\ B_i &= 2d_{i2} \\ C_i &= d_{i2} + d_{i3} \end{aligned} \quad \text{where } i = 1, 2 \quad (3.20)$$

Equation 3.17 takes the form of a quadratic equation and solved using the following expressions:

$$t_i = \frac{-B_i \pm \sqrt{B_i^2 - 4A_iC_i}}{2A_i} \quad (3.21)$$

$$\theta_i = 2 \tan^{-1}(t_i) \quad \text{where } i = 1, 2 \quad (3.22)$$

3.4.3 Direct Kinematics

For the direct kinematics, θ_1 and θ_2 are given and the output link position (x_A, β) is found. This is accomplished by eliminating x_A from Equations 3.07 and 3.13. The equations are rewritten as:

$$x_A + e_{11} \frac{c\beta}{s\beta} + e_{12} = 0 \quad (3.23)$$

$$\begin{aligned} e_{11} &= y_A - a_1 s\theta_1 \\ e_{12} &= -a_1 c\theta_1 \end{aligned} \quad (3.24)$$

$$x_A + e_{21} \frac{s\beta}{c\beta} + e_{22} \frac{1}{c\beta} + e_{23} = 0 \quad (3.25)$$

$$\begin{aligned}
e_{21} &= y_E - y_A - a_2 s \theta_2 \\
e_{22} &= c_2 \\
e_{23} &= a_2 c \theta_2 - x_E
\end{aligned} \tag{3.26}$$

Next, subtracting Equation 3.23 from Equation 3.25 yields:

$$f_{11} s \beta c \beta + f_{12} s^2 \beta + f_{13} c^2 \beta + f_{14} s \beta = 0 \tag{3.27}$$

$$\begin{aligned}
f_{11} &= a_2 c \theta_2 + a_1 c \theta_1 - x_E \\
f_{12} &= y_E - y_A - a_2 s \theta_2 \\
f_{13} &= a_1 s \theta_1 - y_A \\
f_{14} &= c_2
\end{aligned} \tag{3.28}$$

Again, we utilize the half-angle trigonometric identities from Equation 3.18 to rewrite Equation 3.27 as quartic expression, Equation 3.29:

$$g_{11} t^4 + g_{12} t^3 + g_{13} t^2 + g_{14} t + g_{15} = 0 \tag{3.29}$$

$$\begin{aligned}
g_{11} &= f_{13} \\
g_{12} &= 2f_{14} - 2f_{11} \\
g_{13} &= 4f_{12} - 2f_{13} \\
g_{14} &= 2f_{14} + 2f_{11} \\
g_{15} &= f_{13} \\
t &= \tan \frac{\beta}{2}
\end{aligned} \tag{3.30}$$

Upon observation of Equation 3.29, we were not able to identify either a quasi-symmetric case, or a bi-quadratic case to reduce the complexity of the quartic expression. Therefore, in order to find the roots of the quartic equation, we employ Ferrari's method as follows:

$$A = g_{11} \quad B = g_{12} \quad C = g_{13} \quad D = g_{14} \quad E = g_{15} \tag{3.31}$$

$$\begin{aligned}
\alpha &= -\frac{3B^2}{8A^2} + \frac{C}{A} & \varphi &= \frac{B^3}{8A^3} - \frac{BC}{2A^2} + \frac{D}{A} & \gamma &= -\frac{3B^4}{256A^4} + \frac{CB^2}{16A^3} - \frac{BD}{4A^2} + \frac{E}{A} \\
P &= -\frac{\alpha^2}{12} - \gamma & Q &= -\frac{\alpha^3}{108} + \frac{\alpha\gamma}{3} - \frac{\varphi^2}{8} & R &= -\frac{Q}{2} \pm \sqrt{\frac{Q^2}{4} + \frac{P^3}{27}} \\
U &= \sqrt[3]{R} & z &= \begin{cases} -\frac{5\alpha}{6} + U - \frac{P}{3U} & \text{if } U \neq 0 \\ -\frac{5\alpha}{6} + U - \sqrt[3]{Q} & \text{if } U = 0 \end{cases} & W &= \sqrt{\alpha + 2z}
\end{aligned} \tag{3.32}$$

Following Ferrari's method, β is found using Equations 3.33 and 3.34. Generally, there are four solutions of β and therefore four possible configurations. Once the proper configuration is identified, the associated solution for x_A is then found by employing Equation 3.25.

$$t = -\frac{B}{4A} + \frac{\pm_s W \mp_t \sqrt{-\left(3\alpha + 2z \pm_s \frac{2\varphi}{W}\right)}}{2} \tag{3.33}$$

$$\beta = 2 \tan^{-1}(t) \tag{3.34}$$

3.4.4 Jacobian Analysis

In this section, we perform the Jacobian analysis and determine the singularities conditions of the parallel mechanism. Referring to Figure 3.09, a Jacobian matrix is written to describe the relationship between the input joint rates and output velocity about the point A . Recall that the loop-closure equation written for limb 1 in Equation 3.03 is expressed in a simplified form in Equation 3.07, where the passive variables have been eliminated. A simplified form of the velocity vector-loop equation for limb 1 is obtained by taking the derivative of Equation 3.07 with respect to time and is given as:

$$\dot{x}_A s \beta + x_A \dot{\beta} c \beta - y_A \dot{\beta} s \beta - a_1 \dot{\beta} c(\beta + \theta_1) - a_1 \dot{\theta}_1 c(\beta + \theta_1) \tag{3.35}$$

Equation 3.35 is rewritten as follows:

$$j_{11}\dot{x}_A + j_{12}\dot{\beta} = j_{13}\dot{\theta}_1 \quad (3.36)$$

$$\begin{aligned} j_{11} &= s\beta \\ j_{12} &= x_A c\beta - y_A s\beta - a_1 c(\beta + \theta_1) \\ j_{13} &= a_1 c(\beta + \theta_1) \end{aligned} \quad (3.37)$$

In a similar fashion, the simplified loop-closure equation for limb 2 is given by Equation 3.13 and its derivative with respect to time is given by Equation 3.38. It is rewritten into a similar form as limb 1 in Equation 3.39.

$$\dot{x}_A c\beta + (x_E - x_A)\dot{\beta}s\beta + (y_E - y_A)\dot{\beta}c\beta - a_2\dot{\beta}s(\beta + \theta_2) - a_2\dot{\theta}_2s(\beta + \theta_2) \quad (3.38)$$

$$j_{21}\dot{x}_A + j_{22}\dot{\beta} = j_{23}\dot{\theta}_2 \quad (3.39)$$

$$\begin{aligned} j_{21} &= c\beta \\ j_{22} &= (x_E - x_A)s\beta + (y_E - y_A)c\beta - a_2s(\beta + \theta_2) \\ j_{23} &= a_2s(\beta + \theta_2) \end{aligned} \quad (3.40)$$

The two equations are arranged in matrix form to obtain the Jacobian matrices as follows:

$$J_x \dot{x} = J_q \dot{q} \quad \text{and} \quad J = J_q^{-1} J_x \quad (3.41)$$

$$\begin{aligned} J_x &= \begin{bmatrix} j_{11} & j_{12} \\ j_{21} & j_{22} \end{bmatrix} & \dot{x} &= \begin{bmatrix} \dot{x}_A \\ \dot{\beta} \end{bmatrix} \\ J_q &= \begin{bmatrix} j_{13} & 0 \\ 0 & j_{23} \end{bmatrix} & \dot{q} &= \begin{bmatrix} \dot{\theta}_1 \\ \dot{\theta}_2 \end{bmatrix} \end{aligned} \quad (3.42)$$

Inverse kinematic singularities occur when any of the diagonal elements of J_q become zero [58]. Observing the formulations for the diagonally elements, three possible scenarios that will generate an inverse singularity were identified. The first scenario is described as $\beta = \theta_1 = \pi/4$, or limb 1 perpendicular to the output link. The second scenario is described as $\beta = \theta_2 = \pi/2$ or $\beta = \theta_2 = 3\pi/2$, which results in limb 2 and the output link

parallel to the y-axis of the origin. In this configuration, the output link is either pointed directly up or down. The third scenario is described as $\beta = \theta_2 = 0$ or $\beta = 0$ and $\theta_2 = \pi$, which results in limb 2 and the output link parallel to the x-axis of the origin. In this configuration, the output link is either fully extended or contracted. The first two scenarios are outside of the expected range of motion of the mechanism for the given robot application. Additionally, the gaits described in this work do not require the lost DOF at the extreme positions described in the third scenario. Therefore, the identified singularities will not affect the operation of the robot using the gaits presented in this work. This statement is confirmed by modeling and simulation of expected range of motion of the mechanism using Pro/Engineer Wildfire 4.0.

Direct kinematic singularities occur when the determinant of J_x become zero [58]. Although it is difficult to identify all possible direct kinematics singularities as stated in [58], one possible configuration that will generate a singularity was determined by inspection of matrix J_x . This scenario describes the same configuration presented previously as the second possible inverse kinematic singularity condition, where the output link is either pointed directly up or down. The difference is that the inverse kinematic singularity only becomes a direct kinematic singularity if the pivot point, A , has an x-position equal to x_E . It should be noted that this configuration is highly unlikely due to the physical lengths of the input links with respect to the mechanism housing. Again, this scenario is outside of the expected range of motion of the mechanism for the given robot application.

3.4.5 Inverse Dynamics

In inverse dynamics, the time history of a desired trajectory is given in terms of the position, velocity and acceleration of the output link, as well as, any generalized forces contributed by externally applied forces and the required actuator torques and/or forces to generate that trajectory are found [58]. Due to the relative simplicity of the planar parallel mechanism introduced in this work, the inverse dynamics are formulated using the Lagrangian approach and the equations of motion of this type of mechanism are derived. The Lagrangian equations of the first type are written in terms of a set of redundant coordinates [58]. The Lagrangian equations of the first type are given by Equation 3.43. The Lagrange, L , is defined as $L = K - U$ and K is the kinetic energy and U is the potential energy. The vector \mathbf{q} is the generalized coordinates, specifically $[x_A \ \beta \ \theta_1 \ \theta_2]^T$ for this application. The vector \mathbf{Q}_j is the generalized force contributed by an externally applied force for $j = 1$ to k (the number of constraint functions) and the actuator force or torque for $j = k + 1$ to n (the number of coordinates). Due to the planar nature of the parallel mechanism, $k = 2$ and $n = 4$. Therefore, \mathbf{Q}_j represents $[f_{Ax} \ \tau_A \ \tau_1 \ \tau_2]^T$ in this application. Γ_i denotes the i th constraint function derived from the kinematics of a mechanism and λ_i is the Lagrange multiplier [58].

$$\frac{d}{dt} \left(\frac{\partial L}{\partial \dot{q}_j} \right) - \frac{\partial L}{\partial q_j} = Q_j + \sum_{i=1}^k \lambda_i \frac{\partial \Gamma_i}{\partial q_j} \quad \text{for } j=1 \text{ to } n \quad (3.43)$$

Given that the output link is not symmetric about the point A , as illustrated in Figure 3.9, the mass of the output link is given as m_O with its center of mass located a distance r_O from point A . The inertia of the output link is I_O . Note that the output link is mounted to and pivots about a slider referred to as the output slider. The output slider moves only

in the x -direction and its location is described by x_A . The mass of the output slider is given by m_S . The inertia of links DB and EC are represented by I_{a1} and I_{a2} , respectively. Similarly, the links mass are given by m_{a1} and m_{a2} . The inertia and mass of the input sliders mounted on the input links are given by I_{pin} and m_{pin} . Additionally, links BA and CF represent slotted holes and link FA is part of the output link, therefore, none of these links have any individual mass. So the kinetic and potential energy of the individual links are also zero. Therefore, the total kinetic energy of the mechanism is given as:

$$K = K_O + \sum_{i=1}^2 (K_{ai} + K_{bi}) \quad \text{where } i=1,2 \quad (3.44)$$

$$\begin{aligned} K_O &= \frac{1}{2}(m_S + m_O)\dot{x}_A^2 + m_O r_O \dot{x}_A \dot{\beta} s\beta + \frac{1}{2}(I_O + m_O r_O^2)\dot{\beta}^2 \\ K_{a1} &= \frac{1}{2}\left(I_{pin} + m_{pin}a_1^2 + I_{a1} + \frac{1}{4}m_{a1}a_1^2\right)\dot{\theta}_1^2 \\ K_{a2} &= \frac{1}{2}\left(I_{pin} + m_{pin}a_2^2 + I_{a2} + \frac{1}{4}m_{a2}a_2^2\right)\dot{\theta}_2^2 \\ K_{b1} &= K_{b2} = 0 \end{aligned} \quad (3.45)$$

Computation of the kinetic energy, K_O , of the output link and the kinetic energy, K_{ai} , of the input links is straightforward. First, we define position equations for all three links. Then, we differentiated the position equations with respect to time and perform summation of squares to the resulting x and y terms to obtain the squared total velocity term for each limb. Then, the velocity terms and the appropriate mass terms are substituted in the kinetic energy equation to yield the K_O and K_{ai} terms. Next, the total potential energy of the mechanism is given as:

$$U = U_O + \sum_{i=1}^2 (U_{ai} + U_{bi}) \quad (3.46)$$

$$\begin{aligned}
U_o &= m_o g z_o = 0 \\
U_{ai} &= (m_{pin} + m_{ai}) g z_{ai} = 0 \\
U_{bi} &= m_{GT} g z_{bi} = 0
\end{aligned} \tag{3.47}$$

The gravitational acceleration at the center of mass is represented by g and z_o is the distance change along the output link along z -direction. Similarly, z_{ai} and z_{bi} are the distance changes along z -direction for the a_i and b_i links. Since the planar parallel mechanism moves in a plane perpendicular to the direction of the gravitational acceleration, there is no distance change in the z -direction and the total potential energy equals zero. The Lagrangian formulation is given as:

$$L = K_o + K_{a1} + K_{a2} \tag{3.48}$$

Taking the derivative of the Lagrangian formulation with respect to the generalized coordinates yields the following expressions:

$$\frac{d}{dt} \left(\frac{\partial L}{\partial \dot{x}_A} \right) - \frac{\partial L}{\partial x_A} = (m_s + m_o) \ddot{x}_A + m_o r_o \ddot{\beta} s \beta + m_o r_o \dot{\beta}^2 c \beta \tag{3.49}$$

$$\frac{d}{dt} \left(\frac{\partial L}{\partial \dot{\beta}} \right) - \frac{\partial L}{\partial \beta} = m_o r_o \ddot{x}_A s \beta + (I_o + m_o r_o^2) \ddot{\beta} \tag{3.50}$$

$$\frac{d}{dt} \left(\frac{\partial L}{\partial \dot{\theta}_1} \right) - \frac{\partial L}{\partial \theta_1} = \left(I_{pin} + m_{pin} a_1^2 + I_{a1} + \frac{1}{4} m_{a1} a_1^2 \right) \ddot{\theta}_1 \tag{3.51}$$

$$\frac{d}{dt} \left(\frac{\partial L}{\partial \dot{\theta}_2} \right) - \frac{\partial L}{\partial \theta_2} = \left(I_{pin} + m_{pin} a_2^2 + I_{a2} + \frac{1}{4} m_{a2} a_2^2 \right) \ddot{\theta}_2 \tag{3.52}$$

Generally, the dynamic analysis can be accomplished by using just two generalized coordinates, θ_1 and θ_2 , since this is a 2 DOF mechanism. However, this would lead to a cumbersome expression for the Lagrangian function, due to the complex kinematics of the mechanism [58]. Thus two redundant coordinates, x_A and β , are introduced and

therefore the formulation requires two additional constraint equations. These constraint equations can be given by Equations 3.07 and 3.13, and are given as:

$$\Gamma_1 = y_A - a_1 s \theta_1 + s \beta \left(\frac{x_A - a_1 c \theta_1}{c \beta} \right) = 0 \quad (3.53)$$

$$\Gamma_2 = c \beta (x_A - x_E) + s \beta (y_E - y_A) + a_2 c (\beta + \theta_2) + c_2 = 0 \quad (3.54)$$

Taking the partial derivatives of the constraint function Γ_i with respect to the four generalized coordinates yields the following:

$$\begin{aligned} \frac{\partial \Gamma_1}{\partial x_A} &= \frac{s \beta}{c \beta} & \frac{\partial \Gamma_2}{\partial x_A} &= c \beta \\ \frac{\partial \Gamma_1}{\partial \beta} &= \frac{x_A - a_1 c \theta_1}{c^2 \beta} & \frac{\partial \Gamma_2}{\partial \beta} &= c \beta (y_E - y_A) - s \beta (x_A - x_E) - a_2 s (\beta + \theta_2) \\ \frac{\partial \Gamma_1}{\partial \theta_1} &= -a_1 c \theta_1 + \frac{s \beta}{c \beta} a_1 s \theta_1 & \frac{\partial \Gamma_2}{\partial \theta_1} &= \frac{\partial \Gamma_1}{\partial \theta_2} = 0 & \frac{\partial \Gamma_2}{\partial \theta_2} &= -a_2 s (\beta + \theta_2) \end{aligned} \quad (3.55)$$

The first k equations of the system of Lagrangian equations given by Equation 3.43 are solved for the k Lagrange multipliers. The equations are expressed by the following:

$$\sum_{i=1}^k \lambda_i \frac{\partial \Gamma_i}{\partial q_j} = \frac{d}{dt} \left(\frac{\partial L}{\partial \dot{q}_j} \right) - \frac{\partial L}{\partial q_j} - Q_j \quad \text{for } j=1 \text{ to } k \quad (3.56)$$

Substituting the derivatives in Equation 3.56 yield the following system of dynamical equations where f_{Ax} and τ_A represent the externally applied force exerted on the moving output link:

$$\lambda_1 S_1 + \lambda_2 S_2 = S_3 - f_{Ax} \quad (3.57)$$

$$\lambda_1 S_4 + \lambda_2 S_5 = S_6 - \tau_A \quad (3.58)$$

$$\begin{aligned} S_1 &= \frac{\partial \Gamma_1}{\partial x_A} & S_2 &= \frac{\partial \Gamma_2}{\partial x_A} & S_3 &= \frac{d}{dt} \left(\frac{\partial L}{\partial \dot{x}_A} \right) - \frac{\partial L}{\partial x_A} \\ S_4 &= \frac{\partial \Gamma_1}{\partial \beta} & S_5 &= \frac{\partial \Gamma_2}{\partial \beta} & S_6 &= \frac{d}{dt} \left(\frac{\partial L}{\partial \dot{\beta}} \right) - \frac{\partial L}{\partial \beta} \end{aligned} \quad (3.59)$$

The Lagrange multipliers λ_i in terms of joint angles, the position and acceleration of the output link are obtained by solving Equations 3.57 and 3.58 which gives the following:

$$\lambda_1 = \frac{(S_6 - \tau_A)S_2 - (S_3 - f_{Ax})S_5}{S_2S_4 - S_1S_5} \quad (3.60)$$

$$\lambda_2 = \frac{(S_3 - f_{Ax})S_4 - (S_6 - \tau_A)S_1}{S_2S_4 - S_1S_5} \quad (3.61)$$

Once the Lagrange multipliers are found, the actuator torques can be directly determined from the remaining equations given by Equation 3.62.

$$Q_j = \frac{d}{dt} \left(\frac{\partial L}{\partial \dot{q}_j} \right) - \frac{\partial L}{\partial q_j} - \sum_{i=1}^k \lambda_i \frac{\partial \Gamma_i}{\partial q_j} \quad \text{for } j = k+1 \text{ to } n \quad (3.62)$$

Substituting the derivatives in Equation 3.62 yields the following system of dynamical equations where τ_1 and τ_2 represent the actuator torques of the mechanism:

$$\tau_1 = S_7 - \lambda_1 S_8 \quad (3.63)$$

$$\tau_2 = S_9 - \lambda_2 S_{10} \quad (3.64)$$

$$\begin{aligned} S_7 &= \frac{d}{dt} \left(\frac{\partial L}{\partial \dot{\theta}_1} \right) - \frac{\partial L}{\partial \theta_1} & S_8 &= \frac{\partial \Gamma_1}{\partial \theta_1} \\ S_9 &= \frac{d}{dt} \left(\frac{\partial L}{\partial \dot{\theta}_2} \right) - \frac{\partial L}{\partial \theta_2} & S_{10} &= \frac{\partial \Gamma_2}{\partial \theta_2} \end{aligned} \quad (3.65)$$

Note that τ_1 and τ_2 above represents only the actuator torques for the parallel mechanism (horizontally oriented) which can produce yawing motion. The other parallel mechanism (vertically oriented) contained within the module can produce pitching motion. While identical to the first mechanism, the second mechanism is rotated 90 degrees apart about the x -axis of the module. In the second mechanism, gravity acts in the negative y -direction. Therefore, the potential energy terms from Equation 3.47 are not

zero. The potential energy terms for the second mechanism of the module are given by the following:

$$U' = U'_O + \sum_{i=1}^2 (U'_{ai} + U'_{bi}) \quad (3.66)$$

$$U'_O = m_o g(y_A + r_o s \beta)$$

$$U'_{a1} = \left(m_{pin} + \frac{1}{2} m_{a1} \right) g(a_1 s \theta_1) \quad (3.67)$$

$$U'_{a2} = m_{pin} g(y_E - a_2 s \theta_2) + m_{a2} g\left(y_E - \frac{1}{2} a_2 s \theta_2\right)$$

Incorporating the new potential energy terms into the Lagrangian formulation, Equation 3.48, and taking the derivatives with respect to the generalized coordinates yields the following:

$$S'_6 = \frac{d}{dt} \left(\frac{\partial L}{\partial \dot{\beta}} \right) - \frac{\partial L}{\partial \beta} = m_o r_o \ddot{x}_A s \beta + (I_o + m_o r_o^2) \ddot{\beta} + m_o g(r_o c \beta) \quad (3.68)$$

$$S'_7 = \frac{d}{dt} \left(\frac{\partial L}{\partial \dot{\theta}_1} \right) - \frac{\partial L}{\partial \theta_1} = \left(I_{pin} + m_{pin} a_1^2 + I_{a1} + \frac{1}{4} m_{a1} a_1^2 \right) \ddot{\theta}_1 + \left(m_{pin} + \frac{1}{2} m_{a1} \right) g(a_1 c \theta_1) \quad (3.69)$$

$$S'_9 = \frac{d}{dt} \left(\frac{\partial L}{\partial \dot{\theta}_2} \right) - \frac{\partial L}{\partial \theta_2} = \left(I_{pin} + m_{pin} a_2^2 + I_{a2} + \frac{1}{4} m_{a2} a_2^2 \right) \ddot{\theta}_2 - \left(m_{pin} + \frac{1}{2} m_{a2} \right) g(a_2 c \theta_2) \quad (3.70)$$

The revised Lagrange multipliers and actuator torques, τ'_1 and τ'_2 , for the vertical oriented parallel mechanism are given by the following:

$$\lambda'_1 = \frac{(S'_6 - \tau_A) S_2 - (S_3 - f_{Ax}) S_5}{S_2 S_4 - S_1 S_5} \quad (3.71)$$

$$\lambda'_2 = \frac{(S_3 - f_{Ax}) S_4 - (S'_6 - \tau_A) S_1}{S_2 S_4 - S_1 S_5} \quad (3.72)$$

$$\tau'_1 = S'_7 - \lambda'_1 S_8 \quad (3.73)$$

$$\tau'_2 = S'_9 - \lambda'_2 S_{10} \quad (3.74)$$

3.4.6 Validation of Mechanism Analysis

In this section, the equations of motion developed for the new planar parallel mechanism are validated against results generated by the Mechanism Analysis suite of Pro/Engineer Wildfire 4.0. The Pro/Engineer analysis is based on the solid model of the parallel mechanism illustrated in Figure 3.5. For the sake of brevity, the same position inputs, Figure 3.12, were used to verify the kinematics and Jacobian expressions. Figure 3.12a illustrates 91 sets of output link position points (x_A , $Beta$) and Figure 3.12b illustrates the corresponding input link position points ($Theta1$, $Theta2$). The values of the constants used in the model are given by Table 3.2. Figures 3.13, 3.14 and 3.15 illustrate graphic comparison of results between the Pro/Engineer solutions and the solutions from the derived equations of motion for the Kinematics and Jacobian analysis.

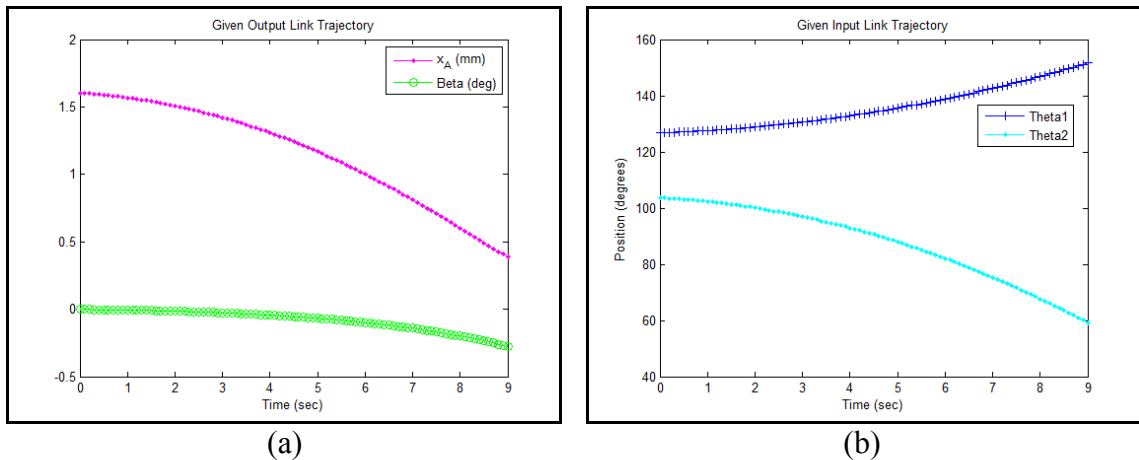
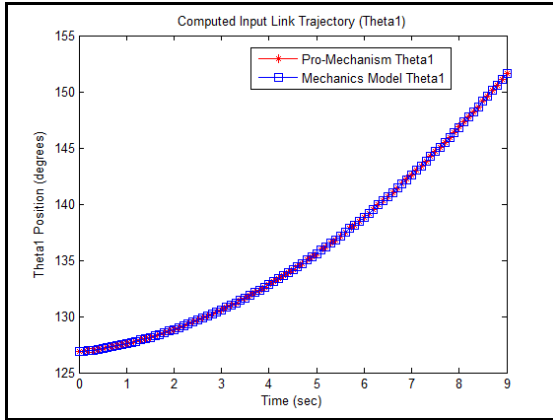


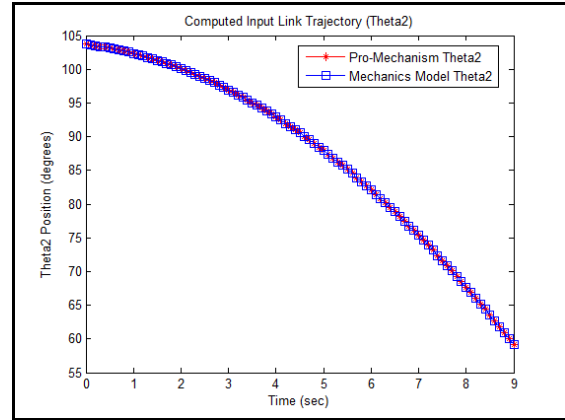
Figure 3.12: Kinematics Model Inputs (a) Output Link and (b) Input Links

a_1	35.56 mm
a_2	38.10 mm
y_A	28.58 mm
y_E	57.15 mm
x_E	63.50 mm
c_2	31.75 mm

Table 3.2: Kinematics Constants

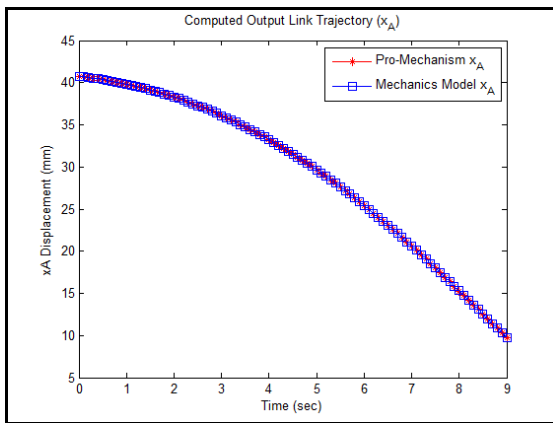


(a)

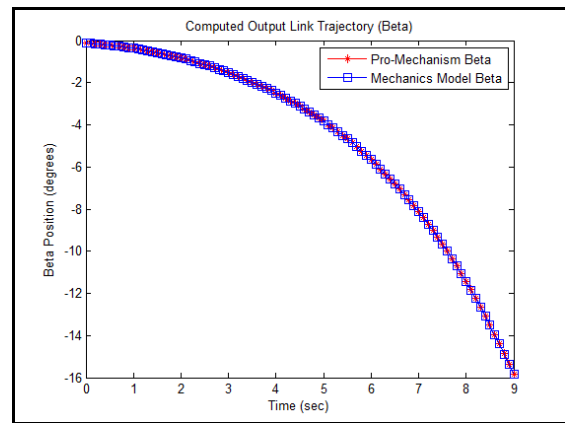


(b)

Figure 3.13: Inverse Kinematics: Pro-E vs. Model: (a) Theta1 and (b) Theta2

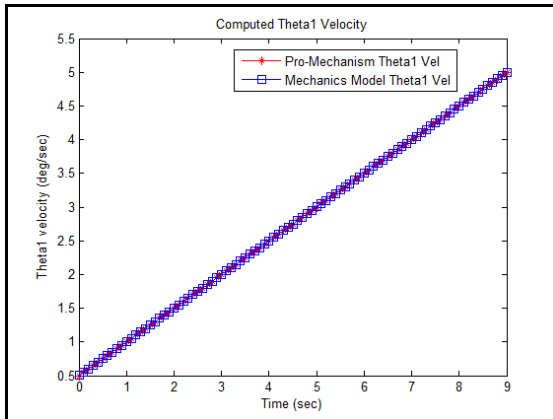


(a)

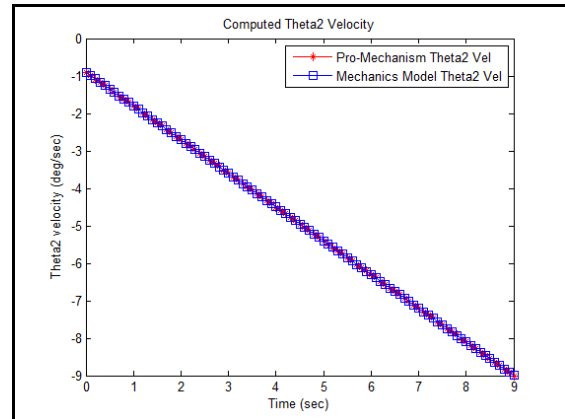


(b)

Figure 3.14: Direct Kinematics: Pro-E vs. Model: (a) xA and (b) Beta



(a)



(b)

Figure 3.15: Jacobian Analysis: Pro-E vs. Model: (a) Theta1 and (b) Theta2 Velocity

m_O	2.49 kg
I_O	4189.17 kg mm ²
r_O	30.28 mm
m_S	0.22 kg
m_{a1}	0.04 kg
I_{a1}	5.53 kg mm ²
m_{a2}	0.05 kg
I_{a2}	6.67 kg mm ²
m_{pin}	0.04 kg
I_{pin}	1.29 kg mm ²

Table 3.3: Dynamics Constants

For the verification of the inverse dynamics, the values of the dynamics constants are given by Table 3.3. Note we use the same constants from Table 3.2. Again, 91 sets of output link positions and forces for the dynamics of the parallel mechanism in the horizontal position within the module (no potential energy) are given by Figure 3.16. The graphic comparison of results between the Pro/Engineer solutions and the solutions from the derived equations of motion is given by Figure 3.17. The sets of output link positions and forces for the dynamics of the parallel mechanism in the vertical position within the module (potential energy) are given by Figure 3.18. Similarly, Figure 3.19 presents results for the vertically positioned parallel mechanism.

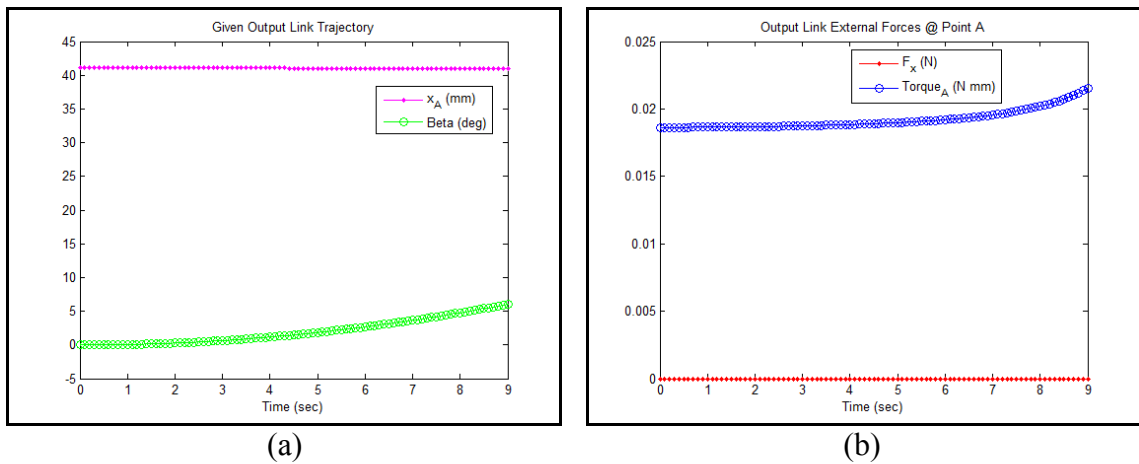
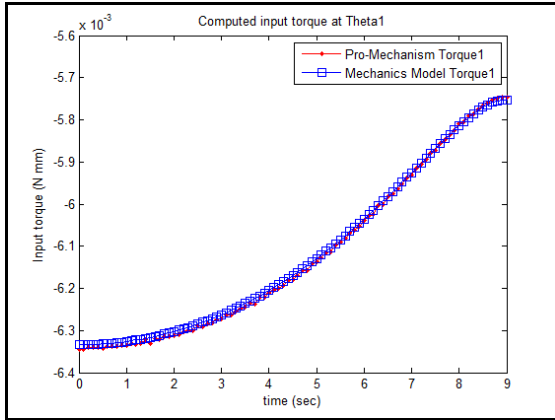
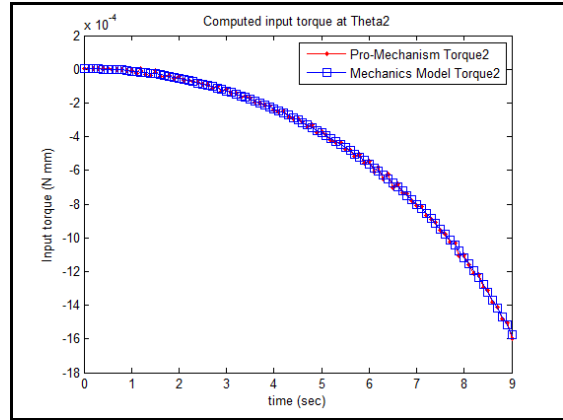


Figure 3.16: Dynamics Inputs: (a) Output Link Kinematics and (b) Forces

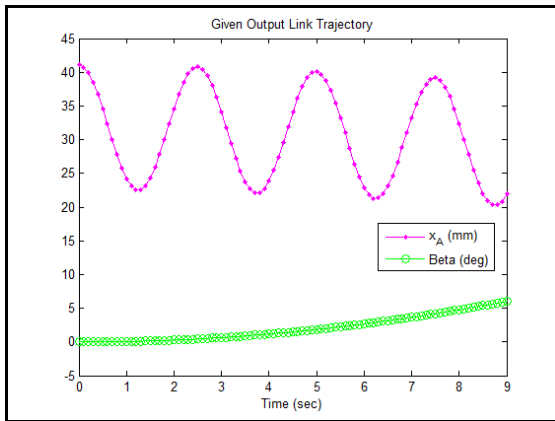


(a)

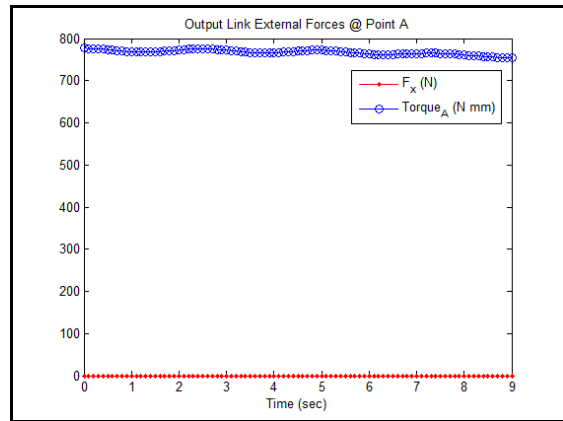


(b)

Figure 3.17: Dynamics: Pro-E vs. Model: (a) Torque1 and (b) Torque2

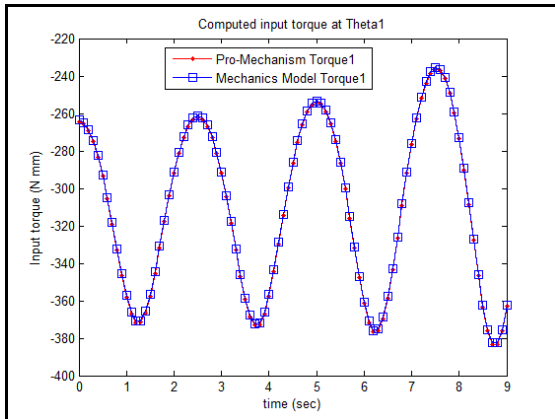


(a)

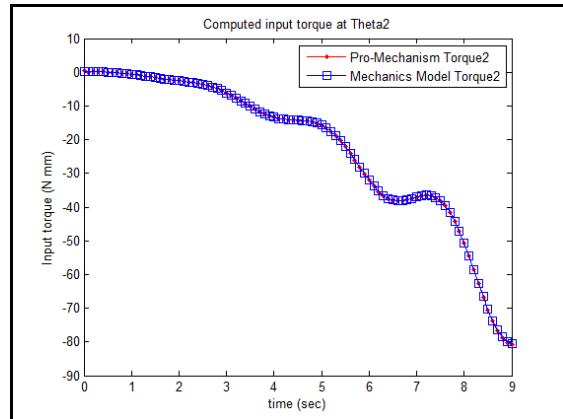


(b)

Figure 3.18: Dynamics Input w/Gravity: (a) Output Link Kinematics and (b) Forces



(a)



(b)

Figure 3.19: Dynamics w/Gravity: Pro-E vs. Model: (a) Torque1 and (b) Torque2

3.5 Design of a Multi-Material Variable Friction Force Anchor

The high speed rectilinear gait concept requires a method of anchoring of the robot to the terrain to provide positive forward displacement during extension. Other robot designs have incorporated features such as pneumatic suction, electromagnets and semi-adhesive surfaces for providing traction. However, these methods are effective only on certain surfaces for providing traction. For locomotion on varying surface types, this work will focus on the use of varying contact friction to obtain traction. This section describes a friction anchoring concept and presents a design for a mechanism which will provide this capability.

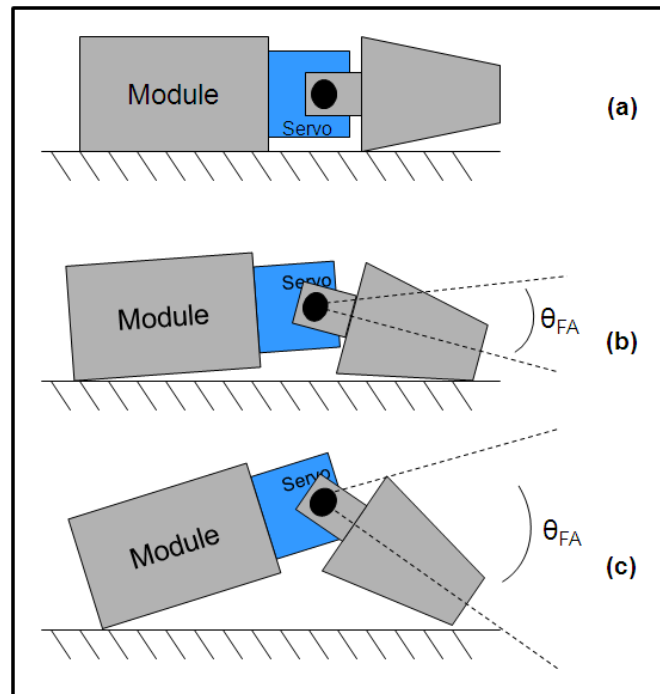


Figure 3.20: Friction Anchor Concept

3.5.1 Variable Friction Force Concept

In addition to the new parallel mechanism, the other important design aspect of this snake-inspired robot architecture is a variable friction force concept used to provide anchoring points on the terminal ends of the robot to enable locomotion. The variable

friction force concept is a simple yet effective method of anchoring robot to the terrain to provide a counter to the reaction forces of the robot during forward or turning gaits. In nature, this type of anchoring can be accomplished by redistributing more of the animal's body weight across the surface of the foot to increase the friction force between the foot and the terrain. This concept adopts a similar approach. The surface of the friction anchor is covered in a material with a much higher coefficient of friction than the rest of the robot's housing material. The friction anchor is placed in contact with the terrain by a revolute joint as illustrated in Figure 3.20.

The friction force, a function of the normal force between the anchor and the terrain, is increased or decreased by varying the angle, θ_{FA} , of the revolute joint which changes the portion of the module weight being supported by the friction anchor. Figure 3.20a depicts the friction anchor in its nominal position, in which the anchor's high coefficient of friction surface is not in contact with the terrain. In the nominal position, the terminal end of the robot is allowed to freely slide under the force of the robot's actuators. Figure 3.20b depicts the friction anchor surface in contact with the terrain with only a slight change of θ_{FA} , useful in low reaction force gaits. Figure 3.20c depicts a large change in the value of θ_{FA} , useful in high reaction force gaits.

3.5.2 Multi-Material Anchor Concept

The mechanism illustrated in Figure 3.20 effectively demonstrates the friction anchoring concept. However, practical use of the mechanism in its current form would be inadequate. The main issue is that the concept in Figure 3.20 can only engage the terrain with one type of high coefficient of friction material when in operation. This limitation relies on a single material to support the snake-inspired robot on multiple surfaces, which

could lead to inefficiency or non-functionality on some terrains. To address this concern, we evaluate a number of concepts which include multiple surfaces for the friction anchor mechanism to support different materials for use in different terrains. Of the various concepts, we have defined five promising solutions: four of which have multiple friction anchor surfaces and the fifth concept has a rotating for selection of the material in contact with the terrain. All five concepts evaluated and down selected to one solution.

3.5.2.1 Multi-Surface Anchor Concepts

In each of the multi-surface anchor concepts, there are four actuated surfaces positioned equally around the perimeter of the robot's forward cross-sectional area. Each surface is simultaneously actuated by a single friction anchor mechanism, causing all surfaces to engage and disengage in unison. The advantage of these concepts is simplicity and in most cases, the concepts only require a single actuator. For each concept, a different high coefficient of friction material is applied to each one of the actuated surfaces. If the robot has issues traversing a terrain, it initiates a rollover maneuver to engage the terrain with a different friction anchor material. Additionally, the robot may function in environments, such as piping, where the conical nature of the internal pipe surface may require traction at multiple points, not only directly below the robot. Candidate concepts for this type of mechanism must act on multiple sides of the robot, yet remain simple and compact enough to avoid significant increase of weight, complexity or volume to the robot. Several concepts were considered, but only four mechanisms were determined to be feasible and meet the requirements. These concepts are illustrated in Figure 3.21.

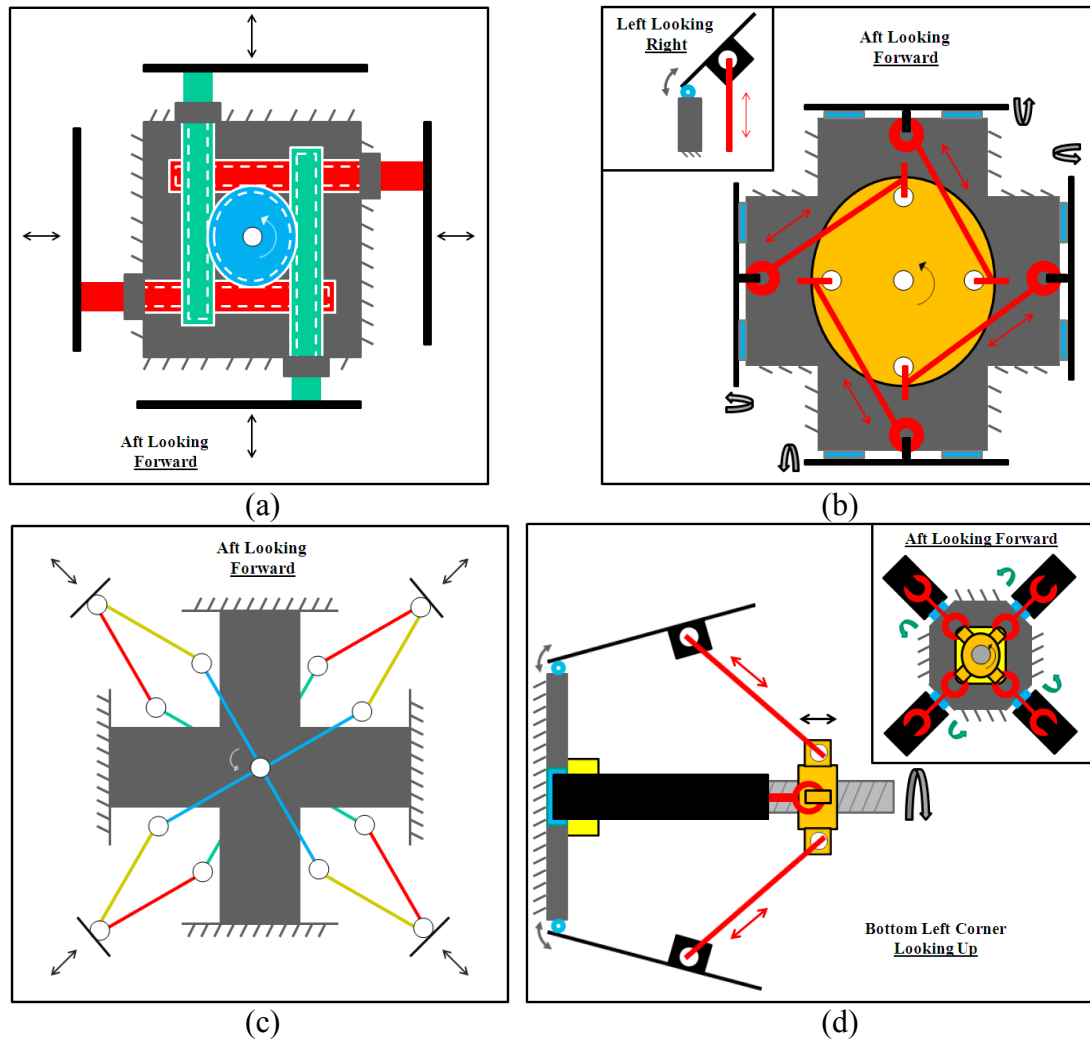


Figure 3.21: Multi-Surface Anchor Concepts (Kinematic Representation)

The friction anchoring concepts presented in Figure 3.21 describe four different mechanisms capable of simultaneously extending high coefficient of friction pads in multiple directions. The extension of the pads causes the robot to grip the terrain and lift the robot's terminal end, thus distributing more weight across the friction pad, which increases the gripping force. In addition to different mechanisms, the concepts present different directions and methods in which the pads are applied to the terrains. For example, Concept A (Figure 3.21a) directly extends a flat friction pad in the direction normal to each side of the robot. However, in Concept B (Figure 3.21b), the friction pads

swing outwardly through a hinged joint from each side of the robot. Descriptions of each concept are below:

- Concept A (Figure 3.21a) – In this mechanism, the friction pads are mounted to each side of the friction anchor module by means of an extendable arm, mounted normal to each side of the module, which extends and retracts the pads from an storage space within the module. Each extendable arm incorporates a gear-toothed rack section along its length. All four rack segments are simultaneously engaged by powered pinion wheel mounted in the center of the module. The horizontal rack segments are offset slightly from the vertical segments along the pinion length, as demonstrated in Figure 3.21a, to allow smooth, synchronized operation of all four mechanisms.
- Concept B (Figure 3.21b) – This mechanism is a direct extension of the concept illustrated in Figure 3.20, which pivots the high friction surface onto the terrain. Each of the friction pads pivots outwardly from the module housing along a hinged joint (mounted on each side of the housing. Each pad is actuated by a rod which forms a ring at its end and is connected to the friction pad through a tab with a mating through-hole. The opposite end of the rod also forms a ring which is oriented with a 90 degree offset from the friction pad end through a twist angle along the rod length. The offset end of each rod is connected to a single input disk by mating through-holes. The input disk is rotated by a powered revolute joint. Depending on the direction of the input disk's rotation the rods actuate the friction pads, pivoting outwardly or retracting into the module housing.
- Concept C (Figure 3.21c) – Concepts A and B operation in the direction normal to the sides of the friction anchor module. As seen in Figure 3.21c, all four friction pads in

Concept C move linearly along lines of actions which are 45 degrees offset from the horizontal and vertical center lines of the module. The offset is measured about the twist angle of an axis that points out of the plane (along the length of the module). Thus, the friction pads extend and retract from the corners of the module defined by the module's sides. Each pad is mounted at a vertex formed by two output links of a four-bar mechanism. The input for each four-bar mechanism is provided by one arm of each of the two cross links (see the cross link mounted in the center of the module in Figure 3.21c) in the module. As the two cross links rotate at the same rate in counter directions, the four-bar mechanisms compress or expand, moving the friction pad linearly from the corners of the friction anchor module.

- Concept D (Figure 3.21d) – In this mechanism, similar to Concept C, the friction pads expand outwardly from the corners defined by the sides of the module housing. However, the method of expansion of the friction pads is similar to Concept B, in which the pads pivot outwardly from the module housing along a hinged joint mounted on each corner of the housing. Like the mechanism in Concept B, each pad is actuated by a rod which forms a ring at its end and is connected to the friction pad through a tab with a mating through-hole. The opposite end of the rod also forms a ring, in the same plane as the friction pad end of the rod. The terminal ends of all four rods are connected to a carrier through tabs with through-holes as shown in Figure 3.21d. Note, in order to better illustrate the mechanism, the main sketch in Figure 3.21d is illustrated from the point of view of the bottom left corner of the mechanism looking upwards towards the top right corner. The carrier moves in a linear manner along a threaded rod which acts as the input to the mechanism and is actuated by a

powered revolute joint, forming a powered lead screw mechanism. As the carrier moves forward and aft, it actuates the rods causing the friction pads to pivot outwardly or retract into the module housing.

3.5.2.2 Multi-Surface Concept Selection

Before discussing the Single Surface, Selectable Material anchor concept, we must first down select to a leading candidate for the Multi-Surface concept. All four mechanisms illustrated in Figure 3.21 appear to be compact, reliable, and can provide simultaneous actuation of the four friction pads. Each mechanism has strengths and weaknesses. The mechanism in Concept A can provide the most precise position control of the friction pads of the four mechanisms. Unfortunately, the rack and pinion mechanism also has high precision requirements in design and fabrication. Also, robustness is a concern due to the potential to damage gear teeth as the friction pads applied force against rigid surfaces, such as internal piping surfaces. The mechanism in Concept B has the least precision in position control due to the need for large rings at the end of the actuation rods in order to function properly (this leads to significant play in the mechanism). Concept B is also the simplest mechanism and most robustness (due to the play in the mechanism). Concept C is the fastest mechanism, considering that small changes in rotational position by both input cross links leads to large changes in linear output of the four-bar mechanism. However, this is the only mechanism that requires two inputs and they must be coordinated to actuate the friction pads in the proper direction. Finally, Concept D requires the least cross-sectional area, while still providing significant expansion capability for the friction pads. Concept D is also inherently the slowest

mechanism due to the need for several rotations of the lead screw to produce significant linear travel, when compared to the other options.

While the strengths and weaknesses of each mechanism were considered, the main factors which ultimately defined the selection were (1) the manner in which the friction pads contacted the terrain and (2) the amount of contact area between friction pads and the terrain. In addressing the first factor, recall that Concepts B and D pivot the friction pads about a hinged joint into contact with the terrain. The issue with this method is that the pivoting motion of the pads, while in contact with the terrain, could cause the entire robot to move forward or aft depending on the direction of the anchor module. This movement of the robot could impact or even counter the progression of the robot as it executes its rectilinear forward and turning gaits. For this reason, Concepts B and D have been eliminated.

To select between Concept A and C, we considered the second decision factor. Due to the need maintain a small cross-sectional area, the width and height of the module are limited and thus the width of the friction pads in Concept A may be quite small. Note that the robot will execute high speed motions and the friction anchor will lift the ends of the robot between these motions. If the robot is only being supported by narrow friction pads during high speed operations, there is a significant chance that robot will perform an uncommanded rollover while executing the gait. Although Concept A has pads on all four sides, the time required for the robot to stabilize after rolling over may significantly affect the rate of progression (assuming that the rollover events are frequent during gait motion). While Concept C will also have narrow friction pads, the fact that the pads extend out from the corners along a diagonal creates a wider support base between the

module and the terrain. This wider base reduces the chance of un-commanded rollover events. Therefore, Concept C was chosen as the leading concept for the Multi-Surface approach. To address the issue of the mechanism requiring two inputs, two servomotors will be used to actuate the device. While, the two inputs could also be reduced to a single input using gearing between the two cross links, the two servomotors option was chosen because it increases the load capacity of the mechanism. In order to verify that that Concept C is feasible, a CAD model was developed and is presented in Figure 3.22a, with friction pads in the stored position, and in Figure 3.22b, with the pads in the fully extended position.

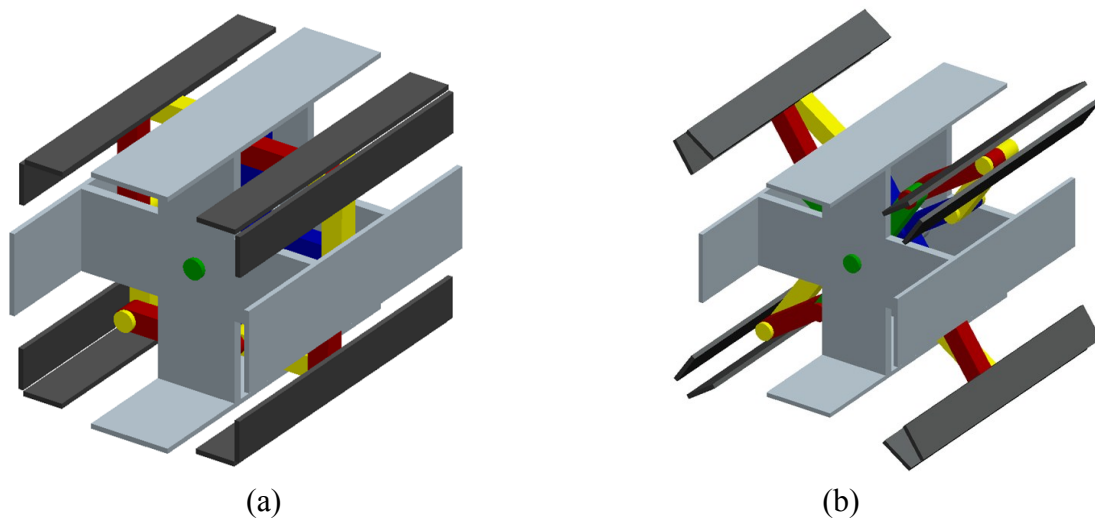


Figure 3.22: Multi-Surface Anchor Down Selected Concept

3.5.2.3 Single Surface, Selectable Anchor Concept

The second type of multi-material friction anchor concept involves a single actuating “arm”, and the anchor can mechanically select the contacting material. This concept was deemed the Single Surface, Selectable Material anchor concept and is illustrated in Figure 3.23. The mechanism consists of a rotating drum, in which multiple friction pads, each of a different material, are mounted to the radial surfaces of the drum. The drum is

spun by a powered revolute joint and is also pivoted by a separate powered revolute joint. The pivoting joint engages the radial surface of the drum with the terrain, as depicted in the anchoring concept in Figure 3.20. The revolute joint “selects” which material type will engage the terrain and therefore allows the mechanism to better adapt to the changes in terrain as the robot progresses.

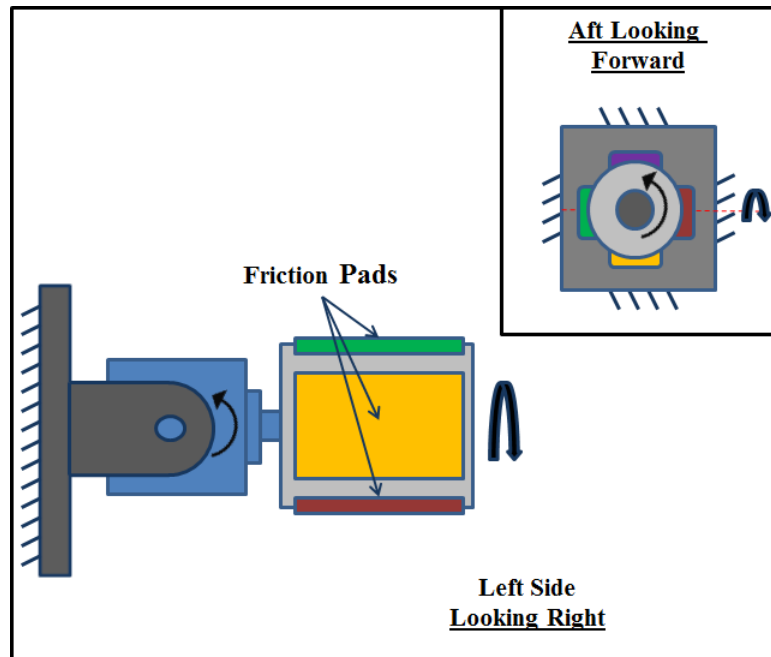


Figure 3.23: Single Surface, Selectable Anchor Concept

3.5.3 Multi-Material, Variable Friction Anchor Final Design

Defining the final configuration of the friction anchor mechanism requires choosing between the concepts in Figure 3.22 and Figure 3.23. We made this selection by considering the advantages and disadvantages of each design relative to one another. The design in Figure 3.22 has an advantage over the Figure 3.23, selectable material concept, in that it is roll over neutral. The anchor mechanism, in Figure 3.22, will continue to function regardless of the orientation of the robot. In addition, the multiple contact surfaces aid the robot in obtaining an effective grip in enclosed spaces. However, the

concept in Figure 3.23 has advantage over the Figure 3.22, multi-surface concept, in that the robot is not required to initiate a rollover event or be placed in a different orientation to change material type. This advantage saves energy and time when adapting to a new terrain. Based on the comparison between the two concepts, it was decided to proceed with the single surface, selectable material concept. The deciding factor was the fact that the robot system is designed for speed and energy efficiency and the Figure 3.22 concept does not contribute to that goal. Therefore, the final design for the Multi-Material, Variable Friction Anchor mechanism is presented in Figure 3.24.

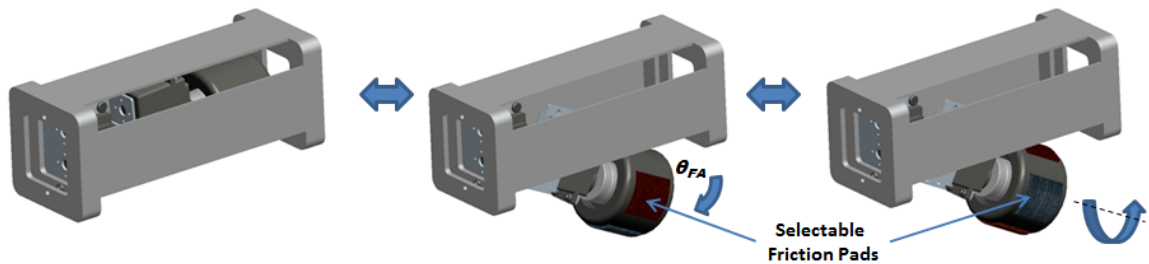


Figure 3.24: Friction Anchor Module Final CAD Model

In order to decide which materials to include in the multi-material friction anchor, we conducted an experimental traction study. While we have conducted similar studies in the past, these experiments were limited to one terrain and one friction anchor engagement angle (θ_{FA}) [89]. In this study, we observe combinations of five friction pad materials, over five terrain types using three friction anchor engagement angles. These options result in a matrix of 75 combinations. In addition, three trials are conducted for each combination resulting in a total of 225 traction experiments. The friction pad materials evaluated include: Al_2O_3 paper 220 grit (M1), Al_2O_3 paper 60 grit (M2), Green Dot™ traction compound (M3), fine emery cloth (M4), and Skid Guard™ tape (M5). The terrains evaluated include: carpet (T1), vinyl flooring (T2), asphalt (T3), plywood

(T4), and simulated grass (T5). Simulated grass was chosen over real grass to reduce randomness in the terrain which may skew the results between trials. Finally, the three friction anchor engagement angles chosen were 15° , 25° , and 35° .

In the past, we evaluated the results in terms of velocity; however this method introduces errors resulting from measuring time as well as measuring distance. In this study, we evaluated results based on actual distance travelled over predicted distance travelled for a set number of cycles. The predicted distance travelled is based on the maximum displacement per cycle for the friction anchor test unit, given ideal traction with the terrain. The test unit, pictured in Figure 3.25, consists of one joint module and two multi-material friction anchors. The test unit has a maximum displacement of 76 mm per cycle and will perform three cycles per trial. The traction experiment results for each anchor combination are averaged and presented in Table 3. For the results, “1” is considered ideal traction and “0” is no measurable traction observed.

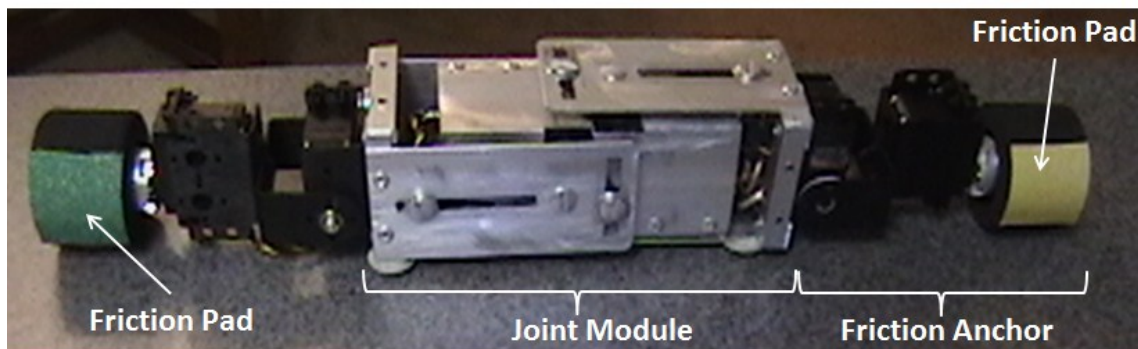


Figure 3.25: Multi-Material, Variable Friction Anchor Prototype

Observing the results in Tables 3.4 through 3.6, almost all the tested materials performed satisfactorily on carpet. However, the test unit performed best using fine emery cloth and a 15° engagement angle. The trials conducted on vinyl flooring, asphalt, and simulated grass indicated that the test unit performed the best using the Green Dot TM

material. Although the performance of the test unit using Green Dot TM on asphalt and simulated grass was only satisfactory (about 60% of ideal displacement), this was the only material to gain traction at any engagement angle on these terrains. Finally, the Skid Guard TM tape material consistently outperformed the other materials on plywood for all engagement angles. From these results, we decided to include three friction pad materials (Skid Guard TM, Green Dot TM, and fine emery cloth) to support adaptability on a wide range of terrains.

	M1	M2	M3	M4	M5
T1	0.17	0.83	0.53	0.86	0.71
T2	0.11	0.24	0.61	0.00	0.35
T3	0.00	0.00	0.06	0.00	0.00
T4	0.00	0.11	0.39	0.36	0.44
T5	0.00	0.00	0.36	0.00	0.00

Table 3.4: Traction Study Results ($\theta_{FA} = 15^\circ$)

	M1	M2	M3	M4	M5
T1	0.44	0.61	0.69	0.58	0.40
T2	0.33	0.36	0.82	0.17	0.28
T3	0.00	0.00	0.64	0.00	0.00
T4	0.00	0.31	0.68	0.50	0.72
T5	0.00	0.00	0.54	0.00	0.00

Table 3.5: Traction Study Results ($\theta_{FA} = 25^\circ$)

	M1	M2	M3	M4	M5
T1	0.11	0.11	0.61	0.17	0.14
T2	0.00	0.51	0.68	0.22	0.31
T3	0.00	0.00	0.22	0.00	0.00
T4	0.00	0.14	0.32	0.53	0.75
T5	0.00	0.00	0.61	0.00	0.00

Table 3.6: Traction Study Results ($\theta_{FA} = 35^\circ$)

3.6 Analysis of Variable Friction Force Anchoring

In order to determine the required friction anchor angle θ_{FA} for effective traction for the robot, we must develop a dynamic model of the anchor that relates θ_{FA} to the change in force normal at the contact point between the friction pad surface and the terrain. We start by defining the motion and interaction of the friction anchor with the terrain, as illustrated in static representation of the variable friction anchor concept in Figure 3.26.

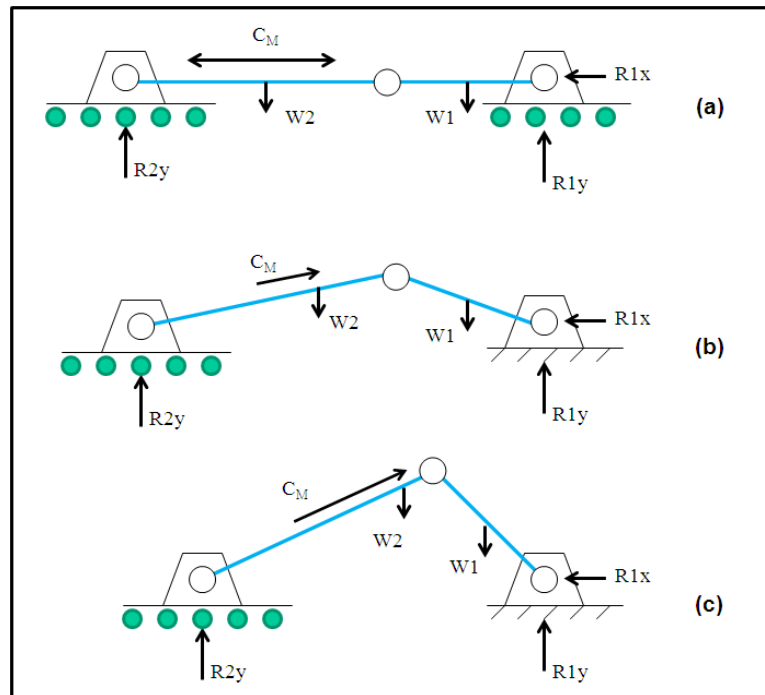


Figure 3.26: Variable Friction Anchoring

The nominal position of the robot with both friction anchors not engaged is illustrated Figure 3.26a. The anchors are depicted as roller supports since the housing material is considered to have a low coefficient of friction and the robot is able to freely slide across the terrain. The reaction forces on the anchors from the terrain are given by $R1y$ and $R2y$. The friction force generated by the anchor to resist the reaction forces from the expansion of the robot is given by $R1x$ and is zero in the nominal position. $W1$ and $W2$ are the weights of the friction anchor and robot, respectively. C_M is the location of the center of mass of the robot and is variable. In Figure 3.26b, the right side anchor is engaged. In this position, the anchor is quasi fixed to the terrain and is treated as a ground link. Due to the angle created by the engagement of the anchor, $R1y$ is now greater than $R2y$ and $R1x$ is now nonzero. In addition to the engagement of the anchor, the forces represented by $R1y$ and $R1x$ are further increased by the shift of C_M closer to the right side of the robot. Finally, Figure 3.26c demonstrates friction anchoring at its extreme configuration. In this configuration, the friction anchor revolute joint is at its maximum angle and C_M is at its closest position to the right side friction anchor. Thus, the friction anchor generates its maximum friction force, $R1x$, on the right side and makes use of this configuration to traverse smooth or low coefficient of friction terrains.

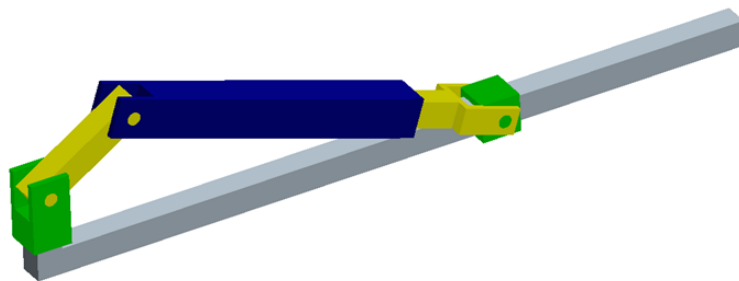


Figure 3.27: Variable Friction Anchoring CAD Model

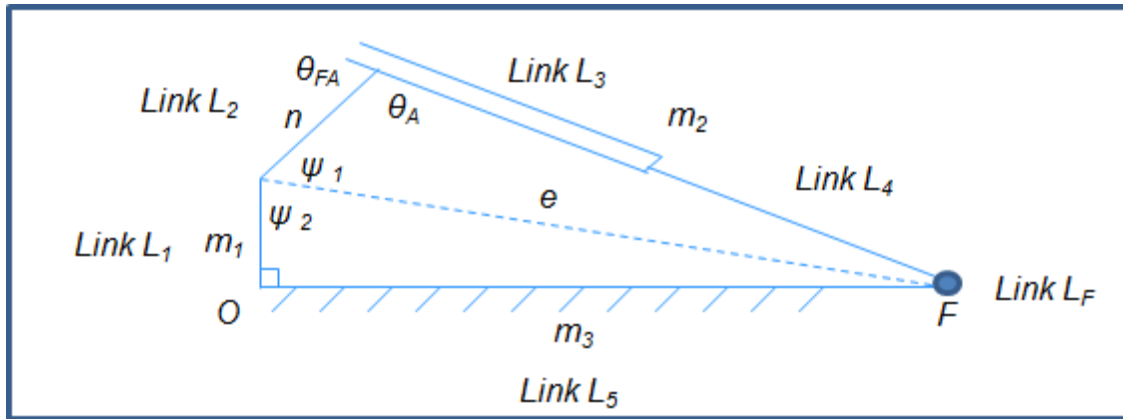


Figure 3.28: Friction Anchoring Geometric Model

The force between the friction anchor and the terrain can be dynamically modeled as a function of θ_{FA} and the extension rate of robot using the solid model illustrated in Figure 3.27. Note, the bottom link, L_5 in the model represents the terrain as a ground link. In addition to θ_{FA} and the prismatic extension joint, the model also incorporates a vertical joint at location of the friction anchor pad. This joint is not actuated throughout the analysis and only serves as an analysis point to directly compute the force normal at the pad location, using analytical dynamics techniques. The Lagrangian formulation is employed to find the inverse dynamic equations of motion for the closed loop model in Figure 3.28. Therefore we must define the relative positions of centers of mass for the moving links with respect to the origin O . To perform the dynamic analysis, we must first define the geometric relationship between the lengths and angles formed by the quadrilateral in Figure 3.27. For the given quadrilateral, only three links and two angles are known. Finding the remaining two angles and link length is not trivial for a general quadrilateral; therefore we divide the quadrilateral into two triangles as shown in Figure 3.28. The variable m_1 is the unactuated joint used to measure the force normal and therefore is a constant. The robot extension is defined by m_2 and location of the forward

end of the robot relative to the contact point of friction anchor is given by m_3 . The length of the friction anchor arm is given by n . Note that since the friction angle θ_{FA} is being held constant during the extension of m_2 , the angle θ_A is treated as a constant. Referring to Figure 3.28, we define the common side, p , of the two triangles which form the quadrilateral using the two following kinematic expressions:

$$p^2 = n^2 + m_2^2 - 2nm_2c\theta_A \quad (3.75)$$

$$p^2 = m_1^2 + m_3^2 \quad (3.76)$$

By substituting Equation 3.76 into 3.75, we define the governing geometric relationship for the quadrilateral in Figure 3.28, which is given by the following:

$$m_3^2 = n^2 + m_2^2 - 2nm_2c\theta_A - m_1^2 \quad (3.77)$$

The position of the center of mass of link L_I with respect to point O is defined by the fixed right angle and m_I . Link L_I represents the line of action of the force normal with respect to the terrain. We define the two unknown angles ψ_A and ψ_B using trigonometry as the following expressions:

$$\begin{aligned} \sin \psi_A &= \frac{m_2 s \theta_A}{p} \\ \cos \psi_A &= \frac{p^2 + n^2 - m_2^2}{2pn} \end{aligned} \quad (3.78)$$

$$\begin{aligned} \sin \psi_B &= \frac{m_1}{p} \\ \cos \psi_B &= \frac{m_3}{p} \end{aligned} \quad (3.79)$$

Now we define the position of link L_2 with respect to the origin by defining the angle ψ (the sum of ψ_A and ψ_B) as such:

$$\begin{aligned}\sin \psi &= \sin(\psi_A + \psi_B) \\ \cos \psi &= \cos(\psi_A + \psi_B)\end{aligned}\quad (3.80)$$

$$\begin{aligned}\sin \psi &= \frac{m_1 m_2 s \theta_A - m_2 m_3 c \theta_A + n m_3}{p^2} \\ \cos \psi &= \frac{n m_1 - m_1 m_2 c \theta_A - m_2 m_3 s \theta_A}{p^2}\end{aligned}\quad (3.81)$$

Finally, to define the location of the centers of mass for links L_3 and L_4 with respect to the origin, we must define the following expressions:

$$\begin{aligned}\sin(\psi + \theta_A) &= \frac{n m_1 s \theta_A + n m_3 c \theta_A - m_2 m_3}{p^2} \\ \cos(\psi + \theta_A) &= \frac{n m_1 c \theta_A - m_1 m_2 - n m_3 s \theta_A}{p^2}\end{aligned}\quad (3.82)$$

The next step is to define the rate change of velocity and acceleration for each of the angles and links which define the quadrilateral. Note, the links L_1 and L_2 and angle θ_A are constants and hence have zero rate changes. Additionally, the remaining unknown angle at point F for the quadrilateral is unnecessary to define the position and rate changes of the links and will not be considered for this analysis. The variables m_2 and m_3 are independent and thus the rate of change is defined directly. Therefore, we need only to define the rate of change of Equations 3.75, 3.81 and 3.82. The rate change of velocity and acceleration for Equation 3.75 are given by Equation 3.83 and 3.84, respectively.

$$p' = \frac{d(p^2)}{dt} = 2m_2 \dot{m}_2 - 2n \dot{m}_2 c \theta_A \quad (3.83)$$

$$p'' = \frac{d^2(p^2)}{dt^2} = 2m_2 \ddot{m}_2 + 2\dot{m}_2^2 - 2n \ddot{m}_2 c \theta_A \quad (3.84)$$

Utilizing Equations 3.83 and 3.84, we define the rate change of velocity and acceleration for Equation 3.81 given by Equation 3.85 and 3.86, respectively.

$$\begin{aligned}
s\psi' &= \frac{d(s\psi)}{dt} = \frac{(m_1\dot{m}_2s\theta_A - c\theta_A\dot{m}_{23} + n\dot{m}_3) - p's\psi}{p^2} \\
c\psi' &= \frac{d(c\psi)}{dt} = \frac{(-m_1\dot{m}_2c\theta_A - s\theta_A\dot{m}_{23}) - p'c\psi}{p^2}
\end{aligned} \tag{3.85}$$

$$\begin{aligned}
s\psi'' &= \frac{d^2(s\psi)}{dt^2} = \frac{(m_1\ddot{m}_2s\theta_A - c\theta_A\ddot{m}_{23} + n\ddot{m}_3)p^4 - p''s\psi - 2p^4p's\psi'}{p^6} \\
c\psi'' &= \frac{d^2(c\psi)}{dt^2} = \frac{(-m_1\ddot{m}_2c\theta_A - s\theta_A\ddot{m}_{23})p^4 - p''c\psi - 2p^4p'c\psi'}{p^6}
\end{aligned} \tag{3.86}$$

Where,

$$\begin{aligned}
\dot{m}_{23} &= \dot{m}_2m_3 + m_2\dot{m}_3 \\
\ddot{m}_{23} &= \ddot{m}_2m_3 + 2\dot{m}_2\dot{m}_3 + m_2\ddot{m}_3 \\
p^2s\psi &= m_1m_2s\theta_A - m_2m_3c\theta_A + nm_3 \\
p^2c\psi &= nm_1 - m_1m_2c\theta_A - m_2m_3s\theta_A
\end{aligned} \tag{3.87}$$

Finally, the rate change of velocity and acceleration for Equation 3.82 is given by Equation 3.8 and 3.89, respectively, as follows:

$$\begin{aligned}
s(\psi + \theta_A)' &= \frac{d(s(\psi + \theta_A))}{dt} = \frac{(n\dot{m}_3c\theta_A - \dot{m}_{23}) - p's(\psi + \theta_A)}{p^2} \\
c(\psi + \theta_A)' &= \frac{d(c(\psi + \theta_A))}{dt} = \frac{(-m_1\dot{m}_2 - n\dot{m}_3s\theta_A) - p'c(\psi + \theta_A)}{p^2}
\end{aligned} \tag{3.88}$$

$$\begin{aligned}
s(\psi + \theta_A)'' &= \frac{d^2(s(\psi + \theta_A))}{dt^2} = \frac{(n\ddot{m}_3c\theta_A - \ddot{m}_{23})p^2 - p''s(\psi + \theta_A) - 2p^4p's(\psi + \theta_A)'}{p^6} \\
c(\psi + \theta_A)'' &= \frac{d^2(c(\psi + \theta_A))}{dt^2} = \frac{(-m_1\ddot{m}_2 - n\ddot{m}_3s\theta_A)p^2 - p''c(\psi + \theta_A) - 2p^4p'c(\psi + \theta_A)'}{p^6}
\end{aligned} \tag{3.89}$$

Next, we define the Lagrangian formulation and kinetic and potential energy terms for each of the links. Note, l_{m_2} is the mass of link L_2 , L_{c_2} is the distance of the center of mass of link from the origin of the link L_2 , and finally, x_2 and y_2 are the x - and y -coordinates of the center of mass of link L_2 with respect to the mechanism origin of the general quadrilateral. The Lagrangian formulation is given by the following:

$$L = K - U$$

Where (3.90)

$$K = K_F + K_{L1} + K_{L2} + K_{L3} + K_{L4}$$

$$U = U_F + U_{L1} + U_{L2} + U_{L3} + U_{L4}$$

$$K_F = \frac{1}{2} l_{mF} \dot{m}_3^2$$

$$K_{L1} = 0$$

$$K_{L2} = \frac{1}{2} l_{m2} L_{c2}^2 (\dot{x}_2^2 + \dot{y}_2^2) \quad (3.91)$$

$$K_{L3} = \frac{1}{2} l_{m3} (\dot{x}_3^2 + \dot{y}_3^2)$$

$$K_{L4} = \frac{1}{2} l_{m4} (\dot{x}_4^2 + \dot{y}_4^2)$$

$$U_F = 0$$

$$U_{L1} = l_{m1} g (m_1 - L_{c1})$$

$$U_{L2} = l_{m2} y_2 g \quad (3.92)$$

$$U_{L3} = l_{m3} y_3 g$$

$$U_{L4} = l_{m4} y_4 g$$

We define the position and velocity terms of link L_2 center of mass as follow:

$$x_2 = L_{c2} s \psi$$

$$y_2 = m_1 - L_{c2} c \psi$$

$$\dot{x}_2^2 = L_{c2}^2 (s \psi')^2 \quad (3.93)$$

$$\dot{y}_2^2 = L_{c2}^2 (c \psi')^2$$

We define the position and velocity terms of link L_3 center of mass as follow:

$$x_3 = n s \psi - L_{c3} s(\psi + \theta_A)$$

$$y_3 = m_1 - n c \psi + L_{c3} c(\psi + \theta_A)$$

$$\dot{x}_3^2 = \left(n(s \psi') - L_{c3} s(\psi + \theta_A)' \right)^2 \quad (3.94)$$

$$\dot{y}_3^2 = \left(-n(c \psi') + L_{c3} c(\psi + \theta_A)' \right)^2$$

Finally, we define the position and velocity terms of link L_4 center of mass as follow:

$$\begin{aligned}
x_3 &= ns\psi - (m_2 - L_{c4})s(\psi + \theta_A) \\
y_3 &= m_1 - nc\psi + (m_2 - L_{c4})c(\psi + \theta_A) \\
\dot{x}_3^2 &= \left(n(s\psi)' - \dot{m}_2s(\psi + \theta_A) - (m_2 - L_{c4})s(\psi + \theta_A)' \right)^2 \\
\dot{y}_3^2 &= \left(-n(c\psi)' + \dot{m}_2c(\psi + \theta_A) + (m_2 - L_{c4})c(\psi + \theta_A)' \right)^2
\end{aligned} \tag{3.95}$$

Now we must define the required partials for the Lagrangian formulation with respect to the joints of the mechanism. Because the goal is to find the magnitude of the force normal acting along the line of action of m_I , we will find the partials of the Lagrangian with respect to m_I , even though m_I is being held constant. We also find the partials with respect to joint m_3 , as it directly defines the movement of the output link L_F of the mechanism. First, we define the partials with respect to m_I as follows:

$$\begin{aligned}
\frac{\partial L}{\partial m_1} &= l_{m2}L_{c2}^2((s\psi')S_{11} + (c\psi')S_{12}) \\
&+ l_{m3}\left(ns\psi' - L_{c3}s(\psi + \theta_A)' \right) \left(nS_{11} + L_{c3}\frac{p'ns\theta_A}{p^4} \right) \\
&- l_{m3}\left(nc\psi' - L_{c3}c(\psi + \theta_A)' \right) (L_{c3}S_{13} - nS_{12}) \\
&+ l_{m4}\left(ns\psi' - \dot{m}_2s(\psi + \theta_A) + (m_2 + L_{c4})s(\psi + \theta_A)' \right) \left(nS_{11} - \dot{m}_2\frac{ns\theta_A}{p^2} + (m_2 - L_{c4})\frac{p'ns\theta_A}{p^4} \right) \\
&+ l_{m4}\left(-n(c\psi)' + \dot{m}_2c(\psi + \theta_A) + (m_2 - L_{c4})c(\psi + \theta_A)' \right) (-nS_{12} + \dot{m}_2S_{14} + (m_2 - L_{c4})S_{13}) \\
&- l_{m1}g - l_{m2}g(1 - L_{c2}S_{15}) - l_{m3}g(1 - nS_{15} + L_{c3}S_{14}) - l_{m4}g(1 - nS_{15} + (m_2 - L_{c4})S_{14})
\end{aligned} \tag{3.96}$$

Where

$$\begin{aligned}
S_{11} &= \frac{\dot{m}_2 p^2 s \theta_A - p' m_2 s \theta_A}{p^4} \\
S_{12} &= \frac{-\dot{m}_2 p^2 c \theta_A - p'(n - m_2 c \theta_A)}{p^4} \\
S_{13} &= \frac{-\dot{m}_2 p^2 - p'(nc \theta_A - m_2)}{p^4} \\
S_{14} &= \frac{nc \theta_A - m_2}{p^2} \\
S_{15} &= \frac{n - m_2 c \theta_A}{p^2}
\end{aligned} \tag{3.97}$$

$$\frac{d}{dt} \left(\frac{\partial L}{\partial \dot{m}_1} \right) = 0 \tag{3.98}$$

Then, we define the partials with respect to m_3 as follows:

$$\begin{aligned}
\frac{\partial L}{\partial m_3} &= l_{m2} L_{c2}^2 ((s \psi') S_{21} + (c \psi') S_{22}) \\
&+ l_{m3} \left(ns \psi' - L_{c3} s(\psi + \theta_A) \right)' (n S_{21} - L_{c3} S_{23}) \\
&- l_{m3} \left(nc \psi' - L_{c3} c(\psi + \theta_A) \right)' \left(-n S_{22} + L_{c3} \frac{p' ns \theta_A}{p^4} \right) \\
&+ l_{m4} \left(ns \psi' - \dot{m}_2 s(\psi + \theta_A) - (m_2 - L_{c4}) s(\psi + \theta_A) \right)' \left(n S_{21} - \dot{m}_2 \frac{nc \theta_A - m_2}{p^2} - (m_2 - L_{c4}) S_{23} \right) \\
&+ l_{m4} \left(-nc \psi' + \dot{m}_2 c(\psi + \theta_A) + (m_2 - L_{c4}) c(\psi + \theta_A) \right)' \left(\dot{m}_2 S_{24} - n S_{22} + (m_2 - L_{c4}) \frac{p' ns \theta_A}{p^4} \right) \\
&- l_{m2} g(L_{c2} S_{25}) - l_{m3} g(n S_{25} + L_{c3} S_{24}) - l_{m4} g(n S_{25} + (m_2 - L_{c4}) S_{24})
\end{aligned} \tag{3.99}$$

Where

$$\begin{aligned}
S_{21} &= \frac{-\dot{m}_2 p^2 c \theta_A - p'(n - m_2)}{p^4} \\
S_{22} &= \frac{-\dot{m}_2 p^2 s \theta_A + p'(m_2 s \theta_A)}{p^4} \\
S_{23} &= \frac{-\dot{m}_2 p^2 - p'(nc \theta_A - m_2)}{p^4} \\
S_{24} &= \frac{-ns \theta_A}{p^2} \\
S_{25} &= \frac{m_2 s \theta_A}{p^2}
\end{aligned} \tag{3.100}$$

$$\begin{aligned}
\frac{d}{dt} \left(\frac{\partial L}{\partial \dot{m}_3} \right) &= l_{mF} \ddot{m}_3 + l_{m2} L_{c2} ((s \psi'') S_{31} + (s \psi') S_{32} + (c \psi'') S_{33} + (c \psi') S_{34}) \\
&+ l_{m3} \left((ns \psi'' - L_{c3} s(\psi + \theta_A)'') (nS_{31} - L_{c3} S_{35}) + (ns \psi' - L_{c3} s(\psi + \theta_A)') S_{32} - L_{c3} S_{36} \right) \\
&+ l_{m3} \left((L_{c3} c(\psi + \theta_A)'' - nc \psi'') (L_{c3} S_{37} - nS_{33}) + (L_{c3} c(\psi + \theta_A)' - nc \psi') S_{34} + L_{c3} S_{38} \right) \\
&+ l_{m4} \left(ns \psi'' - \ddot{m}_2 s(\psi + \theta_A) - 2\dot{m}_2 s(\psi + \theta_A)' - (m_2 - L_{c4}) s(\psi + \theta_A)'' \right) (nS_{31} - (m_2 - L_{c4}) S_{35}) \\
&+ l_{m4} \left(ns \psi' - \dot{m}_2 s(\psi + \theta_A) - (m_2 - L_{c4}) s(\psi + \theta_A)' \right) (nS_{32} - \dot{m}_2 S_{35} - (m_2 - L_{c4}) S_{36}) \\
&+ l_{m4} \left((m_2 - L_{c4}) c(\psi + \theta_A)'' + 2\dot{m}_2 c(\psi + \theta_A)' + \ddot{m}_2 c(\psi + \theta_A) - nc \psi'' \right) ((m_2 - L_{c4}) S_{37} - nS_{33}) \\
&+ l_{m4} \left((m_2 - L_{c4}) c(\psi + \theta_A)' + \dot{m}_2 c(\psi + \theta_A) - nc \psi' \right) ((m_2 - L_{c4}) S_{38} + \dot{m}_2 S_{37} - nS_{34})
\end{aligned} \tag{3.101}$$

Where

$$\begin{aligned}
S_{31} &= \frac{n - m_2 c \theta_A}{p^2} \\
S_{32} &= \frac{(-c \theta_A (\dot{m}_2 p^2 + m_2 p') + n p') - 2 p' (n - m_2 c \theta_A)}{p^4} \\
S_{33} &= \frac{-m_2 s \theta_A}{p^2} \\
S_{34} &= \frac{-s \theta_A (\dot{m}_2 p^2 + m_2 p') + 2 p' (m_2 s \theta_A)}{p^4} \\
S_{35} &= \frac{nc \theta_A - m_2}{p^2} \\
S_{36} &= \frac{(nc \theta_A p' - (\dot{m}_2 p^2 + m_2 p')) - 2 p' (nc \theta_A - m_2)}{p^4} \\
S_{37} &= \frac{-ns \theta_A}{p^2} \\
S_{38} &= \frac{p' (2ns \theta_A - ns \theta_A)}{p^4}
\end{aligned} \tag{3.102}$$

The constraint equation for the quadrilateral mechanism in Figure 3.27 is defined by Equations 3.77, and it and its partial are defined as:

$$\Gamma = m_3^2 - n^2 - m_2^2 + 2nm_2 c \theta_A + m_1^2 = 0 \tag{3.103}$$

$$\frac{\partial \Gamma}{\partial m_1} = 2m_1 \tag{3.104}$$

$$\frac{\partial \Gamma}{\partial m_3} = 2m_3 \tag{3.105}$$

The Lagrange multiplier λ is gives as follows, where f_{cx} is any external force applied to L_F :

$$\lambda \frac{\partial \Gamma}{\partial m_3} = \frac{d}{dt} \left(\frac{\partial L}{\partial \dot{m}_3} \right) - \frac{\partial L}{\partial m_3} - f_{cx} \tag{3.106}$$

Finally, the force normal acting between the friction anchor and the terrain is defined as F_I and found by using the following equation.

$$F_I = \frac{d}{dt} \left(\frac{\partial L}{\partial \dot{m}_1} \right) - \frac{\partial L}{\partial m_1} - \lambda \frac{\partial \Gamma}{\partial m_1} \quad (3.107)$$

The resulting equations of motion are employed to generate the plot in Figure 3.29. The equations are validated using the Mechanism Analysis suite of Pro/Engineer Wildfire 4.0. Figure 3.29 shows how the force normal at the friction pad changes as a function of time and θ_{FA} . Note that the change in time is solely influenced by the rate change of the prismatic joint, m_2 . In this plot, m_2 maintains the same constant acceleration, 0.004 m/s^2 , in all three cases and θ_{FA} is held constant for each curve. These equations of motion are further used to define the friction force in the pad during the execution of the new gaits.

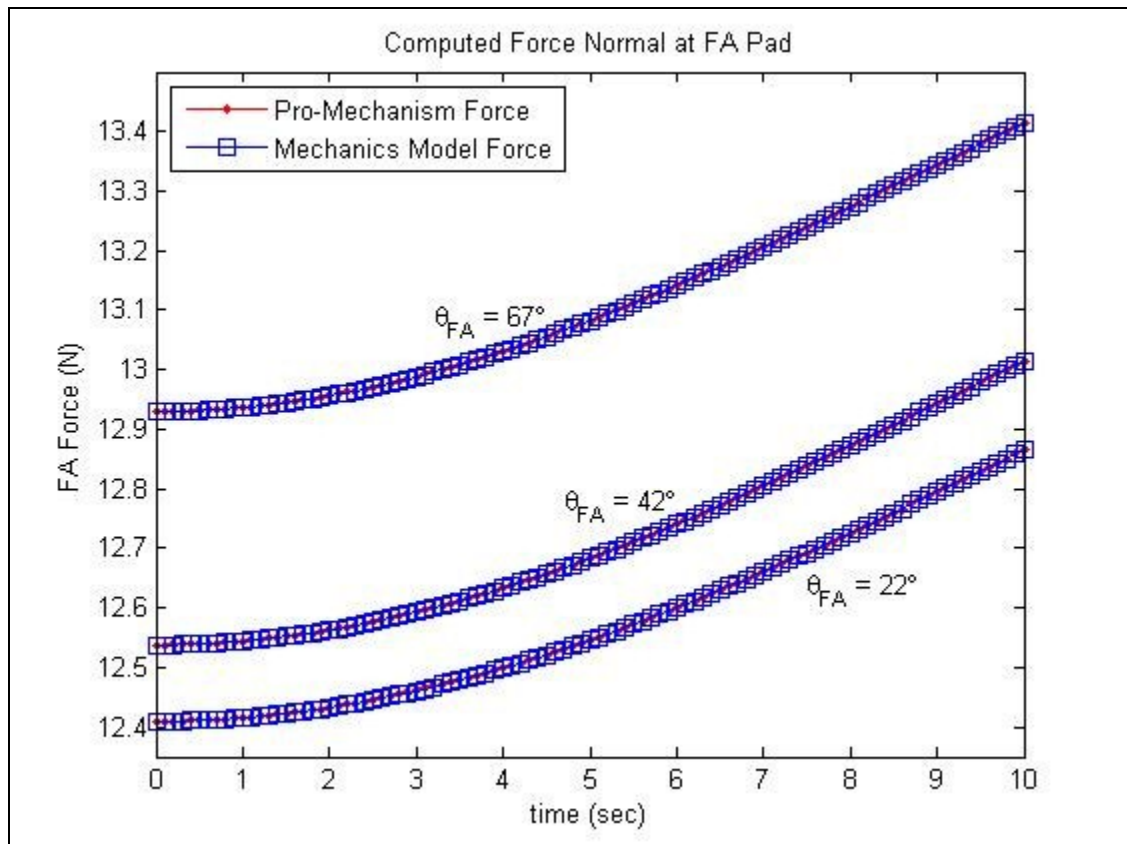


Figure 3.29: Force Normal, F_I , at the Friction Anchor-Terrain Contact

3.7 Snake-Inspired Robot Prototype

3.7.1 Prototype Fabrication Options

During the early phases of the robot design, the fabrication of prototype hardware was done using the metal machining techniques and 6061 aluminum as the primary material. However, prototyping the entire robot from aluminum is infeasible due to weight issues. Principally, this is due to the load capacity limitations of the selected actuators and the need to have multiple modules to achieve the velocity goals. Therefore, the final robot prototype will be fabricated using high strength plastics. Regarding the fabrication method for the prototype, three choices which are suitable for high strength plastics were considered:

- **CNC Milling** – The most traditional method being considered, the advantages and disadvantages of CNC machining are the best understood. The advantages include the ability to mill complex shapes, such as, conical features and vertical steps in a surface. The primary disadvantage is that CNC milling machines are often limited to 2.5D machining. This refers to a surface which is a projection of a plane into a 3rd dimension. It is not possible to have overhanging elements with this type of 3D object. Due to the complexity of the robot design, employing CNC milling would require the fabrication of additional pieces and their assembly through an adhesive method or fasteners.
- **Laser Cutting** – Laser cutting works by directing the output of a high-power laser at the material to be cut. The material is then cut leaving an edge with a high-quality surface finish by melting, burning, or vaporization the material in the path of the laser beam. The primary advantage of laser cutting plastics is the reduced

chance of warping the plastics due to the relatively small localized heating of the material as it is being cut. In addition, laser cutting is generally much faster than tradition machining. The primary disadvantage of this method is that the plastic can only be laser cut as plates. This would require several pieces to be cut and assembled using an adhesive method to form the 3D shapes required by the modular components of the robot design.

- Additive Manufacturing – Additive manufacturing techniques are often used in rapid prototyping to automatically construct physical objects from computer aided design models. Prominent additive manufacturing techniques for thermoplastics include Selective Laser Sintering (SLS), Fused Deposition Modeling (FDM) and Stereolithography (SLA). Due to available of resources, FDM was considered as the primary option for this manufacturing technique. FDM works on an "additive" principle by laying down material in layers. The FDM machine dispenses two materials: one for the actual part and one for a disposable support structure. FDM has the advantage of producing complex parts directly from STL file without changing tools or removing the part for reorientation. The disadvantage of this manufacturing method is time. Depending on the complexity of the part, “printing” can take as long as few hour to more than a day.

After reviewing the differences between the candidate methods, it was decided that FDM would be utilized to fabricate the complete prototype robot. The most important factor in this decision was the fact that FDM is capable of fabricating entire components without additional machining, assembly or finishing of the parts. Although the actual printing of the components may take longer, FDM avoids the additional processing steps.

Beyond this work, future prototypes will be fabricated using multi-material molding techniques. These techniques allow for fabrication of fully functional mechanisms, in-mold without need for post-process assembly, allowing for economical manufacturing of many robot modules [90-94]. These techniques were not considered for this work as designing for molding operations was outside of the scope of this dissertation.

3.7.2 R2G2 Prototype

The complete prototype of the robot design, Robot with Rectilinear Gaits for Ground operations (R2G2), is illustrated in Figure 3.30. A prototype was fabricated in order to demonstrate the new snake-inspired design and rectilinear gaits. The prototype robot is made primarily from ABS plastic using FDM, as observed in Figure 3.31. The robot has a 70 x 70 mm cross-section. The robot has a contracted length of 1003 mm and a fully extended length of 1384 mm. The total mass of the robot is approximately 2.5 kg.

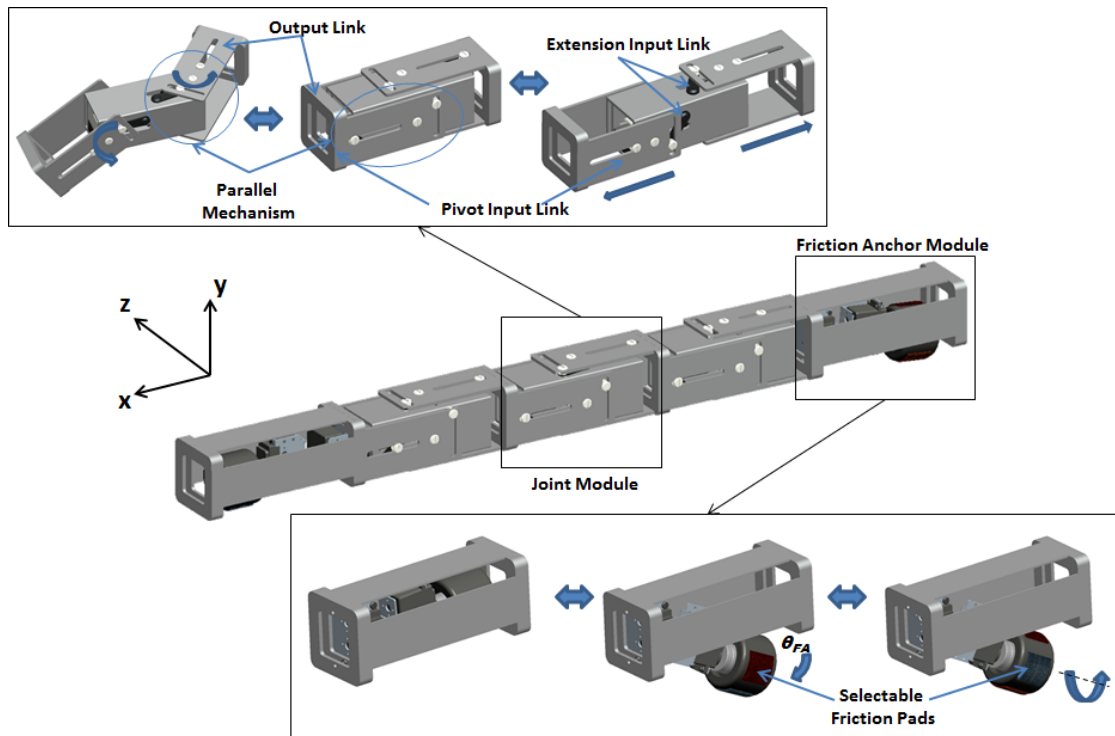


Figure 3.30: R2G2: Final Design CAD Model

The robot consists of four joint modules (each containing two parallel mechanisms) assembled in a serial configuration allowing each module to move in linearly and pivot with respect to the adjacent module. Each mechanism is capable of 90 degrees of motion and 48 mm of extension. Each parallel mechanism consists of two standard sized servomotors: a Hitec HS-7940TH High Voltage Speed servo for extension and a Hitec HS-7950TH High Voltage Torque servo for pivoting. The HS-7940TH servos are capable of 16 kg-cm of maximum torque and a maximum speed of 0.06 s/60 deg. from a 68 g package. They consist of a Titanium gear train providing a range of 180 deg. The HS-7950TH servos are capable of 35 kg-cm of maximum torque and a maximum speed of 0.13 s/60 deg. from a 68 g package. They also consist of a Titanium gear train with a range of 180 deg. The terminal modules of the robot each contain a variable friction force anchor mechanism capable of applying an anchoring or “planting” force against the terrain. Each friction anchor is actuated using Hitec HS-7940TH High Voltage Speed servomotors.

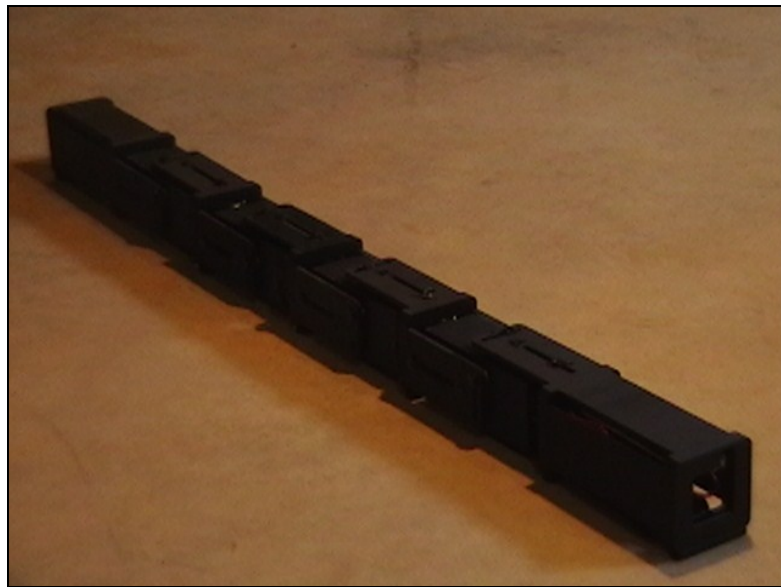


Figure 3.31: R2G2: Prototype of the Snake-Inspired Robot Design

The control of the prototype robot is implemented onboard with an Arduino Mega Microcontroller programmed with the open-source Arduino software. The Mega is a microcontroller board based on the ATmega2560 processor. It has 54 digital input/output pins, a 16 MHz crystal oscillator and a USB connection. The length and width of the board are approximately 102 x 53 mm, respectively. The regulated power supply provided by the board is 3.3 or 5 volt, which is used to provide signals to the servomotors. The servomotors and microcontroller are powered externally by two 7.4V 2100mAh Pro Lite LiPo Batteries. However, a separate 4.8 volt power source provides power for a radio control receiver. The robot is controlled external by a RC transmitter which provides signals directly to microcontroller through the RC receiver to execute general motions using one of the preprogrammed gaits. For example, if the command is given to “turn right” by the transmitter, the microcontroller executes the turning gait specifically programmed for a right turn. An illustration of the control architecture for the robot is provided in Figure 3.32.

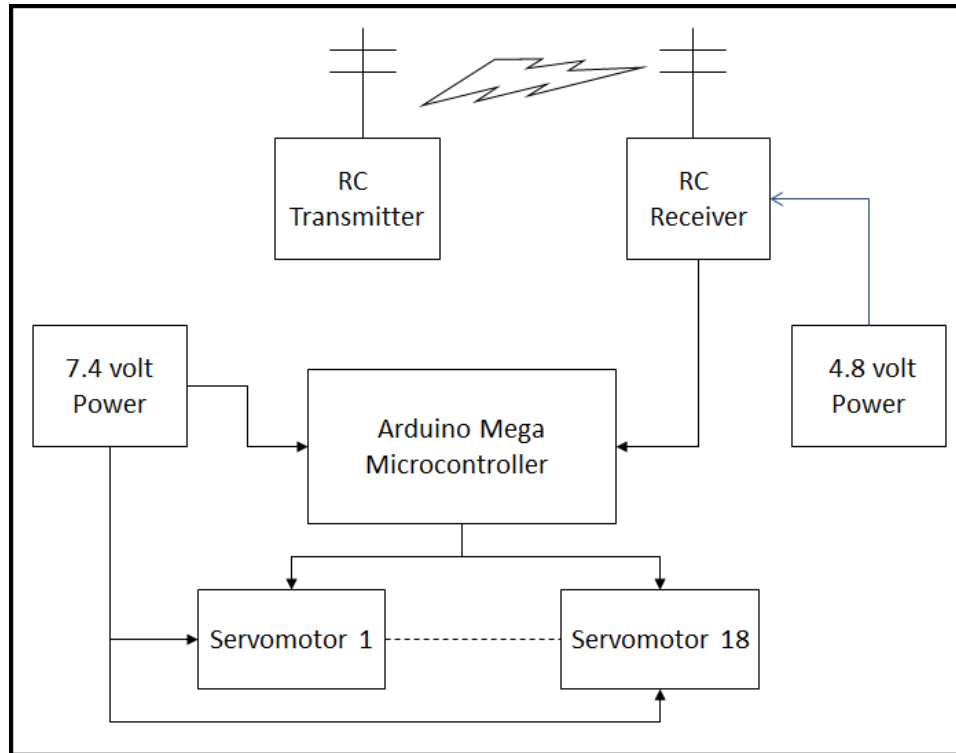


Figure 3.32: Control Architecture Schematic

3.7.3 R2G2 Robot Performance

Upon implementing the high speed forward gait using R2G2, as illustrated in Figure 3.33, we found the maximum demonstrated forward velocity for the prototype was 414 mm/s. Similarly, applying the high speed turning gait, as illustrated in Figure 3.34, the maximum demonstrated turning speed was measured as 14 deg/s. The performance of the robot prototype is characterized through the use of three dimensionless performance metrics. The first metric is a measure of the robot's propulsive efficiency, $\eta_{velocity}$, as defined in Equation 3.108.

$$\eta_{velocity} = \frac{v_m}{v_p} \quad (3.108)$$

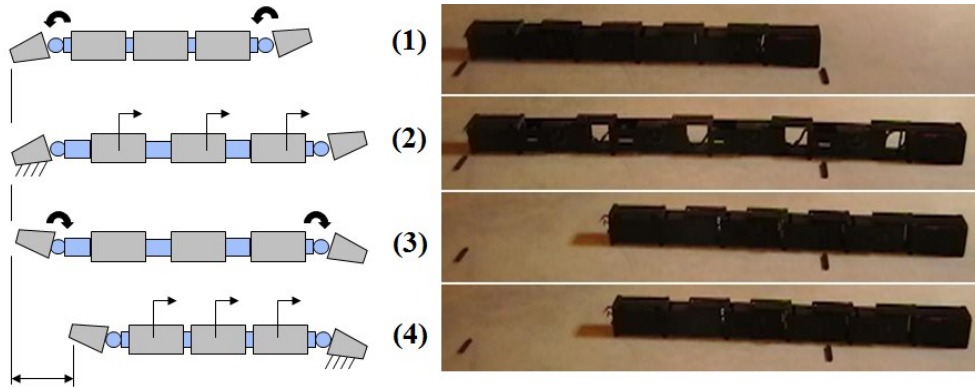


Figure 3.33: High Speed Forward Gait

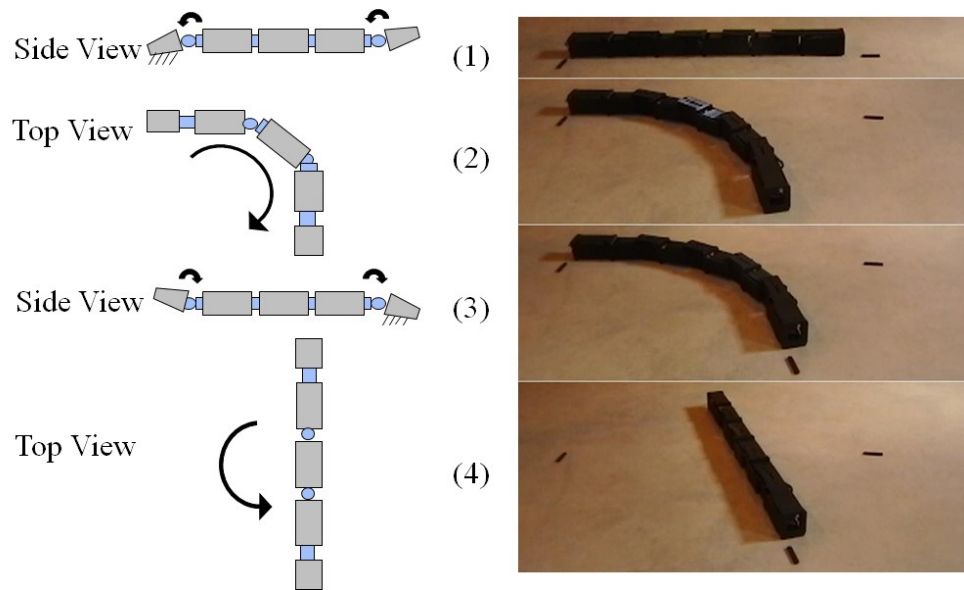


Figure 3.34: High Speed Turning Gait

The predicted velocity, v_p , is calculated based on the gait and module velocity, v_m , and is computed to be 476 mm/s. The variable $\eta_{velocity}$ is calculated as 0.87. This value indicates that there is approximately 13% slippage between the anchor and terrain for the maximum speed. The next metric is a ratio, m_r , between the modular input velocity, m_v , and the resulting robot velocity, v_m , and is defined by Equation 3.109.

$$m_r = \frac{nv_m}{\left(\frac{32}{3}\right)m_v} \quad (3.109)$$

The ratio is computed as $0.33n$, where n is the number of modules in the robot. This number multiplied by a given modular expansion rate defines the expected robot velocity. The modular cyclic rate is calculated as 119 mm/s. The robot velocity is measured as 414 mm/s. The ratio also indicates that an increase in the number of modules (where n is greater than 4) will yield a higher robot speed. Modular velocity improvements may be due to faster motors, higher voltage power supply or reductions in mechanism weight and friction.

In selecting the final performance metric, we desired a metric that would provide a comparison of the performance of our robot to other robot platforms of various sizes. We considered two options: (1) energy cost of transport and (2) Froude number. The energy cost of transport or specific resistance is a dimensionless energy performance metric defined by the power required to move a system a constant velocity divided by the product of the weight of the system and the aforementioned constant velocity [1]. In robotics, the Froude number, F_r , is typically used to normalize walking speed of legged robots to provide a better comparison between the robots and animals. The Froude number is a dimensionless scale-invariant metric defined as ratio of inertial to gravitational forces [1]. Both metrics are often used to compare dissimilar animals and/or systems [1], however, due to the lack of reported data on the power input for most robotics systems, we elected to only utilize the Froude number to describe and compare our robot prototype. The calculation of the Froude number is given by Equation 3.110.

$$F_r = \frac{v}{\sqrt{gl}} \quad (3.110)$$

Where v is the walking speed, l is the leg length, and g is gravity. Usually the formulation of the Froude number for snake-inspired robots is problematic due to the fact that simply

growing the length of a snake-inspired robot might drastically affect the dimensionless value without changing the velocity; hence the Froude number for a snake-inspired robot is contrived [1]. However, in this design, increases in length directly lead to increases in velocity, as seen in Equation 3.109. This is due to the fact that the gait for this robot is similar to the strides made by walking robots. The Froude number range for the robot is calculated to be from $F_r = 0$ to $F_r = 0.12$. The Froude number ranges for some of the state of the art walking robots have been shown as: 'Rabbit' shows a speed range from about $F_r = 0.15$ to $F_r = 0.3$, 'Toddler' from $F_r = 0$ to $F_r = 0.09$ and the relatively fast and small 'RunBot' from $F_r = 0.25$ to $F_r = 0.5$ [95]. In comparison Honda's Asimo has a speed range from $F_r = 0$ to $F_r = 0.3$ and humans from $F_r = 0$ to about $F_r = 1.0$ [95]. Although the current prototype has a relatively small range compared to other robots, this range can easily be increased the simply adding more modules. This allows the robot to increase forward velocity without increasing the time required to complete a gait cycle.

In general, when comparing the performance of various, dissimilar systems, it is desirable to utilize scale-invariant metrics to provide "similitude at different scales," which allows for better fidelity of the comparison [1]. However, caution should be employed when using scale-invariant metrics for direct comparison of snake-inspired robots. Systems with large length-to-cross-sectional-area ratios, such as snake-inspired robots, tend to be at a disadvantage when compared to shorter systems using work-based scale invariant measures, such as normalized work or body lengths per time [1]. As previously stated, due to the general lack of reported data on the input power for most snake-inspired systems, we are unable to employ energy-based scale invariant metrics, such as specific resistance or net propulsive efficiency. Furthermore, even though we

have employed the scale-invariant Froude number to compare our system to other mobile robot systems, in general, the problem with employing Froude number for limbless robots is determining an analogous length dimension which is appropriate for each robot [1]. Taking these considerations into account and given the limited performance data provided for each snake-inspired system, we felt it most appropriate to make direct comparisons between the systems using the maximum speed provided and the given prototype dimensions. Furthermore, we acknowledge that the maximum speeds may not be the limit for the reported system; however, the comparison does provide general indications of how the performance of our design compares with previous work.

Table 3.7 contains dimensional and velocity data for several well-known snake-inspired and snake-like robot platforms [96]. Furthermore, Figure 3.35 and Figure 3.36 provide a graphic depiction of the robot performances in terms of cross-section vs. velocity and robot length vs. velocity, respectively. Koryu-II is the largest and fastest robot from the survey and its data skews the trends established by the other platforms. Therefore, for the sake of clarity, data for the Koryu-II robot was not included in the charts. From the table, we observe that our prototype demonstrates the second highest velocity among the surveyed designs. Our prototype is 7 out of 15 in terms of cross-sectional area. Also, our robot is 10 out of 15 in terms of length. Finally, for the sake of completeness, we compare the calculated Froude number for the surveyed robots and our prototype using Equation 3.110 and the results are displayed in Figure 3.37. From the chart, we observed that R2G2 is the second highest in terms of F_r . However, the highest rated robot, AmphiBot II, is not an expansion type robot and therefore increases length may not necessarily increase velocity, as opposed to R2G2. From the data, we determined

that R2G2 dimensionally falls within the middle of the design space defined by the surveyed platforms. However, the prototype's forward velocity is near the top of range of demonstrated speeds. Therefore, we conclude that our design meets our goal of a high speed, compact platform.

Platform	Data Label	Length (mm)	Cross Section (m²)	Velocity (mm/s)
ACM III	ACM3	2000	0.023	400
AmphiBot I	AB-I	490	0.002	35
AmphiBot II	AB-II	770	0.002	400
Boxerbaum et al. Worm Robot	BWR	1067	0.049	16
CMU Robot, Uncle Sam	CMU	940	0.002	102
JL-I	JL-I	1050	0.038	180
Koryu-I	K-I	1390	0.081	266
Koryu-II	K-II	3300	0.497	500
Kotay et al. 1 st Inchworm Robot	KIR1	250	---	4
Kotay et al. 2 nd Inchworm Robot	KIR2	330	---	13
OmniTread (OT-8)	OT-8	1270	0.034	100
OmniTread (OT-4)	OT-4	940	0.007	150
R2G2 Robot	R2G2	1003	0.005	414
Seok et al. Worm Robot	SWR	200	---	3
Slim Slime Robot	SSR	730	0.013	60

Table 3.7: Robot Performance Data

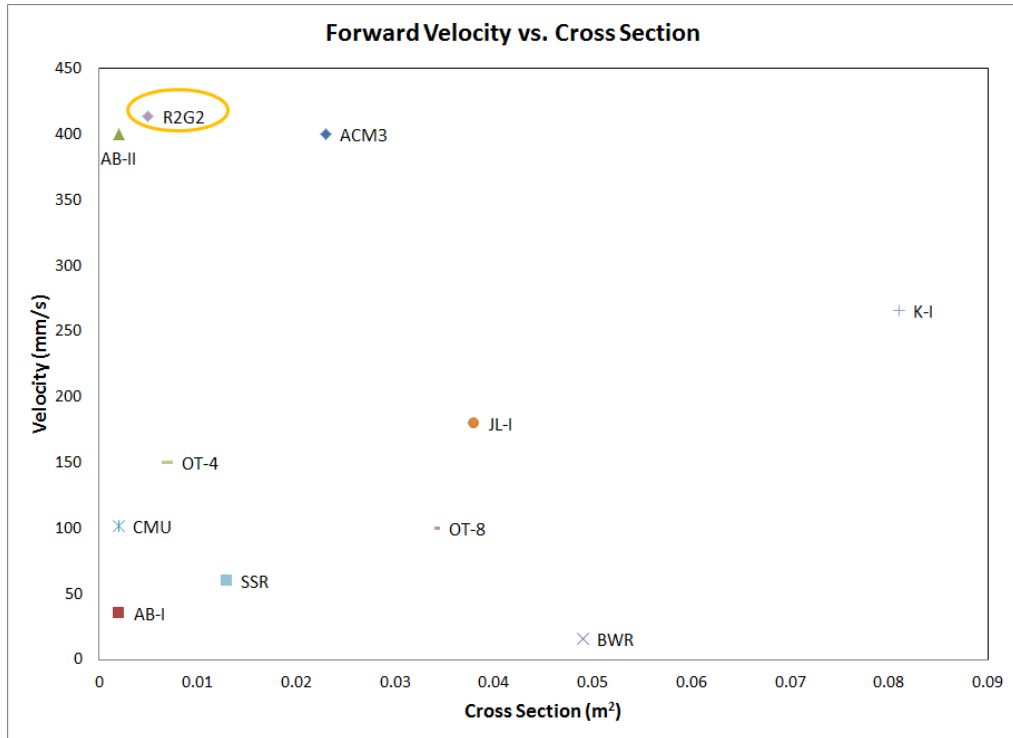


Figure 3.35: Robot Cross-Section vs. Velocity Performance

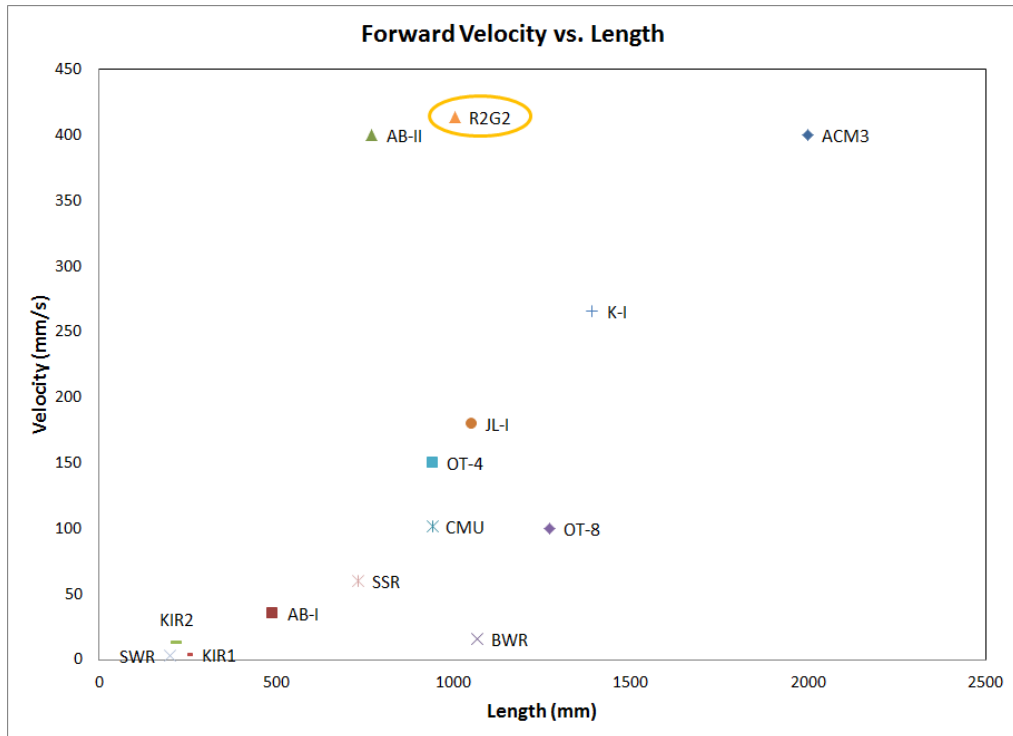


Figure 3.36: Robot Length vs. Velocity Performance

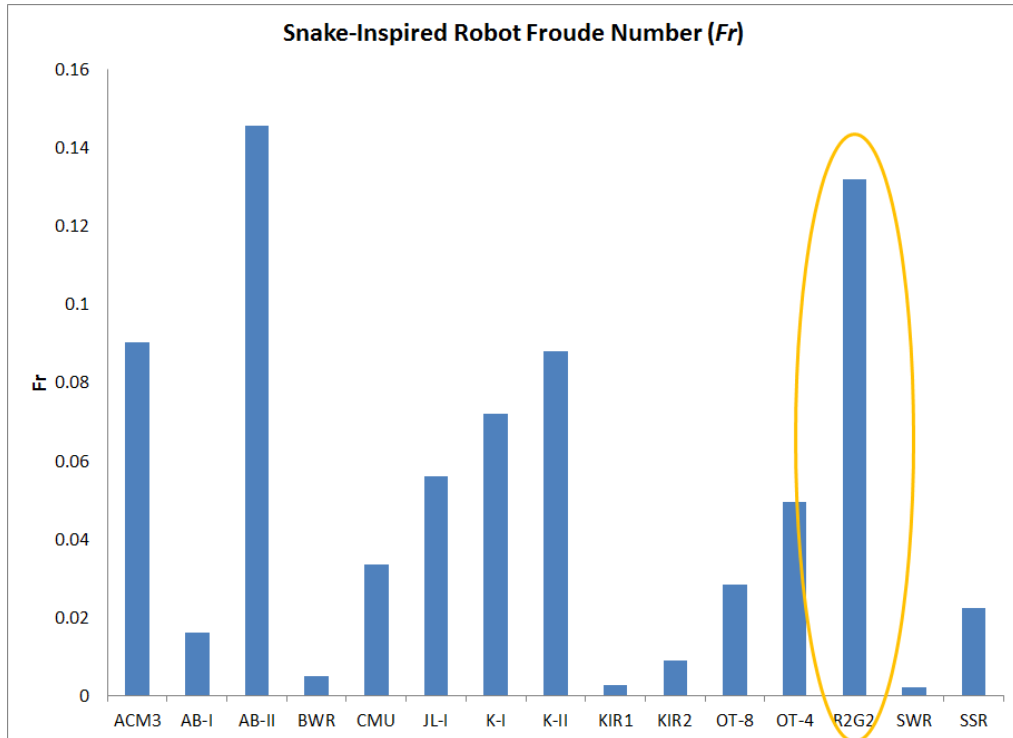


Figure 3.37: Snake-Inspired Robot Froude Number

3.8 Summary

In this chapter, an exaggerated rectilinear gait concept is introduced which emphasizes high speed limbless locomotion, using rapid expansion and contraction of body segments. The exaggerated rectilinear gait class incorporates highly stable motion and variable friction force control to provide effective traction on a variety of surfaces. A novel snake-inspired robot design, based on the kinematics necessary to execute the exaggerated rectilinear motion, was also introduced. The robot design is composed of a number of serially connected planar parallel mechanisms. The planar parallel mechanism, introduced in this work, is capable of linearly extending and pivoting its output link. The robot design also employs a redundant modular, non-tethered architecture. Each module is composed of two parallel mechanisms offset 90 degrees about the x -axis, providing the robot with spatial as well as planar motion. This allows the robot to lift its segments from

the terrain to cross gaps. A 4-module prototype, R2G2, was fabricated to demonstrate the robot architecture and gait concepts. The prototype snake-inspired robot employs a cross sectional area of 70 x 70 mm, allowing the robot to navigate small, tight spaces. The prototype achieved a maximum forward velocity of 414 mm/s and a maximum turning speed of 14 deg/s.

A complete kinematics and dynamics analysis was completed for the planar parallel mechanism. A geometric analysis was conducted and expressions were derived for each of the two input limbs of the mechanism, relating input to output link motion. The inverse and direct kinematics for the mechanism were developed using these relations. Furthermore, by taking the derivative with respect to time of the geometric relationships, a Jacobian matrix was developed for the mechanism to relate input to output link velocities. The inverse dynamics are formulated using the Lagrangian approach and the complete equations of motion of this mechanism were derived. The equations of motion were verified using the Mechanism suite of the Pro/Engineer Wildfire 4.0 edition. Additionally, a dynamic analysis and model for the variable friction anchoring concept were developed and validated using the Mechanism suite of the Pro/Engineer.

4 Development of a Dynamics Model for an Exaggerated Rectilinear Gait

4.1 Overview

The concept for the new exaggerated rectilinear gait, which has been presented in Chapter 3, centers about the ability of the snake-inspired robot to rapidly expand and contract its segments linearly with little to no vertical displacement. This ability allows most of the joint motion and energy to be directly utilized in forward displacement. The concept also employs a method of anchoring the robot to the terrain through frictional forces to provide traction on multiple surfaces. A design for a robot platform capable of executing the exaggerated rectilinear gait is illustrated in the top image of Figure 4.1. In order to properly fabricate reliable platforms, which utilize the exaggerated rectilinear gait, we must understand the forces generated in the robot throughout the gait execution. We address this need through the development of a dynamics model of the gait. In addition, this model will be capable of being directly applied to a platform with a variable number of modules. The model treats the snake-inspired robot as a serial robot capable of planar motion, shown in the bottom image of Figure 4.1. Note that while the robot design is capable of more than planar motion, the exaggerated rectilinear gaits described in this work are planar. Therefore, the dynamics model will only represent planar motion. The “base” of the serial robot is defined as a quasi-link between the anchoring mechanism and the terrain, during anchor engagement. At any point in time, at least one anchoring mechanism is engaged with the terrain. To account for the variable number of modules, the Lagrangian formulation [58] for serial robotics was chosen to model the robot. This formulation was chosen due to the fact that both the Lagrangian formulation of the

manipulator inertia matrix and velocity vector allows for addition and subtraction of robot links while the equations of motion remain closed form.

In addition to the development of the dynamics model, we will also employ the model to develop a second set of exaggerated rectilinear gaits: forward and turning gaits which emphasize traction. The first exaggerated rectilinear gait set, which emphasized high speed forward and turning gaits presented in Chapter 3, are effective on terrains, where planting the anchor only is sufficient for providing adequate traction to move forward. However, on smooth, hard terrains, the use of the friction anchor alone may not be effective. Therefore a high traction gait was developed that utilizes the ability of the snake-inspired robot to shift its center of mass to provide additional traction. The dynamics model is used to demonstrate and validate the gait concept.

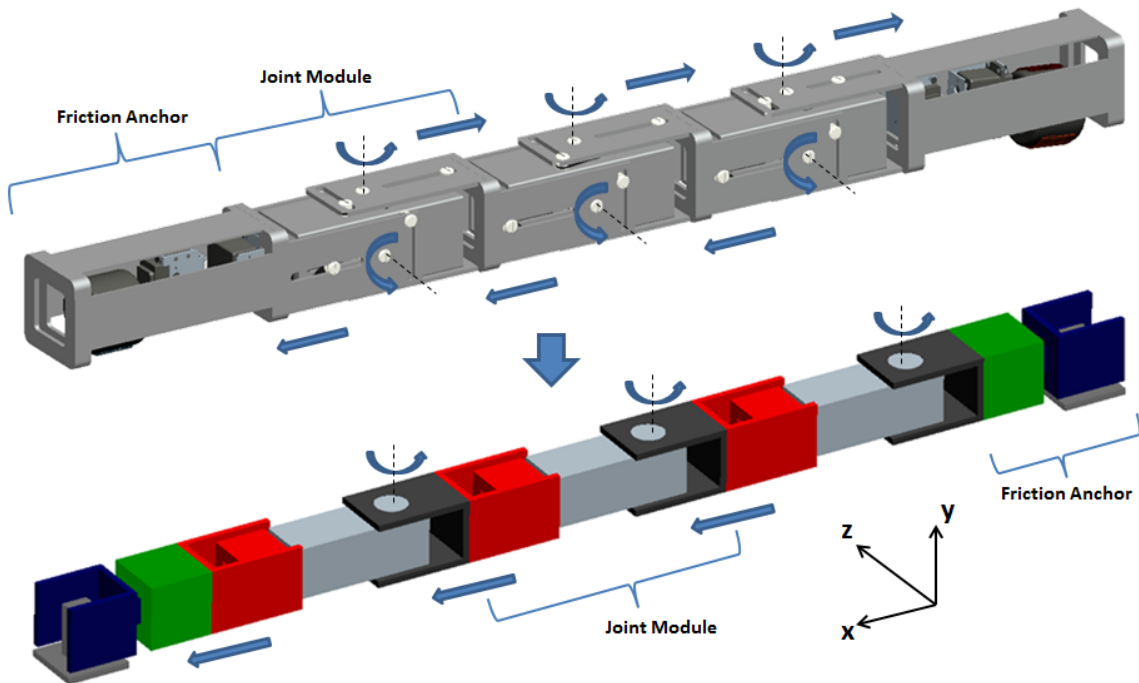


Figure 4.1: Snake-Inspired Robot Design and Simplified Kinematic Representation

4.2 Friction Anchor Module Dynamics Model

Before defining the robot dynamics model, we must first define a dynamics model representation of the robot anchoring mechanism and joint module. The engagement and disengagement of the anchoring mechanism, referred to as a friction anchor (FA) module and pictured in Figure 4.2, has little to no effect on body changes of the robot, therefore, we choose not to model the actual anchor kinematics for the robot dynamics model. Alternatively, we model the anchor in the following manner, as illustrated in Figure 4.3.

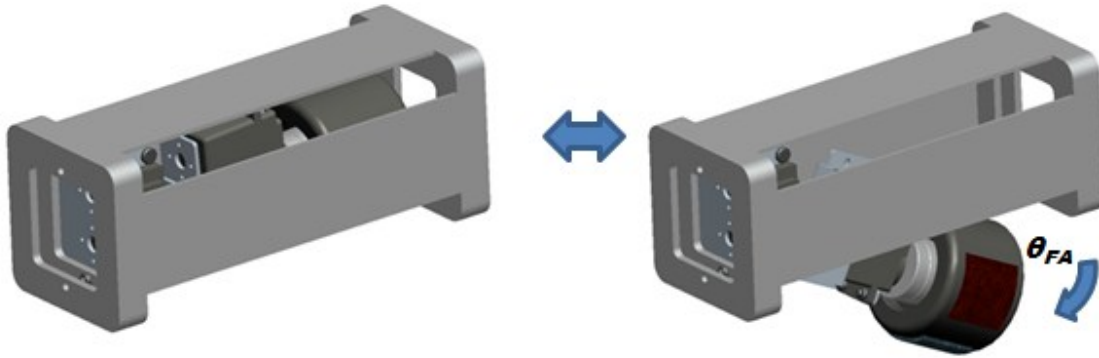


Figure 4.2: CAD Model of Actual Friction Anchor

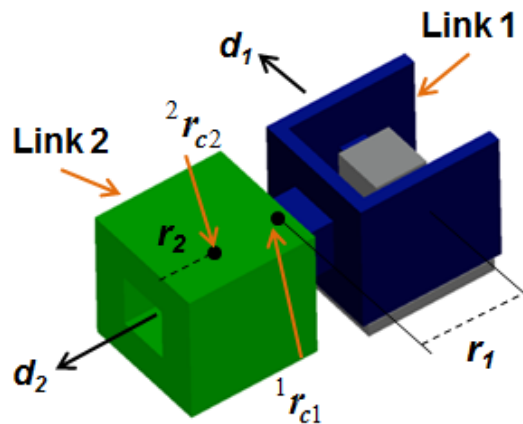


Figure 4.3: Dynamics Model Representation of a Friction Anchor

The model possesses two unactuated joints: one in planar z -direction, d_1 , and one in x -direction, d_2 . Note that the coordinate system for the robot as seen in Figure 4.1 is defined

by the base link (Link 0 illustrated in Figure 4.4) of the FA module. The variables r_1 and r_2 are the z -distance for Link 1 and y -distance for Link 2, respectively, from the individual link frames to the centers of mass. The unactuated joints are utilized to compute the reaction forces in the x - and z -directions at the friction anchor point of contact with the terrain, as a result of gait motion, by solving for the joint forces using Lagrangian dynamics. These forces, coupled with the equations of motions of the actual friction anchor, are used to define the friction force and direction at the point of contact. We find the Lagrangian dynamics of the gait model representation of the FA by first defining the Link Characteristics. Next, using D-H Link Parameters, we determine the Link Inertia and Jacobian Matrices. Finally, we solve for the Lagrangian Equations of Motion.

4.2.1 Friction Anchor Link Characteristics

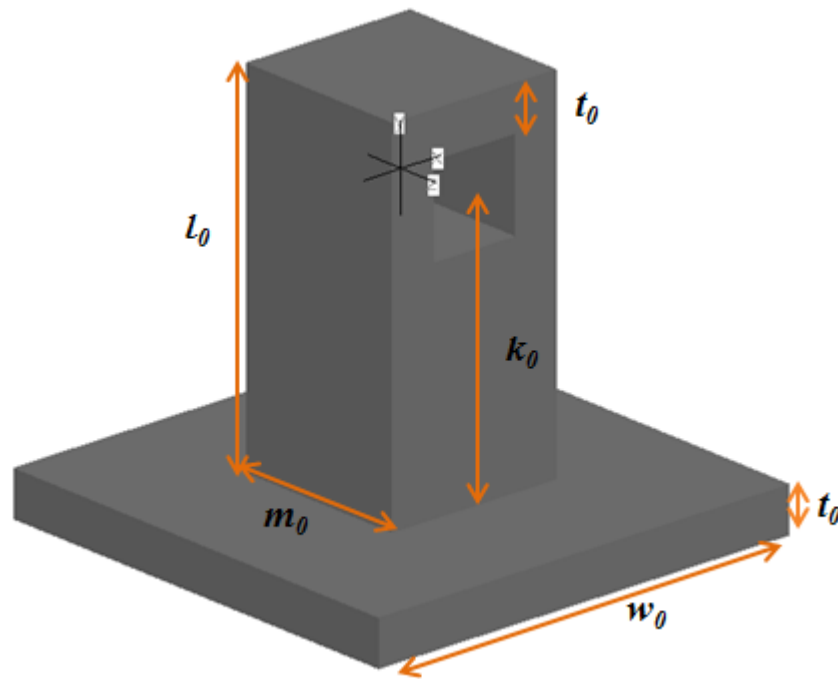


Figure 4.4: CAD Model of FA Link 0

The mass of Link 0 is defined by Equation 4.01, where ρ is an arbitrary density for FA:

$$l_{m_0} = \rho(m_0^2 l_0 + w_0^2 t_0 - m_0(m_0 - 2t_0)^2) \quad (4.01)$$

The position of the center of mass with respect to the Link 0 frame is given by:

$${}^0r_{c_0} = \begin{bmatrix} 0 \\ r_0 \\ 0 \end{bmatrix}$$

where (4.02)

$$r_0 = \frac{m_0^2 l_0 (l_0 - 2k_0) - w_0^2 t_0 (t_0 + 2k_0)}{2m_0^2 l_0 + 2w_0^2 t_0 - 2m_0(m_0 - 2t_0)^2}$$

The inertia matrices of Link 0 with respect to the Link 0 frame and about the center of mass, expressed in the Link 0 frame are given by the following:

$${}^0I_0 = \begin{bmatrix} xx_0 & 0 & 0 \\ 0 & yy_0 & 0 \\ 0 & 0 & zz_0 \end{bmatrix} \quad \text{and} \quad {}^0I_{c_0} = \begin{bmatrix} xc_0 & 0 & 0 \\ 0 & yc_0 & 0 \\ 0 & 0 & zc_0 \end{bmatrix} \quad (4.03)$$

Where, the moments of inertia with respect to the x -axis of Link 0 frame and the center of mass are given by the following:

$$xx_0 = xx_{01} + xx_{02} - xx_{03}$$

$$xc_0 = xx_0 - l_{m_0} r_0^2$$

where (4.04)

$$xx_{01} = \rho m_0^2 l_0 \left(\frac{1}{12} (m_0^2 + l_0^2) + \left(\frac{l_0 - 2k_0}{2} \right)^2 \right)$$

$$xx_{02} = \rho w_0^2 t_0 \left(\frac{1}{12} (w_0^2 + t_0^2) + \left(\frac{t_0 + 2k_0}{2} \right)^2 \right)$$

$$xx_{03} = \rho \frac{m_0}{12} (m_0 - 2t_0)^2 (m_0^2 + (m_0 - 2t_0)^2)$$

Where, the moments of inertia with respect to the y -axis of Link 0 frame and the center of mass are given by the following:

$$\begin{aligned} \mathcal{Y}\mathcal{Y}_0 &= \mathcal{Y}\mathcal{Y}_{01} + \mathcal{Y}\mathcal{Y}_{02} - \mathcal{Y}\mathcal{Y}_{03} \\ \mathcal{Y}\mathcal{C}_0 &= \mathcal{Y}\mathcal{Y}_0 \end{aligned}$$

where (4.05)

$$\mathcal{Y}\mathcal{Y}_{01} = \rho \frac{m_0^4 l_0}{6}$$

$$\mathcal{Y}\mathcal{Y}_{02} = \rho \frac{w_0^4 l_0}{6}$$

$$\mathcal{Y}\mathcal{Y}_{03} = \rho \frac{m_0}{12} (m_0 - 2t_0)^2 (m_0^2 + (m_0 - 2t_0)^2)$$

Where, the moments of inertia with respect to the z-axis of Link 0 frame and the center of mass are given by the following:

$$\mathcal{Z}\mathcal{Z}_0 = \mathcal{Z}\mathcal{Z}_{01} + \mathcal{Z}\mathcal{Z}_{02} - \mathcal{Z}\mathcal{Z}_{03}$$

$$\mathcal{Z}\mathcal{C}_0 = \mathcal{Z}\mathcal{Z}_0 - l_{m0} r_0^2$$

where (4.06)

$$\mathcal{Z}\mathcal{Z}_{01} = \rho m_0^2 l_0 \left(\frac{1}{12} (m_0^2 + l_0^2) + \left(\frac{l_0 - 2k_0}{2} \right)^2 \right)$$

$$\mathcal{Z}\mathcal{Z}_{02} = \rho w_0^2 t_0 \left(\frac{1}{12} (w_0^2 + t_0^2) + \left(\frac{t_0 + 2k_0}{2} \right)^2 \right)$$

$$\mathcal{Z}\mathcal{Z}_{03} = \rho \frac{m_0}{6} (m_0 - 2t_0)^4$$

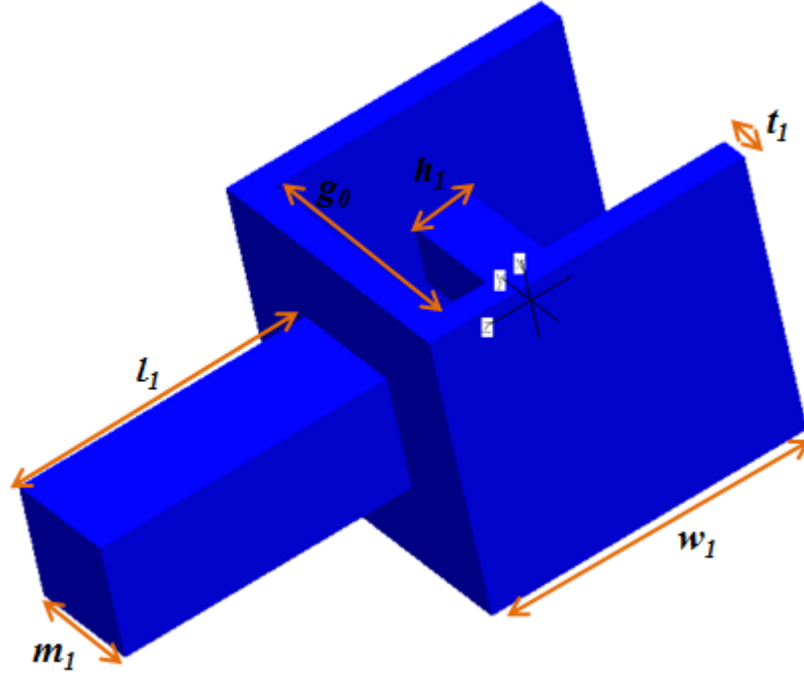


Figure 4.5: CAD Model of FA Link 1

The mass of Link 1 is defined by:

$$l_{m1} = \rho(m_1^2 l_1 + h_1^2 g_1 + 3w_1^2 t_1) \quad (4.07)$$

The position of the center of mass with respect to the Link 1 frame is given by:

$${}^1r_{c1} = \begin{bmatrix} 0 \\ 0 \\ r_1 \end{bmatrix}$$

where

$$r_1 = \frac{m_1^2 l_1 (w_1 + l_1 + 2t_1) + w_1^2 t_1 (w_1 + t_1)}{2m_1^2 l_1 + 2h_1^2 g_1 + 6w_1^2 t_1} \quad (4.08)$$

The inertia matrices of Link 1 with respect to the Link 1 frame and about the center of mass, expressed in the Link 1 frame are given by the following:

$${}^1I_1 = \begin{bmatrix} xx_1 & 0 & 0 \\ 0 & yy_1 & 0 \\ 0 & 0 & zz_1 \end{bmatrix} \quad \text{and} \quad {}^1I_{c1} = \begin{bmatrix} xc_1 & 0 & 0 \\ 0 & yc_1 & 0 \\ 0 & 0 & zc_1 \end{bmatrix} \quad (4.09)$$

Where, the moments of inertia with respect to the x -axis of Link 1 frame and the center of mass are given by the following:

$$xx_1 = xx_{11} + xx_{12} + 2xx_{13} + xx_{14}$$

$$xc_1 = xx_1 - l_m r_1^2$$

where

$$xx_{11} = \rho m_1^2 l_1 \left(\frac{1}{12} (m_1^2 + l_1^2) + \left(\frac{w_1 + l_1 + 2t_1}{2} \right)^2 \right) \quad (4.10)$$

$$xx_{12} = \rho w_1^2 t_1 \left(\frac{1}{12} (w_1^2 + t_1^2) + \left(\frac{w_1 + t_1}{2} \right)^2 \right)$$

$$xx_{13} = \rho w_1^2 t_1 \left(\frac{1}{12} (w_1^2 + t_1^2) + \left(\frac{g_1 + t_1}{2} \right)^2 \right)$$

$$xx_{14} = \rho \frac{h_1^2 g_1}{12} (h_1^2 + g_1^2)$$

The moments of inertia with respect to the y -axis of Link 1 frame and the center of mass are given by the following:

$$yy_1 = yy_{11} + yy_{12} + 2yy_{13} + yy_{14}$$

$$yc_1 = yy_1 - l_m r_1^2$$

where

$$yy_{11} = \rho m_1^2 l_1 \left(\frac{1}{12} (m_1^2 + l_1^2) + \left(\frac{w_1 + l_1 + 2t_1}{2} \right)^2 \right) \quad (4.11)$$

$$yy_{12} = \rho w_1^2 t_1 \left(\frac{1}{12} (w_1^2 + t_1^2) + \left(\frac{w_1 + t_1}{2} \right)^2 \right)$$

$$yy_{13} = \rho \frac{w_1^4 t_1}{6}$$

$$yy_{14} = \rho \frac{h_1^4 g_1}{6}$$

The moments of inertia with respect to the z -axis of Link 1 frame and the center of mass are given by the following:

$$zz_1 = zz_{11} + zz_{12} + 2zz_{13} + zz_{14}$$

$$zc_1 = zz_1$$

where

$$zz_{11} = \rho \frac{m_1^4 l_1}{6}$$

$$zz_{12} = \rho \frac{w_1^4 t_1}{6}$$

$$zz_{13} = \rho w_1^2 t_1 \left(\frac{1}{12} (w_1^2 + t_1^2) + \left(\frac{g_1 + t_1}{2} \right)^2 \right)$$

$$zz_{14} = \rho \frac{h_1^2 g_1}{12} (h_1^2 + g_1^2)$$
(4.12)

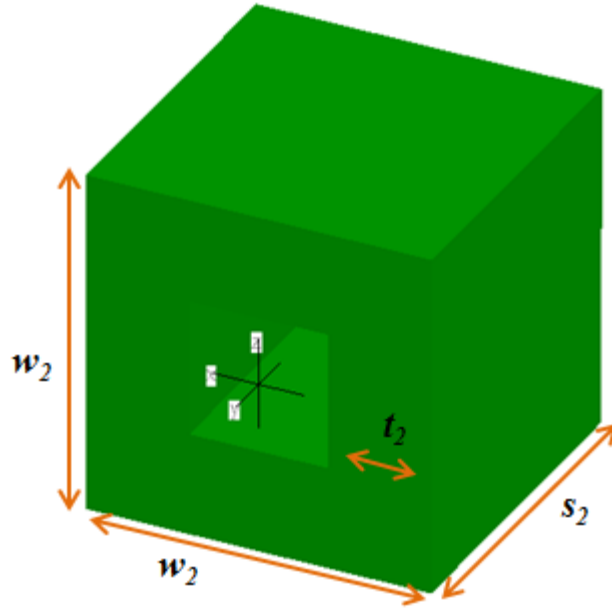


Figure 4.6: CAD Model of FA Link 2

The mass of Link 2 is defined by:

$$l_{m2} = \rho (w_2^2 s_2 - s_2 (w_2 - 2t_2)^2)$$
(4.13)

The position of the center of mass with respect to the Link 2 frame is given by:

$${}^2r_{c_2} = \begin{bmatrix} 0 \\ r_2 \\ 0 \end{bmatrix}$$

where

$$r_2 = \frac{s_2((w_2 - 2t_2)^2 - w_2^2)}{2(w_2^2 - (w_2 - 2t_2)^2)}$$

The inertia matrices of Link 2 with respect to the Link 2 frame and about the center of mass, expressed in the Link 2 frame are given by the following:

$${}^2I_2 = \begin{bmatrix} xx_2 & 0 & 0 \\ 0 & yy_2 & 0 \\ 0 & 0 & zz_2 \end{bmatrix} \quad \text{and} \quad {}^2I_{c_2} = \begin{bmatrix} xc_2 & 0 & 0 \\ 0 & yc_2 & 0 \\ 0 & 0 & zc_2 \end{bmatrix} \quad (4.15)$$

The moments of inertia with respect to the x - and z -axis of Link 2 frame and the center of mass are given by the following:

$$xx_2 = zz_2 = xx_{21} - xx_{22}$$

$$xc_2 = zc_2 = xx_2 - I_{m_2} r_2^2$$

where

$$xx_{21} = (\rho w_2^2 s_2) \left(\left(\frac{1}{12} \right) (w_2^2 + s_2^2) + \left(\frac{s_2}{2} \right)^2 \right) \quad (4.16)$$

$$xx_{22} = (\rho s_2 (w_2 - 2t_2)^2) \left(\left(\frac{1}{12} \right) (s_2^2 + (w_2 - 2t_2)^2) + \left(\frac{s_2}{2} \right)^2 \right)$$

The moments of inertia with respect to the y -axis of Link 2 frame and the center of mass are given by the following:

$$\begin{aligned} \mathcal{Y}_2 &= \mathcal{Y}_{21} - \mathcal{Y}_{22} \\ \mathcal{Y}_{c_2} &= \mathcal{Y}_2 \end{aligned}$$

where (4.17)

$$\begin{aligned} \mathcal{Y}_{21} &= \rho \frac{w_2^4 s_2}{6} \\ \mathcal{Y}_{22} &= \rho \frac{s_2}{6} (w_2 - 2t_2)^4 \end{aligned}$$

4.2.2 Friction Anchor Link Inertia and Jacobian Matrices

First, we identify the kinematic link parameters and develop the transformation matrices. Based on the assignment of the link coordinates systems, the D-H parameters are defined and presented in Table 4.1.

i	α_i	a_i	d_i	θ_i
1	$\pi/2$	0	d_1	$\pi/2$
2	$\pi/2$	0	d_2	$\pi/2$

Table 4.1: D-H Link Parameters for FA Module

Using this table, the D-H transformations matrices are developed and given by the following:

$${}^0A_1 = \begin{bmatrix} 0 & 0 & 1 & 0 \\ 1 & 0 & 0 & 0 \\ 0 & 1 & 0 & d_1 \\ 0 & 0 & 0 & 1 \end{bmatrix} \quad {}^1A_2 = \begin{bmatrix} 0 & 0 & 1 & 0 \\ 1 & 0 & 0 & 0 \\ 0 & 1 & 0 & d_2 \\ 0 & 0 & 0 & 1 \end{bmatrix} \quad (4.18)$$

Also using the D-H convention, the following rotations are found:

$${}^0R_1 = \begin{bmatrix} 0 & 0 & 1 \\ 1 & 0 & 0 \\ 0 & 1 & 0 \end{bmatrix} \quad {}^0R_2 = \begin{bmatrix} 0 & 1 & 0 \\ 0 & 0 & 1 \\ 1 & 0 & 0 \end{bmatrix} \quad (4.19)$$

Utilizing the following expression,

$$I_i = {}^0R_i {}^iI_{c_i} ({}^0R_i)^T \quad (4.20)$$

where

$$i = 1 \text{ to } 2$$

the inertia matrices for Links 1 and 2 about their respective centers of mass and expressed in the base frame are obtained and given as:

$$I_1 = \begin{bmatrix} zc_1 & 0 & 0 \\ 0 & xc_1 & 0 \\ 0 & 0 & yc_1 \end{bmatrix} \quad I_2 = \begin{bmatrix} yc_2 & 0 & 0 \\ 0 & zc_2 & 0 \\ 0 & 0 & xc_2 \end{bmatrix} \quad (4.21)$$

Next, we define the position vectors of the centers of mass of FA Links 1 and 2 with respect to the various link frames of the FA mechanism and expressed in the base frame. These vectors are defined using the following expression:

$${}^{j-1}p_{c_i}^* = p_{c_i} - p_{j-1} \quad (4.22)$$

Where, p_{c_i} is the position vector of the center of mass of the i^{th} link frame with respect to the base link frame and p_{j-1} is the position vector of the origin of the $j-1$ link frame with respect to the base link frame. Therefore, the position vectors of the centers of mass for the various link frames are given as follows:

$${}^0p_{c1}^* = \begin{bmatrix} r_1 \\ 0 \\ d_1 \end{bmatrix} \quad {}^1p_{c2}^* = \begin{bmatrix} d_2 + r_2 \\ 0 \\ 0 \end{bmatrix} \quad {}^0p_{c2}^* = \begin{bmatrix} d_2 + r_2 \\ 0 \\ d_1 \end{bmatrix} \quad (4.23)$$

Finally, we compute the Jacobian submatrices for link linear and angular velocity, represented by variables J_{vi} and $J_{\omega i}$, respectively. The procedure for developing these matrices is based on the rotational matrices and the above position vectors of the various link centers of mass. The procedure is described in detail in [58] and yields the following matrices for the FA module:

$$J_{v1} = \begin{bmatrix} 0 & 0 \\ 0 & 0 \\ 1 & 0 \end{bmatrix} \quad J_{v2} = \begin{bmatrix} 0 & 1 \\ 0 & 0 \\ 1 & 0 \end{bmatrix} \quad J_{\omega1} = J_{\omega2} = \begin{bmatrix} 0 & 0 \\ 0 & 0 \\ 0 & 0 \end{bmatrix} \quad (4.24)$$

4.2.3 Friction Anchor Lagrangian Equations of Motion

In order to define the equations of motion for the FA module, we utilize the following dynamical equation [58], where M is the mechanism inertia matrix, V is the velocity coupling vector and G is the vector of gravitational forces:

$$Q_i = \sum_{j=1}^n M_{ij} \ddot{q}_j + V_i + G_i \quad (4.25)$$

for $i = 1, 2, \dots, n$

The mechanism inertia matrix for the FA module is obtained by using Equation 4.26 from [58] which yields expression in Equation 4.27.

$$M = \sum_{i=1}^n (J_{vi}^T m_i J_{vi} + J_{\omega i}^T I_i J_{\omega i}) \quad (4.26)$$

$$\begin{aligned} M_{FA} &= J_{v1}^T l_{m1} J_{v1} + J_{\omega1}^T I_1 J_{\omega1} + J_{v2}^T l_{m2} J_{v2} + J_{\omega2}^T I_2 J_{\omega2} \\ &= \begin{bmatrix} l_{m1} + l_{m2} & 0 \\ 0 & l_{m2} \end{bmatrix} \end{aligned} \quad (4.27)$$

The velocity coupling vector for the FA module is found by taking the partial derivatives of the FA inertia matrix with respect to the joints in accordance to Equation 4.28 [58].

$$V_i = \sum_{j=1}^n \sum_{k=1}^n \left(\frac{\partial M_{ij}}{\partial q_k} - \frac{1}{2} \frac{\partial M_{jk}}{\partial q_i} \right) \dot{q}_j \dot{q}_k \quad (4.28)$$

The coupling vector terms are computed as the following:

$$V_1 = V_2 = 0 \quad (4.29)$$

The gravitational terms are obtained by using the following expression from [58]:

$$G_i = -\sum_{j=1}^n m_j g^T J_{vj}^i \quad (4.30)$$

Note for the FA module, the gravity vector is defined as:

$$g = \begin{bmatrix} 0 \\ 0 \\ -g_c \end{bmatrix} \quad (4.31)$$

Utilizing the above expressions yields the following gravitation terms for the FA:

$$G_1 = G_2 = 0 \quad (4.32)$$

We assume no external forces and substitute the FA module inertia matrix, velocity coupling vector, and gravitation terms into Equation 4.25, which results in the following two Lagrange equations of motion:

$$f_1 = (l_{m1} + l_{m2})\ddot{d}_1 \quad (4.33)$$

$$f_2 = l_{m2}\ddot{d}_2 \quad (4.34)$$

The equations of motion are validated against the forces computed by the Mechanism Analysis suite of Pro/Engineer Wildfire 4.0. The results are presented in Figure 4.7.

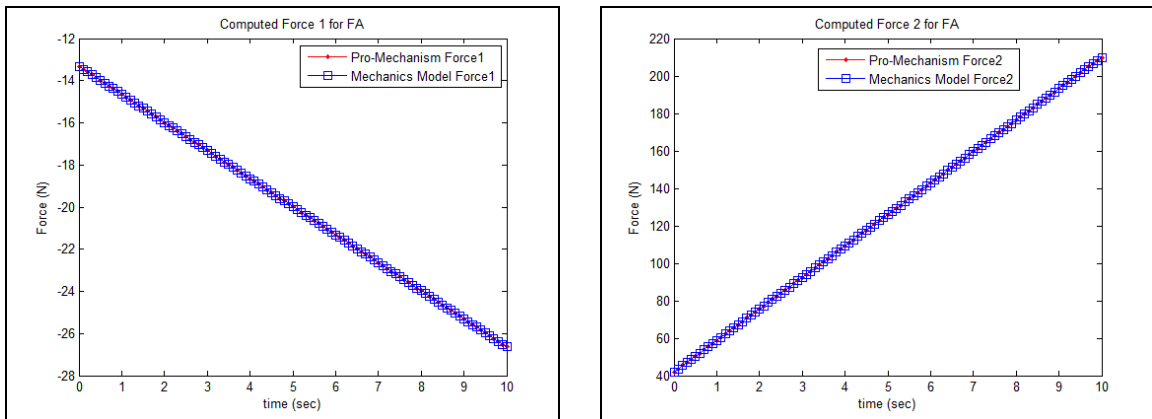


Figure 4.7: Validation Results of FA Dynamics Equations

By inspection of the FA model, the preceding solution for the equations of motion may seem obvious. However, the procedure was necessary to define the inertia matrix, velocity coupling vector and vector of gravitational forces for the FA for the general robot dynamics model. The validation curves in Figure 4.7 also confirm that the equations which define the link characteristics are correct.

4.3 Joint Mechanism Module Dynamics Model

Although the actual joint module, illustrated in Figure 4.8, has three degrees of freedom and four points of articulation, the gaits presented in this work only make use of yawing and extension movements. Due to the planar nature of the gait concept, the Joint Mechanism (JM) is modeled with only one pivot joint, θ_3 , and one extension joint, d_4 , as shown in Figure 4.9. Note that the base link of the mechanism is defined as Link 2 to support the continuity of D-H parameters when assembled to the friction anchor module. The variables r_3 and r_4 are the z -distance for Link 3 and y -distance for Link 4, respectively, from the individual link frames to the centers of mass.

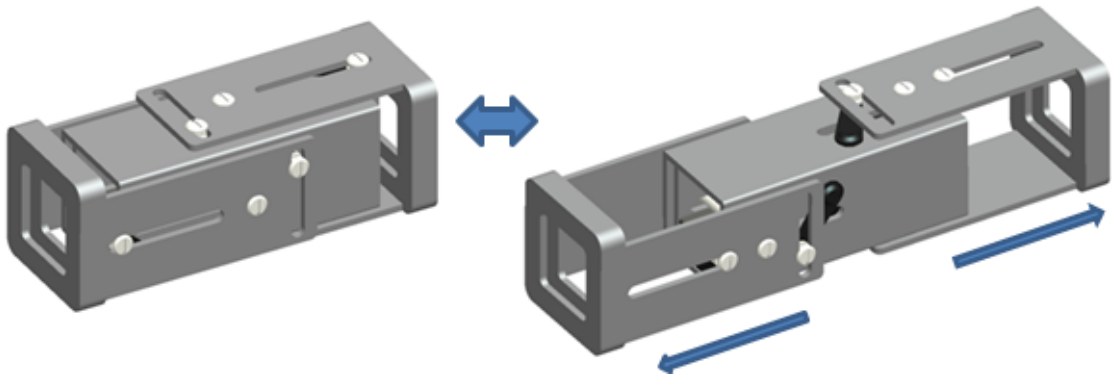


Figure 4.8: CAD Model of Actual Joint Mechanism Module

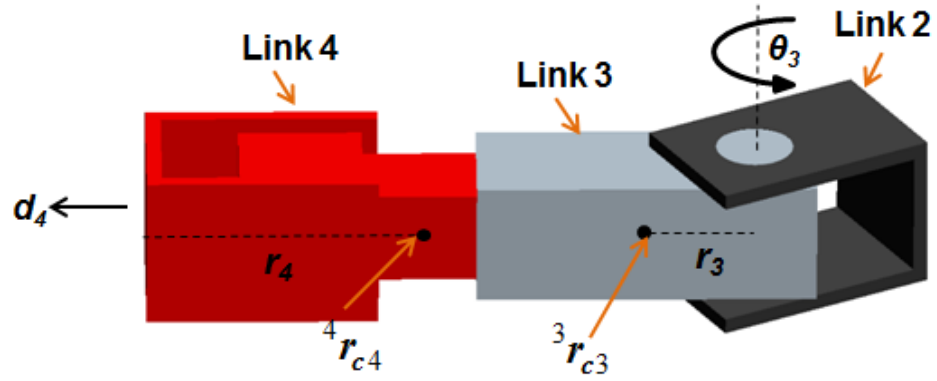


Figure 4.9: Dynamics Model Representation of a Joint Mechanism Module

4.3.1 Joint Mechanism Module Link Characteristics

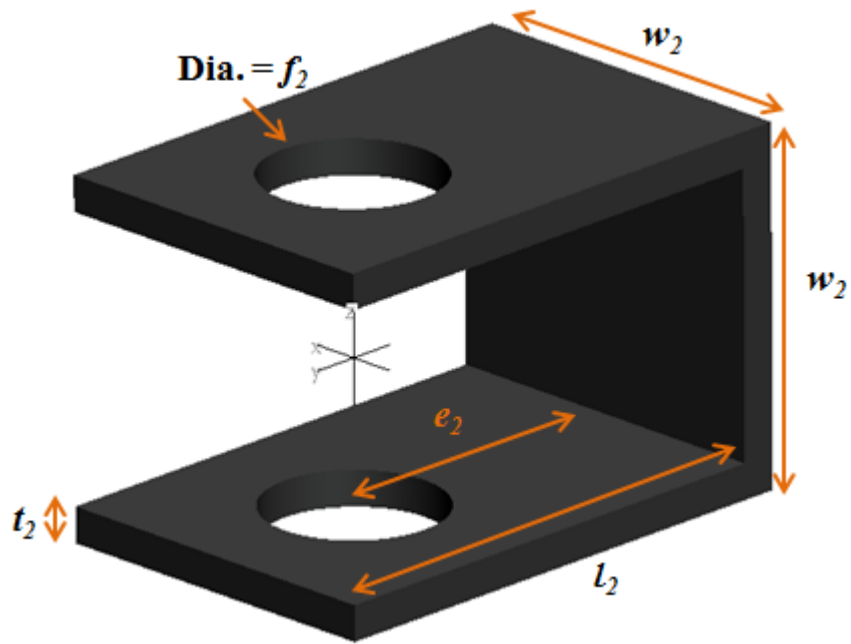


Figure 4.10: CAD Model of JM Link 2 (Base Link)

The mass of Link 2 is defined by Equation 4.35, where ρ is density for the JM:

$$l_{m2} = \rho \left(w_2^2 t_2 + 2w_2 l_2 t_2 - \pi \frac{f_2^2 t_2}{2} \right) \quad (4.35)$$

The position of the center of mass with respect to the Link 2 frame is given by:

$${}^2r_{c2} = \begin{bmatrix} 0 \\ r_2 \\ 0 \end{bmatrix}$$

where

$$r_2 = \frac{w_2^2(t_2 - 2e_2) + 2w_2l_2(l_2 + 2t_2 - 2e_2)}{2w_2(w_2 + 2l_2) - f_2^2\pi}$$

The inertia matrices of Link 2 with respect to the Link 2 frame and about the center of mass, expressed in the Link 2 frame are given by the following:

$${}^2I_2 = \begin{bmatrix} xx_2 & 0 & 0 \\ 0 & yy_2 & 0 \\ 0 & 0 & zz_2 \end{bmatrix} \quad \text{and} \quad {}^2I_{c2} = \begin{bmatrix} x_{c2} & 0 & 0 \\ 0 & y_{c2} & 0 \\ 0 & 0 & z_{c2} \end{bmatrix} \quad (4.37)$$

Where, the moments of inertia with respect to the x -axis of Link 2 frame and the center of mass are given by the following:

$$xx_2 = xx_{21} + 2xx_{22} - 2xx_{23}$$

$$x_{c2} = xx_2 - l_{m2}r_2^2$$

where

$$xx_{21} = \rho w_2^2 t_2 \left(\frac{1}{12} (w_2^2 + t_2^2) + \left(\frac{t_2}{2} - e_2 \right)^2 \right)$$

$$xx_{22} = \rho w_2 l_2 t_2 \left(\frac{1}{12} (l_2^2 + t_2^2) + \left(\frac{w_2 - t_2}{2} \right)^2 + \left(t_2 - e_2 + \frac{l_2}{2} \right)^2 \right)$$

$$xx_{23} = \rho \pi \frac{f_2^2 t_2}{4} \left(\frac{1}{12} \left(\frac{3f_2^2}{4} + t_2^2 \right) + \left(\frac{w_2}{2} - \frac{t_2}{2} \right)^2 \right)$$

The moments of inertia with respect to the y -axis of Link 2 frame and the center of mass are given by the following:

$$yy_2 = yy_{21} + 2yy_{22} - 2yy_{23}$$

$$y_{c2} = yy_2$$

where

$$yy_{21} = \rho \frac{w_2^4 t_2}{6} \tag{4.39}$$

$$yy_{22} = \rho w_2 l_2 t_2 \left(\frac{1}{12} (w_2^2 + t_2^2) + \left(\frac{w_2 - t_2}{2} \right)^2 \right)$$

$$yy_{23} = \rho \pi \frac{f_2^2 t_2}{4} \left(\frac{1}{12} \left(\frac{3f_2^2}{4} + t_2^2 \right) + \left(\frac{w_2 - t_2}{2} \right)^2 \right)$$

The moments of inertia with respect to the z -axis of Link 2 frame and the center of mass are given by the following:

$$zz_2 = zz_{21} + 2zz_{22} - 2zz_{23}$$

$$z_{c2} = zz_2 - l_{m2} r_2^2$$

where

$$zz_{21} = \rho w_2^2 t_2 \left(\frac{1}{12} (w_2^2 + t_2^2) + \left(\frac{t_2}{2} - e_2 \right)^2 \right) \tag{4.40}$$

$$zz_{22} = \rho w_2 l_2 t_2 \left(\frac{1}{12} (w_2^2 + l_2^2) + \left(t_2 - e_2 + \frac{l_2}{2} \right)^2 \right)$$

$$zz_{23} = \rho \pi \frac{f_2^4 t_2}{32}$$

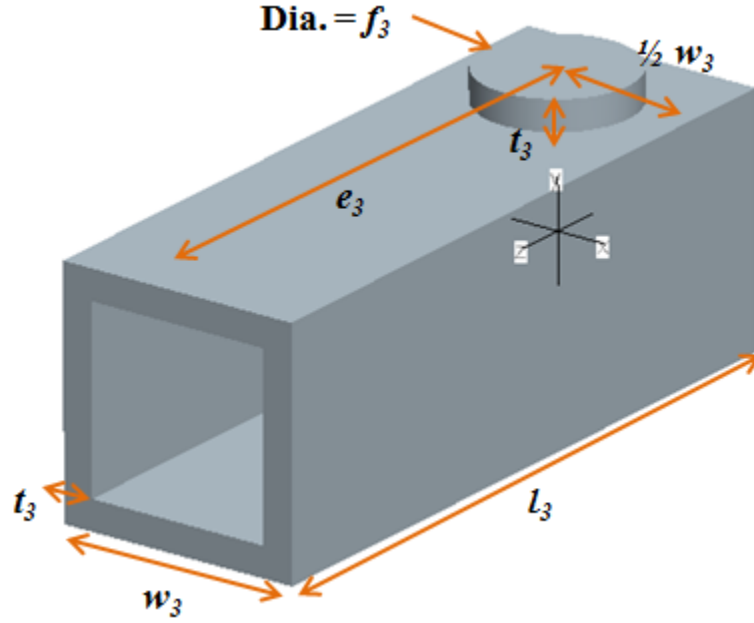


Figure 4.11: CAD Model of JM Link 3 (2nd Link)

The mass of Link 3 is defined by:

$$l_{m3} = \rho \left(w_3^2 l_3 - l_3 (w_3 - 2t_3)^2 + \pi \frac{f_3^2 t_3}{2} \right) \quad (4.41)$$

The position of the center of mass with respect to the Link 3 frame is given by:

$${}^3r_{c3} = \begin{bmatrix} 0 \\ 0 \\ r_3 \end{bmatrix} \quad (4.42)$$

where

$$r_3 = \frac{(2e_3 - l_3) l_3 (w_3^2 - (w_3 - 2t_3)^2)}{2w_3^2 l_3 - 2(w_3 - 2t_3)^2 l_3 + f_3^2 t_3 \pi}$$

The inertia matrices of Link 3 with respect to the Link 3 frame and about the center of mass, expressed in the Link 3 frame are given by the following:

$${}^3I_3 = \begin{bmatrix} xx_3 & 0 & 0 \\ 0 & yy_3 & 0 \\ 0 & 0 & zz_3 \end{bmatrix} \quad \text{and} \quad {}^3I_{c3} = \begin{bmatrix} x_{c3} & 0 & 0 \\ 0 & y_{c3} & 0 \\ 0 & 0 & z_{c3} \end{bmatrix} \quad (4.43)$$

Where, the moments of inertia with respect to the x -axis of Link 3 frame and the center of mass are given by the following:

$$xx_3 = xx_{31} - xx_{32} + 2xx_{33}$$

$$x_{c3} = xx_3 - l_{m3}r_3^2$$

where

$$xx_{31} = \rho w_3^2 l_3 \left(\frac{1}{12} (w_3^2 + l_3^2) + \left(e_3 - \frac{l_3}{2} \right)^2 \right) \quad (4.44)$$

$$xx_{32} = \left(\rho (w_3 - 2t_3)^2 l_3 \right) \left(\frac{1}{12} ((w_3 - 2t_3)^2 + l_3^2) + \left(e_3 - \frac{l_3}{2} \right)^2 \right)$$

$$xx_{33} = \rho \pi \frac{f_3^2 t_3}{4} \left(\frac{1}{12} \left(\frac{3f_3^2}{4} + t_3^2 \right) + \left(\frac{w_3 + t_3}{2} \right)^2 \right)$$

The moments of inertia with respect to the y -axis of Link 3 frame and the center of mass are given by the following:

$$yy_3 = yy_{31} - yy_{32} + 2yy_{33}$$

$$y_{c3} = yy_3 - l_{m3}r_3^2$$

where

$$yy_{31} = \left(\rho w_3^2 l_3 \right) \left(\frac{1}{12} (w_3^2 + l_3^2) + \left(e_3 - \frac{l_3}{2} \right)^2 \right) \quad (4.45)$$

$$yy_{32} = \left(\rho l_3 (w_3 - 2t_3)^2 \right) \left(\frac{1}{12} ((w_3 - 2t_3)^2 + l_3^2) + \left(e_3 - \frac{l_3}{2} \right)^2 \right)$$

$$yy_{33} = \rho \pi \frac{f_3^4 t_3}{32}$$

The moments of inertia with respect to the z -axis of Link 3 frame and the center of mass are given by the following:

$$zz_3 = zz_{31} - zz_{32} + 2zz_{33}$$

$$z_{c3} = zz_3$$

where

$$zz_{31} = \rho \frac{w_3^4 l_3}{6} \quad (4.46)$$

$$zz_{32} = \rho \frac{l_3 (w_3 - 2t_3)^4}{6}$$

$$zz_{33} = \rho \pi \frac{f_3^2 t_3}{4} \left(\frac{1}{12} \left(\frac{3f_3^2}{4} + t_3^2 \right) + \left(\frac{w_3 + t_3}{2} \right)^2 \right)$$

The mass of the Link 4 is defined by:

$$l_{m4} = \rho (m_4^2 t_4 + 2m_4 k_4 t_4 + n_4^3 + w_4^2 l_4 - (w_4 - 2t_4)^2 (l_4 + n_4)) \quad (4.47)$$

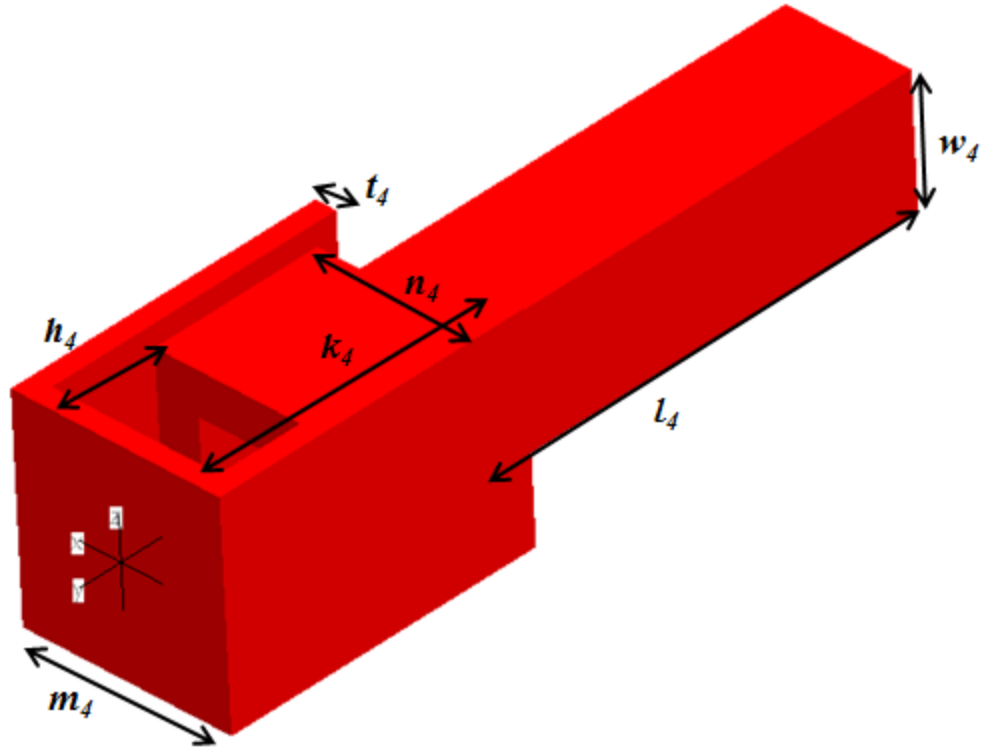


Figure 4.12: CAD Model of JM Link 4 (3rd Link)

The position of the center of mass with respect to the Link 4 frame is given by:

$${}^4r_{c4} = \begin{bmatrix} 0 \\ r_4 \\ 0 \end{bmatrix}$$

where (4.48)

$$r_4 = \frac{\left(\begin{array}{l} (w_4 - 2t_4)^2(l_4 + n_4)(2h_4 + l_4 + n_4) - 2m_4k_4t_4(2t_4 + k_4) \\ -n_4^3(2h_4 + n_4) - w_4^2l_4(2h_4 + 2n_4 + l_4) - m_4^2t_4 \end{array} \right)}{2(m_4^2t_4 + 2m_4k_4t_4 + n_4^3 + w_4^2l_4 - (w_4 - 2t_4)^2(l_4 + n_4))}$$

The inertia matrices of Link 4 with respect to the Link 4 frame and about the center of mass, expressed in the Link 4 frame are given by the following:

$${}^4I_4 = \begin{bmatrix} xx_4 & 0 & 0 \\ 0 & yy_4 & 0 \\ 0 & 0 & zz_4 \end{bmatrix} \quad \text{and} \quad {}^4I_{c4} = \begin{bmatrix} x_{c4} & 0 & 0 \\ 0 & y_{c4} & 0 \\ 0 & 0 & z_{c4} \end{bmatrix} \quad (4.49)$$

Where, the moments of inertia with respect to the x -axis of Link 4 frame and the center of mass are given by the following:

$$\begin{aligned} xx_4 &= xx_{41} + 2xx_{42} + xx_{43} + xx_{44} - xx_{45} \\ x_{c4} &= xx_4 - l_{m4}r_4^2 \end{aligned}$$

where

$$\begin{aligned} xx_{41} &= \rho m_4^2 t_4 \left(\frac{1}{12} (m_4^2 + t_4^2) + \left(\frac{t_4}{2} \right)^2 \right) \\ xx_{42} &= \rho m_4 k_4 t_4 \left(\frac{1}{12} (k_4^2 + m_4^2) + \left(t_4 + \frac{k_4}{2} \right)^2 \right) \\ xx_{43} &= \rho n_4^3 \left(\frac{n_4^2}{6} + \left(h_4 + \frac{n_4}{2} \right)^2 \right) \\ xx_{44} &= \rho w_4^2 l_4 \left(\frac{1}{12} (w_4^2 + l_4^2) + \left(h_4 + n_4 + \frac{l_4}{2} \right)^2 \right) \\ xx_{45} &= \rho (w_4 - 2t_4)^2 (l_4 + n_4) \left(\frac{1}{12} ((w_4 - 2t_4)^2 + (l_4 + n_4)^2) + \left(h_4 + \frac{l_4 + n_4}{2} \right)^2 \right) \end{aligned} \quad (4.50)$$

The moments of inertia with respect to the y -axis and z -axis of Link 4 frame and the center of mass are given by the following:

$$\begin{aligned} yy_4 &= yy_{41} + 2yy_{42} + yy_{43} + yy_{44} - yy_{45} \\ y_{c4} &= yy_4 - l_{m4}r_4^2 \end{aligned}$$

where

$$\begin{aligned} yy_{41} &= \rho \frac{m_4^4 t_4}{6} \\ yy_{42} &= \rho m_4 k_4 t_4 \left(\frac{1}{12} (m_4^2 + t_4^2) + \left(\frac{m_4 - t_4}{2} \right)^2 \right) \\ yy_{43} &= \rho \frac{n_4^5}{6} \\ yy_{44} &= \rho \frac{w_4^4 l_4}{6} \\ yy_{45} &= \rho \frac{(w_4 - 2t_4)^4 (l_4 + n_4)}{6} \end{aligned} \tag{4.51}$$

$$\begin{aligned} zz_4 &= zz_{41} + 2zz_{42} + zz_{43} + zz_{44} - zz_{45} \\ z_{c4} &= zz_4 - l_{m4}r_4^2 \end{aligned}$$

where

$$\begin{aligned} zz_{41} &= \rho m_4^2 t_4 \left(\frac{1}{12} (m_4^2 + t_4^2) + \left(\frac{t_4}{2} \right)^2 \right) \\ zz_{42} &= \rho m_4 k_4 t_4 \left(\frac{1}{12} (k_4^2 + t_4^2) + \left(t_4 + \frac{k_4}{2} \right)^2 + \left(\frac{m_4 - t_4}{2} \right)^2 \right) \\ zz_{43} &= \rho n_4^3 \left(\frac{n_4^2}{6} + \left(h_4 + \frac{n_4}{2} \right)^2 \right) \\ zz_{44} &= \rho w_4^2 l_4 \left(\frac{1}{12} (w_4^2 + l_4^2) + \left(h_4 + n_4 + \frac{l_4}{2} \right)^2 \right) \\ zz_{45} &= \rho (w_4 - 2t_4)^2 (l_4 + n_4) \left(\frac{1}{12} ((w_4 - 2t_4)^2 + (l_4 + n_4)^2) + \left(h_4 + \frac{l_4 + n_4}{2} \right)^2 \right) \end{aligned} \tag{4.52}$$

4.3.2 Joint Mechanism Module Link Inertia and Jacobian Matrices

Similar to the FA module, we identify the kinematic link parameters and develop the transformation matrices. The D-H parameters are defined and presented in Table 4.2.

i	α_i	a_i	d_i	θ_i
3	$\pi/2$	0	0	θ_3
4	$\pi/2$	0	d_4	π

Table 4.2: D-H Link Parameters for JM Module

Using this table, the D-H transformations matrices are developed and given by the following:

$${}^2A_3 = \begin{bmatrix} c_3 & 0 & s_3 & 0 \\ s_3 & 0 & -c_3 & 0 \\ 0 & 1 & 0 & 0 \\ 0 & 0 & 0 & 1 \end{bmatrix} \quad {}^3A_4 = \begin{bmatrix} -1 & 0 & 0 & 0 \\ 0 & 0 & 1 & 0 \\ 0 & 1 & 0 & d_4 \\ 0 & 0 & 0 & 1 \end{bmatrix} \quad (4.53)$$

Also using the D-H convention, the following rotations are found. Note, $s_3 = \sin\theta_3$.

$${}^2R_3 = \begin{bmatrix} c_3 & 0 & s_3 \\ s_3 & 0 & -c_3 \\ 0 & 1 & 0 \end{bmatrix} \quad {}^2R_4 = \begin{bmatrix} -c_3 & s_3 & 0 \\ -s_3 & -c_3 & 0 \\ 0 & 0 & 1 \end{bmatrix} \quad (4.54)$$

Utilizing the following expression,

$$I_i = {}^2R_i {}^iI_{ci} ({}^2R_i)^T \quad (4.55)$$

where

$i = 3 \text{ to } 4$

the inertia matrices for Links 3 and 4 about their respective centers of mass and expressed in the base frame are obtained and given as:

$$I_3 = \begin{bmatrix} x_{c3}c_3^2 + z_{c3}s_3^2 & (x_{c3} - z_{c3})c_3s_3 & 0 \\ (x_{c3} - z_{c3})c_3s_3 & x_{c3}s_3^2 + z_{c3}c_3^2 & 0 \\ 0 & 0 & y_{c3} \end{bmatrix} \quad (4.56)$$

$$I_4 = \begin{bmatrix} x_{c4}c_3^2 + y_{c4}s_3^2 & (x_{c4} - y_{c4})c_3s_3 & 0 \\ (x_{c4} - y_{c4})c_3s_3 & x_{c4}s_3^2 + y_{c4}c_3^2 & 0 \\ 0 & 0 & z_{c4} \end{bmatrix} \quad (4.57)$$

Next, we define the position vectors of the centers of mass of JM Links 3 and 4 with respect to the various link frames of the JM mechanism and expressed in the base frame using Equation 4.22. The position vectors of the centers of mass for the various link frames are given as follows:

$${}^2p_{c3}^* = \begin{bmatrix} r_3s_3 \\ -r_3c_3 \\ 0 \end{bmatrix} \quad {}^3p_{c4}^* = \begin{bmatrix} (d_4 + r_4)s_3 \\ -(d_4 + r_4)c_3 \\ 0 \end{bmatrix} \quad {}^2p_{c4}^* = \begin{bmatrix} (d_4 + r_4)s_3 \\ -(d_4 + r_4)c_3 \\ 0 \end{bmatrix} \quad (4.58)$$

Finally, we compute the Jacobian submatrices for link linear and angular velocity for the JM as the following matrices:

$$J_{v3} = \begin{bmatrix} r_3c_3 & 0 \\ r_3s_3 & 0 \\ 0 & 0 \end{bmatrix} \quad J_{v4} = \begin{bmatrix} (d_4 + r_4)c_3 & s_3 \\ (d_4 + r_4)s_3 & -c_3 \\ 0 & 0 \end{bmatrix} \quad J_{\omega3} = J_{\omega4} = \begin{bmatrix} 0 & 0 \\ 0 & 0 \\ 1 & 0 \end{bmatrix} \quad (4.59)$$

4.3.3 Joint Mechanism Module Lagrangian Equations of Motion

In order to define the equations of motion for the JM module, we again utilize Equation 4.25, which yields the following:

$$\begin{aligned} M_{JM} &= J_{v3}^T l_{m3} J_{v3} + J_{\omega3}^T I_3 J_{\omega3} + J_{v4}^T l_{m4} J_{v4} + J_{\omega4}^T I_4 J_{\omega4} \\ &= \begin{bmatrix} m_{11} & 0 \\ 0 & m_{22} \end{bmatrix} \end{aligned} \quad (4.60)$$

where

$$\begin{aligned} m_{11} &= l_{m3}r_3^2 + l_{m4}(d_4 + r_4)^2 + y_{c3} + z_{c4} \\ m_{22} &= l_{m4} \end{aligned}$$

The velocity coupling vector for the JM module is found by taking the partial derivatives of the JM inertia matrix with respect to the joint variables in accordance to Equation 4.28.

The coupling vector terms are given as the following:

$$\begin{aligned} V_3 &= 2l_{m4}(d_4 + r_4)\dot{\theta}_3\dot{d}_4 \\ V_4 &= -l_{m4}(d_4 + r_4)\dot{\theta}_3^2 \end{aligned} \quad (4.61)$$

The gravitational terms are obtained by using Equation 4.30 and 4.31, which yield:

$$G_3 = G_4 = 0 \quad (4.62)$$

We assume no external forces and substitute the JM module inertia matrix, velocity coupling vector, and gravitation terms into Equation 4.25, which results in the following two Lagrange equations of motion:

$$\tau_3 = (l_{m3}r_3^2 + l_{m4}(d_4 + r_4)^2 + y_{c3} + z_{c4})\ddot{\theta}_3 + 2l_{m4}(d_4 + r_4)\dot{\theta}_3\dot{d}_4 \quad (4.63)$$

$$f_4 = l_{m4}\ddot{d}_4 - l_{m4}(d_4 + r_4)\dot{\theta}_3^2 \quad (4.64)$$

The equations of motion are validated against the forces computed by the Mechanism Analysis suite of Pro/Engineer Wildfire 4.0. The results are presented in Figure 4.13. The validation curves in Figure 4.13 confirm that the equations of motions and the equations which define the link characteristics are correct.

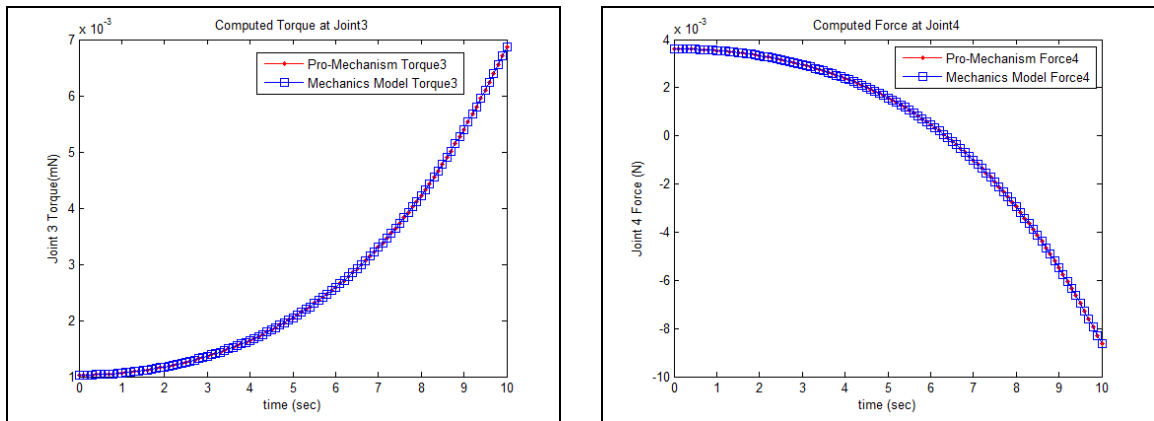


Figure 4.13: Validation Results of JM Dynamics Equations

4.4 1-Module Gait Dynamics Model

The next step in defining the general gait dynamics model is to build a 1-module gait model, which is used to analyze the simplest form of the robot design, a 1-module robot as illustrated in Figure 4.14. The 1-module gait model is defined by combining the FA and JM module models in a single model. The combined physical model is illustrated in Figure 4.15. Note that a small “block” has been added to the end of the joint mechanism model to simulate the mass of the inactive friction anchor in the robot.

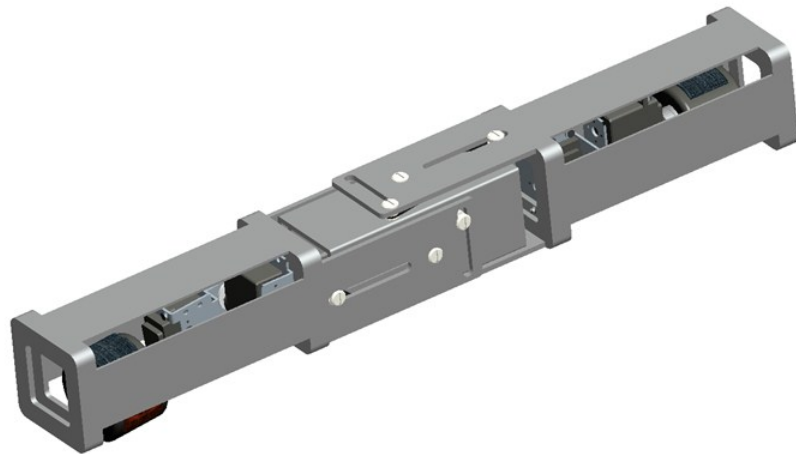


Figure 4.14: CAD Model of a 1-Module Robot

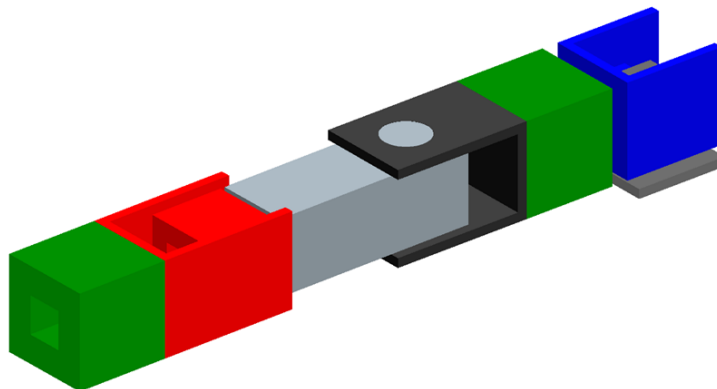


Figure 4.15: Dynamics Model Representation of a 1-Module Robot

4.4.1 1-Module Dynamics Model Link Characteristics

Observing the model in Figure 4.15, we determine the need to define a new Link 2, since the model combines Link 2 from the FA model and Link 2 from the JM model. Also, we must define a new Link 4 to account for the inactive friction anchor mass attached to the end of the JM.

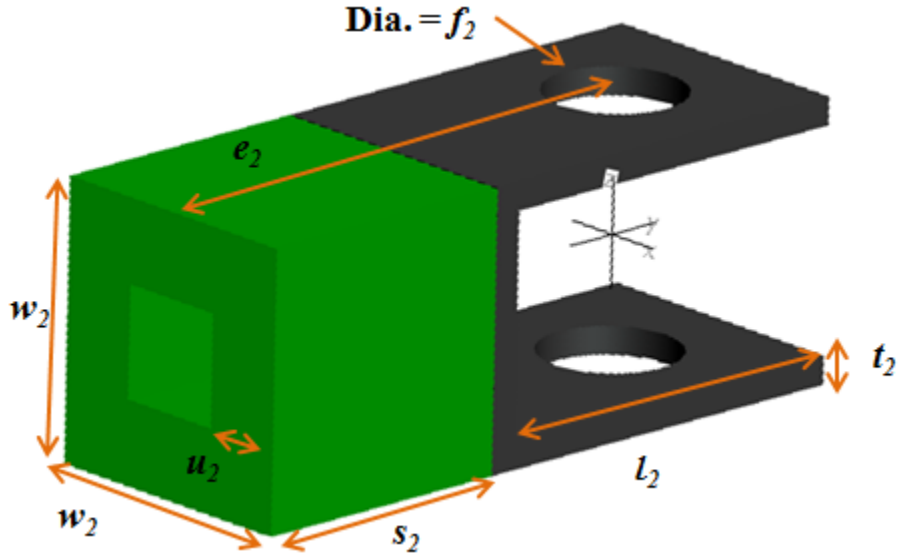


Figure 4.16: CAD Model of 1-Module Model Link 2

The mass of the new Link 2 is defined by Equation 4.65, where ρ is density:

$$l_{m2} = \rho \left(w_2^2 t_2 + 2w_2 l_2 t_2 - \pi \frac{f_2^2 t_2}{2} + w_2^2 s_2 - s_2 (w_2 - 2u_2)^2 \right) \quad (4.65)$$

The position of the center of mass with respect to the Link 2 frame is given by:

$${}^2r_{c2} = \begin{bmatrix} 0 \\ r_2 \\ 0 \end{bmatrix}$$

where

$$r_2 = \frac{w_2^2 \left((w_2 - 2u_2)^2 - w_2^2 + (t_2 - 2e_2) \right) + 2w_2 l_2 (l_2 + 2t_2 - 2e_2)}{2 \left(w_2^2 s_2 - s_2 (w_2 - 2u_2)^2 + w_2 t_2 (w_2 + 2l_2) \right) - f_2^2 t_2 \pi} \quad (4.66)$$

The inertia matrices of Link 2 with respect to the Link 2 frame and about the center of mass, expressed in the Link 2 frame are given by the following:

$${}^2I_2 = \begin{bmatrix} xx_2 & 0 & 0 \\ 0 & yy_2 & 0 \\ 0 & 0 & zz_2 \end{bmatrix} \quad \text{and} \quad {}^2I_{c_2} = \begin{bmatrix} x_{c_2} & 0 & 0 \\ 0 & y_{c_2} & 0 \\ 0 & 0 & z_{c_2} \end{bmatrix} \quad (4.67)$$

The moments of inertia with respect to the x -axis of Link 2 frame and the center of mass are given by the following:

$$xx_2 = xx_{21} + 2xx_{22} - 2xx_{23} + xx_{24} - xx_{25}$$

$$x_{c_2} = xx_2 - l_{m2}r_2^2$$

where

$$xx_{21} = \rho w_2^2 t_2 \left(\frac{1}{12} (w_2^2 + t_2^2) + \left(\frac{t_2}{2} - e_2 \right)^2 \right)$$

$$xx_{22} = \rho w_2 l_2 t_2 \left(\frac{1}{12} (l_2^2 + t_2^2) + \left(\frac{w_2 - t_2}{2} \right)^2 + \left(t_2 - e_2 + \frac{l_2}{2} \right)^2 \right) \quad (4.68)$$

$$xx_{23} = \rho \pi \frac{f_2^2 t_2}{4} \left(\frac{1}{12} \left(\frac{3f_2^2}{4} + t_2^2 \right) + \left(\frac{w_2}{2} - \frac{t_2}{2} \right)^2 \right)$$

$$xx_{24} = \rho w_2^2 s_2 \left(\frac{1}{12} (w_2^2 + s_2^2) + \left(\frac{s_2}{2} + e_2 \right)^2 \right)$$

$$xx_{25} = \rho s_2 (w_2 - 2t_2)^2 \left(\frac{1}{12} (s_2^2 + (w_2 - 2t_2)^2) + \left(\frac{s_2}{2} + e_2 \right)^2 \right)$$

The moments of inertia with respect to the y -axis of Link 2 frame and the center of mass are given by the following:

$$yy_2 = yy_{21} + 2yy_{22} - 2yy_{23} + yy_{24} - yy_{25}$$

$$y_{c2} = yy_2$$

where

$$yy_{21} = \rho \frac{w_2^4 t_2}{6}$$

$$yy_{22} = \rho w_2 l_2 t_2 \left(\frac{1}{12} (w_2^2 + t_2^2) + \left(\frac{w_2 - t_2}{2} \right)^2 \right)$$

$$yy_{23} = \rho \pi \frac{f_2^2 t_2}{4} \left(\frac{1}{12} \left(\frac{3f_2^2}{4} + t_2^2 \right) + \left(\frac{w_2 - t_2}{2} \right)^2 \right)$$

$$yy_{24} = \rho \frac{w_2^4 s_2}{6}$$

$$yy_{25} = \rho \frac{s_2}{6} (w_2 - 2t_2)^4$$
(4.69)

The moments of inertia with respect to the z -axis of Link 2 frame and the center of mass are given by the following:

$$zz_2 = zz_{21} + 2zz_{22} - 2zz_{23} + zz_{24} - zz_{25}$$

$$z_{c2} = zz_2 - l_{m2} r_2^2$$

where

$$zz_{21} = \rho w_2^2 t_2 \left(\frac{1}{12} (w_2^2 + t_2^2) + \left(\frac{t_2}{2} - e_2 \right)^2 \right)$$

$$zz_{22} = \rho w_2 l_2 t_2 \left(\frac{1}{12} (w_2^2 + l_2^2) + \left(t_2 - e_2 + \frac{l_2}{2} \right)^2 \right)$$

$$zz_{23} = \rho \pi \frac{f_2^4 t_2}{32}$$

$$zz_{24} = \rho w_2^2 s_2 \left(\frac{1}{12} (w_2^2 + s_2^2) + \left(\frac{s_2}{2} + e_2 \right)^2 \right)$$

$$zz_{25} = \rho s_2 (w_2 - 2t_2)^2 \left(\frac{1}{12} (s_2^2 + (w_2 - 2t_2)^2) + \left(\frac{s_2}{2} + e_2 \right)^2 \right)$$
(4.70)

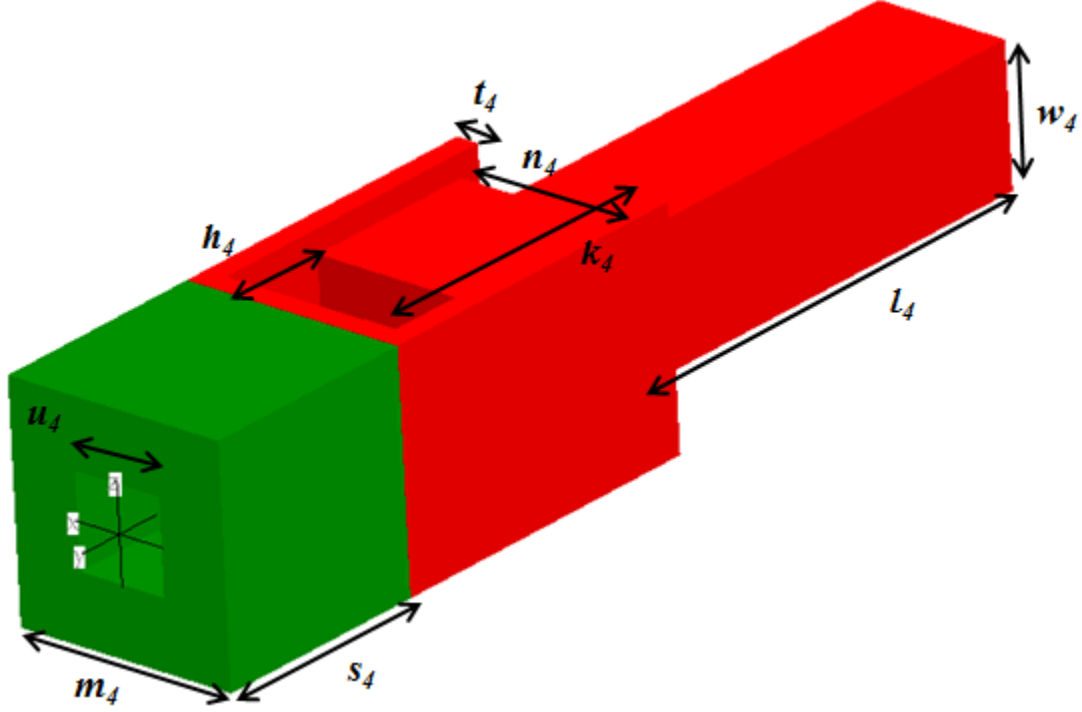


Figure 4.17: CAD Model of 1-Module Model Link 4 (End Link)

The mass of the new Link 4 is defined by:

$$l_{m4} = \rho \left(m_4^2 s_4 + m_4^2 t_4 + 2m_4 k_4 t_4 + n_4^3 + w_4^2 l_4 - u_4^2 s_4 - (w_4 - 2t_4)^2 (l_4 + n_4) \right) \quad (4.71)$$

The position of the center of mass with respect to the Link 4 frame is given by:

$${}^4r_{c4} = \begin{bmatrix} 0 \\ r_4 \\ 0 \end{bmatrix}$$

where

$$r_4 = \frac{\left((w_4 - 2t_4)^2 (l_4 + n_4) (2s_4 + 2h_4 + l_4 + n_4) + u_4^2 s_4^2 - m_4^2 s_4^2 - m_4^2 t_4 (2s_4 + t_4) \right)}{2 \left(m_4^2 s_4 + m_4^2 t_4 + 2m_4 k_4 t_4 + n_4^3 + w_4^2 l_4 - u_4^2 s_4 - (w_4 - 2t_4)^2 (l_4 + n_4) \right)} \quad (4.72)$$

The inertia matrices of Link 4 with respect to the Link 4 frame and about the center of mass, expressed in the Link 4 frame are given by the following:

$${}^4I_4 = \begin{bmatrix} xx_4 & 0 & 0 \\ 0 & yy_4 & 0 \\ 0 & 0 & zz_4 \end{bmatrix} \quad \text{and} \quad {}^4I_{c4} = \begin{bmatrix} x_{c4} & 0 & 0 \\ 0 & y_{c4} & 0 \\ 0 & 0 & z_{c4} \end{bmatrix} \quad (4.73)$$

Where, the moments of inertia with respect to the x -axis of Link 4 frame and the center of mass are given by the following:

$$xx_4 = xx_{41} - xx_{42} + xx_{43} + 2xx_{44} + xx_{45} + xx_{46} - xx_{47}$$

$$x_{c4} = xx_4 - l_{m4} r_4^2$$

where

$$xx_{41} = \rho m_4^2 s_4 \left(\frac{1}{12} (m_4^2 + s_4^2) + \left(\frac{s_4}{2} \right)^2 \right)$$

$$xx_{42} = \rho u_4^2 s_4 \left(\frac{1}{12} (u_4^2 + s_4^2) + \left(\frac{s_4}{2} \right)^2 \right)$$

$$xx_{43} = \rho m_4^2 t_4 \left(\frac{1}{12} (m_4^2 + t_4^2) + \left(s_4 + \frac{t_4}{2} \right)^2 \right)$$

$$xx_{44} = \rho m_4 k_4 t_4 \left(\frac{1}{12} (k_4^2 + m_4^2) + \left(s_4 + t_4 + \frac{k_4}{2} \right)^2 \right)$$

$$xx_{45} = \rho n_4^3 \left(\frac{n_4^2}{6} + \left(s_4 + h_4 + \frac{n_4}{2} \right)^2 \right)$$

$$xx_{46} = \rho w_4^2 l_4 \left(\frac{1}{12} (w_4^2 + l_4^2) + \left(s_4 + h_4 + n_4 + \frac{l_4}{2} \right)^2 \right)$$

$$xx_{47} = \rho (w_4 - 2t_4)^2 (l_4 + n_4) \left(\frac{1}{12} ((w_4 - 2t_4)^2 + (l_4 + n_4)^2) + \left(s_4 + h_4 + \frac{l_4 + n_4}{2} \right)^2 \right)$$
(4.74)

The moments of inertia with respect to the y -axis of Link 4 frame and the center of mass are given by the following:

$$\begin{aligned}
yy_4 &= yy_{41} - yy_{42} + yy_{43} + 2yy_{44} + yy_{45} + yy_{46} - yy_{47} \\
y_{c4} &= yy_4 - l_{m4}r_4^2
\end{aligned}$$

where

$$\begin{aligned}
yy_{41} &= \rho \frac{m_4^4 s_4}{6} \\
yy_{42} &= \rho \frac{u_4^4 s_4}{6} \\
yy_{43} &= \rho \frac{m_4^4 t_4}{6} \\
yy_{44} &= \rho m_4 k_4 t_4 \left(\frac{1}{12} (m_4^2 + t_4^2) + \left(\frac{m_4 - t_4}{2} \right)^2 \right) \\
yy_{45} &= \rho \frac{n_4^5}{6} \\
yy_{46} &= \rho \frac{w_4^4 l_4}{6} \\
yy_{47} &= \rho \frac{(w_4 - 2t_4)^4 (l_4 + n_4)}{6}
\end{aligned} \tag{4.75}$$

The moments of inertia with respect to the z-axis of Link 4 frame and the center of mass are given by the following:

$$\begin{aligned}
zz_4 &= zz_{41} - zz_{42} + zz_{43} + 2zz_{44} + zz_{45} + zz_{46} - zz_{47} \\
z_{c4} &= zz_4 - l_{m4}r_4^2
\end{aligned}$$

where

$$\begin{aligned}
zz_{41} &= \rho m_4^2 s_4 \left(\frac{1}{12} (m_4^2 + s_4^2) + \left(\frac{s_4}{2} \right)^2 \right) \\
zz_{42} &= \rho u_4^2 s_4 \left(\frac{1}{12} (u_4^2 + s_4^2) + \left(\frac{s_4}{2} \right)^2 \right) \\
zz_{43} &= \rho m_4^2 t_4 \left(\frac{1}{12} (m_4^2 + t_4^2) + \left(s_4 + \frac{t_4}{2} \right)^2 \right) \\
zz_{44} &= \rho m_4 k_4 t_4 \left(\frac{1}{12} (k_4^2 + t_4^2) + \left(s_4 + t_4 + \frac{k_4}{2} \right)^2 + \left(\frac{m_4}{2} - \frac{t_4}{2} \right)^2 \right) \\
zz_{45} &= \rho n_4^3 \left(\frac{n_4^2}{6} + \left(s_4 + h_4 + \frac{n_4}{2} \right)^2 \right) \\
zz_{46} &= \rho w_4^2 l_4 \left(\frac{1}{12} (w_4^2 + l_4^2) + \left(s_4 + h_4 + n_4 + \frac{l_4}{2} \right)^2 \right) \\
zz_{47} &= \rho (w_4 - 2t_4)^2 (l_4 + n_4) \left(\frac{1}{12} ((w_4 - 2t_4)^2 + (l_4 + n_4)^2) + \left(s_4 + h_4 + \frac{l_4 + n_4}{2} \right)^2 \right)
\end{aligned} \tag{4.76}$$

4.4.2 1-Module Model Link Inertia and Jacobian Matrices

The D-H parameters for the combined FA-JM model are defined and presented in Table 4.3.

i	α_i	a_i	d_i	θ_i
1	$\pi/2$	0	d_1	$\pi/2$
2	$\pi/2$	0	d_2	$\pi/2$
3	$\pi/2$	0	0	θ_3
4	$\pi/2$	0	d_4	π

Table 4.3: D-H Link Parameters for FA-JM Model

The rotations for Links 1 and 2 with respect to the base link are given by Equation 4.19.

The rotations for Links 3 and 4 with respect to the base link are defined as follows:

$${}^0R_3 = \begin{bmatrix} s_3 & 0 & -c_3 \\ 0 & 1 & 0 \\ c_3 & 0 & s_3 \end{bmatrix} \quad {}^0R_4 = \begin{bmatrix} -s_3 & -c_3 & 0 \\ 0 & 0 & 1 \\ -c_3 & s_3 & 0 \end{bmatrix} \quad (4.77)$$

Inertia matrices for Links 1 and 2 about their respective centers of mass and expressed in the base frame are provided by Equation 4.21. Inertia matrices for Links 3 and 4 for the 1-module model are given by the following using Equation 4.20:

$$I_3 = \begin{bmatrix} x_{c3}s_3^2 + z_{c3}c_3^2 & 0 & (x_{c3} - z_{c3})c_3s_3 \\ 0 & y_{c3} & 0 \\ (x_{c3} - z_{c3})c_3s_3 & 0 & x_{c3}c_3^2 + z_{c3}s_3^2 \end{bmatrix} \quad (4.78)$$

$$I_4 = \begin{bmatrix} x_{c4}s_3^2 + y_{c4}c_3^2 & 0 & (x_{c4} - y_{c4})c_3s_3 \\ 0 & z_{c4} & 0 \\ (x_{c4} - y_{c4})c_3s_3 & 0 & x_{c4}c_3^2 + y_{c4}s_3^2 \end{bmatrix} \quad (4.79)$$

Next, utilizing Equation 4.22, we define the position vectors of the centers of mass each links with respect to the various link frames of the gait model and expressed in the base frame. The position vectors for Links 1 and 2 are provided by Equation 4.23. The position vectors for Link 3 are given as follows:

$${}^2p_{c3}^* = \begin{bmatrix} -r_3c_3 \\ 0 \\ r_3s_3 \end{bmatrix} \quad {}^1p_{c3}^* = \begin{bmatrix} d_2 - r_3c_3 \\ 0 \\ r_3s_3 \end{bmatrix} \quad {}^0p_{c3}^* = \begin{bmatrix} d_2 - r_3c_3 \\ 0 \\ d_1 + r_3s_3 \end{bmatrix} \quad (4.80)$$

The position vectors for link 4 are given as follows:

$${}^3p_{c4}^* = {}^2p_{c4}^* = \begin{bmatrix} -(d_4 + r_4)c_3 \\ 0 \\ (d_4 + r_4)s_3 \end{bmatrix} \quad {}^1p_{c4}^* = \begin{bmatrix} d_2 - (d_4 + r_4)c_3 \\ 0 \\ (d_4 + r_4)s_3 \end{bmatrix} \quad {}^0p_{c4}^* = \begin{bmatrix} d_2 - (d_4 + r_4)c_3 \\ 0 \\ d_1 + (d_4 + r_4)s_3 \end{bmatrix} \quad (4.81)$$

Finally, we compute the Jacobian submatrices for link linear and angular velocity. The Jacobian submatrices for Links 1 and 2 are given by Equation 4.24. The Jacobian

submatrices for Links 3 and 4 for the 1-module model are provided by the following expressions:

$$J_{\omega_3} = J_{\omega_4} = \begin{bmatrix} 0 & 0 & 0 & 0 \\ 0 & 0 & 1 & 0 \\ 0 & 0 & 0 & 0 \end{bmatrix} \quad (4.82)$$

$$J_{v_3} = \begin{bmatrix} 0 & 1 & r_3 s_3 & 0 \\ 0 & 0 & 0 & 0 \\ 1 & 0 & r_3 c_3 & 0 \end{bmatrix} \quad J_{v_4} = \begin{bmatrix} 0 & 1 & (d_4 + r_4) s_3 & -c_3 \\ 0 & 0 & 0 & 0 \\ 1 & 0 & (d_4 + r_4) c_3 & s_3 \end{bmatrix} \quad (4.83)$$

4.4.3 1-Module Model Lagrangian Equations of Motion

As before, we define the equations of motion for the 1-module gait model using utilize Equation 4.25, which yields the following:

$$M_{1m} = M_{FA} + J_{v_3}^T l_{m3} J_{v_3} + J_{\omega_3}^T I_3 J_{\omega_3} + J_{v_4}^T l_{m4} J_{v_4} + J_{\omega_4}^T I_4 J_{\omega_4}$$

$$= \begin{bmatrix} m_{11} & 0 & m_{13} & m_{14} \\ 0 & m_{22} & m_{23} & m_{24} \\ m_{31} & m_{32} & m_{33} & 0 \\ m_{41} & m_{42} & 0 & m_{44} \end{bmatrix}$$

where

$$\begin{aligned} m_{11} &= l_{m1} + l_{m2} + l_{m3} + l_{m4} \\ m_{22} &= l_{m2} + l_{m3} + l_{m4} \\ m_{33} &= l_{m3} r_3^2 + l_{m4} (d_4 + r_4)^2 + y_{c3} + z_{c4} \\ m_{44} &= l_{m4} \\ m_{31} = m_{13} &= l_{m3} r_3 c_3 + l_{m4} (d_4 + r_4) c_3 \\ m_{41} = m_{14} &= l_{m4} s_3 \\ m_{32} = m_{23} &= l_{m3} r_3 s_3 + l_{m4} (d_4 + r_4) s_3 \\ m_{42} = m_{24} &= -l_{m4} c_3 \end{aligned} \quad (4.84)$$

The velocity coupling vector for the 1-module gait model is found by taking the partial derivatives of the 1-module model inertia matrix with respect to the joint variables in accordance to Equation 4.28. The coupling vector terms are given as the following:

$$\begin{aligned}
V_1 &= 2l_{m4}c_3\dot{\theta}_3\dot{d}_4 - (l_{m3}r_3s_3 + l_{m4}(d_4 + r_4)s_3)\dot{\theta}_3^2 \\
V_2 &= 2l_{m4}s_3\dot{\theta}_3\dot{d}_4 + (l_{m3}r_3c_3 + l_{m4}(d_4 + r_4)c_3)\dot{\theta}_3^2 \\
V_3 &= 2l_{m4}(d_4 + r_4)\dot{\theta}_3\dot{d}_4 \\
V_4 &= -l_{m4}(d_4 + r_4)\dot{\theta}_3^2
\end{aligned} \tag{4.85}$$

Since there are no gravitation terms for either FA or JM component, we can assume that there are no terms for the combined model. We confirm this by computing the gravitational terms using Equation 4.30 and 4.31, which yield:

$$G_1 = G_2 = G_3 = G_4 = 0 \tag{4.86}$$

We assume no external forces and substitute the 1-module model inertia matrix, velocity coupling vector, and gravitation terms into Equation 4.25, which results in the following four Lagrange equations of motion:

$$\begin{aligned}
f_1 &= (l_{m1} + l_{m2} + l_{m3} + l_{m4})\ddot{d}_1 + (l_{m3}r_3c_3 + l_{m4}(d_4 + r_4)c_3)\ddot{\theta}_3 \\
&+ l_{m4}s_3\ddot{d}_4 + 2l_{m4}c_3\dot{\theta}_3\dot{d}_4 - (l_{m3}r_3s_3 + l_{m4}(d_4 + r_4)s_3)\dot{\theta}_3^2
\end{aligned} \tag{4.87}$$

$$\begin{aligned}
f_2 &= (l_{m2} + l_{m3} + l_{m4})\ddot{d}_2 + (l_{m3}r_3s_3 + l_{m4}(d_4 + r_4)s_3)\ddot{\theta}_3 \\
&- l_{m4}c_3\ddot{d}_4 + 2l_{m4}s_3\dot{\theta}_3\dot{d}_4 + (l_{m3}r_3c_3 + l_{m4}(d_4 + r_4)c_3)\dot{\theta}_3^2
\end{aligned} \tag{4.88}$$

$$\begin{aligned}
\tau_3 &= (l_{m3}r_3c_3 + l_{m4}(d_4 + r_4)c_3)\ddot{d}_1 + (l_{m3}r_3s_3 + l_{m4}(d_4 + r_4)s_3)\ddot{d}_2 \\
&+ (l_{m3}r_3^2 + l_{m4}(d_4 + r_4)^2 + y_{c3} + z_{c4})\ddot{\theta}_3 + 2l_{m4}(d_4 + r_4)\dot{\theta}_3\dot{d}_4
\end{aligned} \tag{4.89}$$

$$f_4 = l_{m4}s_3\ddot{d}_1 - l_{m4}c_3\ddot{d}_2 + l_{m4}\ddot{d}_4 - l_{m4}(d_4 + r_4)\dot{\theta}_3^2 \tag{4.90}$$

The equations of motion are validated against the forces computed by the Mechanism Analysis suite of Pro/Engineer Wildfire 4.0. The results are presented in Figures 4.18 and 4.19. The validation curves confirm that the equations of motions are correct.

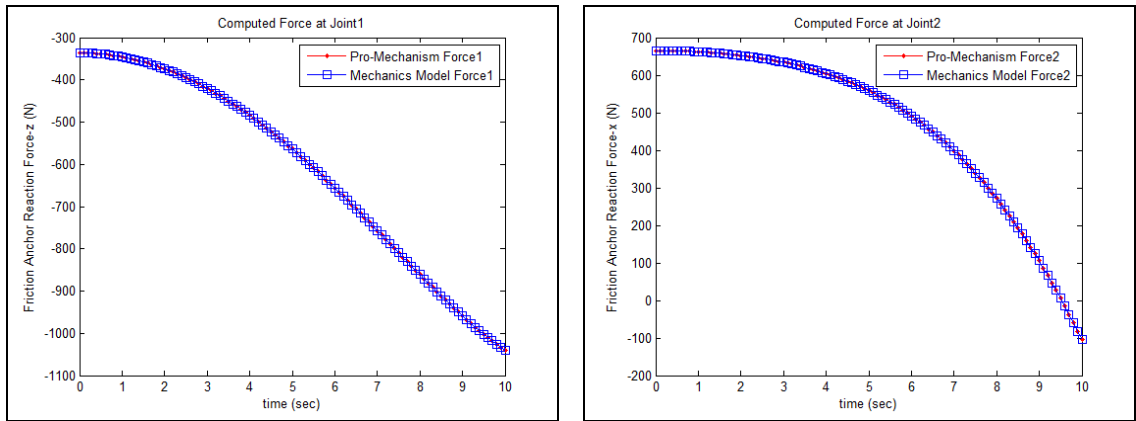


Figure 4.18: FA Validation Results of 1-Module Model Dynamics Equations

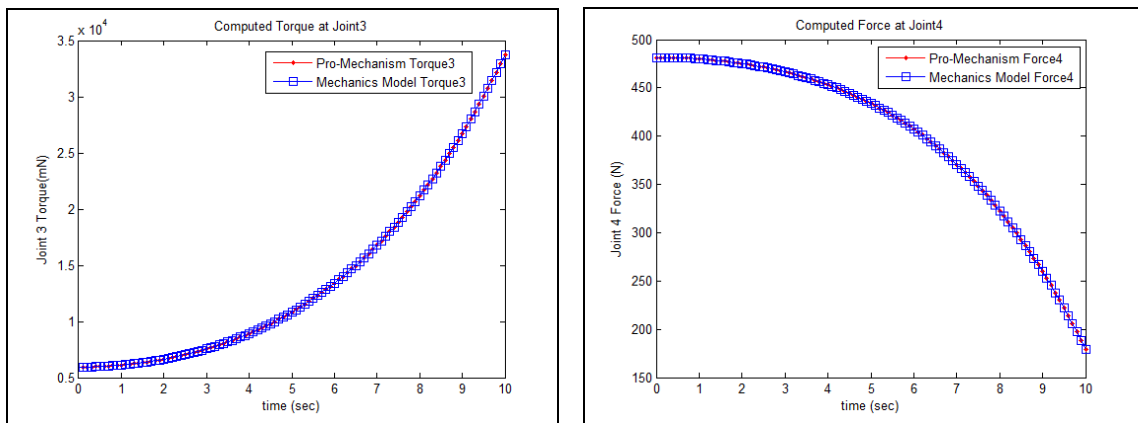


Figure 4.19: JM Validation Results of 1-Module Model Dynamics Equations

4.5 General n -Module Exaggerated Rectilinear Gait Dynamics Model

We derived the general n -module gait dynamics model by observing the pattern that develops as the inertia matrix changes between various robot models with a progressively increasing number of JM modules. We derived and observed the equations of motion for four dynamics models: 1-module, 2-module, 3-module and 4-module dynamics models. For each additional joint module, we used the same mass and D-H parameters presented in Table 4.2, until the pattern emerged. This pattern is presented in the following and describes how to assembly a dynamics model for any n number of modules. As a result of our observations, we determined that Link 0, 1 and 2 will always be defined by Figures

4.4, 4.5 and 4.16, respectively, and their associated link characteristic equations. The end link will always be defined by Figure 4.17. Link $2m + 1$ is represented by Figure 4.11 and associated equations, where m is the JM module number. Finally, we define the joining link, Link 4', between two JM modules, Figure 4.20. This link is only employed for models with 2 or more JM modules. Figure 4.20 defines every Link $2m + 2$, where $n > 1$ except for the end link, which defaults to Figure 4.17.

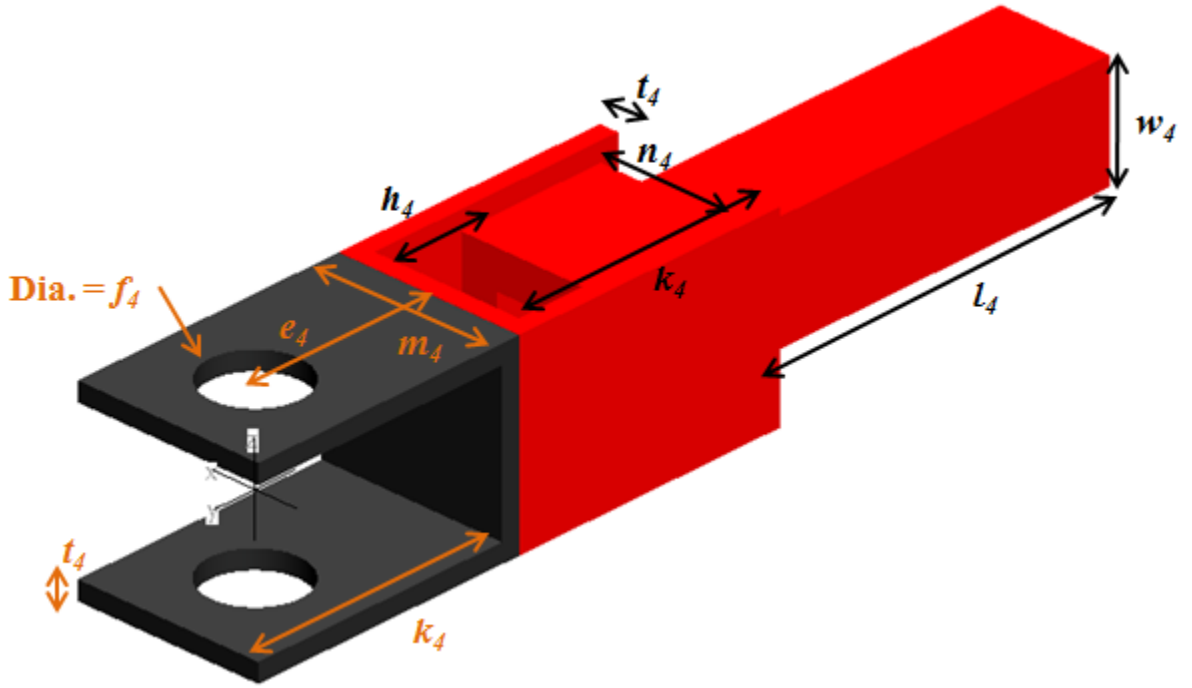


Figure 4.20: CAD Model of n-Module Model Link 4'

The mass of the Link 4 is defined by:

$$l_{m4} = \rho \left(2m_4^2 t_4 + 4m_4 k_4 t_4 + n_4^3 + w_4^2 l_4 - (w_4 - 2t_4)^2 (l_4 + n_4) - \pi \frac{f_4^2 t_4}{2} \right) \quad (4.91)$$

The position of the center of mass with respect to the Link 4 frame is given by:

$${}^4r_{c4} = \begin{bmatrix} 0 \\ r_4 \\ 0 \end{bmatrix}$$

where (4.92)

$$r_4 = \frac{\left((w_4 - 2t_4)^2 (l_4 + n_4)(2h_4 + l_4 + n_4) - 4m_4^2 t_4 e_4 \right. \\ \left. - 8m_4 k_4 t_4 e_4 - n_4^3 (2h_4 + n_4) - w_4^2 l_4 (2h_4 + 2n_4 + l_4) \right)}{4m_4^2 t_4 + 8m_4 k_4 t_4 + 2n_4^3 + 2w_4^2 l_4 - 2(w_4 - 2t_4)^2 (l_4 + n_4) - \rho f_4^2 t_4}$$

The inertia matrices of Link 4 with respect to the Link 4 frame and about the center of mass, expressed in the Link 4 frame are given by the following:

$${}^4I_4 = \begin{bmatrix} xx_4 & 0 & 0 \\ 0 & yy_4 & 0 \\ 0 & 0 & zz_4 \end{bmatrix} \quad \text{and} \quad {}^4I_{c4} = \begin{bmatrix} x_{c4} & 0 & 0 \\ 0 & y_{c4} & 0 \\ 0 & 0 & z_{c4} \end{bmatrix} \quad (4.93)$$

Where, the moments of inertia with respect to the x -axis of Link 4 frame and the center of mass are given by the following:

$$xx_4 = -xx_{41} + 2xx_{42} + xx_{43} + xx_{44} + 2xx_{45} + xx_{46} + xx_{47} - xx_{48}$$

$$x_{c4} = xx_4 - l_{m4} r_4^2$$

where

$$xx_{41} = \rho \frac{m_4 f_4^2 t_4}{4} \left(\frac{1}{12} \left(\frac{3f_4^2}{4} + t_4^2 \right) + \left(\frac{m_4 - t_4}{2} \right)^2 \right)$$

$$xx_{42} = \rho m_4 k_4 t_4 \left(\frac{1}{12} (k_4^2 + t_4^2) + \left(\frac{m_4 - t_4}{2} \right)^2 + \left(t_4 - e_4 + \frac{k_4}{2} \right)^2 \right)$$

$$xx_{43} = \rho m_4^2 t_4 \left(\frac{1}{12} (m_4^2 + t_4^2) + \left(\frac{t_4}{2} - e_4 \right)^2 \right)$$

$$xx_{44} = \rho m_4^2 t_4 \left(\frac{1}{12} (m_4^2 + t_4^2) + \left(e_4 + \frac{t_4}{2} \right)^2 \right)$$
(4.94)

also

$$\begin{aligned}
xx_{45} &= \rho m_4 k_4 t_4 \left(\frac{1}{12} (k_4^2 + m_4^2) + \left(e_4 + t_4 + \frac{k_4}{2} \right)^2 \right) \\
xx_{46} &= \rho n_4^3 \left(\frac{n_4^2}{6} + \left(h_4 + \frac{n_4}{2} \right)^2 \right) \\
xx_{47} &= \rho w_4^2 l_4 \left(\frac{1}{12} (w_4^2 + l_4^2) + \left(h_4 + n_4 + \frac{l_4}{2} \right)^2 \right) \\
xx_{48} &= \rho (w_4 - 2t_4)^2 (l_4 + n_4) \left(\frac{1}{12} ((w_4 - 2t_4)^2 + (l_4 + n_4)^2) + \left(h_4 + \frac{l_4 + n_4}{2} \right)^2 \right)
\end{aligned} \tag{4.95}$$

The moments of inertia with respect to the y-axis of Link 4 frame and the center of mass are given by the following:

$$\begin{aligned}
yy_4 &= -yy_{41} + 2yy_{42} + 2yy_{43} + 2yy_{44} + yy_{45} + yy_{46} - yy_{47} \\
y_{c4} &= yy_4 - l_{m4} r_4^2
\end{aligned}$$

where

$$\begin{aligned}
yy_{41} &= \rho \frac{m_4 f_4^2 t_4}{4} \left(\frac{1}{12} \left(\frac{3f_4^2}{4} + t_4^2 \right) + \left(\frac{m_4 - t_4}{2} \right)^2 \right) \\
yy_{42} &= \rho m_4 k_4 t_4 \left(\frac{1}{12} (m_4^2 + t_4^2) + \left(\frac{m_4 - t_4}{2} \right)^2 \right) \\
yy_{43} &= \rho \frac{m_4^4 t_4}{6} \\
yy_{44} &= \rho m_4 k_4 t_4 \left(\frac{1}{12} (m_4^2 + t_4^2) + \left(\frac{m_4 - t_4}{2} \right)^2 \right) \\
yy_{45} &= \rho \frac{n_4^5}{6} \\
yy_{46} &= \rho \frac{w_4^4 l_4}{6} \\
yy_{47} &= \rho \frac{(w_4 - 2t_4)^4 (l_4 + n_4)}{6}
\end{aligned} \tag{4.96}$$

The moments of inertia with respect to the z -axis of Link 4 frame and the center of mass are given by the following:

$$\begin{aligned} zz_4 &= -zz_{41} + 2zz_{42} + zz_{43} + zz_{44} + 2zz_{45} + zz_{46} + zz_{47} - zz_{48} \\ z_{c4} &= zz_4 - l_{m4}r_4^2 \end{aligned}$$

where

$$\begin{aligned} zz_{41} &= \rho\pi \frac{f_4^4 t_4}{32} \\ zz_{42} &= \rho m_4 k_4 t_4 \left(\frac{1}{12} (m_4^2 + k_4^2) + \left(t_4 - e_4 + \frac{k_4}{2} \right)^2 \right) \\ zz_{43} &= \rho m_4^2 t_4 \left(\frac{1}{12} (m_4^2 + t_4^2) + \left(\frac{t_4}{2} - e_4 \right)^2 \right) \\ zz_{44} &= \rho m_4^2 t_4 \left(\frac{1}{12} (m_4^2 + t_4^2) + \left(e_4 + \frac{t_4}{2} \right)^2 \right) \\ zz_{45} &= \rho m_4 k_4 t_4 \left(\frac{1}{12} (k_4^2 + t_4^2) + \left(e_4 + t_4 + \frac{k_4}{2} \right)^2 + \left(\frac{m_4 - t_4}{2} \right)^2 \right) \\ zz_{46} &= \rho n_4^3 \left(\frac{n_4^2}{6} + \left(h_4 + \frac{n_4}{2} \right)^2 \right) \\ zz_{47} &= \rho w_4^2 l_4 \left(\frac{1}{12} (w_4^2 + l_4^2) + \left(h_4 + n_4 + \frac{l_4}{2} \right)^2 \right) \\ zz_{48} &= \rho (w_4 - 2t_4)^2 (l_4 + n_4) \left(\frac{1}{12} ((w_4 - 2t_4)^2 + (l_4 + n_4)^2) + \left(h_4 + \frac{l_4 + n_4}{2} \right)^2 \right) \end{aligned} \quad (4.97)$$

Based on the repetition of the D-H parameters for Link 3 and 4 in Table 4.3 for each additional module, the kinematics equations for the n -module model are defined. The rotation matrices, \mathbf{R} , and position vectors, \mathbf{p} , are given by the following:

$${}^0R_{2+2n} = {}^0R_1 {}^1R_2 \cdots {}^{2n}R_{1+2n} {}^{1+2n}R_{2+2n} \quad (4.98)$$

Where,

$${}^0R_1 = \begin{bmatrix} 0 & 0 & 1 \\ 1 & 0 & 0 \\ 0 & 1 & 0 \end{bmatrix} \quad (4.99)$$

$${}^1R_2 = \begin{bmatrix} 0 & 1 & 0 \\ 0 & 0 & 1 \\ 1 & 0 & 0 \end{bmatrix} \quad (4.100)$$

For $m = 1$ to n ,

$${}^{2m}R_{1+2m} = \begin{bmatrix} c_{1+2m} & 0 & s_{1+2m} \\ s_{1+2m} & 0 & -c_{1+2m} \\ 0 & 1 & 0 \end{bmatrix} \quad (4.101)$$

$${}^{1+2m}R_{2+2m} = \begin{bmatrix} -1 & 0 & 0 \\ 0 & 0 & 1 \\ 0 & 1 & 0 \end{bmatrix}$$

$${}^0p = \begin{bmatrix} 0 \\ 0 \\ d_1 \end{bmatrix} \quad {}^1p = \begin{bmatrix} 0 \\ 0 \\ d_2 \end{bmatrix} \quad (4.102)$$

For $m = 2$ to $1 + 2n$,

$${}^m p = \begin{bmatrix} 0 \\ 0 \\ 0 \end{bmatrix}, \text{ if } m \text{ is even,}$$

$${}^m p = \begin{bmatrix} 0 \\ 0 \\ d_{m+1} \end{bmatrix}, \text{ if } m \text{ is odd} \quad (4.103)$$

The joint torques are found using Equation 4.25. Where, \mathbf{M} is the manipulator inertia matrix and h is the total number of joints, q , defined as $h = 2n + 2$. The velocity coupling vector, \mathbf{V} , is found by taking the partial derivatives of the \mathbf{M} with respect to the joint

variables in accordance to Equation 4.28. Note, due to the planar nature of the robot model, there are no gravitational terms. Therefore, the vector \mathbf{G} is zero. The matrix \mathbf{M} is defined by the following set of equations:

$$\mathbf{M} = \mathbf{M}_{FA} + \mathbf{M}_n \quad (4.104)$$

$$\begin{aligned} \mathbf{M}_{FA} &= \mathbf{M}'_{(2+2n,2+2n)} = \mathbf{0} \\ \text{Except, } \mathbf{M}'_{(1,1)} &= l_{m1} + l_{m2} \\ \mathbf{M}'_{(2,2)} &= l_{m2} \end{aligned} \quad (4.105)$$

Where, l_{m1} and l_{m2} are the masses for the FA module Link 1 and Link 2, respectively. \mathbf{M}_n is a matrix containing additional inertia terms defined by n and is given by the following:

$$\mathbf{M}_n = \sum_{m=1}^{m=n} \left(\begin{aligned} &J\omega_m^T y_{1+2m} J\omega_m + J\mathbf{V}_{1+2m}^T \kappa_{1+2m} J\mathbf{V}_{1+2m} + \\ &J\omega_m^T z_{2+2m} J\omega_m + J\mathbf{V}_{2+2m}^T \kappa_{2+2m} J\mathbf{V}_{2+2m} \end{aligned} \right) \quad (4.106)$$

$$J\omega_m = J\omega'_{(3,2+2n)} = \mathbf{0} \quad (4.107)$$

$$\text{Except, } J\omega'_{(2,1+2j)} = 1, \text{ for } j = 1 \text{ to } m$$

Where, y_{1+2m} and z_{2+2m} are the inertia tensor elements at I_{yy} for Link 1 + 2m and I_{zz} for Link 2 + 2m, respectively, at their centers of mass. The mass for Link 1 + 2m and Link 2 + 2m are given by κ_{1+2m} and κ_{2+2m} , respectively. The matrix $J\mathbf{V}_i$ is defined as:

$$J\mathbf{V}_i = [J\mathbf{V}_i^1, \dots, J\mathbf{V}_i^{2+2n}] \quad (4.108)$$

Where,

$$J\mathbf{V}_i^1 = \begin{bmatrix} 0 \\ 0 \\ 1 \end{bmatrix} \quad (4.109)$$

For $j = 2$ to i ,

$$J\mathcal{V}_i^j = {}^0R_{j-1} \begin{bmatrix} 0 \\ 0 \\ 1 \end{bmatrix}, \text{ if } j \text{ is even}$$

$$J\mathcal{V}_i^j = \begin{bmatrix} 0 \\ 1 \\ 0 \end{bmatrix} \times {}^{j-1}P\mathcal{C}_i^*, \text{ if } j \text{ is odd}$$
(4.110)

For $j = i + 1$ to $2 + 2n$,

$$J\mathcal{V}_i^j = \begin{bmatrix} 0 \\ 0 \\ 0 \end{bmatrix}$$
(4.111)

Finally, we find a vector, which is a position vector defined from the origin of the $j-1$ link frame to the center of mass of Link i and expressed in the base frame. Defining the position vector for each $j-1$ link frame is an iterative process and is described by the following procedure:

$${}^{j-1}P\mathcal{C}_i = {}^{j-1}p + {}^{j-1}R_j {}^jP\mathcal{C}_i$$

$${}^{j-1}P\mathcal{C}_i^* = {}^0R_{j-1} {}^{j-1}P\mathcal{C}_i$$
(4.112)

$${}^iP\mathcal{C}_i = \begin{bmatrix} 0 \\ 0 \\ r_i \end{bmatrix}, \text{ if } i \text{ is odd}$$

$${}^iP\mathcal{C}_i = \begin{bmatrix} 0 \\ r_i \\ 0 \end{bmatrix}, \text{ if } i \text{ is even}$$
(4.113)

Where, r_i is the distance from the link frame to the center of mass for Link i . This completes the procedure for defining the kinematics and dynamics equations of motion for the general n -module gait model. To validate the n -module gait model, we choose to predict the joint reaction forces and torques for a 5-module robot executing the second

step of the high speed turning gait, illustrated in Figure 4.21 and 4.22. A gait model is developed for the 5-module robot using the procedure from Equation 4.98 to Equation 4.113 and the reaction forces are computed. The forces are compared the reaction forces computed by the Mechanism Analysis suite of Pro/Engineer Wildfire 4.0 [97]. The comparison is presented in the plots given by Figures 4.23 through 4.28. The plots indicate that the procedure is effective at providing an accurate analytical model capable of predicting joint reaction forces given joint inputs based on the rectilinear gait. We then utilized this model defined the number of modules and the servomotor type that will provide the maximum speed for a high speed gait. The results of that study defined the configuration of the prototype in Figure 3.31.

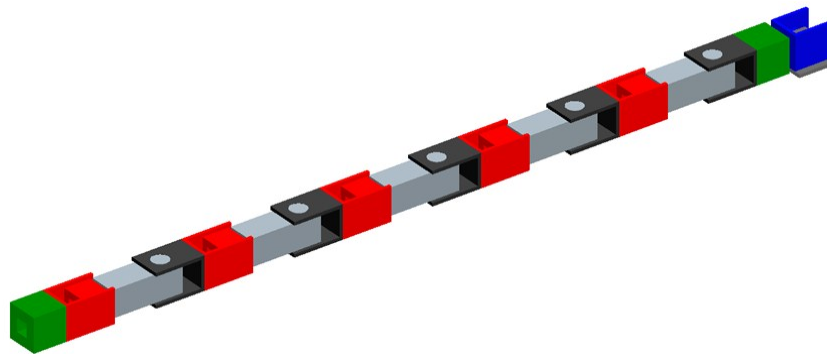


Figure 4.21: 5-Module Robot Initial Position before High Speed Turning Gait Step 2

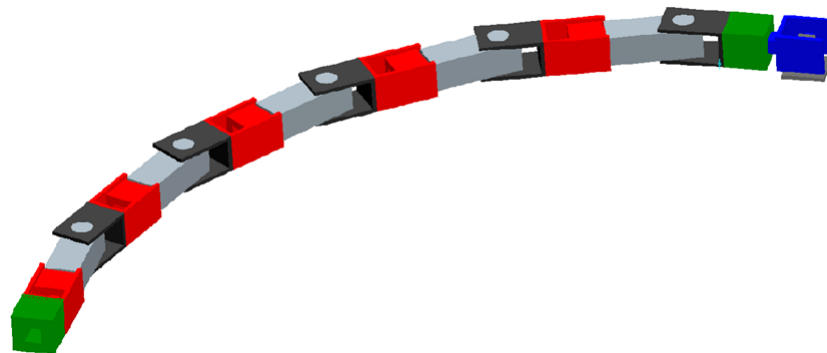


Figure 4.22: 5-Module Robot Final Position after High Speed Turning Gait Step 2

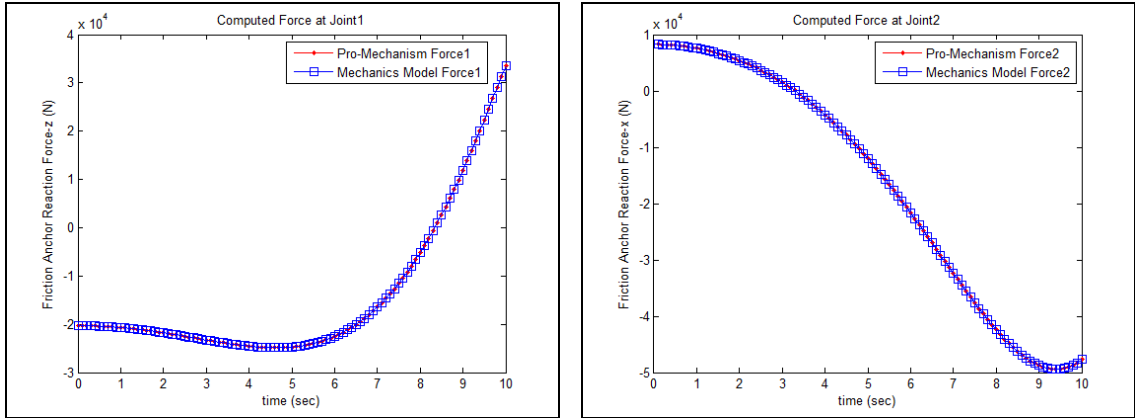


Figure 4.23: *n*-Module Model Validation, FA Reaction Forces

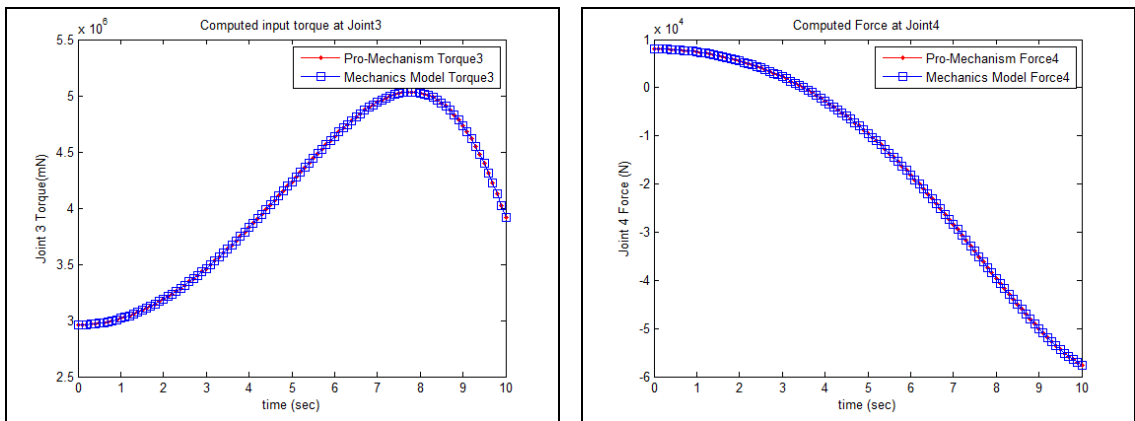


Figure 4.24: *n*-Module Model Validation, JM 1 Reaction Forces

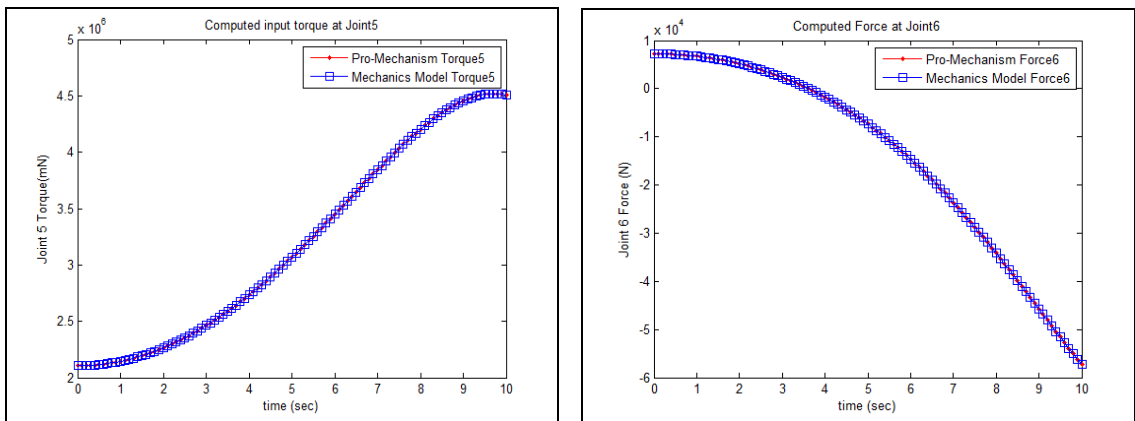


Figure 4.25: *n*-Module Model Validation, JM 2 Reaction Forces

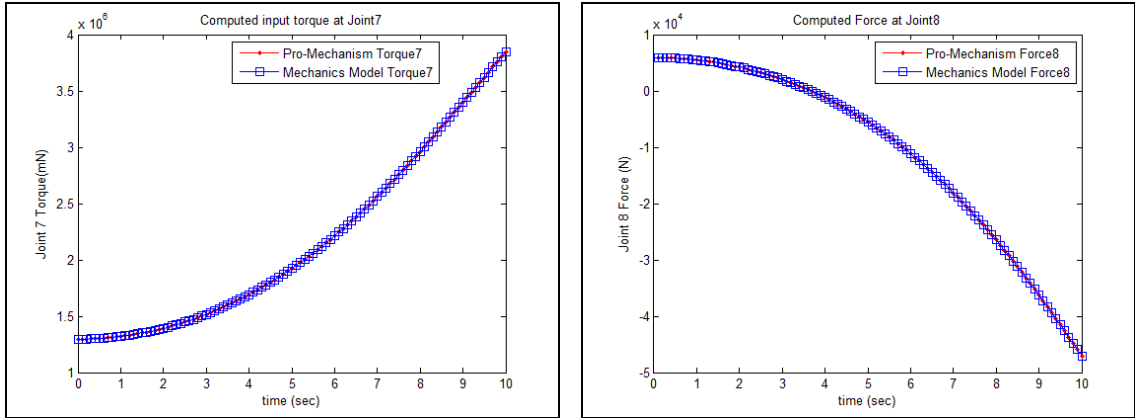


Figure 4.26: *n*-Module Model Validation, JM 3 Reaction Forces

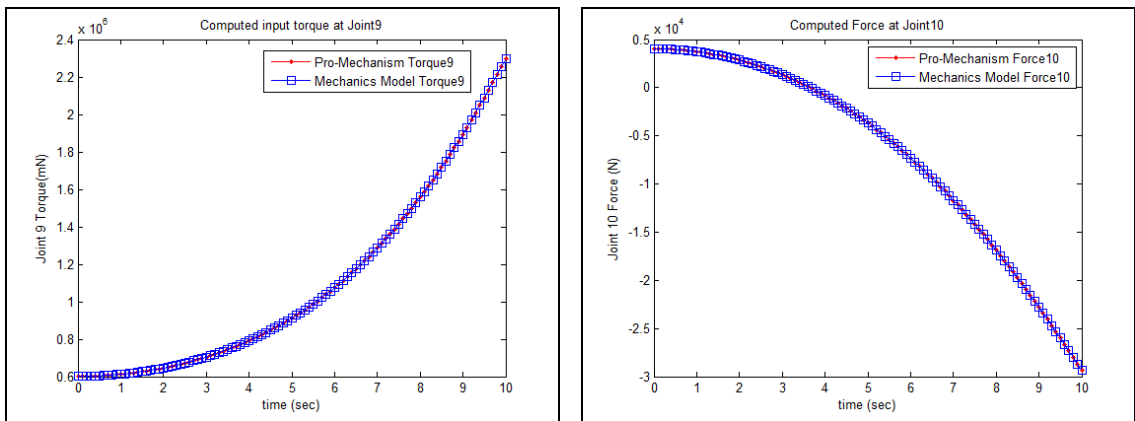


Figure 4.27: *n*-Module Model Validation, JM 4 Reaction Forces

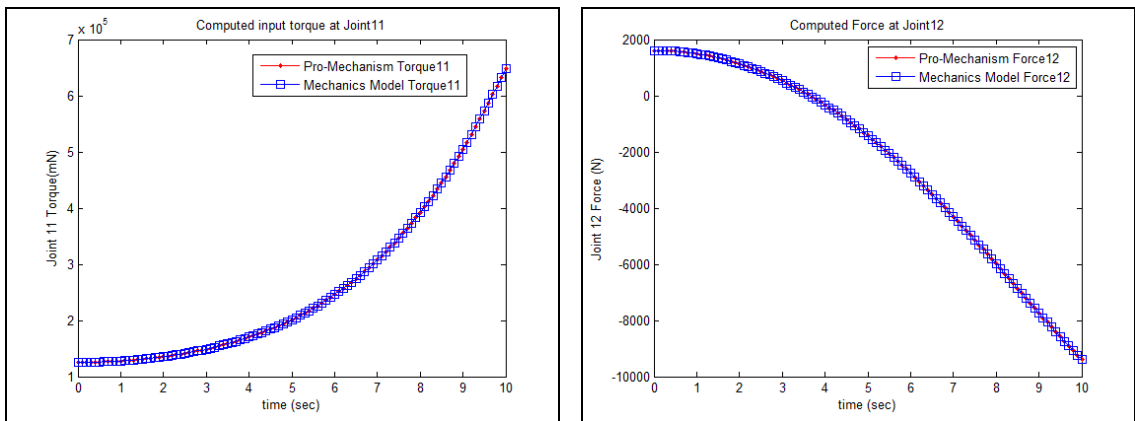


Figure 4.28: *n*-Module Model Validation, JM 5 Reaction Forces

4.6 Developing an Exaggerated Rectilinear Gait for High Traction

Referring back to the friction anchoring concept, introduced in Chapter 3 and illustrated in Figure 3.20, we observe that in a short snake-inspired robot, the use of the friction anchors alone would be sufficient. With only a small number of modules, the friction anchor is effective at resisting the reaction forces from the movement of the robot and thus providing positive traction as the robot progresses. However, in significantly longer robots or when traversing hard, smooth surfaces, the friction forces generated by only redistributing the mass locally around the anchor will be ineffective in countering the reaction forces produced by the movement of the robot. Thus, we sought to address these issues by developing another exaggerated rectilinear gait which emphasizes high traction over high speed to operate in these scenarios [98].

4.6.1 High Traction Exaggerated Rectilinear Gait Concept

We develop the high traction gait concept by employing the robot design's ability to shift its center of mass as it progresses forward. By the nature of the parallel mechanism-based modular design, the robot is able to redistribute its concentration of mass along its body length by expanding and contracting its segments, as illustrated in Figure 4.29. By concentrating the majority of robot's mass closer to the terminal end of the robot, the friction anchor's effectiveness in resisting reaction forces and preventing linear travel of the robot's terminal end is greatly increased. Figure 4.29a illustrates the robot in its nominal position, with all modules contracted. In this position, both ends of the robot are equally distant from the center of mass. Figure 4.29b illustrates the right side anchor engaged and one module expanding on the left side, with the left side anchor free. In this scenario, the amount of mass locally near the engaged anchor is much greater than the

mass local to the moving end of the robot. Therefore, the reaction forces generated by the moving end are effectively counter. Figure 4.29c illustrates the same idea, however, less mass is local to the engaged anchor but the left side expands to a greater length. This scenario is useful when the terrain is rough and less mass redistribution is necessary to generate the necessary friction force to resist expansion of the robot. As a result, the robot is able to travel greater distances per expansion cycles and achieve higher velocities.

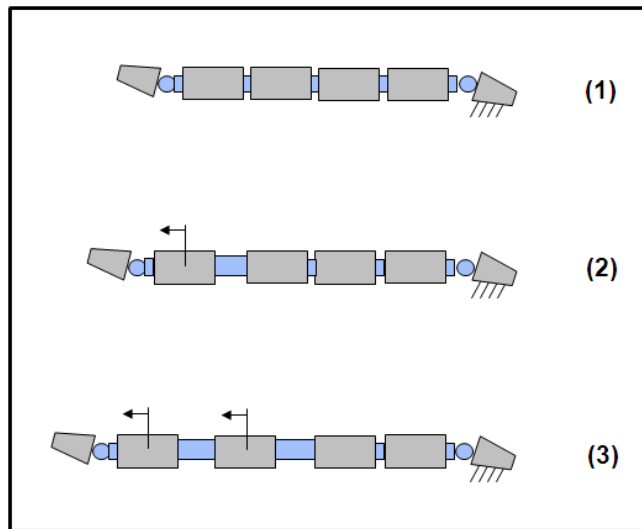


Figure 4.29: Shifting Center of Mass

Utilizing the concept in Figure 4.29, we defined the high traction forward gait, illustrated in Figure 4.30. In the gait, the robot extends and contracts its forward half first followed by the aft half in order to provide positive traction. The gait sequence is described as follows:

- Step 1 – Observing from the side view of the robot, the robot begins in its nominal configuration where the internal segments are contracted and the friction anchors are not in contact with the terrain. The rear friction anchor is engaged with the terrain to resist the reaction forces of the robot's internal joints and

ensure that the position of the rear end of the robot remains unchanged during the change of position and orientation of the segments during step two.

- Step 2 – The joint mechanism modules of the forward half of the robot simultaneously extends to their maximum length.
- Step 3 – The forward friction anchor plants to prevent position change of the front end of the robot during the remaining gait steps.
- Step 4 – The joint mechanism modules of forward half of the robot contract, while simultaneously the modules of the rear half extend, allowing the robot to shift more mass near the forward anchor and provide more traction.
- Step 5 – With the forward friction anchor is still engaged, the rear friction anchor is disengaged from the terrain.
- Step 6 – The joint mechanism modules of the rear half of the robot contract, returning the robot to its nominal configuration. The gait is complete.

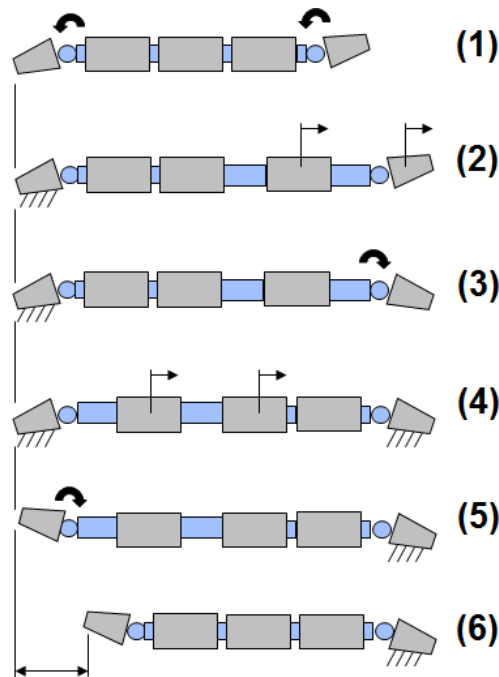


Figure 4.30: Theoretical High Traction Forward Gait Sequence

Next, we expand the high traction gait concept to include a gait designed for effective turning in scenarios where the robot is significantly long or when traversing hard, smooth surfaces. The high traction turning gait is actually a version of the high traction forward rectilinear gait, which can be described as the robot crawling around the perimeter of a circle using the high traction gait to change its orientation. The turning gait concept is presented in Figure 4.31 and the gait sequence is described as follows:

- Step 1 – The robot begins in its nominal configuration with all joint mechanism modules contracted and both friction anchors disengaged.
- Step 2 – Each of the horizontally mounted parallel mechanisms in each joint mechanism module simultaneously change the orientation of the adjacent joint modules, causing the robot's length to curl in the intended direction.
- Step 3 – While the length of the robot is still curled, the rear friction anchor plants and then the joint mechanism modules of the first half of the robot simultaneously extend.
- Step 4 – Similar to the high traction forward gait, the forward friction anchor engages to prevent sliding for the front end of the robot. The joint modules of the forward half of the robot contract while simultaneously the joint modules rear half extend, allowing the robot to shift more mass near the forward friction anchor and provide additional traction.
- Step 5 – The rear friction anchor is disengaged from the terrain and the joint modules of the rear half of the robot contract resulting in a global change of orientation of the robot. The forward friction anchor disengages from the terrain.

Steps three through five are repeated until the robot reaches the desired orientation.

- Step 6 – When the desired orientation is achieved, the robot uncurls into its nominal, contracted configuration in-line with the orientation of the center most joint mechanism module. The gait is now complete.

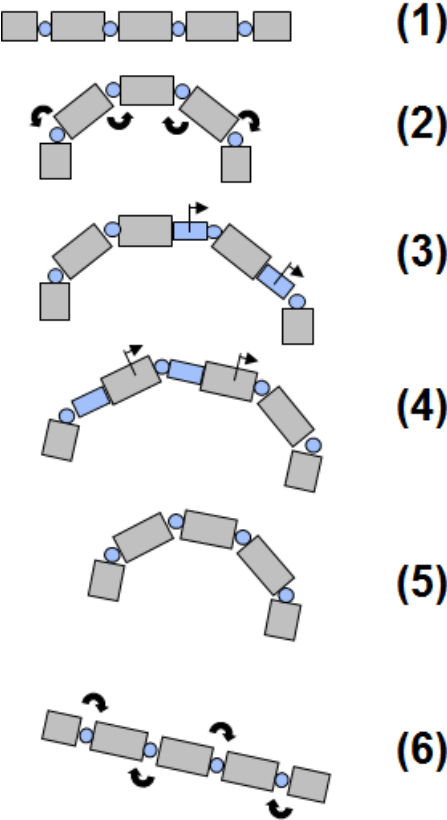


Figure 4.31: Theoretical High Traction Turning Gait Sequence

4.6.2 Modeling High Traction Gait using *n*-Module Gait Model

In order to confirm the positive effects of the high traction gait on required friction anchor traction, we perform a comparison between the high speed and high traction forward gaits using the general *n*-module gait dynamics model from Section 4.5. To conduct the comparison, we first generate a 4-module robot model using the dynamics model. We then simulate the joints movements between Steps 1-2 for the high speed gait

and monitor reaction forces generated at engaged friction anchor, d_1 and d_2 . Next, we simulate the joints movements between Steps 1-4 for the high traction gait and monitor reaction forces generated at engaged friction anchor. Finally, we compare the two sets of friction anchor reaction forces to confirm that implementation of the high traction gait does indeed reduce the required engagement forces from friction anchor to resist the reaction forces from forward movement.

We begin with 4-module model with arbitrary physical parameters developed using the general gait model, illustrated in Figure 4.32. The model executes the transition from Step 1 to Step 2 of the high speed forward gait, as observed in Figure 4.23 and 4.33.

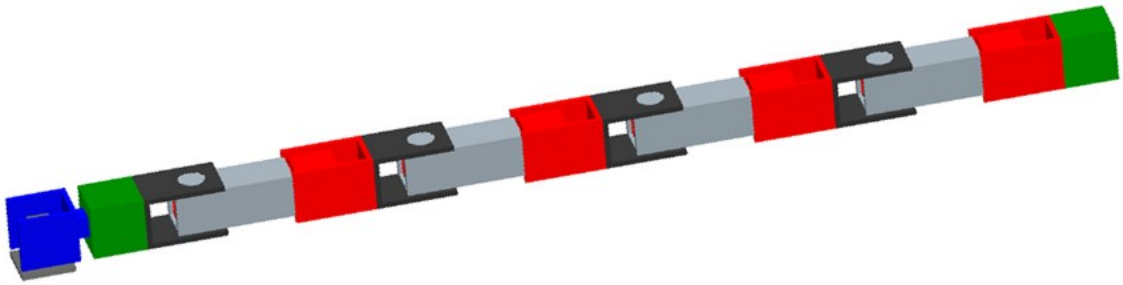


Figure 4.32: n -Module Model of High Speed Forward Gait Step 1

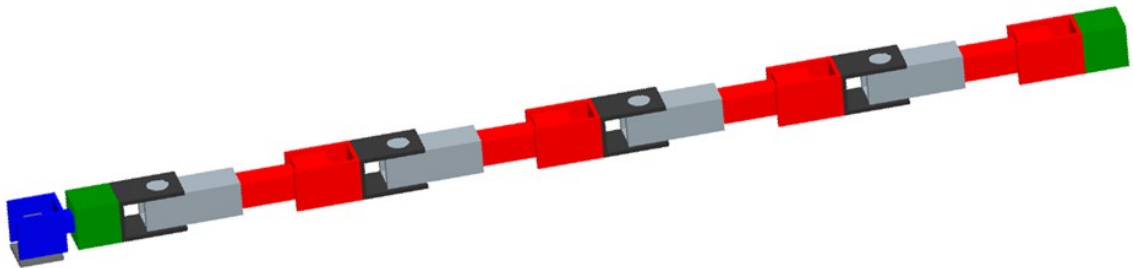


Figure 4.33: n -Module Model of High Speed Forward Gait Step 2

The resulting planar z -direction, d_1 , and x -direction, d_2 , reaction forces at the engaged friction anchor during the Step 1-2 transition are displayed in Figure 4.34. While observing Figure 4.34, we notice that the reaction forces in the z -direction are zero

throughout the transition between states. This is as expected since the robot is only actuating in the x -direction and therefore, there should be not lateral forces to react in the friction anchor. Next we observe that the reaction force in the x -direction is constant. This is due to the fact that all joint mechanism modules are actuating using the same constant acceleration at the same time.

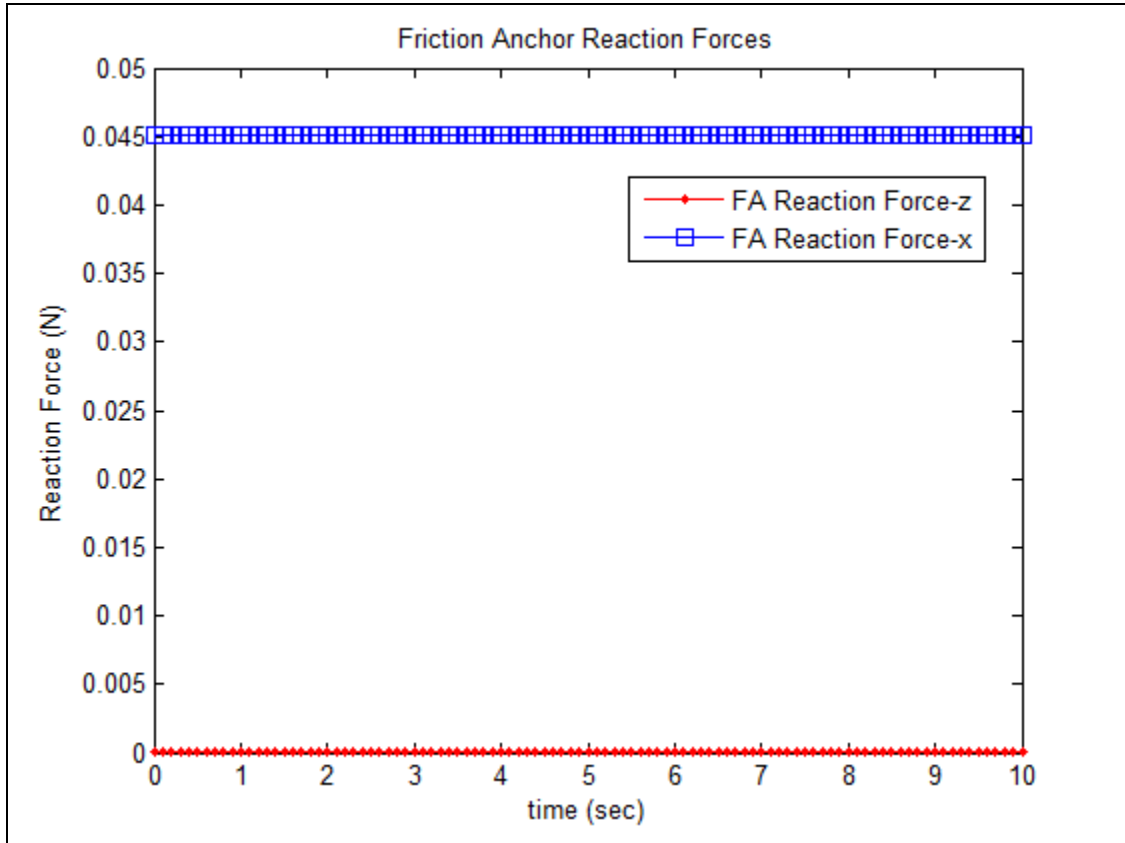


Figure 4.34: Friction Anchor Reaction Forces for High Speed Forward Gait Steps 1-2

Next, we used the same 4-module model with the same arbitrary physical parameters to execute the transition from Step 1 to Step 2 of the high traction forward gait. This trial also uses the same initial starting configuration as the previous high speed gait trial, as observed in Figure 4.35 and 4.36. The resulting planar z -direction, d_1 , and x -direction, d_2 , reaction forces at the engaged friction anchor during the Step 1-2 transition are displayed in Figure 4.37.

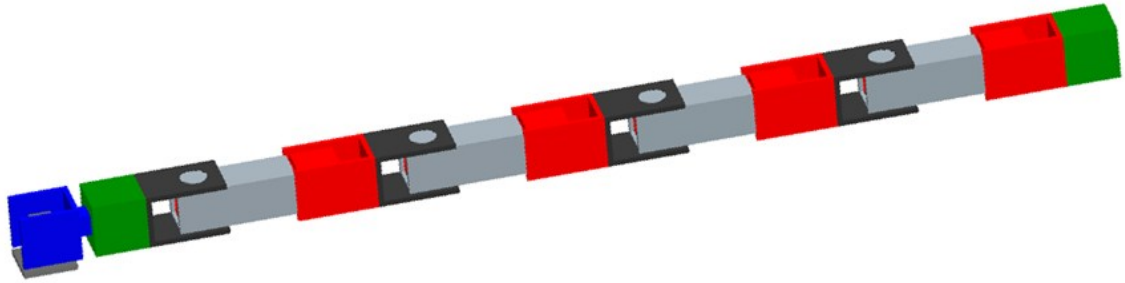


Figure 4.35: *n*-Module Model of High Traction Forward Gait Step 1

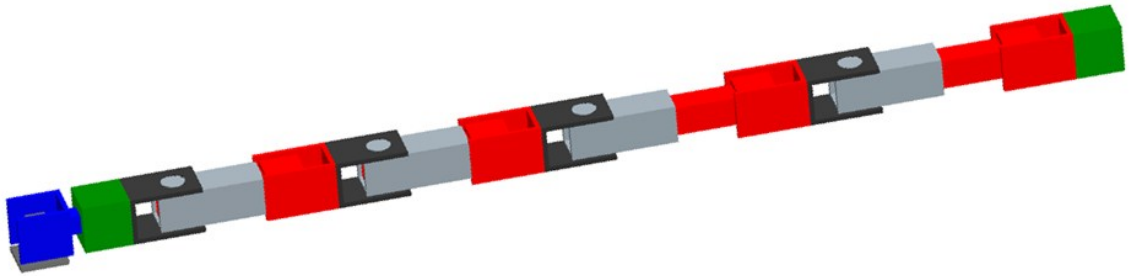


Figure 4.36: *n*-Module Model of High Traction Forward Gait Step 2

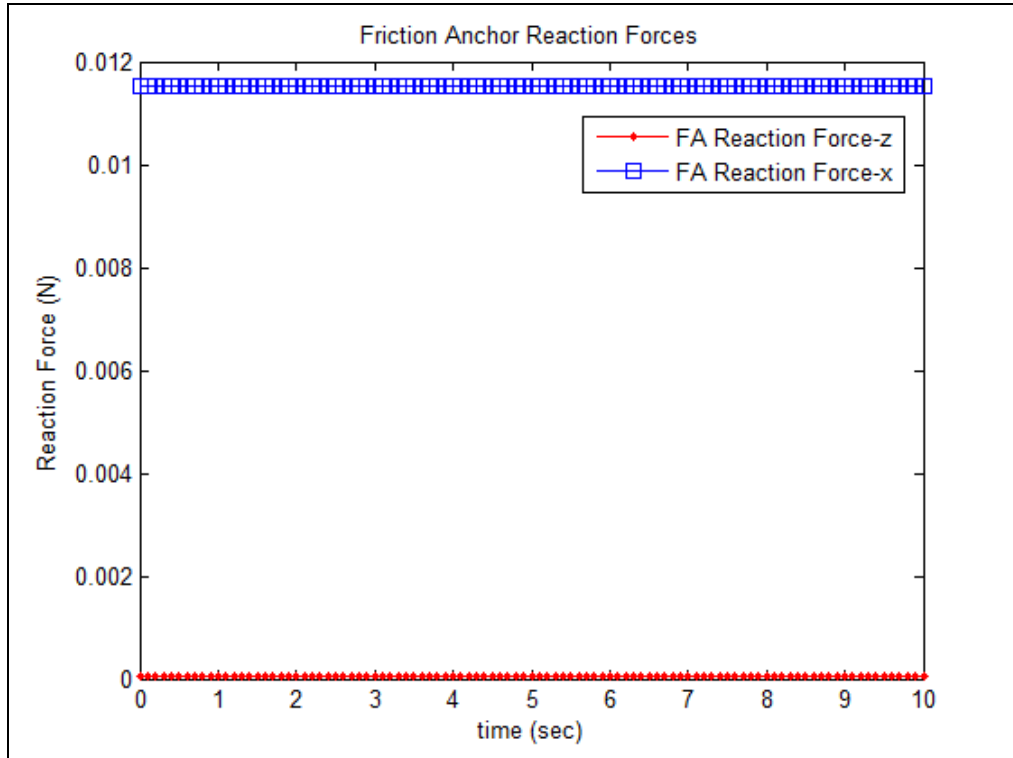


Figure 4.37: FA Reaction Forces for High Traction Forward Gait Steps 1-2

Finally, due to the nature of the traction gait sequence, we must also observe the transition from Step 2 to Step 4, as illustrated in Figure 4.36 and 4.38, to get a clear picture of the total reaction forces developed in the engaged friction anchor. The resulting reaction forces at the engaged friction anchor during the Step 2-4 transition are displayed in Figure 4.39.

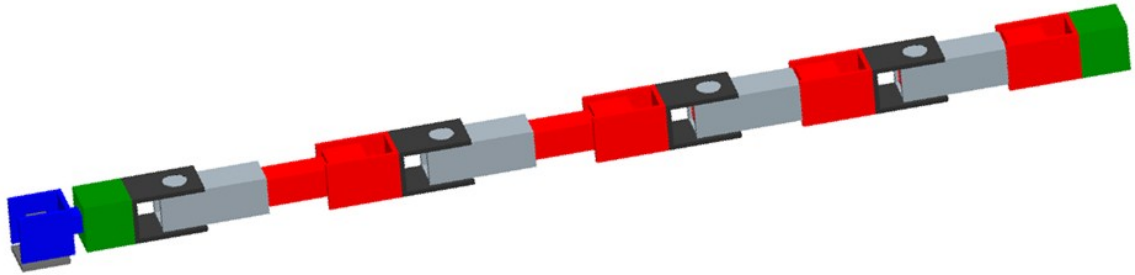


Figure 4.38: *n*-Module Model of High Traction Forward Gait Step 4

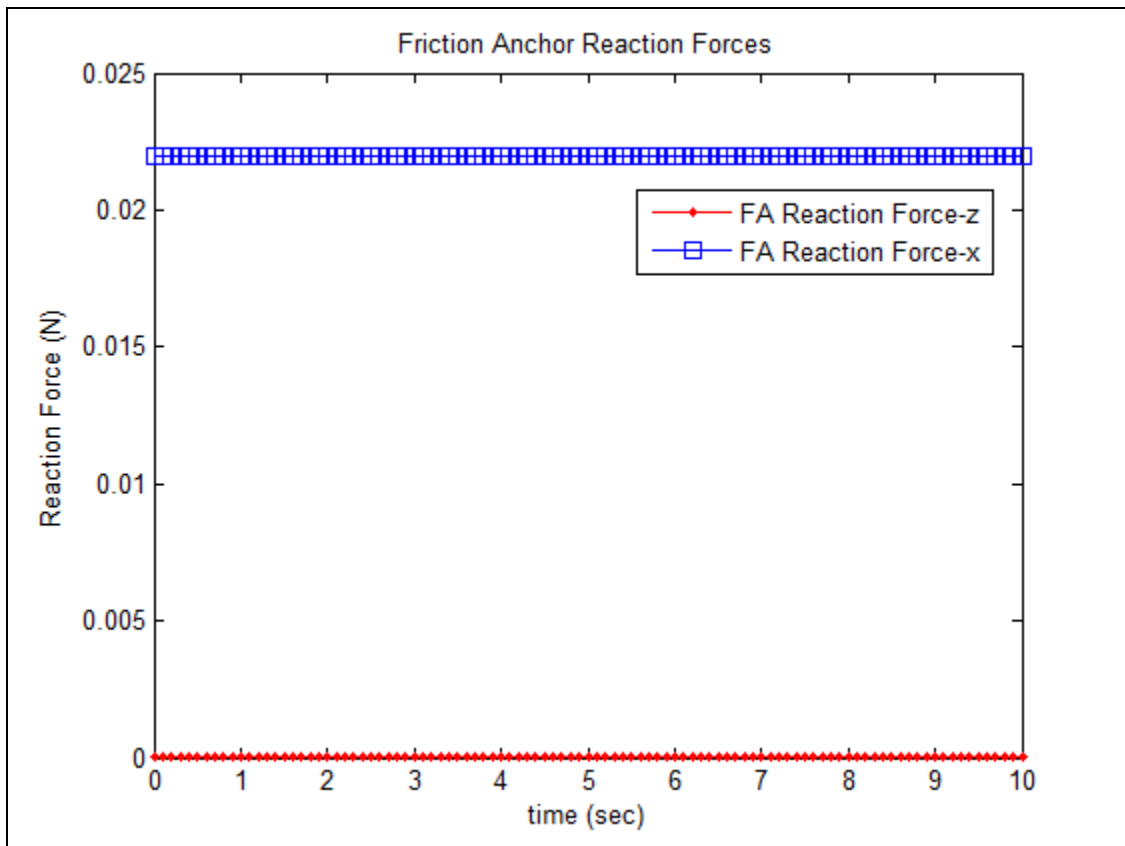


Figure 4.39: FA Reaction Forces for High Traction Forward Gait Steps 2-4

Comparing Figure 4.34 to Figures 4.37 and 4.39, we clearly see that the reaction forces developed in the friction anchor during the high traction gait never exceed half of the forces generated using the high speed gait. Therefore, assuming the anchor between to the two cases is engaged at the same friction anchor angle and employs the same friction material, the anchor in the high traction gait will effectively provide more traction than in the high speed gait.

4.6.3 High Traction Exaggerated Rectilinear Gait Performance

We utilize the snake-inspired robot prototype, R2G2, introduced in Chapter 3 and pictured in Figure 3.31, to demonstrate and physically verify the functionality of the high traction forward gait, as observed in Figure 4.40. The maximum forward velocity observed in the 4-module prototype for this gait sequence is 167 mm/s.

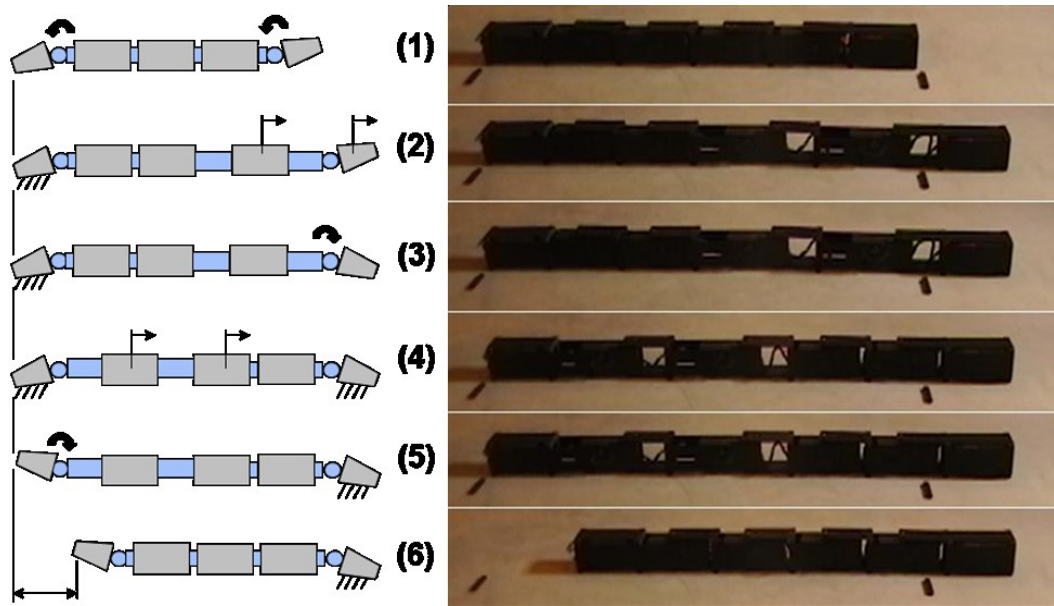


Figure 4.40: High Traction Forward Gait

For performance analysis of the gait using the n -module gait dynamics model, we developed joint mapping schemes as presented in Table 4.4 for an odd n and in Table 4.5 for an even n . For $n = 1$, use the high speed forward gait mapping scheme presented in

Table 4.6. In each gait sequence, the position of each revolute joint, θ_i , can take one of the following values: π (the neutral position), θ_{min} (maximum clockwise position of the joint), or θ_{max} (maximum counterclockwise position of the joint). Each prismatic joint, d_i , can take one of the following values: d_{min} (both parallel mechanism are contracted in the module), d_{mid} (one parallel mechanism is extended and the other contracted) or d_{max} (both parallel mechanisms are extended). The joints d_1 and d_2 are not actuated and therefore are set = 0 throughout the gaits.

Step	θ_3 to θ_n	θ_{n+2}	θ_{n+4} to θ_{2n+1}
1-6	π	π	Π
Step	d_4 to d_{n+1}	d_{n+3}	d_{n+5} to d_{2n+2}
1	d_{min}	d_{min}	d_{min}
2-3	d_{min}	d_{mid}	d_{max}
4-5	d_{max}	d_{mid}	d_{min}
6	d_{min}	d_{min}	d_{min}

Table 4.4: High Traction Forward Gait Mapping to Gait Model for Odd n -Modules

Step	θ_3 to θ_{n+1}	θ_{n+3} to θ_{2n+1}
1-6	π	Π
Step	d_4 to d_{n+2}	d_{n+4} to d_{2n+2}
1	d_{min}	d_{min}
2-3	d_{min}	d_{max}
4-5	d_{max}	d_{min}
6	d_{min}	d_{min}

Table 4.5: High Traction Forward Gait Mapping to Gait Model for Even n -Modules

Step	θ_3 to θ_n	θ_{n+2}	θ_{n+4} to θ_{2n+1}
1-4	π	π	π
Step	d_4 to d_{n+1}	d_{n+3}	d_{n+5} to d_{2n+2}
1	d_{min}	d_{min}	d_{min}
2-3	d_{max}	d_{max}	d_{max}
4	d_{min}	d_{min}	d_{min}

Table 4.6: High Speed Forward Gait Mapping to Gait Model for all n -Modules

We also used R2G2 to demonstrate the high traction turning, as observed in Figure 4.41. The maximum turning speed observed in the 4-module prototype for this gait sequence is 5 deg/s. The joint mapping schemes for the high traction turning gait presented in Table 4.7 for an odd n and in Table 4.8 for an even n . For $n = 1$, use the high speed turning gait mapping scheme presented in Table 4.9.

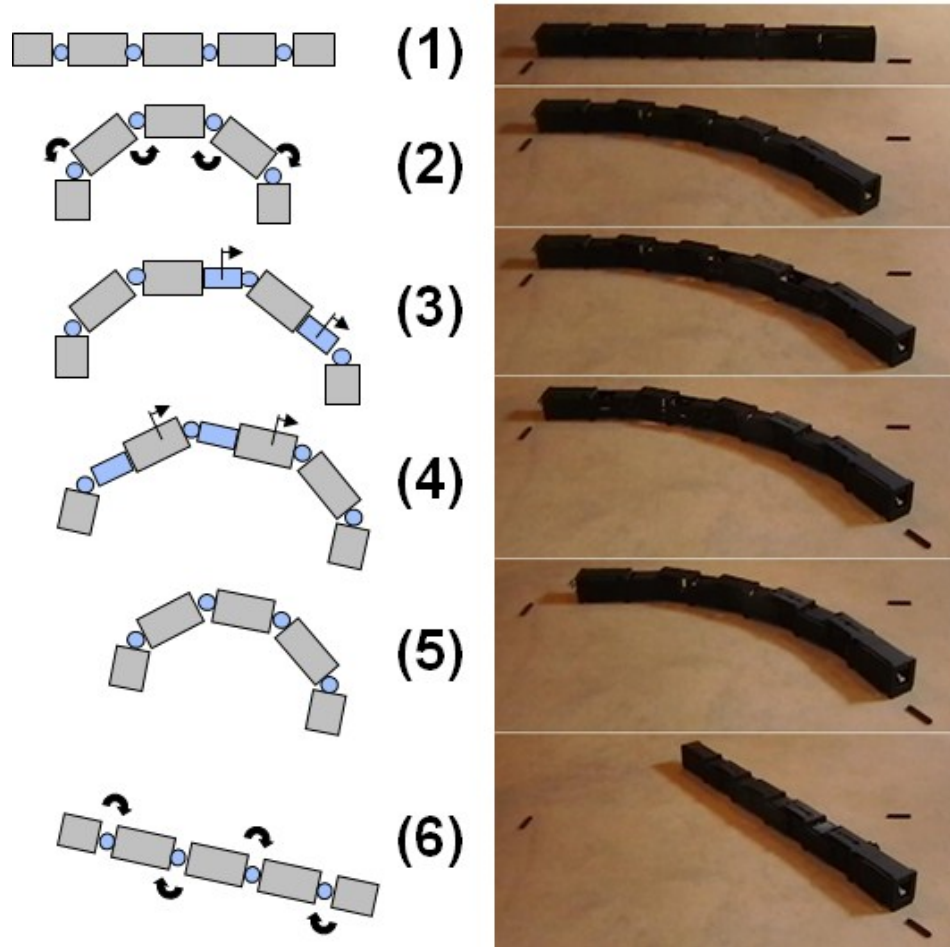


Figure 4.41: High Traction Turning Gait

Step	θ_3 to θ_n	θ_{n+2}	θ_{n+4} to θ_{2n+1}
1	π	π	Π
2-5	θ_{max}	θ_{max}	θ_{max}
6	π	π	Π
Step	d_4 to d_{n+1}	d_{n+3}	d_{n+5} to d_{2n+2}
1-2	d_{min}	d_{min}	d_{min}
3	d_{min}	d_{min}	d_{mid}
4	d_{mid}	d_{min}	d_{min}
5-6	d_{min}	d_{min}	d_{min}

Table 4.7: High Traction Turning Gait Mapping to Gait Model for Odd n -Modules

Step	θ_3 to θ_{n+1}	θ_{n+3} to θ_{2n+1}
1	π	Π
2-5	θ_{max}	θ_{max}
6	π	Π
Step	d_4 to d_{n+2}	d_{n+4} to d_{2n+2}
1-2	d_{min}	d_{min}
3	d_{min}	d_{mid}
4	d_{mid}	d_{min}
5-6	d_{min}	d_{min}

Table 4.8: High Traction Turning Gait Mapping to Gait Model for Even n -Modules

Step	θ_3 to θ_n	θ_{n+2}	θ_{n+4} to θ_{2n+1}
1	π	π	Π
2-3	θ_{max}	θ_{max}	θ_{max}
4	π	π	Π
Step	d_4 to d_{n+1}	d_{n+3}	d_{n+5} to d_{2n+2}
1-4	d_{min}	d_{min}	d_{min}

Table 4.9: High Speed Turning Gait Mapping to Gait Model for all n -Modules

4.7 Summary

In this chapter, we developed and presented a dynamics gait model for the new exaggerated rectilinear gait introduced in Chapter 3. Due to the possibility of high impact forces generated during sudden stops in the exaggerated rectilinear gaits, it was necessary to develop the dynamics gait model so that we can predict the forces generated between

robot segments throughout gait execution. The gait model also allows us to predict reaction forces at the contact points between the friction anchor and the terrain. We developed the gait model based on the Lagrangian formulation. This method was chosen due to the fact that it allowed addition and subtraction of robot links while the equations of motion remain closed form. This feature allows the gait model to handle a variable number of segments or modules.

In addition to the dynamics gait model, we also introduced another set of exaggerated rectilinear gaits: high traction forward and turning gaits. The high traction gait is intended for locomotion on smooth, hard terrains where the use of the friction anchor alone may not be effective. The high traction gait utilizes the ability of the snake-inspired robot design to shift its center of mass to provide additional traction. The effectiveness of the gait was demonstrated using the dynamics gait model to compare reaction forces generated at the friction anchor by the high speed gait to the reaction forces generated by the high traction gait. Furthermore, the R2G2 prototype was employed to physically demonstrate the functionality of the new gait concept.

5 Analysis of an Low Effort Exaggerated Rectilinear Gait

5.1 Overview

Many published snake-inspired robots mimic rectilinear motion by propagating a vertical wave from the aft end of the robot towards the front through changing topography of the body. This motion results in the forward progression of the robot through the lifting and displacement of adjacent segments relative to one another as the wave passes through the body. However, much of the motion observed in the robot throughout the gait cycle is normal to the surface being traversed and does not directly contribute to the change the forward position. Therefore, these gaits tend to be highly energy inefficient and limited in terms of critical performance factors, such as, range. As a result, heavier power supplies will need to be incorporated to increase range, which will require larger motors to carry the increased load. Ultimately, the entire robotic system will be required to be larger, resulting in a platform which is unsuitable for use in small, tight enclosed spaces.

The solution to this problem is to utilize an exaggerated rectilinear gait which more closely mimics the natural snake's motion: moving in a straight line. The exaggerated rectilinear gait will propagate a wave throughout the body of the robot via expansions and contractions of the segments, nearly eliminating all vertical motion in the robot during gait execution, increasing the energy efficiency of the robot's movements. In this chapter, we will characterize the improvement in energy efficiency by performing an analysis of the joint energy in the expansion type rectilinear gait and comparing it to a typical vertical wave type rectilinear gait. In addition, we will test the low effort exaggerated rectilinear gait on our snake-inspired robot prototype, R2G2, introduced in Chapter 3 and

pictured in Figure 3.31, and demonstrate the improvement in energy efficiency. Finally, we will perform a case study the show how an energy efficient gait may require less input power, thereby maintaining a smaller robot platform capable of extended duty.

5.2 *Gait Performance Metric*

Before defining a more efficient rectilinear gait, we must first select an appropriate metric for comparison to the vertical wave rectilinear gait. In earlier attempts to measure robot gait performance, total gait cycle time was often considered [99]. However, the total amount of energy expended during execution of the gait was not addressed with a simple reduction in gait cycle [100]. Effort was considered to be a better gait performance metric as it takes into account the amount of torque, time and energy to achieve the desired joint motion [101, 102]. Hence we will use effort as the metric to describe an energy efficient gait. The formulation for effort is presented as follows:

$$J = \frac{1}{2} \int_0^t \|\tau\|^2 dt. \quad (5.1)$$

$$J = \frac{1}{2} \sum_{i=1}^{n-1} \left(\frac{t}{n} \right) \left[\sum_{j=1}^m \tau_{(i+1)j}^2 + \sum_{j=1}^m \tau_{ij}^2 \right] \quad (5.2)$$

Equation 5.2 gives the trapezoidal approximation of the effort function from Equation 5.1. The variable m represents the number of powered joints in the mechanism. The number of intervals of time is given by the variable n and the total cycle time is given by the variable t . Finally, the variable τ_{ij} is the value of torque for joint j at time interval i .

The individual joint torque values used in formulating the effort metric are obtained as a result of the kinematics and dynamics models for the gaits. The joint trajectories used to generate the joint torques will have their time history of joint parameters represented by B-spline curves or functions. A cubic B-spline with five control points was chosen to

represent the joint positions, based on successful results observed in other robot gait problems [103, 104]. The parameterization of the curve was done from 0 to t_4 , to describe the step time, the time required to change the configuration of the sub-mechanism in each gait step. The knot vector, T , for each B-spline function of the parameterized curve is given as follows, where an evenly spaced time interval is assumed:

$$T = \left[0 \quad 0 \quad 0 \quad 0 \quad \frac{t_4}{4} \quad \frac{t_4}{2} \quad \frac{3t_4}{4} \quad t_4 \quad t_4 \quad t_4 \quad t_4 \right] \quad (5.3)$$

Although there are seven control points, there are only five distinct points. The two exterior control points are repeated to achieve the desired boundary condition, zero angular velocity at the terminal states of the joint motion. The exterior points are the beginning, θ_i , and ending angles, θ_f , of the interval. The interior control points, designated as C are the free variables. The control points are given as:

$$P = [\theta_i \quad \theta_i \quad C_1 \quad C_2 \quad C_3 \quad \theta_f \quad \theta_f] \quad (5.4)$$

Since the gaits described in this work are comprised of several discrete steps, we elected to compare the energy efficiency of each gait using cumulative effort. We define cumulative effort as the additive effort of each step over the entire gait cycle. Thus for a given gait, the magnitude of the cumulative effort at the final time interval of the cycle is the sum of all effort for each step of the gait. Furthermore, a plot of cumulative effort over gait cycle time provides an indication of the energy consumption of the robot throughout the gait cycle. Utilizing these cumulative effort plots, we are able to make general comparisons of the gaits in terms of energy consumption per cycle.

5.3 *Analysis of a Typical Vertical Wave Rectilinear Gait*

In order to define an energy efficient rectilinear gait, we must first establish a baseline gait for comparison. Since the objective of this work is to demonstrate energy efficiency beyond the vertical wave type rectilinear gait, we begin with a well-defined gait of that type. We select a gait, introduced by Merino et al. and later modified and dynamically modeled by Spranklin, as observed in Figure 5.1 [77, 84]. This gait was selected because Spranklin conducted a complete analysis of the joint energy required for its execution.

The sequence for Spranklin's gait can be described by three unique mechanisms: $M1$, $M2$ and $M3$ formed as the vertical wave travels through the length of the robot as observed in Figure 5.1. In Step 1, the last three links lift from the terrain, while the tip of last link of the robot remains in contact with the surface (acting as a coupled slider and revolute joint), forming $M1$. Note that $M1$ involves the use of three joints. In step 2, the last link returns to its rest configuration, while the link's tip remains in the new location due to friction (advanced a distance from the initial location at the beginning of the gait). Simultaneously, the remaining two lifted links and the adjacent link forward of the pair form a trapezoidal configuration with the terrain, forming $M2$. $M2$ involves the use of four joints. In step 3, the vertical wave is advanced through the center of the robot. The last lifted link in the chain from $M2$ returns to the rest configuration, again while the remaining lifted links and the next adjacent forward link form the trapezoid, forming $M3$. $M3$ involves a total of five revolute joints. To complete the gait sequence, the robot executes step 4 and 5, which are the reverse sequences of step 2 and step 1, respectively. Once the cycle has completed, the robot has advanced a distance equal to the length traveled by the tip of the last link in step 1.

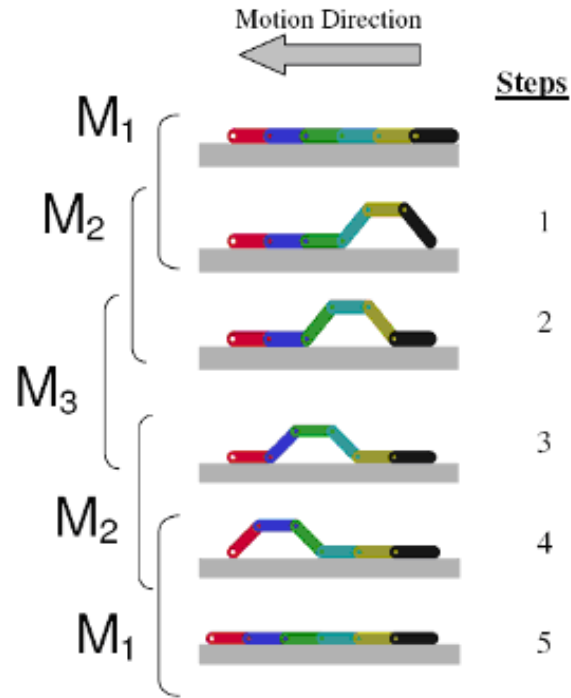


Figure 5.1: Vertical Wave Rectilinear Gait [84]

To provide a proper comparison for an energy efficient gait, we must define a set of global gait parameters for use in each gait. We maintained the same number of modules, module mass and module length, l , for each gait, as described in Table 5.1.

Number of Modules	5
Joints per Module	1
Module Length (l)	0.14 m
Module Mass	0.75 kg
Time per Gait Step (k)	1 s

Table 5.1: Vertical Wave Gait Parameters

In addition to the general gait parameters, the vertical wave type gait has one unique parameter which must be addressed: gait angle, α . Gait angle defines the maximum amount of radial travel allowed for any revolute joint in the robot [84]. It defines the shape of the traveling vertical pulse in the gait. Gait angle also defines cyclic displacement, d , (Equation 5.3) and effort of the gait.

$$d = 2l - 2l \cos(\alpha) \tag{5.3}$$

In Figure 5.2, we plotted cumulative effort for the vertical wave gait using the Table 5.1 gait parameters, Equation 5.2 and Spranklin’s dynamics model for a vertical wave gait [105, 106]. The only parameter varied in each plot was the gait angle. From the plot, it can be observed that small increases in gait angle results in significant increases in effort. However, according to Equation 5.3, smaller gait angles results in significantly smaller displacements per cycle. The cyclic displacements for the vertical wave gaits from Figure 5.2 ranged from 0.04 m per cycle (30 deg) to 0.14 m per cycle (60 deg).

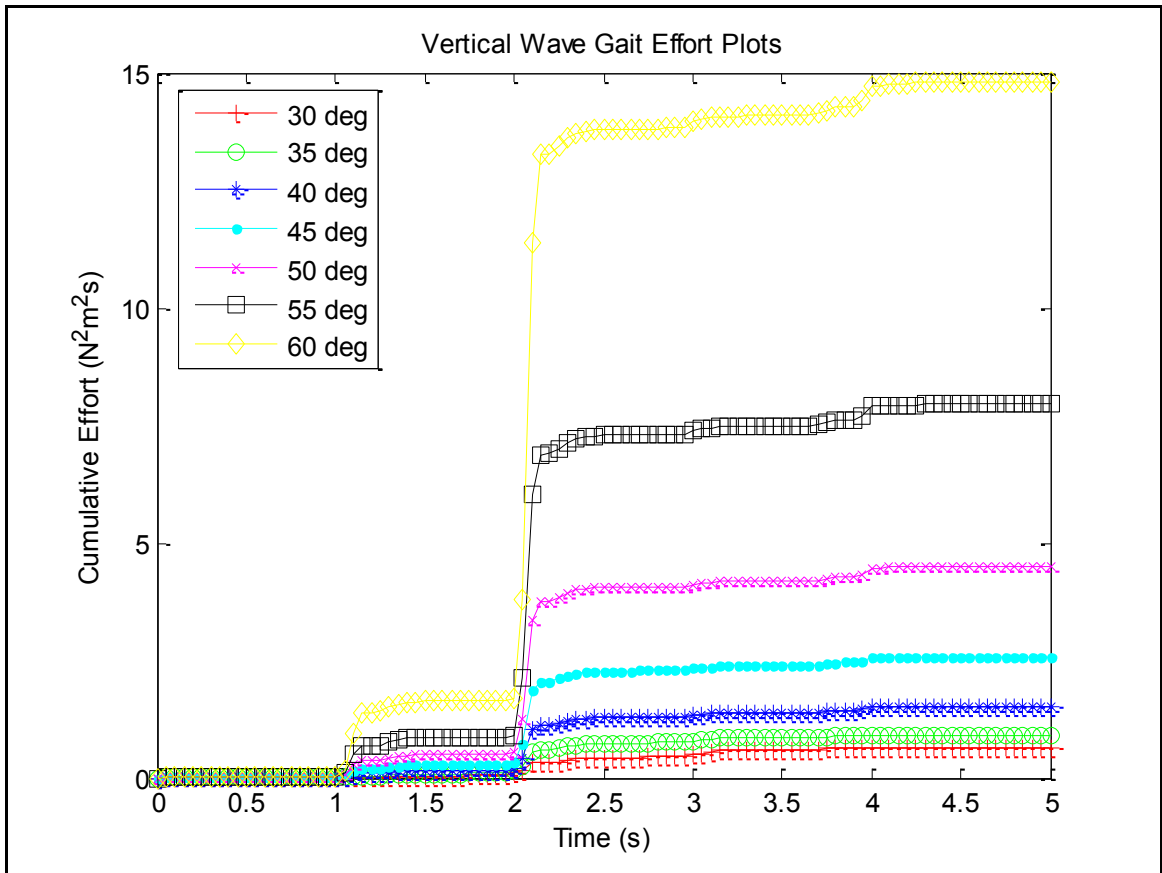


Figure 5.2: Cumulative Effort over Time for Typical Vertical Wave Rectilinear Gait

5.4 Low Effort Exaggerated Rectilinear Gait

The main theory of this work suggests that a robot executing an expansion type rectilinear gait-based on the propagation of a wave through pure linear expansion and contraction is far more energy efficient compared the vertical wave type rectilinear gait. This theory is based on the fact that gaits, such as the one pictured in Figure 5.1, expend a significant amount of joint energy in the changing robot topography for a relatively small advancement per cycle. In defining an energy efficient rectilinear gait, we reviewed the literature and found a very promising gait in the work from Chen et al. [46] for inchworm motion. Chen's gait linearly advances one module at a time, while propagating a wave forward through the robot. We theorize that this gait yields a very low effort per cycle, since no more than two joints are actuated at any given time and no links are lifted from the terrain. However, Chen's gait was design to be used for an inchworm robot in channel, a rail-like track, using grippers on each module to anchor against the sides of the channel. Thus, we slightly modified the gait for use on our snake-inspired robot, R2G2, introduced in Chapter 3 and pictured in Figure 3.31, with high speed linear actuators in each module and anchors only on each terminal module. The modified low effort rectilinear gait sequence is observed in Figure 5.3.

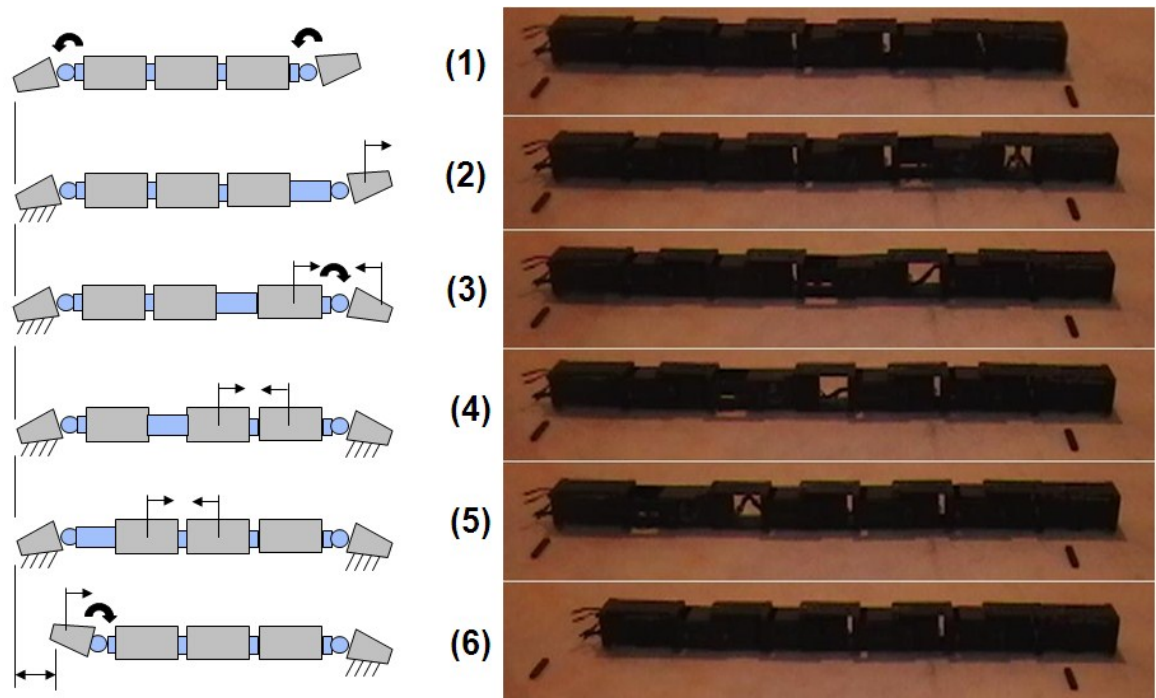


Figure 5.3: Low Effort Rectilinear Gait

The sequence for the low effort rectilinear gait, pictured in Figure 5.3, can be described by the following:

- Step 1 – The robot begins in its nominal configuration, where all modules are contracted and the anchors are not engaged with the surface. The anchor on the aft end of the robot engages to absorb reaction forces from the expansion of the robot while maintaining the position of the rear end of the robot.
- Step 2 – The forward module expands to its maximum length – locating the forward most portion of the platform a distance from the rear, equal to the robot’s contracted length plus the displacement of the first module.
- Step 3 – The forward friction anchor engages to prevent any further global position change of the robot. The front module contracts, while simultaneously, the adjacent module, aft of the forward module, expands. Observe that the global

position of the platform has not changed, however, the position of forward module is now displaced a distance equal to the expansion length of the module.

- Step 4–5 – Step 3 is repeated with the remaining modules and their rear, adjacent neighboring module until the resulting wave reaches the last module in the series.
- Step 6 – The rear friction anchor is disengaged from the terrain. The last module contracts, resulting in the entire robot platform advancing a distance equal to the displacement of a single module's expansion. The robot returns to its nominal configuration and the gait cycle is complete.

Examining the gait sequence in Figure 5.3, it can be inferred that while the gait may yield low instantaneous and cumulative effort values, depending on the number of modules, the sequence may require significant time to complete the cycle. In addition, through modifications of the gait sequence, the distance traveled per cycle can be increased and time required to complete the cycle decreased at the cost of increased effort per cycle. Two such gait modifications were developed and introduced as the high speed rectilinear gait, from Chapter 3, and the high traction rectilinear gait, from Chapter 4. The high speed gait was designed to maximize distance traveled per cycle, while the high traction gait serves as a hybrid between the high speed and low effort gaits. It should be noted that for the high speed and high traction gaits, an increase in the module number increases the distance traveled per cycle, while for the low effort gait, a decrease in the module number decreases cycle time. In a cycle-to-cycle comparison for an equal number of modules greater than two, each of the above gaits would surpass the low effort gait in terms of distance traveled and cycle time. However, the main question is whether or not the two gaits would surpass the low effort gait in terms of distance traveled per energy

expended? In others words, would a robot platform executing the low effort gait travel farther on a single battery charge compared to the platform utilizing the high speed gait and high traction gait? To answer this question, we need to perform an analysis of effort for each gait and conduct a set of experiments using the gaits to verify energy consumption per distance traveled. We present the results in the next section.

5.5 *Robot Parametric Model*

In order to compare the various gaits in terms of energy efficiency, we must first define a method for computing the effort of expansion type gaits. Thus we introduce Figure 5.4, which graphically depicts our procedure for computing total joint effort for an expansion gait.

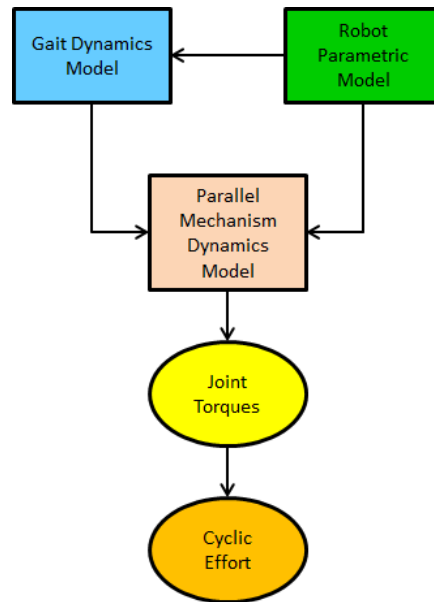


Figure 5.4: Computing Effort for an Expansion Rectilinear Gait

According the Figure 5.4, we must begin with a rectilinear gait dynamics model, introduced in Chapter 4. The gait dynamics model calculates module level joint forces and torques as a result of global robot motion, as defined by the expansion type rectilinear gait sequences. Next we must employ a dynamics model of the joint

mechanism which defines the robot modules. In our design, this is the dynamics model developed for our two degree of freedom parallel mechanism, introduced in Chapter 3. The mechanism dynamics model is required to compute the joint torques for the robot actuators based on the module level motion, forces and torques, which were defined by the gait dynamics model. The calculated joint torque, for each actuator in the robot, is utilizing to compute the total effort for the rectilinear gait using Equation 5.2.

In observing Figure 5.4, we have also determined that there is need for another model, which relates the physical parameters between the parallel mechanism and gait dynamics models, namely a robot parametric model. The robot parametric model is required to define the physical parameters of the parallel mechanism based on the robot parameters. As the robot dimensions scale, the dimensions of the parallel mechanism and its internal components change with a fixed relationship. These changes in the mechanism parameters will have an effect on the joint torques and therefore have to be defined. Therefore, the parametric model is defined and presented in the following.

First we define the parameters for the input links for each of the parallel mechanisms in each module. The mechanism input links of each parallel mechanism are described in detail in Section 3.3.2.2 and are illustrated in Figure 3.9 and Figure 5.5. We define the length of the pivot input arm, p_l , as such:

$$p_l = \frac{e_l}{2 \cos\left(\frac{\pi}{4}\right)} \quad (5.4)$$

Where e_l is given and is the length of the extension input arm. The variable e_l is defined by the extension distance required of the module. The mass of each input arm is defined by the following expressions:

$$e_m = \rho(t_a^2)(e_l + t_a) \quad (5.5)$$

$$p_m = \rho(t_a^2)(p_l + t_a) \quad (5.6)$$

Where e_m and p_m are the masses of the extension input arm and the pivot input arm, respectively. The variable t_a is the thickness of each input arm and is defined by the strength of materials properties and expected load requirement of the input arm material. The density of the arm material is given by ρ . Next we define the parameters for the joint mechanism module, illustrated in Figure 5.5.

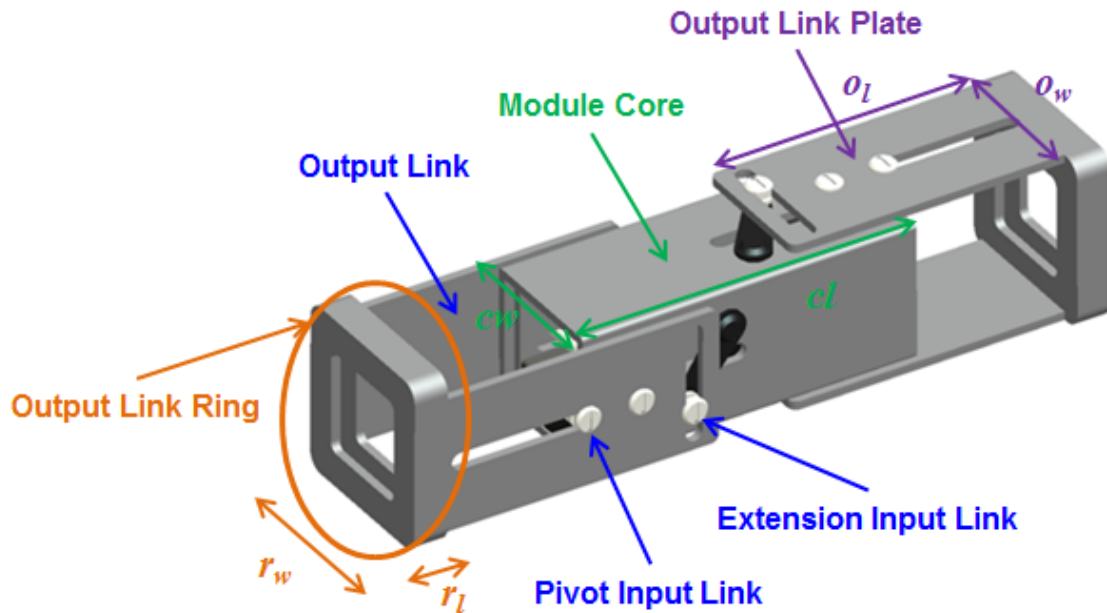


Figure 5.5: Joint Mechanism Module

To define the joint mechanism module, we must first we define the parameters for the module core. The core, as illustrated in Figure 5.5, includes the housing of the servomotor actuators and the actuators. The module core dimensions are defined as follows:

$$c_w = e_l + s_w + 2t_h \quad (5.7)$$

$$c_l = 4s_o + 2e_l \quad (5.8)$$

$$c_m = \rho \left(c_l c_w^2 + c_l t_h (c_w - 2t_h) - c_l (c_w - 2t_h)^2 \right) \quad (5.9)$$

The variables c_w and c_l are the width and length of each module core, respectively. Note, due to the arrangement of the two parallel mechanisms in each module, the width and height of the module core are also equal. In Equation 5.7, s_w is the width each of the servomotor which actuates the input links. The variable t is the thickness of the housing walls. In Equation 5.8, s_o is a constant that describes the offset distance between the servomotor output shaft and the center of the servomotor. Thickness of the plate is defined by t_h . The core's mass is given by c_m and computed by Equation 5.9.

Next we define the parameter of the module output link. Observing Figure 5.5, we define the output link as two components: the ring and the plate. This necessary because adjoining joint modules share an output link, requiring the plate components to be replicated on the free side of the output links shown in Figure 5.5. Therefore to properly describe both a single module and multiple modules in the parametric model, we must define the output link as described. The output link ring parameters are described as follows:

$$r_w = t_a + c_w \quad (5.10)$$

$$r_l = 4t_h \quad (5.11)$$

$$r_m = \rho \left(4t_h (t_a + c_w)^2 - 2t_h (t_a + c_w - 2t_h)^2 - 2t_h (t_a + c_w - 8t_h)^2 \right) \quad (5.12)$$

The variables r_w and r_l are the width and length of each output link ring, respectively. Again, due to the arrangement of the two parallel mechanisms in each module, the width

and height of the rings are also equal. The mass of each ring is given by r_m . Each output link plate is defined as follows:

$$o_w = c_w - 2t_h \quad (5.13)$$

$$o_l = 6t_h + 2e_l + \frac{e_l}{2} \tan\left(\frac{\pi}{4}\right) \quad (5.14)$$

$$o_m = \rho(t_h o_w o_l - 2t_h d_p e_l - t_h d_p (o_w - 2t_h)) \quad (5.15)$$

The variables o_w and o_l are the width and length of each output link ring, respectively. The constant d_p is the diameter of the pivot pin for the parallel mechanism. The mass of each ring is given by o_m .

Finally, the parameters for the complete joint mechanism module are given as follows:

$$m_w = t_a + c_w \quad (5.16)$$

$$m_l = 2r_l + c_l \quad (5.17)$$

$$m_m = c_m + 2r_m + 4o_m + 4s_m + 2e_l + 2p_m \quad (5.18)$$

The variables m_w and m_l are the width and length of each joint module, respectively. The width and height of the joint module are also equal. The mass of each servomotor mechanism is given by s_m . The mass of the module is given by m_m .

The next component in the robot parametric model is the friction anchor module. The friction anchor module is illustrated in Figure 5.6 and its housing parameters are given as:

$$f_w = t_a + c_w \quad (5.19)$$

$$f_l = 2r_l + c_l + 4t_h \quad (5.20)$$

$$h_m = 2r_m + 4\rho c_w t_h (c_l + 4t_h) \quad (5.21)$$

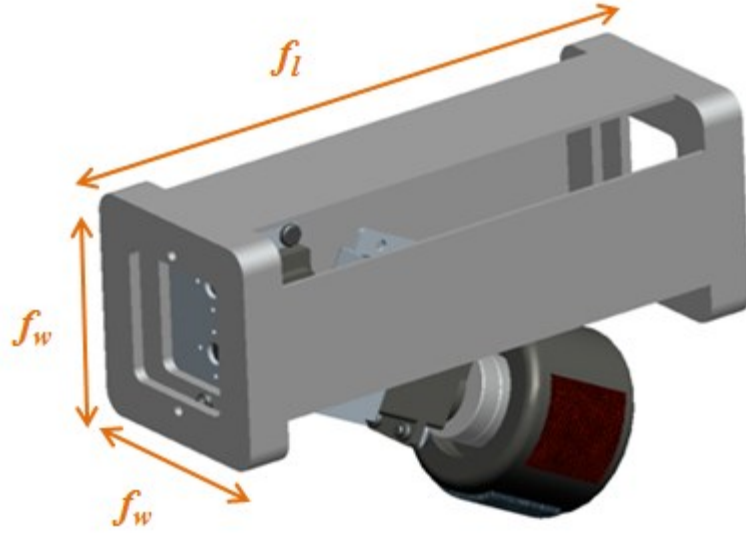


Figure 5.6: Friction Anchor Module

The variables f_w and f_l are the width and length of the friction anchor module housing, respectively. The width and height of the module are also equal. The mass of the module housing is given by h_m . The mass of the friction anchor actuation arm, g_m , is given by Equation 5.22. Therefore, the mass of the friction anchor module, f_m , is given by Equation 5.23.

$$g_m = 2s_m + \rho \left(\frac{f_w^2 t_h}{4} + f_w f_l t_h \right) \quad (5.22)$$

$$f_m = g_m + h_m \quad (5.23)$$

Now that all the robot model components are defined, we are able to define the physical parameters of a complete robot, as illustrated in Figure 5.7. The robot width, Γ_w , robot length, Γ_l , and robot mass, Γ_m , are given as follows:

$$\Gamma_w = t_a + c_w \quad (5.24)$$

$$\Gamma_l = 2f_l + n(c_l) + (n-1)(r_l) \quad (5.25)$$

$$\Gamma_m = 2f_m + n(c_m) + (n-1)(r_m + 4p_m) \quad (5.26)$$

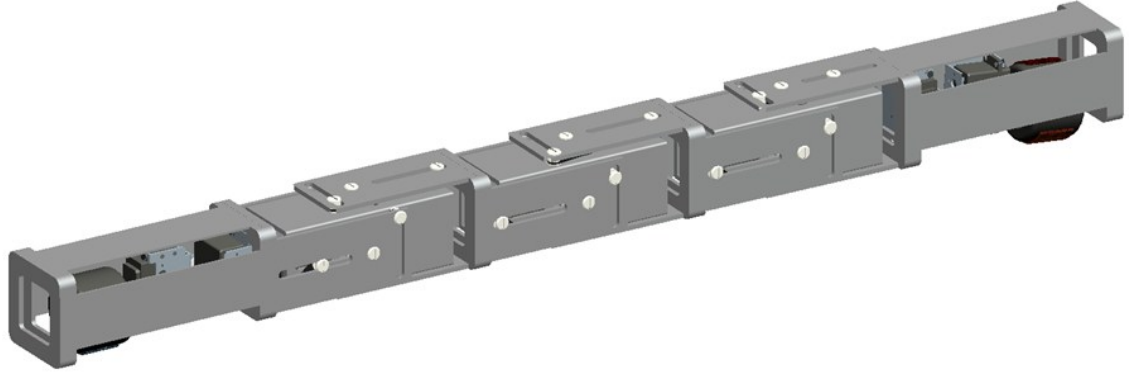


Figure 5.7: Complete R2G2 Robot CAD Model

5.6 *Analysis of Extension Type Rectilinear Gaits*

Utilizing the procedure described in Figure 5.4 and the newly defined robot parametric model presented in Section 5.5, we compute and plot the cumulative effort for each of the expansion type rectilinear gaits. To conduct a comparison between the vertical wave-type rectilinear gait, illustrated in Figure 5.1, and the expansion type gaits, we utilize the same global gait parameters. The gait parameters for the expansion type gaits are given in Table 5.2.

Number of Modules	5
Joints per Module	4
Module Length (l)	0.14 m
Module Extension (e)	0.20 m
Module Mass	0.75 kg
Time per Gait Step (k)	1 s

Table 5.2: Expansion Type Gait Parameters

The modular expansion, e , in Table 2, is based on the kinematics of the parallel mechanism for the joint mechanism module and is computed using the following expression:

$$e = 4e_l \quad (5.27)$$

Since the module is composed of two parallel mechanisms, it is possible to have a

modular expansion length greater than the length of the compressed module, as in Table 2. The cyclic displacement for each expansion type gait is determined using the gait cycle descriptions (Figures 5.3, 5.8 and 5.9) and Equation 5.27. Gait speed is defined by cyclic displacement over the cycle time for each gait as observed in Table 5.3 based on a k equal to 1 s.

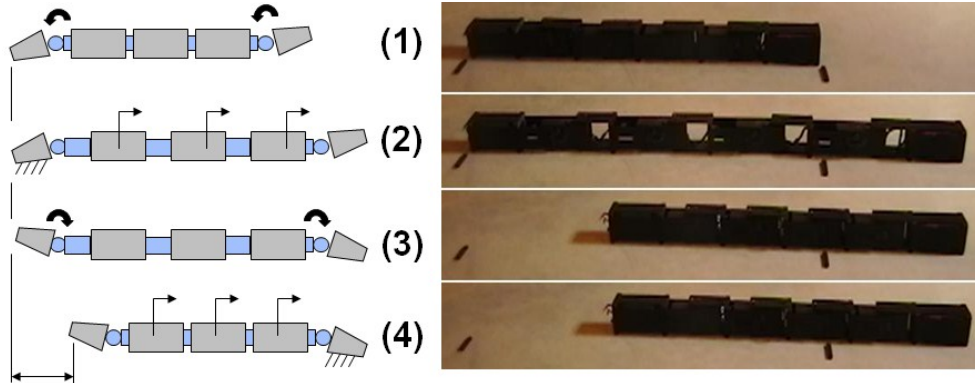


Figure 5.8: High Speed Forward Gait

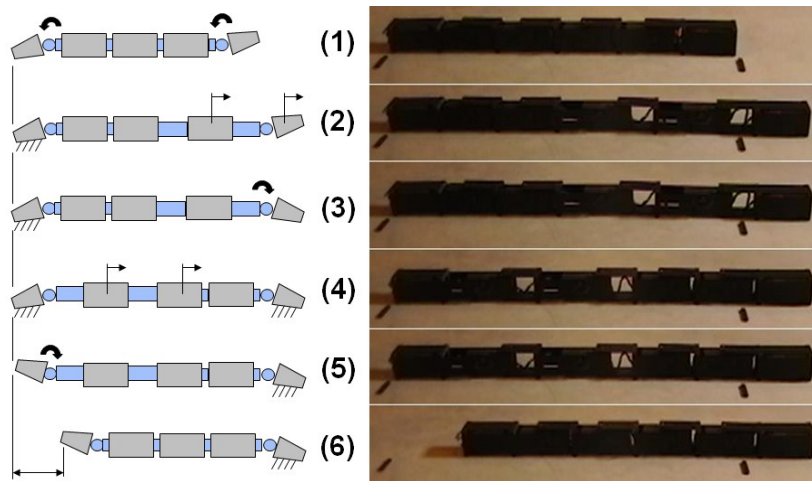


Figure 5.9: High Traction Forward Gait

Expansion Type	Cyclic Displacement	Gait speed
Rectilinear Gait		
Low Effort	0.20 m	0.03 m/s
High Traction	0.52 m	0.17 m/s
High Speed	1.02 m	0.51 m/s

Table 5.3: Cyclic Performance of Gaits

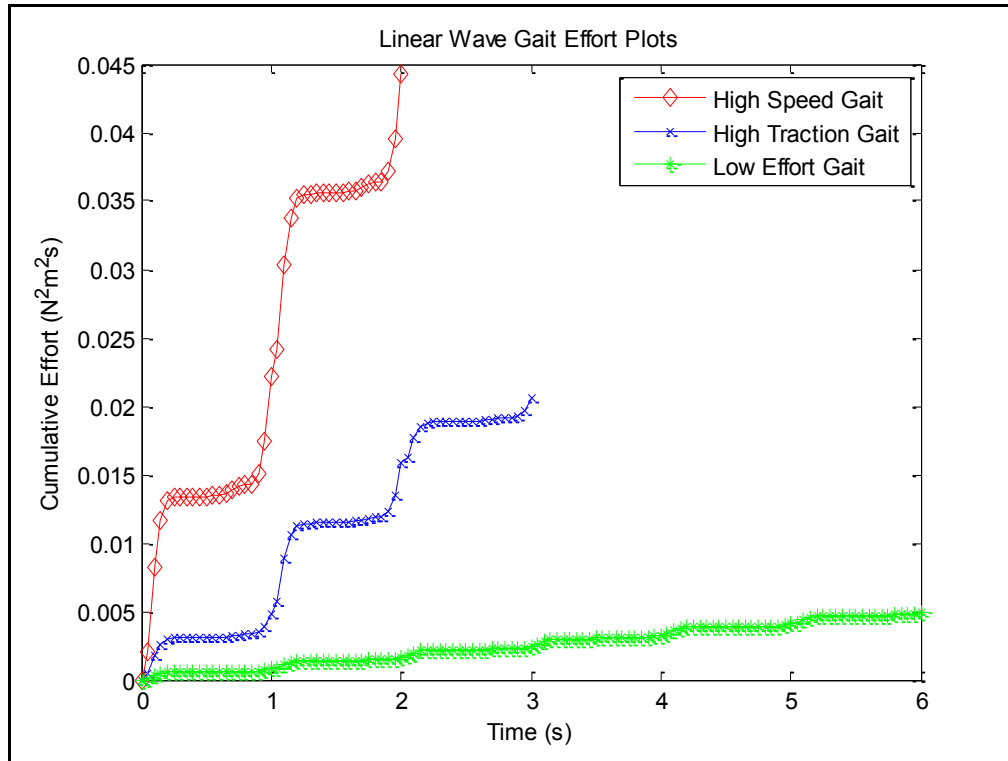


Figure 5.10: Cumulative Effort over Time for Expansion Type Rectilinear Gaits

Using the procedure in Figure 5.4, the cumulative effort for the three expansion type rectilinear gaits is computed and plotted against gait cycle time in Figure 5.8. From Figures 5.2 and 5.10, we observe that the lowest cumulative effort for the vertical wave gaits presented ($\alpha = 30$ degrees) is $0.64 \text{ N}^2\text{m}^2\text{s}$ and the highest cumulative effort for an expansion type gait (high speed) is $0.04 \text{ N}^2\text{m}^2\text{s}$. Therefore, the analysis supports the main theory of this work, that an expansion type rectilinear gait is far more energy efficient than a vertical wave type. Furthermore, Table 5.3 indicates that the high speed gait has 5x the cyclic displacement in $1/3$ the cycle time of the low effort gait and the high traction gait has 2.5x the cyclic displacement in $1/2$ the cycle time than the low effort gait. These results are not unexpected given that more modules tend favor the high speed gait and high traction gait in terms of speed. However, the effort plots indicate that the low effort gait for the given robot platform generates 11% of the effort of the high speed gait and

24% of the effort of the high traction gait. Therefore in this 5-module robot example, for the same energy consumption, the low effort gait travels 1.8x farther than the high speed gait and 1.7x farther than the high traction gait.

While the results of the analysis clearly demonstrate the range advantage of the low effort gait compared to the high speed and high traction gaits, the analysis does not account for actual gait efficiency, such as anchor slippage against the terrain. Therefore to further validate the performance advantage of the low effort, a set of experiments were conducted using the 4-module prototype robot, R2G2 [107]. Note that only the expansion type gaits will be experimentally compared, since the analysis clearly depicts a significant difference in energy consumption for the vertical wave gait. The prototype has a cross section of 0.07 x 0.07 m, a contracted length of 1.00 m, an extended length of 1.38 m, and a mass of 2.5 kg. The robot's on-board batteries were fully charged and the robot traveled a distance equal to the robot's contracted length using each gait. One of the low effort gait trial runs is pictured in Figure 5.11.

Each trial was conducted in a narrow channel, providing a solid reference to ensure each trial run completed the same distance. The number of cycles completed and battery recharge time per trial were recorded. The battery charger used was an IMAX B6 LiPro Balance Charger, which displaced charge time, voltage and amperage. During each full recharge, the battery charger supplied 8.4v at an average current of 0.5A per second. The charger time and charge data were used to approximate the energy drain per gait trial. Prior to the experiment, the cycle time for each gait was programmed and experimentally verified as follows: low effort (2.0 s), high speed (1.0 s) and high traction (1.5 s). Using the energy drain per trial, the number of cycle per trial and the cycle time, the energy

consumed per meter traveled is calculated and presented in Table 5.4.

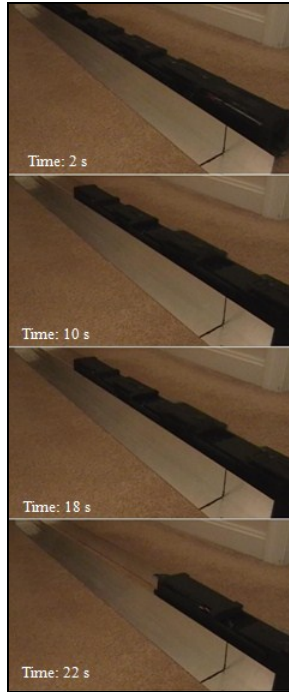


Figure 5.11: Experimental Low Effort Gait Trial

Gait Type	Trial Runs	Charge Time (s)	Energy (J) per m
Low Effort	1	387	2864
	2	466	3448
	3	419	3100
High Traction	4	576	4262
	5	549	4062
	6	518	3833
High Speed	7	640	4736
	8	588	4351
	9	653	4832

Table 5.4: Experimental Gait Performance Data

From Table 5.4, for the same energy consumption, we determine that the low effort gait travels 1.5x farther than the high speed gait and 1.3x farther than the high traction gait. These results show higher energy efficiency for the low effort gait than the

theoretical results due to the very low slippage observed in the low effort gait compared to the other two gaits. The experimental data confirms the results of the analytical study and suggests that a robot operating with the low effort gait possesses a greater range potential than the other gaits. This data suggests that the low effort gait is most useful for two possible scenarios: (1) when maintaining low energy consumption and speed is not critical, such as loitering in an area for data collection; or (2) when minimizing battery consumption to use a mounted device, such as an end-effector or high powered sensor. The latter scenario will be explored in the following case study section.

5.7 Case Study

In order to demonstrate the value of the low effort gait, a case study was conducted to simulate an exploration mission for the snake-inspired robot platform. The mission consists of a robot surveying a stretch of terrain for Improvised Explosive Devices (IEDs) using a metal detector. The robot is also equipped with a powerful solenoid mechanism for detonating possible IEDs. When the detector indicates a possible IED, the robot continuously engages the solenoid until it passes over the object. Engaging the solenoid also rapidly increases the current drain on the on-board batteries. The solenoid mechanism's predicted periods of engagement, duration and energy consumption for the mission are presented in Figure 5.12. The requirement of the mission is to traverse the entire distance to be surveyed (20 m) without recharging the robot. This requirement is critical since approaching the robot before it has completely surveyed the area may be dangerous to personnel. The objective is to evaluate the performance of the robot for this mission using each of the three exaggerated rectilinear gaits (low effort, high speed and high traction) and determine which gait is most appropriate for this scenario. Due to the

analytical comparison of the vertical wave and expansion type gaits, we will not consider the vertical wave gait for this case study as the expansion type gaits surpasses it in terms of effort and gait performance. The subject robot is defined by the gait and robot parameters given in Table 5.5.

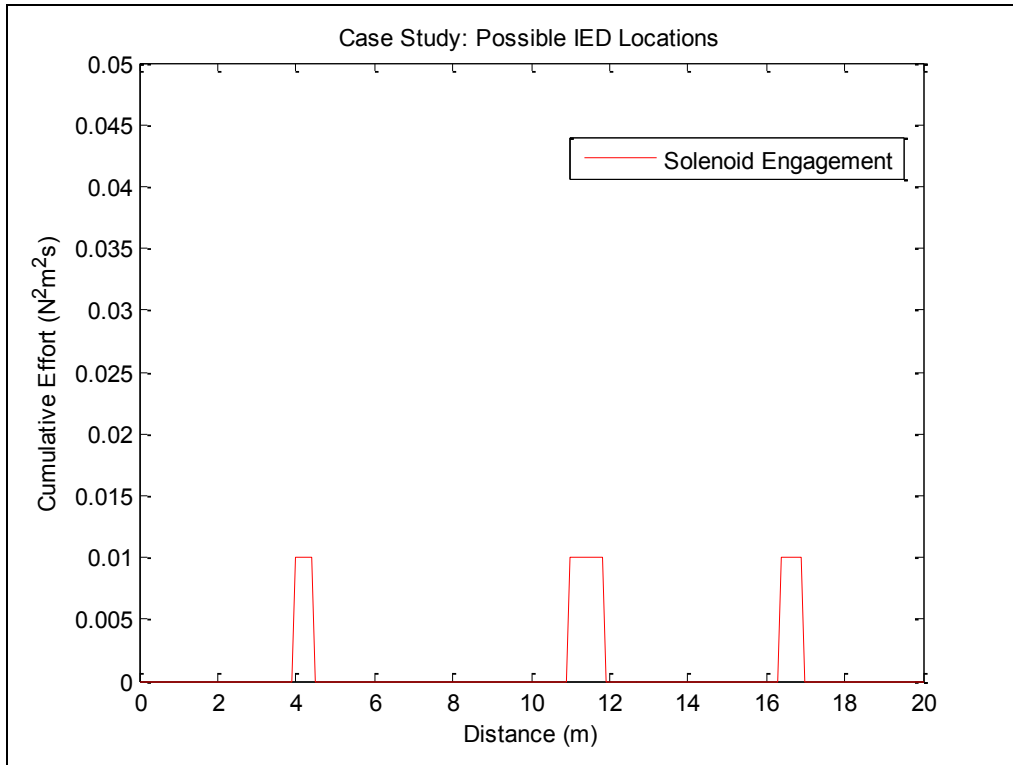


Figure 5.12: Predicted Solenoid Mechanism Engagement

Number of Modules	4
Joints per Module	4
Module Length (l)	0.12 m
Module Extension (e)	0.16 m
Module Mass	0.60 kg
Time per Gait Step (k)	1 s

Table 5.5: Case Study Expansion Type Gait Parameters

Using the robot parameters in Table 5.5, the cumulative effort for each of the three expansion type rectilinear gaits is computed and plotted against gait cycle time in Figure 5.13. The data in Figure 5.13 indicates that the low effort gait for the given robot

platform generates 17% of the effort of the high speed gait and 36% of the effort of the high traction gait. The cyclic performance for each gait type, given in Table 5.6, is calculated using Table 5.5 and Figure 5.13 data.

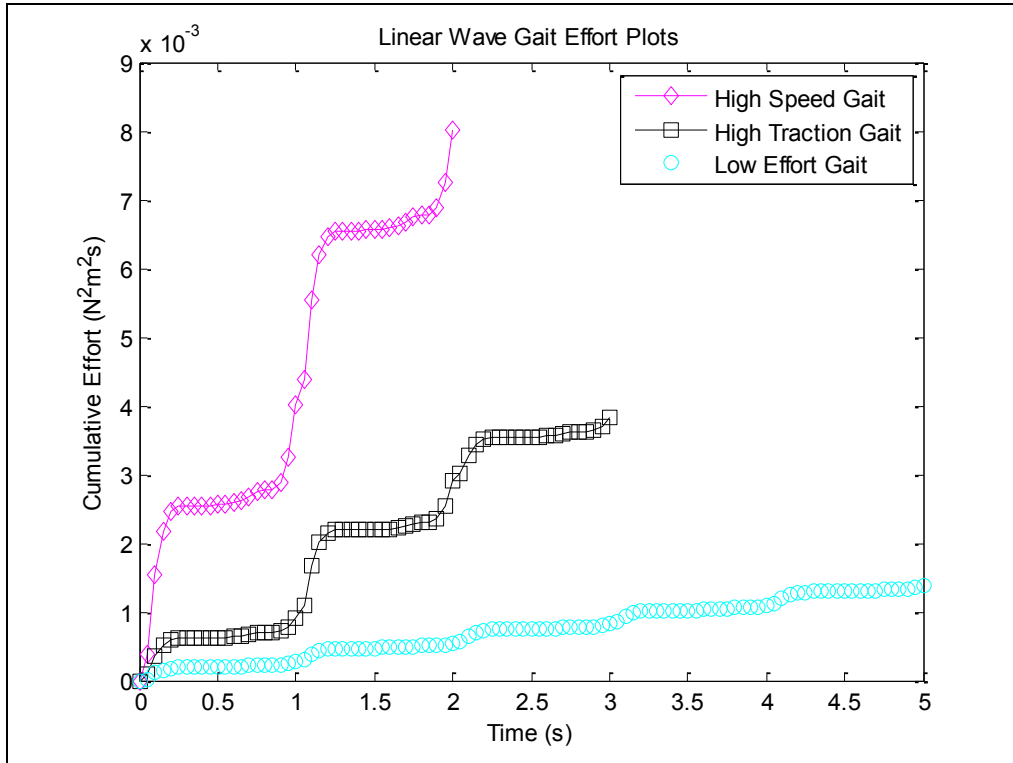


Figure 5.13: Cumulative Effort over Time for Case Study Expansion Gaits

Rectilinear Gait	Cyclic Displacement	Gait speed	Effort (N²·m²·s) per meter
Low Effort	0.16 m	0.03 m/s	0.0086
High Speed	0.64 m	0.32 m/s	0.0125
High Traction	0.32 m	0.11 m/s	0.0120

Table 5.6: Case Study Gait Performance

In addition to the cyclic displacement and gait speed data, Table 5.6 also presents the calculated cumulative effort per meter traveled for the robot for each gait type. Using this parameter, we can predict the distance traveled by the robot before the on-board battery is depleted. Before evaluating the mission, we first verify that the robot is capable of traversing the required distance (20 m) with a fully charged battery, as shown in Figure

5.14. Next, we apply the expected solenoid engagement profile from Figure 5.12 and observe the performance of the three gaits, as pictured in Figure 5.15.

Observing Figure 5.14, it is clear that all three gaits have significant margin to traverse the required distance on a single charge. In this scenario, if the solenoid mechanism was not engaged, the high speed gait would have been preferable since it would have completed the mission 10x faster than the low effort gait and 3x faster than the high traction gait. If the terrain was very smooth and the high speed gait could not gain positive traction, the high traction gait would be a better option, as it is still 3x faster than the low effort gait. However, when the solenoid mechanism is engaged as predicted, shown in Figure 5.15, we observe that only the low effort gait can complete the mission before depleting the robot power supply. The high speed and high traction gaits both cross the battery total charge available threshold during the final solenoid engagement period. As result, the robot will execute the low effort gait for the given mission, providing the safest option for the operator.

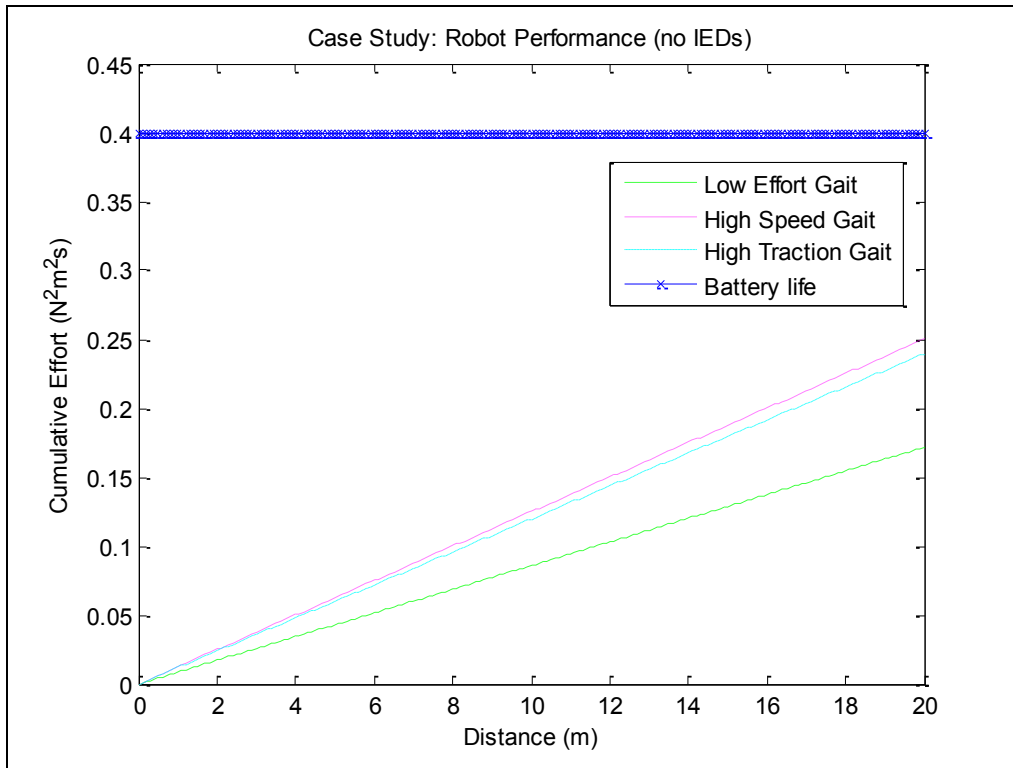


Figure 5.14: Performance of Expansion Type Gaits with no Potential IEDs

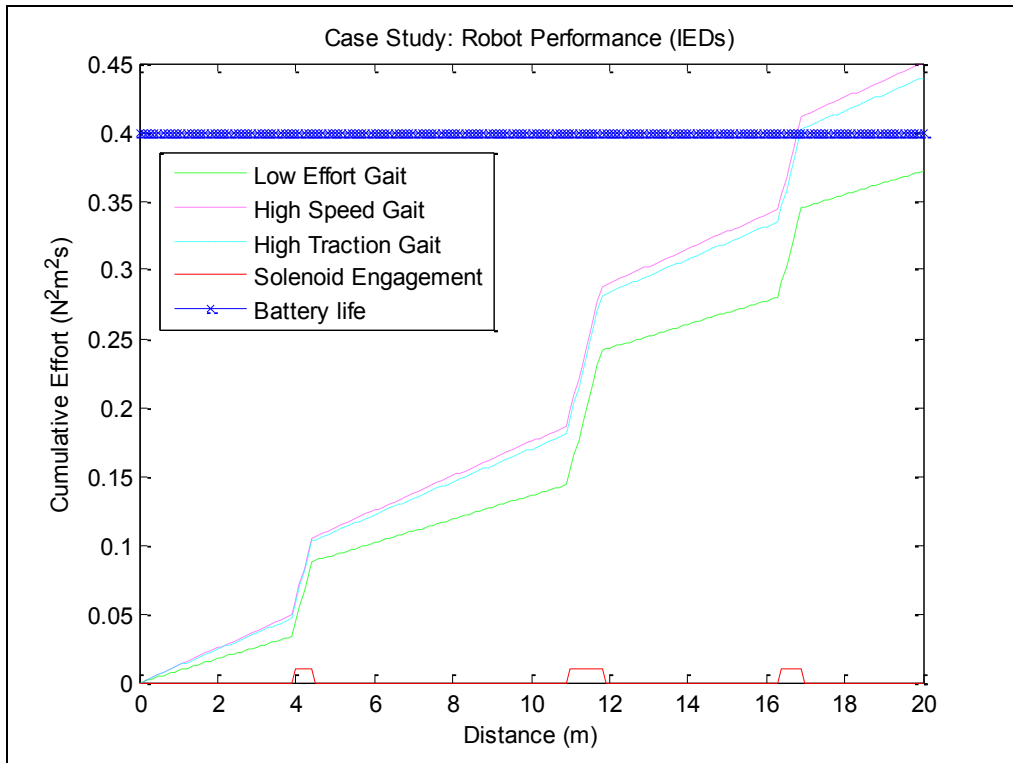


Figure 5.15: Performance of Expansion Type Gaits with Potential IEDs

5.8 *Summary*

In this chapter, we presented the analysis of a low effort exaggerated rectilinear gait for the energy efficient operation of a snake-inspired robot. In this work, we defined and modeled an expansion type exaggerated rectilinear gait characterized by low energy consumption per cycle. The low effort gait was compared to a conventional traveling vertical wave type rectilinear gait in terms of energy consumption. Also, the low effort gait was compared to other exaggerated rectilinear gaits: the high speed gait introduced in Chapter 3 and the high traction gait introduced in Chapter 4. The results of the comparisons indicate that the subject low effort gait has significant range potential over the other rectilinear gaits, examined in this work. In addition to the analysis, a set of locomotion experiments and a case study were conducted and presented to further support the analytical conclusions and illustrate the benefits of the gait.

While the analysis and experimental data presented to support our theory are based on our specific robot mechanism, the conclusions regarding the dynamic behavior of the low effort rectilinear gait can be applied to snake-inspired robots with different linear actuator designs. This assertion is based on the fact that each linear actuator will experience a significantly reduced load at any given moment in time during the execution of the low effort gait in comparison to the high speed and high traction gaits, for a robot with identical modules. However, the delta between the range potential of the expansion type gaits may be influenced by several design and mission factors including: load capacity of the linear actuator, weight of the modules, number of modules, friction within the mechanism, and roughness of the terrain. Selection of these and other factors will determine if the range benefit of the low effort gait is worth the reduction in speed.

Due to the range benefit of the low effort gait, potential applications of the gait include: (1) internal pipe inspection for cracks or other flaws and (2) inspection of a nuclear or potentially radioactive location. During internal pipe inspection, range may be more critical than speed due to the difficulty of retrieving a robot which has run out of power, especially if the robot is tetherless. Inspection of sites with a potential for radioactive contamination may require traversing small, enclosed spaces, which is an ideal task for a snake-inspired robot. Furthermore, due to the potential danger of radioactivity to personnel, maximizing the robot's range is essential to reducing personnel risk.

6 Conclusion

6.1 Intellectual Contributions

The completion of this work makes several contributions to the documented research in the area of snake-inspired robotics. The three most important and potentially useful contributions are: (1) development of a snake-inspired robot capable of executing exaggerated rectilinear gaits, (2) kinematics and dynamics model for exaggerated rectilinear gaits, and (3) identification of a low effort exaggerated rectilinear for supporting various mission type.

6.1.1 Robot Capable of Executing Exaggerated Rectilinear Gaits

The first major contribution of this dissertation is the design and fabrication of a snake-inspired robot capable of executing a high speed exaggerated rectilinear gait. The robot design is composed of a number of serially connected parallel mechanisms. The robot design includes a new high speed planar parallel mechanism capable of linear extension and pivoting its output link. The robot design also employs a redundant modular, non-tethered architecture. Each module is composed of two parallel mechanisms offset 90 degrees about the x -axis, providing the robot with planar as well as spatial motion. This allows the robot to lift its segments from the terrain to cross gaps. The robot design also employs a multi-material, variable friction force anchor mechanism. The anchor mechanism allows robot to obtain positive traction on multiple surfaces. The anchor is capable of selecting the friction material mid-mission to adapt to changing terrain. A 4-module prototype, R2G2, was fabricated to demonstrate the robot architecture and gait concepts. The prototype employs a cross section of 70 x 70 mm,

allowing the robot to traverse small spaces. The prototype achieved a maximum forward velocity of 414 mm/s and a maximum turning speed of 14 deg/s.

6.1.2 Dynamics-Based Gait Model for Exaggerated Rectilinear Gaits

The second major contribution of this dissertation is a kinematics and dynamics-based gait model for the new class of forward and turning exaggerated rectilinear gaits, which is based on high speed actuation and variable static friction force control. The gait model is developed based on the Lagrangian formulation. This method was chosen to accommodate addition and subtraction of robot links while the resulting equations of motion remain closed form. This feature allows the gait model to handle a variable number of segments or modules. Additionally, the model can be used for all gaits developed in this work without modification. The gait model will be beneficial for any future researchers or users of the exaggerated rectilinear gait class: since they will be able to determine all of the relevant forces and torques experienced by a robot during gait execution. Understanding these torques and forces will aid researchers and designers in the selection of critical design features, such as materials for a robot's structure or appropriate actuators for the robot's joint mechanism.

6.1.3 Low Effort Exaggerated Rectilinear Gait for Various Missions

The third major contribution of this dissertation is the identification of a low effort exaggerated rectilinear gait. In theory, this gait yields a very low effort per cycle, since no more than two joints are actuated at any given time and no links are lifted from the terrain. We confirmed this theory by analyzing the gait and comparing the gait to the other expansion type rectilinear gaits introduced in this work in terms of cumulative effort per gait cycle. Also, we compared the gait to a typical example of a vertical wave

rectilinear gait. In conclusion, we demonstrated that the gait generated significantly lower cumulative effort per gait cycle compared to all other analyzed gaits and therefore, the low effort gait provides greater energy efficiency per distance travelled.

6.2 *Anticipated Industrial Benefits*

6.2.1 Enabling New Applications for Snake-Inspired Robots

The first benefit of this dissertation is the enabling of new high speed applications for snake-inspired robots. One such application is the inspection of a structurally unstable building for trapped or incapacitated people. By first surveying the structure for human occupants before committing human rescuers, the risk to the rescue team is greatly reduced by not unnecessarily exposing humans to a dangerous environment. This task is most appropriate for a snake-inspired robot because of its mobility and the fact that the weight distribution of a snake-inspired robot may impart lower stresses in a structurally unstable environment. Although current snake-inspired robots are functionally capable of executing this type of mission, the critical factor is the time required to complete the inspection, as time in a rescue mission may mean the difference between life and death for both the occupants and the rescuers. In this application, a snake-inspired robot executing a high speed exaggerated rectilinear gait would be highly valuable.

6.2.2 Enabling More Efficient Operation

The second benefit of this dissertation is the demonstration of how a snake-inspired robot, operating with a low effort exaggerated rectilinear gait, may enable more efficient operation of the robot for a given task. Due to the range benefit of the low effort gait, potential applications of the gait include: (1) internal pipe inspection for cracks or other

flaws and (2) inspection of a nuclear or potentially radioactive location. One possible outcome of not utilizing an energy efficient gait is that the robot may simply cease functioning prior to the completion of the task, since its on-board power supply is limited. Another possible outcome is that the robot may perform the mission in a wasteful manner and consume more power than is necessary for the mission.

6.3 *Future Research*

6.3.1 Expanding the Gait Dynamics Model for Spatial Applications

The first future research path for this work is to expand the exaggerated rectilinear gait dynamics model to include the pitch motion of each the robot's joint mechanism modules. While the new gait model can be effectively used for analysis of all the rectilinear gaits introduced in this work, the model is limited to planar motion only. The design for the snake-inspired robot is physically capable of spatial motion, such as crossing gaps or inclines. Therefore, future work will include the expansion of the general robot model to include the additional degree of freedom in each module. Furthermore, gaits utilizing the expanded range of motion will be developed for handling obstacles and paths in difficult terrain.

6.3.2 System Level Optimization of the Gait and Robot

The second future research path for this work is the simultaneously optimization of both the gait and module parameters of the high speed robot for a given mission and its performance-based constraints. The system level optimization model would be composed of two sub-models: (1) a flexible parametric system model and (2) meta-model for estimating gait behavior. The flexible parametric system model allows the system level optimization model to define a wide variety of missions. The meta-model allow the

system level optimization model to estimate the physics-based gait behavior associated with the optimal gait for a given set of module parameters. The most useful benefit of the system level optimization model is the ability for a designer to customize the high speed robot design to a specified mission without repeating the analysis work outlined in this dissertation proposal. The model will allow the designer to quickly evaluate many design solutions.

Bibliography

- [1] Dowling, K., 1997, "Limbless Locomotion: Learning to Crawl with a Snake Robot," Ph.D. thesis, The Robotics Institute, Carnegie Mellon University, Pittsburgh, PA.
- [2] Gray, J., 1946, "The Mechanism of Locomotion in Snakes," *Journal of Experimental Biology*, **23**, pp. 101-120.
- [3] Lissman, H. W., 1950, "Rectilinear Motion in a Snake (*Boa occidentalis*)," *Journal of Experimental Biology*, **26**, pp. 368-379.
- [4] Anderson, F. C., and Pandy, M. G., 2001, "Dynamic Optimization of Human Walking," *Journal of Biomechanical Engineering*, **123**(5), pp. 381-390.
- [5] Hirose, S., 1993, *Biologically Inspired Robots: Snake-Like Locomotors and Manipulators*, Oxford University Press, USA.
- [6] Shan, Y., and Koren Y., 1993, "Design and Motion Planning of a Mechanical Snake," *IEEE Transactions on Systems, Man and Cybernetics*, **23**(4), pp. 1091-1100.
- [7] Chirikjian, G. S., and Burdick, J. W., 1993, "Design and Experiments with a 30 DOF Robot," *IEEE International Conference on Robotics and Automation (ICRA)*, Atlanta, GA, **3**, pp. 113-119.
- [8] Chirikjian, G. S., and Burdick, J. W., 1994, "A Hyper-Redundant Manipulator," *IEEE Robotics and Automation Magazine*, **1**(4), pp. 22-29.
- [9] Chirikjian, G. S., and Burdick, J. W., 1995, "The Kinematics of Hyper-Redundant Robot Locomotion," *IEEE Transactions on Robotics and Automation*, **11**(6), pp. 781-793.

- [10] Miller, G. S. P., 2000, "Research on Biomimetic Snakes," *Neurotechnology for Biomimetic Robots*, Nahant, MA.
- [11] Miller, G. S. P., 2002, "Snake Robots for Search and Rescue," In Ayers, J., Davis, J. L., and Rudolph, A., Eds., *Neurotechnology for Biomimetic Robots*, Massachusetts Institute of Technology Press.
- [12] Miller, G. S. P., n.d., "Snake Robots," from www.snakerobots.com.
- [13] Dalilsafaei, S., 2008, "Dynamic Analyze of Snake Robot," *International Journal of Mechanical Systems Science and Engineering*, **1**, pp. 305-310.
- [14] Fukushima Robotics Lab, 2013, "Snake Like Robots," from http://www-robot.mes.titech.ac.jp/robot/snake_e.html.
- [15] Mori, M., and Hirose, S., 2001, "Development of Active Cord Mechanism ACM-R3 with Agile 3D Mobility," *IEEE/RSJ International Conference on Intelligent Robots and Systems (IROS)*, Maui, Hawaii, **3**, pp. 1552-1557.
- [16] Mori, M., and Hirose, S., 2002, "Three-dimensional Serpentine Motion and Lateral Rolling by Active Cord Mechanism ACM-R3," *IEEE/RSJ International Conference on Intelligent Robots and Systems (IROS)*, Lausanne, Switzerland, **1**, pp. 829-834.
- [17] HiBot, n.d., "ACM-R5H" from http://www.hibot.co.jp/en/products/robots_1/acm-r5h_33.
- [18] Expo AICHI Japan 2005, 2005, "Robot Project: Prototype Robot Exhibition," from http://www.expo2005.or.jp/en/robot/robot_project_02.html.

- [19] Crespi, A., Badertscher, A., Guignard, A., and Ijspeert, A. J., 2005, "AmphiBot I: an Amphibious Snake-like Robot." *Robotics and Autonomous Systems*, **50**(4), pp. 163-175.
- [20] Crespi, A., and Ijspeert, A. J., 2006, "AmphiBot II: An Amphibious Snake Robot that Crawls and Swims using a Central Pattern Generator," *9th International Conference on Climbing and Walking Robots (CLAWAR 2006)*, Brussels, Belgium, pp. 19-27.
- [21] Kimura, H., and Hirose, S., 2002, "Development of Genbu: Active Wheel Passive Joint Articulated Mobile Robot" *IEEE/RSJ International Conference on Intelligent Robots and Systems (IROS)*, Lausanne, Switzerland, **1**, pp. 823-828.
- [22] Klaassen, B., and Paap, K. L., 1999, "GMD-SNAKE2: A Snake-like Robot Driven by Wheels and a Method for Motion Control," *IEEE International Conference on Robotics and Automation (ICRA)*, Detroit, Michigan, **4**, pp. 3014-3019.
- [23] Kyriakopoulos, K. J., Migadis, G., and Sarrigeorgidis, K., 1999, "The NTUA Snake: Design, Planar Kinematics, and Motion Planning," *Journal of Robotic Systems*, **16**(1), pp. 37-72.
- [24] Tadokoro, S., Matsuno, F., Onosato, M., and Asama, H., 2003, "Japan National Special Project for Earthquake Disaster Mitigation in Urban Areas," *1st International Workshop on Synthetic Simulation and Robotics to Mitigate Earthquake Disaster*, Padova, Italy, pp. 1-5.

- [25] Osuka, K., and Kitajima, H., 2003, "Development of Mobile Inspection Robot for Rescue Activities: MOIRA," *IEEE/RSJ International Conference on Intelligent Robots and Systems (IROS)*, Las Vegas, Nevada, **4**, pp. 3373-3377.
- [26] Borenstein, J., Granosik, G., and Hansen, M., 2005, "The OmniTread Serpentine Robot – Design and Field Performance," *SPIE Defense and Security Conference, Unmanned Ground Vehicle Technology VII*, Orlando, FL, **5804**(1), pp. 324-332.
- [27] Borenstein, J., Hansen, M. G., and Nguyen, H., 2006, "The OmniTread OT-4 Serpentine Robot for Emergencies and Hazardous Environments," *International Joint Topical Meeting: "Sharing Solutions for Emergencies and Hazardous Environments"*, Salt Lake City, Utah.
- [28] Borenstein, J., and Hansen, M., 2007, "OmniTread OT-4 Serpentine Robot – New Features and Experiments," *SPIE Defense and Security Conference, Unmanned Systems Technology IX*, Orlando, Florida.
- [29] Zhang, H., Wang, W., Deng, Z., Zong, G., and Zhang, J., 2006, "A Novel Reconfigurable Robot for Urban Search and Rescue," *International Journal of Advanced Robotic Systems*, **3**(4), pp. 359-366.
- [30] Zhang, H., Deng, Z., Wang, W., Zhang, J., and Zong, G., 2006, "Locomotion Capabilities of a Novel Reconfigurable Robot with 3 DOF Active Joints for Rugged Terrain," *IEEE/RSJ International Conference on Intelligent Robots and Systems (IROS)*, Beijing, China, pp. 5588-5593.
- [31] Ikeda, H., and Takanashi, N., 1987, "Joint Assembly Moveable Like a Human Arm," U. S., Patent Number 4683406.

- [32] Paap, K. L., Dehlwisch, M., and Klaassen, B., 1996, "GMD-Snake: A Semi-Autonomous Snake-like Robot," *Distributed Autonomous Robotic Systems 2*, Springer-Verlag, Tokyo, pp. 71-77.
- [33] Worst, R., and Linnemann, R., 1996, "Construction and Operation of a Snake-like Robot," *IEEE International Joint Symposia on Intelligence and Systems*, Rockville, MD, pp. 164-169.
- [34] Worst, R., 1998, "Robotic Snakes," *3rd German Workshop on Artificial Life*, Verlag Harri Deutsch, Germany, pp. 113-126.
- [35] Rincon, D. M., and Sotelo, J., 2003, "Ver-vite: Dynamic and Experimental Analysis for Inchwormlike Biomimetic Robots," *IEEE Robotics and Automation Magazine*, **10**(4), pp. 53-57.
- [36] University of Southern California Polymorphic Robotics Laboratory, n.d., "CONRO: Self-Reconfigurable Robots," from <http://www.isi.edu/robots/conro/>.
- [37] Kamimura, A., Kurokawa, H., Yoshida, E., Murata, S., Tomita K., and Kokaji, S., 2005, "Automatic Locomotion Design and Experiments for a Modular Robotic System," *IEEE/ASME Transactions on Mechatronics*, **10**(3), pp. 314-325.
- [38] Gonzalez-Gomez, J., Gonzalez-Quijano, J., Zhang, H., and Abderrahim, M., 2010, "Toward the Sense of Touch in Snake Modular Robots for Search and Rescue Operations," *IEEE International Conference on Robotics and Automation (ICRA) Workshop: "Modular Robots: State of the Art,"* Anchorage, Alaska, pp. 63-68.

- [39] Ohashi, T., Yamada, H., and Hirose, S., 2010, "Loop Forming Snake-like Robot ACM-R7 and its Serpenoid Oval Control," *IEEE/RSJ International Conference on Intelligent Robots and Systems (IROS)*, Taipei, Taiwan, pp. 413-418.
- [40] Kotay, K. D., and Rus, D. L., 1996, "Navigating 3D Steel Web Structures with an Inchworm Robot," *IEEE/RSJ International Conference on Intelligent Robots and Systems (IROS)*, **1**, pp. 368-375.
- [41] Kotay, K. D., and Rus, D. L., 2000, "The Inchworm Robot: A Multi-Functional System," *Autonomous Robots*, **8**(1), pp. 53-69.
- [42] Yim, M., Duff, D. G., and Roufas, K., 2000, "Modular Reconfigurable Robots: An Approach to Urban Search and Rescue," *1st International Workshop on Human Welfare Robotics Systems*, Taejon, Korea.
- [43] Carnegie Mellon University Biorobotics Laboratory, 2013, "Modular Snake Robots," from <http://biorobotics.ri.cmu.edu/projects/modsnake/>.
- [44] Wright, C., Buchan, A., Brown, B., Geist, J., Schwerin, M., Rollinson, D., Tesch, M., and Choset, H., 2012, "Design and Architecture of the Unified Modular Snake Robot," *IEEE International Conference on Robotics and Automation (ICRA)*, Saint Paul, MN, pp. 4347-4354.
- [45] Enner, F., Rollinson, D., and Choset, H., 2012, "Simplified Motion Modeling for Snake Robots," *IEEE International Conference on Robotics and Automation (ICRA)*, Saint Paul, MN, pp. 4216-4221.
- [46] Chen, I-M., Yeo, S. H., and Gao, Y., 2001, "Locomotive Gait Generation for Inchworm-like Robots using Finite State Approach," *Robotica*, **19**(5), pp. 535-542.

- [47] Marvi, H., Meyers, G., Russell, G., and Hu, D., 2011, "Scalybot: A Snake-Inspired Robot with Active Control of Friction," *ASME Dynamic Systems and Control Conference*, Arlington, VA, **8**, pp. 443-450.
- [48] Ohno, H., and Hirose, S., 2000, "Study on Slime Robot (Proposal of Slime Robot and Design of Slim Slime Robot)," *IEEE/RSJ International Conference on Intelligent Robots and Systems (IROS)*, Takamatsu, Kagawa, Japan, **3**, pp. 2218-2223.
- [49] Yeo, S. H., Chen, I. M., Senanayake, R. S., and Wong, P. S., 2000, "Design and Development of a Planar Inchworm Robot," *International Association for Automation and Robotics in Construction (IAARC) 17th International Symposium on Automation and Robotics in Construction*, Taipei, Taiwan, pp. 1-6.
- [50] Chen, I. M., and Yeo, S. H., 2003, "Locomotion of a Two-dimensional Walking-Climbing Robot using a Closed-loop Mechanism: from Gait Generation to Navigation," *The International Journal of Robotics Research*, **22**(1), pp. 21-40.
- [51] Suh, J. W., Homans, S. B., and Yim, M., 2002, "Telecubes: Mechanical Design of a Module for Self-Reconfigurable Robotics," *IEEE International Conference on Robotics and Automation (ICRA)*, Washington, D.C., **4**, pp. 4095-4101.
- [52] Saga, N., and Nakamura, T., 2004, "Development of a Peristaltic Crawling Robot using Magnetic Fluid on the Basis of the Locomotion Mechanism of the Earthworm," *Smart Materials and Structures*, **13**(3), pp. 566-569.
- [53] Lim, J., Park, H., Moon, S., and Kim, B., 2007, "Pneumatic Robot based on Inchworm Motion for Small Diameter Pipe Inspection," *IEEE International Conference on Robotics and Biomimetics (ROBIO)*, Sanya, China, pp. 330-335.

- [54] Yanagida, T., Adachi, K., Yokojima, M., and Nakamura, T., 2012, Development of a Peristaltic Crawling Robot attached to a Large Intestine Endoscope using Bellows-type Artificial Rubber Muscles,” *IEEE/RSJ International Conference on Intelligent Robots and Systems (IROS)*, Vilamoura, Algarve, Portugal, pp. 2935-2940.
- [55] Seok, S., Onal, C. D., Wood, R., Rus, D., and Kim, S., 2010, “Peristaltic Locomotion with Antagonistic Actuators in Soft Robotics,” *IEEE International Conference on Robotics and Automation (ICRA)*, Anchorage, AK, pp. 1228-1233.
- [56] Boxerbaum, A. S., Chiel, H. J., and Quinn, R. D., 2010, “A New Theory and Methods for Creating Peristaltic Motion in a Robotic Platform,” *IEEE International Conference on Robotics and Automation (ICRA)*, Anchorage, AK, pp. 1221-1227.
- [57] Ueno, S., Takemura, K., Yokota, S., and Edamura, K., 2012, “An Inchworm Robot using Electro-Conjugate Fluid,” *IEEE International Conference on Robotics and Biomimetics (ROBIO)*, Guangzhou, China, pp. 1017-1022.
- [58] Tsai, L. W., 1999, *Robot Analysis: The Mechanics of Serial and Parallel Manipulators*, John Wiley and Sons, New York, NY.
- [59] Chirikjian, G. S., and Burdick, J. W., 1995, “The Kinematics of Hyper-Redundant Robot Locomotion,” *IEEE Transactions on Robotics and Automation*, **11**(6), pp.781-793.
- [60] Burdick, J. W., Radford, J., and Chirikjian, G. S., 1993, “A 'Sidewinding' Locomotion Gait for Hyper-Redundant Robots,” *IEEE International Conference on Robotics and Automation (ICRA)*, Atlanta, GA, **3**, pp. 101-106.

- [61] Krishnaprasad, P. S., and Tsakiris, D. P., 1994, "G-Snakes: Nonholonomic Kinematic Chains on Lie Groups," *IEEE Conference on Decision and Control*, Lake Buena Vista, Florida, **3**, pp. 2955-2960.
- [62] Ostrowski, J., and Burdick, J., 1996, "Gait Kinematics for a Serpentine Robot," *IEEE International Conference on Robotics and Automation (ICRA)*, Minneapolis, MN, **2**, pp. 1294-1299.
- [63] Sarrigeorgides, K., and Kyriakopoulos, K. J., 1997, "Steering of a Robotic Snake," *IEEE Mediterranean Conference on Systems and Control*, Pafos, Cyprus.
- [64] Kyriakopoulos, K. J., Migadis, G., and Sarrigeorgidis, K., 1999, "The NTUA Snake: Design, Planar Kinematics, and Motion Planning," *Journal of Robotic Systems*, **16**(1), pp. 37-72.
- [65] Nilsson, M., 2004, "Serpentine Locomotion on Surfaces with Uniform Friction," *IEEE/RSJ International Conference on Intelligent Robots and Systems (IROS)*, Sendai, Japan, pp. 1451-1455.
- [66] Shamma, E. A., Choset, H., and Rizzi, A. A., 2005, "Natural Gait Generation Techniques for Principally Kinematic Systems," *Robotics: Science and Systems I*, Cambridge, Massachusetts, pp. 113-120.
- [67] Shamma, E., Schmidt, K., and Choset, H., 2005, "Natural Gait Generation Techniques for Multi-Bodied Isolated Mechanical Systems," *IEEE International Conference on Robotics and Automation (ICRA)*, Barcelona, Spain, pp. 3664-3669.

- [68] Vossoughi, G., Pendar, H., Heidari, Z., and Mohammadi, S., 2007, "Assisted Passive Snake-Like Robots: Conception and Dynamic Modeling using Gibbs-Appell Method," *Robotica*, **26**(3), pp. 267-276.
- [69] Saito, M., Fukaya M., and Iwasaki, T., 2002, "Modeling, Analysis, and Synthesis of Serpentine Locomotion with a Multilink Robotic Snake," *IEEE Control Systems Magazine*, **22**(1), pp. 64-81.
- [70] Ma, S. Li, W. J., and Wang, Y., 2001, "A Simulator to Analyze Creeping Locomotion of a Snake-like Robot," *IEEE International Conference on Robotics and Automation (ICRA)*, Seoul, Korea, 4, pp. 3656-3661.
- [71] Ma, S., Tadokoro, N., Li, B., and Inoue, K., 2003, "Analysis of Creeping Locomotion of a Snake Robot on a Slope," *IEEE International Conference on Robotics and Automation (ICRA)*, Taipei, Taiwan, **2**, pp. 2073-2078.
- [72] Cortes, J., Martinez, S., Ostrowski, J. P., and McIsaac, K. A., 2001, "Optimal Gaits for Dynamic Robotic Locomotion," *International Journal of Robotics Research*, **20**(1), pp. 707-728.
- [73] Migadis, G., and Kyriakopoulos, K. J., 1997, "Design and Forward Kinematic Analysis of a Robotic Snake," *IEEE International Conference of Robotics and Automation (ICRA)*, Albuquerque, NM, **4**, pp. 3493-3498.
- [74] Nia, H. T., Pishkenari, H. N., and Meghdari, A., 2005, "A Recursive Approach for the Analysis of Snake Robots Using Kane's Equation," *Robotica*, **24**(2) pp. 251-256.

- [75] Hicks, G., and Ito, K., 2005, "A Method for Determination of Optimal Gaits with Application to a Snake-like Serial-link Structure," *IEEE Transactions on Automatic Control*, **50**(9), pp. 1291-1306.
- [76] Chen, L., Wang, Y., Ma, S., and Li, B., 2004, "Studies on Lateral Rolling Locomotion of a Snake Robot," *IEEE International Conference on Robotics and Automation (ICRA)*, New Orleans, LA, **5**, pp. 5070-5074.
- [77] Merino, C. S., and Tosunoglu, S., 2004, "Design of a Crawling Gait for a Modular Robot," *17th Florida Conference on Recent Advances in Robotics (FCRAR)*, Orlando, Florida.
- [78] Poi, G., Scarabeo, C., and Allotta, B., 1998, "Traveling Wave Locomotion Hyper-redundant Mobile Robot," *IEEE International Conference on Robotics and Automation (ICRA)*, **1**, Leuven, Belgium, pp. 418-423.
- [79] Kulali, G. M., Gevher, M., Erkmen, A. M., and Erkmen, I., 2002, "Intelligent Gait Synthesizer for Serpentine Robots," *IEEE International Conference on Robotics and Automation (ICRA)*, Washington, DC, **2**, pp. 1513-1518.
- [80] Chen, L., Wang, Y., Ma, S., and Li, B., 2003, "Analysis of Traveling Wave Locomotion of Snake Robot," *IEEE International Conference on Robotics, Intelligent Systems and Signal Processing*, Changsha, China, **1**, pp. 365-369.
- [81] Rincon, D. M., and Sotelo, J., 2004, "Optimization in the Design of a Dynamically Efficient Inchworm-like Robot," *International Journal of Robotics and Automation*, **19**(3), 105-110.
- [82] Greenfield, A., Rizzi, A. A., and Choset, H., 2005, "Dynamic Ambiguities in Frictional Rigid-body Systems with Application to Climbing via Bracing," *IEEE*

- International Conference on Robotics and Automation (ICRA)*, Barcelona, Spain, pp. 1947-1952.
- [83] Transeth, A. A., Leine, R. I., Glocker, C., and Pettersen, K. Y., 2006, “Non-smooth 3D Modeling of a Snake Robot with Frictional Unilateral Constraints,” *IEEE International Conference on Robotics and Biomimetics (ROBIO)*, Kunming, China, pp. 1181-1188.
- [84] Spranklin, B. W., 2006, “Design, Analysis, and Fabrication of a Snake-Inspired Robot with a Rectilinear Gait,” M.S. thesis, Department of Mechanical Engineering, University of Maryland, College Park.
- [85] Andersson, S. B., 2006, “Pulse-based Gaits for Motion of a Snake-Like Robot,” *8th International Federation of Automatic Control (IFAC) Symposium on Robot Control*, Bologna, Italy.
- [86] Tsai, L. W., 2001, *Mechanism Design: Enumeration of Kinematic Structures According to Function*, CRC Press LLC, Boca Raton, FL.
- [87] Hopkins, J. K., and Gupta, S. K., 2011, “Design of a Drive Mechanism for a Rectilinear Gait-Based Snake-Inspired Robot,” *ASME Mechanisms and Robotics Conference*, Washington DC, **6**, pp. 817-825.
- [88] Bejgerowski, W., Gerdes, J., Hopkins, J., Lee, L., Narayanan, M. S., Mendel, F., Krovi, V., and Gupta, S. K., 2014, “An Engineering Approach to Utilizing Bio-Inspiration in Robotics Applications,” In Goel, A., McAdams, D., and Stone, R., Eds., *Biologically Inspired Design*, Springer-Verlag.

- [89] Hopkins, J. K., and Gupta, S. K., 2012, "Characterization of Forward Rectilinear-Gait Performance for a Snake-Inspired Robot," *Performance Metrics for Intelligent Systems (PerMIS'12) Workshop*, College Park, MD, pp. 136-144.
- [90] Gouker, R. M., Gupta, S. K., Bruck, H. A., and Holzschuh, T., 2006, "Manufacturing of Multi-Material Compliant Mechanisms using Multi-Material Molding," *International Journal of Advanced Manufacturing Technology*, **30**(11-12), pp. 1049-1075.
- [91] Priyadarshi, A. K., Gupta, S. K., Gouker, R., Krebs, F., Shroeder, M., and Warth, S., 2007, "Manufacturing Multi-Material Articulated Plastic Products Using In-Mold Assembly," *International Journal of Advanced Manufacturing Technology*, **32**(3-4), pp. 350-365.
- [92] Banerjee, A. G., Li, X., Fowler, G., and Gupta, S. K., 2007, "Incorporating Manufacturability Considerations During Design of Injection Molded Multi-Material Objects," *Research in Engineering Design*, **17**(4), pp. 207-231.
- [93] Bejgerowski, W. Gupta, S. K., and Bruck, H. A., 2009, "A Systematic Approach for Designing Multi-Functional Thermally Conducting Polymer Structures with Embedded Actuators," *ASME Journal of Mechanical Design*, **131**(11), 111009.
- [94] Bejgerowski, W., Gerdes, J. W., Gupta, S. K., and Bruck, H. A., 2011, "Design and Fabrication of a Miniature Compliant Hinges for Multi-Material Compliant Mechanisms," *International Journal of Advanced Manufacturing Technology*, **57**(5), pp. 437-452.
- [95] Hobbelen, D., and Wisse, M., 2007, "Limit Cycle Walking," In Hackel, M., Ed., *Humanoid Robots: Human-Like Machines*, Itech, Vienna, Austria.

- [96] Hopkins, J. K., Spranklin, B. W., and Gupta, S. K., 2009, "A Survey of Snake-Inspired Robot Designs," *Bioinspiration and Biomimetics*, **4**(2), 021001.
- [97] Hopkins, J. K., and Gupta, S. K., 2012, "Dynamics-Based Model for a New Class of Rectilinear-Gait for a Snake-Inspired Robot," *ASME Mechanisms and Robotics Conference*, Chicago, IL, **4**, pp. 151-160.
- [98] Hopkins, J. K., and Gupta, S. K., 2014, "Design and Modeling of a New Drive System and Exaggerated Rectilinear-Gait for a Snake-Inspired Robot" *ASME Journal of Mechanisms and Robotics*, **6**(2), 021001.
- [99] Sahar, G., and Hollerbach, J. M., 1985, "Planning a Minimum-time Trajectories for Robot Arms," *IEEE International Conference on Robotics and Automation (ICRA)*, St. Louis, Missouri, **2**, pp. 751-758.
- [100] Malladi, S. R., Mulder, M. C., Valavanis, K. P., and Zhang, Y., 1992, "Behavior of a Minimum-Effort Control Algorithm for a Multi-Jointed Robotic Arm," *IEEE International Symposium on Intelligent Control*, Glasgow, Scotland, pp. 34-41.
- [101] Martin, B. J., and Bobrow, J. E., 1999, "Minimum-Effort Motions for Open-Chain Manipulators with Task-Dependent End-Effector Constraints," *The International Journal of Robotics Research*, **18**(2), pp. 213-224.
- [102] Lee, S. H., Kim, J., Park, F. C., Kim, M., and Bobrow, J. E., 2005, "Newton-type Algorithms for Dynamics-based Robot Movement Optimization," *IEEE Transactions on Robotics*, **21**(4), pp. 657-667.
- [103] Martin, B. J., and Bobrow, J. E., 1995, "Determination of Minimum-effort Motions for General Open Chains," *IEEE International Conference on Robotics and Automation (ICRA)*, Nagoya, Aichi, Japan, **1**, pp. 1160-1165.

- [104] Kim, J., Baek, J., and Park, F. C., 1999, "Newton-type Algorithms for Robot Motion Optimization," *IEEE International Conference on Intelligent Robots and Systems (IROS)*, Kyongju, Korea, **3**, pp. 1842-1847.
- [105] Hopkins, J. K., Spranklin, B. W., and Gupta, S. K., 2008, "System-Level Optimization Model for a Snake-Inspired Robot Based on a Rectilinear Gait," *ASME Mechanisms and Robotics Conference*, Brooklyn, NY, **2**, pp. 913-924.
- [106] Hopkins, J. K., Spranklin, B. W., and Gupta, S. K., 2011, "A Case Study in Optimization of Gait and Physical Parameters for a Snake-Inspired Robot Based on a Rectilinear Gait," *ASME Journal of Mechanisms and Robotics*, **3**(1), 014503.
- [107] Hopkins, J. K., and Gupta, S. K., 2013, "Analysis of a Low Effort Gait for a Snake-Inspired Robot," *ASME Mechanisms and Robotics Conference*, Portland, OR.